Laboratoire de Mathématiques Raphaël Salem

N° d'ordre: 1234

THÈSE

Présentée pour obtenir

LE GRADE DE DOCTEUR EN SCIENCES DE
L'UNIVERSITÉ DE ROUEN

Spécialité: Mathématiques

par

Raluca Moglan

Modeling and numerical simulation of flow and heat phenomena in a telecommunication outdoor cabinet

Soutenue le 29 Novembre 2013 devant la Commission d'examen:

Prof.	B. J. Boersma	(Rapporteur, Delft University of Technology, Pays Bas)
Prof.	L. Dumas	(Rapporteur, Université de Versailles)
Prof.	F. Hecht	(Examinateur, Université Paris 6 Pierre et Marie Curie)
Mcf.	H. Louahlia-Gualous	(Examinateur, Université de Caen Basse Normandie)
Prof.	I. Danaila	(Directeur de thèse, Université de Rouen)
Dr.	S. Le Masson	(Codirecteur de thèse, Orange Labs R&D, Lannion)
Prof.	L. Glangetas	(Président du jury, Université de Rouen)

Thèse préparée au
Département de Mathématiques de l'Université de Rouen
Laboratoire de Mathématiques Raphaël Salem (UMR-6085 CNRS), BP.12
Université de Rouen
76 801 Saint-Étienne-du-Rouvray

Abstract

In this thesis we present a new 3D approach for solving the incompressible Navier-Stokes equations, under the Boussinesq approximation. The advantage of the developed numerical code is the use of high order methods for time integration (3rd order Runge-Kutta method) and spatial discretization (6th order finite difference schemes). A study of the order of the numerical method was made, followed by an extensive validation for several cases of natural convection. A finite element simulation code for the same problem was developed using FreeFem++, and was validated with respect to the same cases of natural convection. The case of a telecommunication cabinet was treated by modelling interior obstacles generating heat using an immersed boundary method. This method was validated with respect to the finite element simulation, and many other cases from the literature. We present the results for different 2D and 3D configurations, with obstacles differently placed inside the cavity. Results are also presented for the comparison with experimental measurements in a cabinet with two components dissipating heat. The finite element code is finally extended and tested to simulate phase change materials that could serve as passive cooling devices.

Keywords : Natural convection, high-order methods, study of the order, finite difference, finite element, immersed boundary method, numerical study. .

Simulation numérique des phénomènes thermo-aérauliques dans les armoires de télécommunications

Résumé

Nous proposons dans cette étude une nouvelle approche 3D pour la résolution des équations de Navier-Stokes incompressibles sous l'approximation de Boussinesq. La nouveauté du code développé est l'utilisation des méthodes d'ordre élevé pour l'intégration en temps (schéma de Ruge-Kutta à l'ordre trois) et pour la discrétisation spatiale (schéma aux différences finies à l'ordre six). Une étude de l'ordre de la méthode numérique a été faite, suivie par une validation détaillée pour plusieurs cas de convection naturelle. Une méthode d'éléments finis a été développée pour le même problème, codée avec FreeFem++, et validée pour les mêmes cas de convection naturelle. Nous avons considéré ensuite le cas d'une armoire de télécommunications, modélisée sous la forme d'un domaine rectangulaire, avec des objets (obstacles) intérieurs, représentés par une méthode de type frontière immergée. Cette méthode a été validée par rapport aux cas existants dans la littérature et par rapport aux résultats obtenus avec le code éléments finis (qui représente exactement les obstacles). Nous présentons des résultats pour plusieurs configurations, avec des obstacles chauffants placés différemment à l'intérieur de la cavité. Une comparaison avec les mesures expérimentales effectuées dans une armoire avec deux composantes dissipant de la chaleur est aussi effectuée. Le code de type éléments finis est finalement développé et testé pour simuler des matériaux à changement de phase.

Mots-clefs : Convection naturelle, méthodes d'ordre élevé, étude de l'ordre, différences finies, éléments finis, méthode de frontières immergées, étude numérique..

Acknowledgements

First and foremost I would like to express my special appreciation and thanks to my advisers Professor Ionut Danaila and Doctor Stephane Le Masson. They have been mentors to me and they taught me both consciously an unconsciously how numerical methods as well as experimental methods should be treated and analysed. They represented my YIN and YANG between numerics and experimental. I would like to thank them for encouraging my research and for allowing me to grow as a research scientist. I greatly appreciate all their contributions of time, ideas and funding to make my Ph.D. experience productive and stimulating. Their advice on both research as well as on my career have been priceless. Their encouragement and support were motivational for me, even during tough times in the Ph.D pursuit. Under their guidance I successfully overcame many difficulties and learned a lot.

Professor Ionut Danaila received me into his beautiful family and treated me as one of his children with protective care, support and guidance as well as the necessary gentle 'corrections' during the chaotic times when I lost my way. I could not have imagined having a better advisor and mentor for my Ph.D study. Special thanks to his wife Professor Luminita Danaila for her help during my thesis and patience to answered my many questions.

I would also like to express my deepest gratitude to my coordinating professor during my undergraduate studies and masters thesis, Professor Sterian Danaila without whom I would have never discovered my love for research. I will always remember fondly his advice, support and patience. I thank him for the systematic guidance and great effort he put into training me in the scientific field. I could not be prouder of my academic roots and hope that I can in turn pass on the research values and the dreams that they have given to me.

I gratefully acknowledge the funding sources that made my Ph.D. work possible. I was funded by Orange Labs (France Télécom R&D).

My time at Orange Labs as well as at University of Paris 6 first and during my last year at University of Rouen was made enjoyable due to the many friends and groups that became a part of my life. I am grateful for time spent with colleagues that easily became friends, for my coffee breakers spent together brainstorming and and for many other people and memories. I have been surrounded by wonderful people, both communities have provided a rich and fertile environment to study and explore new ideas. I would also like to thank my committee members and examiners Prof. B. J. Boersma, Prof. L. Dumas, Prof. F. Hecht, Mcf. H. Louahlia-Gualous and Prof. L. Glangetas for serving as my committee members even at hardship. I also want to thank them for letting my defence be an enjoyable moment, and for their brilliant comments and suggestions.

The road to my Ph.D started with training at the National Institute for Aerospace Research Elie Carafoli, Bucharest. I take this opportunity to say heartfelt thanks to Dr. S. Radnef for providing very good training and guiding me through my firs year of work experience in research. I am indebted to my many friends and colleagues for providing a stimulating and fun filled environment. Above all, I would like to thank my husband Adi for his personal support and great patience at all times, for which my mere expression of thanks does not suffice. He was an inspiration throughout my research work lifting me uphill this phase of life, I am grateful to him for never letting me doubt myself and for reminding me there is a whole world outside of my PhD.

I would not have contemplated this road if not for my parents, Maria and Florin, who instilled within me a love of creative pursuits, science and languages, all of which finds a place in this thesis. I take this opportunity to express the profound gratitude from my deep heart to my beloved brother Cata for his love and continuous support. He helped me in ways he doesn't even know and I love and admire him greatly.

My heart felt regard goes to my mother in law, Florica and father in law, Radu for their love and moral support.

It's my fortune to gratefully acknowledge the support of some special individuals. Words fail me to express my appreciation to Alisa, Camelia, Cristi, Andreea, Dragos, Radu and Bogdan. Thank you doesn't seem sufficient but it is said with appreciation and respect to them for their support,encouragement, care,understanding and precious friendship. I am eternally gratefully to Diana who was my ethic advisor in times I most needed. I would also like to acknowledge my friend Gabi, even though are ways split after my first year, he was a dear friend whom I shall miss.

I would also like to extend huge, warm thanks to my best and oldest friend Monica for her kind encouragement and support at hard times. Special thanks to Doina who was my on call psychologist, to whom I believe Orange should also give thanks for great amounts spent on phone bills. I am most grateful to Flori who was my go to person during this thesis at all times of day and night, and has sometimes played the role of my personal chef during many late working night as well as companion and advisor during my shopping therapy sprees. I would also like to thank Cristi for his help and encouragement during this period. Last but not least, I would like to thank Cornelia, who shares my passions and was a role model for me. I wish her best of luck in the endeavour of finishing her own thesis, which I am sure will be exceptional.

It would not have been possible to write this doctoral thesis without the help and support of this kind people around me. I doubt that I will ever be able to convey my appreciation fully, but I owe them my eternal gratitude. **Thank you all!**

Raluca Moglan

2013

Contents

1. Introduction

1.1. Outdoor telecommunication cabinet problem

Due to the deployment of high-speed internet networks it becomes necessary to implement active equipments in outdoor cabinets (see fig. 1.1). An important issue when increasing the number of connected clients is the management of the thermal load of such devices. There are two phenomena generating heat in outdoor cabinets:
• their shells are subjected to severe uncontrolled climate changes and the effects of solar gain can be significant, depending on the size of the enclosure and its orientation relative to the sun;
• internal electronic components generate heat must be evacuated while maintaining the temperature of air within certain limits (prescribed by the ETSI standards, see ETSI (2000)).
Technological progress in electronics allows to install more equipments within smaller spaces. As a consequence, the power dissipated per unit volume increases and leads to a higher operating temperatures that can decrease performance, cause irreversible changes in the operating system, and even failure. Therefore, the power that can be installed in such cabinets is limited, which reduces the number of connected clients.

Figure 1.1.: Outdoor telecommunication cabinet.

The thermal management of telecommunication outdoor cabinets plays an important role in increasing the installed power. A wide variety of thermal cooling methods can be used. These include conventional techniques ranging from passive natural convection to the use of active air conditioners or heat pumps with phase change materials. The internal heat is transferred by convection/radiation inside the enclosure, by conduction through the walls of the chamber, by convection and or radiation with the external environment. Each of these methods has its advantages and disadvantages. In the choice of appropriate cooling, it is necessary to consider not only the thermal parameters of the equipment that is cooled, but also the design and stability of the system, sustainability, technology, price, demand, etc.. An important issue is the balance between the thermal load (or power supply) and maintenance intervals costs. Active systems require a backup power supply and higher levels of maintenance compared to passive systems. On the other hand passive systems do not require power and maintenance, but the increased power density and resulting higher operating temperatures can lead to inefficiencies.

The requirements for an efficient thermal management of outdoor cabinets are numerous. At the component level, some components dissipate heat and warm up until the temperature difference between them and the surrounding environment, serving as heat sinks, is sufficient to remove all heat generated. The heat flow must be such that the temperature rise of the inside electronic devices remain in the operating limits. Since this is not generally possible, cooling systems are added. The first limitations applied to cooling devices are related to the laws of thermodynamics and fluid mechanics. These limitations are not the only ones and, in fact, they may not even be the most important ones. In general there are five criteria that must be considered in the design of a cooling system: cooling capacity, reliability, facility of use, compatibility, and price.

Finally, cooling systems must be able to perform their function in a repeatable and predictable manner. Even faced with a changing external environment, their performance must be sustained over a lifetime, with minimal maintenance. As the reliability of components or sets of components can be increased by redundancy, the reliability of a cooling system can be ensured by doubling some critical parts as: relays, valves or devices for moving the refrigerant fluid. The failure rate of a cooling system must be lower than the components they protect.

1.2. Purpose of the thesis

The purpose of the present work is to investigate the fundamental features of the flow and heat phenomena developing in a telecommunication outdoor cabinet. From a fundamental point of view, this is a multi-disciplinary problem, involving the study of a fluid flow in three-dimensional complex geometries, coupled with various modes of heat transfer: conduction, convection, radiation and, eventually, phase change.

The main investigation tool used in this thesis is the numerical simulation. Preliminary attempts in using available commercial softwares for this problem have shown major difficulties in treating in a flexible and transparent manner the particular features of outdoor cabinet problem. As a consequence, the approach adopted for this study was the development of a new numerical system allowing to progressively take into account different fluid dynamics and heat transfer phenomena. A complementary experimental study was also undertaken using a simplified configuration of an outdoor cabinet (see fig. 1.2). The final goal of the thesis is to assess the role of fundamental mechanisms, as natural convection, and use this information in designing passive cooling methods, or reducing the amount of energy necessary for active devices.

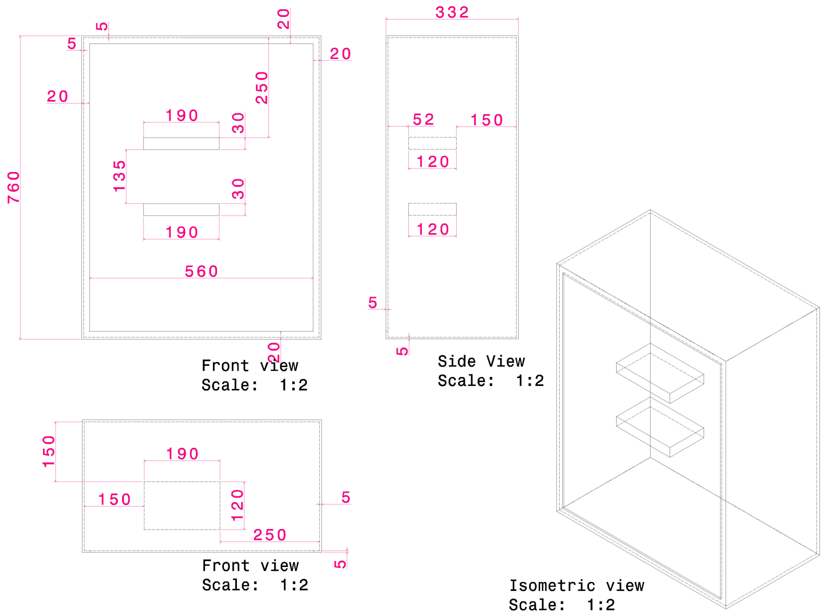

Figure 1.2.: Schematic representation of an outdoor telecommunication cabinet.

1.3. Present numerical approach for modeling the outdoor cabinet

We develop in this thesis a new numerical system for solving the 3D incompressible Navier-Stokes equations, under the Boussinesq approximation, and apply it to simulate the flow and heat transfer in enclosures with heated obstacles. A typical configuration considered in this study is displayed in fig. 1.2. The starting point of this thesis was the JETLES code, developed at the Laboratoire Jaques-Louis Lions by I. Danaila (Danaila, 1999–2008) (see also Ballestra (2002); Benteboula (2006)). This second-order finite difference code solves the 3D incompressible Navier-Stokes equations in cylindrical coordinates and was successfully used in the simulation of axisymmetric jet flows and vortex rings (Danaila and Hélie, 2008; Danaila et al., 2009).

The numerical work realized during this thesis follow two different, but complementary paths:

- The development of a new numerical code for the Navier-Stokes-Boussinesq equations. The equations are discretized on a three-dimensional (3D) Cartesian finite-difference grid. This code is written in Fortran 90 and follows the structure of the JETLES code, developed at the Laboratoire Jaques-Louis Lions by I. Danaila (Danaila, 1999–2008) (see also Ballestra (2002); Benteboula (2006)). JETLES is a second-order finite difference code solving the 3D incompressible Navier-Stokes equations in cylindrical coordinates; it was successfully used in the simulation of axisymmetric jet flows and vortex rings (Danaila and Hélie, 2008; Danaila et al., 2009).

  The main novelty in the new code is the use of Cartesian coordinates and sixth-order compact finite-difference schemes, with corresponding high-order interpolation schemes. The numerical scheme was also revisited and modified accordingly to the new problem configuration. The time integration is based on a fractional step (projection) method, using an explicit third order Runge-Kutta scheme adapted from Kim and Moin (1985); Orlandi and Verzicco (1993); Orlandi (2000). At each substep of the Runge-Kutta scheme, the pressure gradient is treated explicitly and a Poisson equation is solved for the pressure correction. The Poisson solver uses a fast cosine transform following one direction and an effective cyclic reduction method (Fishpack subroutine) for solving the remaining two-dimensional system. Particular care was devoted to the numerical integration of the temperature equation using TVD (total variation diminishing) schemes that avoid spurious oscillations near sharp fronts of temperature.

An important development effort was devoted to the implementation in the numerical code of an immersed boundary method to model heated obstacles inside the computational domain (see fig. 1.2). This method tries to bring the fluid at rest on the surface of the immersed body by applying a boundary-like treatment inside the computational domain and not at its borders as usually done. This is achieved by explicitly prescribing the force acting on the fluid flow due to the presence of the solid body. Suitable volume forces are numerically introduced as source terms in the Navier-Stokes equations. The initial solver can thus be used over the entire computational domain, with the advantage to preserve initial computational performances of the code. Several versions of the method for different applications have been published (for a recent review, see Mittal and Iaccarino, 2005a). For this study we used the method of Mohd-Yosuf (1997) with the interpolation procedure proposed by Liao et al. (2010). New improvements of the immersed boundary method were necessary to accurately take into account heat boundary conditions on the immersed obstacles.

The numerical system was first validated on classical natural convection test cases (without obstacles), considering the heat driven squared cavity with vertical or horizontal temperature gradients. Very good agreement with previously published results were obtained for a large range of Rayleigh numbers (from 10^4 to 10^6). In a second stage, simulations of the heat driven cavity with obstacles were considered. Several cases were simulated considering many obstacles present in the cavity, with different types of heat boundary conditions on immersed bodies.

- The development of an alternative finite-element solver.
  An alternative finite-element algorithm for solving the 2D Navier-Stokes-Boussinesq equations was developed and implemented using the FreeFem++ software (Hecht et al., 2012). Since the finite-element method offers an exact representation of immersed obstacles, this distinct numerical systems was mainly used to validate results obtained with the finite-difference code with the immersed boundary approach, for which benchmarks were not available. It also proved valuable in assessing for different properties of numerical schemes (order of precision, influence of the mesh refinement, etc).

  A Newton algorithm system based on a penalty finite-element formulation of the Navier-Stokes equations was implemented and extensively tested. The advantage of this formulation is to permit a straightforward implementation of different types of non-linearities in the system of equations. As an original application of the method, we used this algorithm to simulate phase-change systems with convection. With this numerical system we were able to tackle a large range of problems, from natural convection to melting and solidification.

1.4. Thesis plan

Chapter 2 sets the mathematical and physical basis of the numerical system used to simulate the flow inside a cavity. We present in detail the incompressible Navier-Stokes system of equations and introduce the Boussinesq approximation for buoyancy effects. The numerical algorithm for solving this system of equations is described in detail: integration schemes, finite difference (FD) discretization, projection method and Poisson solver, boundary conditions. The structure of the newly developed FD code (written in F90) is also presented. Finally, we present some basic theoretical tests to assess for the accuracy of the high-order finite-difference scheme used for the spatial discretization.

Simulations of natural convection flows in cavities are presented in chapter 3 using the FD code. Natural convection inside enclosures is one of the most widely studied configurations in thermodynamics and numerous benchmarks exists. We have selected the commonly used natural convection benchmarks to validate the finite difference code: the Rayleigh-Bénard convection case and the differentially heated cavity case. For both cases, we present the benchmark (steady) solution followed by a quantitative and a qualitative analysis of each numerical model considered (for space discretization and time advancement). We compare results obtained using different integration schemes (Euler, Adams-Bashforth, third order Runge-Kutta) and finite difference schemes (second order on uniform or stretched grids and sixth-order on uniform grids). The results are used to set the final numerical system for the simulations performed in the following chapters.

A second numerical method based on finite elements (FE) for the resolution of the Navier-Stokes-Boussinesq equations is considered in chapter 4. The idea behind this new development is to use the capability of the FE discretization to cope with complex geometries; the FE code will be used latter to validate computations of configurations with obstacles using the finite difference (FD) method in conjunction with the immersed boundary method (IBM). The development of the FE code was greatly simplified by the use of the FreeFem++ software, offering a friendly environment to work with different types of finite elements. We develop in this chapter a Newton algorithm to solve the Navier-Stokes-Boussinesq equations. The FE numerical system is validated against the same natural convection benchmarks as the FD code.

Chapter 5 addresses the implementation in the FD code of an Immersed Boundary Method (IBM) for modeling obstacles in the cavity. We first explain the principle of the IBM method, together with its advantages and disadvantages. Then, the code based on FD+IBM is compared to the one based on finite elements. Extensive tests are performed, with one or several obstacles in the cavity, with rectangular or circular shapes of obstacles. The good agreement between the two codes offers a validation of the FD+IBM numerical system, since the FE method provides an exact representations of the immersed bodies.

The experimental approach for studying the outdoor telecommunication cabinet is described in chapter 6. Temperature measurement were made inside a simplified cabinet placed inside a thermal chamber. Measurements were afterwards compared with numerical simulations and a good agreement was obtained.

Chapter 7 presents a numerical study of phase change materials which have begun to be more and more used as passive cooling solutions. We use the flexibility of the Newton algorithm developed in chapter 4 for Navier-Stokes-Boussinesq equations to introduce new nonlinearities related to phase-change phenomena. The numerical system is validated against benchmarks for the melting of a paraffin phase-change material.

Chapter 8 draws the conclusion of this study and some perspectives for future developments.

2. Numerical resolution of the Navier-Stokes-Boussinesq model

This chapter sets the mathematical and physical basis of the numerical system used to simulate the flow inside a cavity. To start with, we present the incompressible Navier-Stokes system of equations and introduce the Boussinesq approximation for buoyancy effects. The system of equations is then written in a non-dimensional form appropriate for numerical simulations. The numerical algorithm for solving this system of equations is described in detail (integration scheme, finite-difference discretization, projection method and Poisson solver, boundary conditions). Finally, we present some basic theoretical tests to assess for the accuracy of the high-order finite-difference scheme used for the spatial discretization.

2.1. Motivation for the choice of the numerical method

Nowadays, there are so many in-house or commercial codes for simulating fluid flows or heat transfer phenomena. The main idea in developing this new code was to combine high-order methods, that are validated and popular in fluid dynamics community, to simulate natural convection (Boussinesq) flows. The reference benchmarks in this field are based on simulations using spectral methods (Quéré, 1987; Le Quéré and Behnia, 1998; Quéré, 1991). Spectral methods may become cumbersome when simulating configurations with obstacles (complex geometries) and non-standard boundary conditions, as is the case of outdoor telecommunication cabinets. Therefore, we have chosen to use high-order compact finite-difference methods offering spectral-like resolution and more flexibility in modeling immersed boundaries and non-linear boundary conditions.

Compact schemes are high-order implicit finite-difference schemes that have became very popular in fluid dynamics after the publication of the seminal paper by Lele (1992). Lele used for the first time sixth order compact schemes for solving the compressible Navier-Stokes equations on a staggered grid and proved the spectral-like accuracy of the method. Since then, compact schemes have been successfully applied to a large range of flow configurations from direct numerical simulation (DNS) of compressible (Lee et al., 1997; Mahesh et al., 1997; Freund et al., 2000) or incompressible flows Hussein et al. (1994); Chu and Fan (1998); Verstappen and Veldman (2003) to computational aeroacoustics (Colonius et al., 1997) and large eddy simulations (LES) (Moin et al., 1991; Constantinescu and Lele, 1991). A large amount of literature exists in this field.

The mesh arrangement of the computational nodes proved to be important for the accuracy of results. The collocated arrangement (velocity and pressure are computed at the same location) introduces aliasing errors which could be larger than for explicit finite difference schemes (Moin et al., 1991; Constantinescu and Lele, 1991). This effect was removed by the use of a staggered grid (velocity and pressure nodes are shifted) which lead to improved robustness (Nagarajan et al., 2003). High order schemes on staggered meshes were recently proposed for compressible (Boersma, 2005; Moore et al., 2007) and incompressible (Boersma, 2011) Navier-Stokes equations. Compact Padé-type schemes for other types of meshes were derived: stretched grids (Gamet et al., 1999), stretched, curvilinear, and deforming meshes (Visbal and Gaitonde, 2002).

Most of the numerical methods used in the numerical heat transfer community use finite volume methods. Classical second-order finite difference methods are also used, but there are very few applications of high-order finite difference schemes for Boussinesq flows. Ghader et al. (2012) used a forth-order compact scheme for the vorticity-stream function-density formulation of Navier-Stokes-Boussinesq equations - this approach is limited to 2D flows. In this context, the novelty of our approach is to apply sixth order compact schemes for the 3D velocity-pressure description of Boussinesq flows. This high-order spatial discretization will be combined with high order integration schemes (third order Runge-Kutta) and accurate (TVD) methods for capturing the temperature evolution.

2.2. Physical problem and Navier-Stokes-Boussinesq equations

The flow inside an outdoor telecommunication cabinet is submitted to unsteady thermal effects due to internal heat sources (electronic components) and exchanges with the external atmosphere (solar flux). These temperature gradients trigger inside the cabinet a main natural convection air flow, driven by the buoyancy force. For natural convection flows, a widely used simplification of the governing equations is the Boussinesq approximation: the fluid is supposed incompressible (the velocity vector field is divergence free) and density variations are taken into account only in the body-force (gravity) term of the momentum equations, through a linearized model.

More in detail, we present in the following the exact form of the equations together with the underlying simplifying hypothesis. The equations are non-dimensionalized using a length-scale L_{ref} and a reference state $(\rho_{ref}, V_{ref}, T_{ref})$, defining the following scaling for the space, velocity, temperature and time variables:

$$\vec{x} = \frac{\vec{x}^*}{L_{ref}}, \quad \vec{v} = \frac{\vec{v}^*}{V_{ref}}, \quad \theta = \frac{T - T_{ref}}{T_h - T_c}, \quad t = \frac{t^*}{t_{ref}}, \quad t_{ref} = L_{ref}/V_{ref}, \tag{2.1}$$

where *star* variables are in physical units and hot T_h and, respectively, cold T_c temperatures define the temperature gradient driving the natural convection flow. In this setting, the incompressible Navier-Stokes equations with the Boussinesq approximation can be derived as follows:

The continuity (mass conservation) equation. The flow is supposed incompressible and thus:

$$\nabla \vec{v}^* = 0 \quad \Longrightarrow \quad \nabla \vec{v} = 0. \tag{2.2}$$

The momentum equation. The model assumes that density variations around a reference state are very small and their effect on the inertia terms are negligible. As a consequence, the variations of the density are taken into account only in the buoyancy (gravity) term of the Navier-Stokes momentum equations:

$$\rho_{ref} \left[\frac{\partial \vec{v}^*}{\partial t} + (\vec{v}^* \, \nabla) \vec{v}^* \right] = -\nabla p^* + \Delta \vec{v}^* + \rho \vec{g}. \tag{2.3}$$

The buoyancy therm is then linearized around the reference value ρ_{ref}:

$$\rho\vec{g} = \rho_{ref}\vec{g} + (\rho - \rho_{ref})\vec{g}, \quad \text{and} \quad (\rho - \rho_{ref})\vec{g} = -\rho_{ref}\beta(T - T_{ref})\vec{g}, \tag{2.4}$$

where β is the volume (bulk) expansion coefficient:

$$\beta = -\frac{1}{\rho_{ref}}\left(\frac{\partial\rho}{\partial T}\right)_{p=constant} \tag{2.5}$$

The momentum equation (2.3) becomes (since $\vec{g} = -g\vec{e}_z = -g\nabla z$):

$$\rho_{ref}\left[\frac{\partial\vec{v}^*}{\partial t} + (\vec{v}^*\,\nabla)\vec{v}^*\right] = -\nabla(p^* + \rho_{ref}gz) + \Delta\vec{v}^* + \rho_{ref}\beta(T - T_{ref})g\vec{e}_z. \tag{2.6}$$

Denoting by $\bar{p}^* = p^* + \rho_{ref}gz$ the kinetic pressure, we notice that the pressure p^* of the system is the sum between the kinetic pressure and the hydrostatic pressure $(-\rho_{ref}gz)$. Since the hydrostatic component of the pressure has a simple universal form, we need to compute only the kinetic portion of the pressure. We therefore use in the equations the dimensionless pressure defined by $p = \bar{p}^*/(\rho_{ref}V_{ref}^2)$ and finally obtain the non-dimensional form of the momentum equation:

$$\frac{\partial\vec{v}}{\partial t} + (\vec{v}\,\nabla)\vec{v} = -\nabla p + \frac{1}{Re}\triangle\vec{u} + \frac{\mathcal{R}a}{\mathcal{R}e^2\mathcal{P}r}T\vec{e}_z. \tag{2.7}$$

The non-dimensional (similarity) parameters of the flow are the Reynolds, Prandtl and Rayleigh numbers, defined as:

$$\mathcal{R}e = \frac{\rho_{ref}V_{ref}L_{ref}}{\mu}, \quad \mathcal{P}r = \frac{\nu}{\alpha}, \quad \mathcal{R}a = \frac{g\beta L_{ref}^3(T_h - T_c)}{\nu\alpha}. \tag{2.8}$$

Two other non-dimensional parameters are usually defined for natural convection flows, the Grashof and Bousinesq numbers:

$$\mathcal{G}r = \frac{g\beta L_{ref}^3(T_h - T_c)}{\nu^2} = \frac{\mathcal{R}a}{\mathcal{P}r}, \qquad \mathcal{B}o = \mathcal{R}a\mathcal{P}r = \mathcal{G}r\mathcal{P}r^2. \tag{2.9}$$

We recall that in previous definitions, μ denotes the viscosity, ν the kinematic viscosity, α the thermal diffusivity, β the volume (bulk) expansion coefficient and g the gravitational acceleration. We also recall the physical meaning of these parameters:

- the Reynolds number gives a measure of the ratio of inertial forces to viscous forces; for each flow, a critical value of the Reynolds number defines the transition between the laminar and turbulent regimes;
- the Prandtl number represents the ratio of momentum diffusivity (kinematic viscosity) to thermal diffusivity; it allows to evaluate the relative thickness of the momentum (velocity) and thermal boundary layers in heat transfer problems;
- the Grashof number represents the ratio of the buoyancy to viscous force acting on the fluid; it characterizes thermal effects in natural convection flows;
- the Rayleigh number plays the role of a Reynolds number for buoyancy driven flow (natural convection); in regard to it's critical value, it determines if the heat transfer is dominated by convection or conduction.

The energy equation. For the energy conservation equation, the Boussinesq approximation supposes that the interior forces are negligible, as well as the dependence of the internal energy with pressure. The thermodynamic coefficients are also presumed constants. These assumptions stand only when temperature variations δT are small: for air $\delta T < 15°$ and for water $\delta T < 2°$. As a consequence, the temperature is governed by a general *passive scalar* equation:

$$\frac{\partial T^*}{\partial t} + (\vec{v}\,\nabla)T^* = \left(\frac{\lambda}{\rho_{ref} C_p}\right) \Delta T, \tag{2.10}$$

where λ is the thermal conductivity and C_p the specific heat. The non-dimensional form of the energy equation follows since $\alpha = \lambda/(\rho_{ref} C_p)$:

$$\frac{\partial T}{\partial t} + (\vec{v}\,\nabla T) = \frac{1}{\mathcal{R}e\mathcal{P}r} \Delta T. \tag{2.11}$$

Final equations. We recall here the final system of equations to be solved:

$$\begin{aligned} \nabla \vec{v} &= 0, && (2.12)\\ \frac{\partial \vec{v}}{\partial t} + (\vec{v}\,\nabla)\vec{v} &= -\nabla p + \frac{1}{Re}\triangle \vec{u} + \frac{\mathcal{R}a}{\mathcal{R}e^2\mathcal{P}r} T\vec{e}_z, && (2.13)\\ \frac{\partial T}{\partial t} + (\vec{v}\,\nabla T) &= \frac{1}{\mathcal{R}e\mathcal{P}r}\Delta T. && (2.14) \end{aligned}$$

It is important to note that the characteristic scales in (2.1) could be defined accordingly to the physics of the considered problem. Several choices are used in the literature:

$$\begin{aligned} V_{ref}^{(1)} &= \frac{\nu}{L_{ref}} && \Longrightarrow t_{ref}^{(1)} = \frac{\nu}{L_{ref}^2} && \Longrightarrow \mathcal{R}e = 1, && (2.15)\\ V_{ref}^{(2)} &= \frac{\alpha}{L_{ref}} && \Longrightarrow t_{ref}^{(2)} = t_{ref}^{(1)}\mathcal{P}r && \Longrightarrow \mathcal{R}e = 1/\mathcal{P}r, && (2.16)\\ V_{ref}^{(3)} &= \frac{\nu_l}{L_{ref}}\sqrt{\frac{\mathcal{R}a}{\mathcal{P}r}} && \Longrightarrow t_{ref}^{(3)} = t_{ref}^{(1)}\sqrt{\frac{\mathcal{P}r}{\mathcal{R}a}} && \Longrightarrow \mathcal{R}e = \sqrt{\frac{\mathcal{R}a}{\mathcal{P}r}}, && (2.17) \end{aligned}$$

The last choice (2.17) is generally used for classical natural convection problems, while the first two choices are preferred for melting/freezing problems (Wang et al., 2010a).

We shall use in the following the last scaling choice (2.17), setting $\mathcal{R}e = \sqrt{\frac{\mathcal{R}a}{\mathcal{P}r}}$, so the buoyancy term in (2.13) is simplified to $T\vec{e}_z$.

2.3. Numerical method

2.3.1. Time integration method

Time integration is based upon a classical projection method Chorin (1968) consisting in the following steps:

(A) Predictor step: the momentum equations (2.13) are advanced in time using an explicit treatment of the pressure through a classical integration scheme. Explicit schemes are preferred to facilitate a further MPI-parallel implementation of the code. First-order Euler, second-order Adams-Bashforth and third order Runge-Kutta methods are available in the code.

At the end of this step, a non-divergence free velocity field ($\widetilde{u}$) is computed, following the general discretization for an integration scheme with l steps :

$$\frac{\widetilde{u}_c^i - u_c^i}{\delta t} = \gamma_i H_c^i + \rho_i H_c^{i-1} - \alpha_i G_c p^i \tag{2.18}$$

where $c = x, y, z$ denotes each spatial direction, $i = 1, 2, \cdots, l$ the substep of the method. G stands for the pressure gradient and H regroups for convective, diffusive and buoyancy terms.

A third-order Runge-Kutta method was adapted from the *fractional-step* method widely used in fluid dynamics computations (Rai and Moin, 1991; Verzicco and Orlandi, 1996; Orlandi, 2000). The coefficients of the scheme ($i = 1, 2, 3$) are

$$\begin{aligned} \gamma_1 &= \frac{8}{15}, \quad \gamma_2 = \frac{5}{12}, \quad \gamma_3 = \frac{3}{4}, \\ \rho_1 &= 0, \quad \rho_2 = -\frac{17}{60}, \quad \rho_3 = -\frac{5}{12}, \end{aligned} \tag{2.19}$$

and $\alpha_i = \gamma_i + \rho_i$. We notice that $\rho_1 = 0$ allows the integration procedure to begin without the need of having previous values (self-starting scheme).

For the second-order Adams-Bashforth scheme $l = 1$ and $\gamma_1 = 3/2$, $\rho_1 = -1/2$ and $\alpha_1 = 1$. This is not a self-starting scheme and needs a first Euler step to start the computation.

For the first-order Euler backward scheme, $l = 1$ and $\gamma_1 = 0$, $\rho_1 = 1$ and $\alpha_1 = 1$.

All these schemes were implemented in a compact manner in the code, allowing to easily switch from one scheme to another.

(B) Projection step: The projection equation

$$u^{i+1} = \widetilde{u}^i - \alpha_i \cdot \delta t \nabla \phi, \tag{2.20}$$

introduces a supplementary pressure-related variable ϕ. Since the velocity u^{i+1} has to be divergence free field, we obtain from the previous relationship a Poisson equation for ϕ:

$$\Delta \phi = \frac{1}{\alpha_i \, \delta t} \nabla \widetilde{u}. \tag{2.21}$$

Two methods were employed for solving the Poisson equation: firstly, a periodical case was considered, and secondly a non-periodical case was tested in order to obtain the three-dimensional cavity case. For the periodical case we use a FFT (Fast Fourier Transform) following the periodic direction (in our case x). For the second case, without periodicity, a cosine series expansion following the same direction (x) was derived and implemented based on classical FFTs (for details, see Danaila, 1999–2008). Compared to the Fourier series development, the cosine expansion permits to simulate a closed 3D cavity, with no-slip wall conditions following the three directions. It also benefits from the performances of basic FFTs subroutines.

In both cases the resulting 2D system is solved by a cyclical reduction method, with the use of the BLKTRI Fortran library: FISHPACK. The idea of the cyclical reduction is the recursive reduction of the linear system size by successively eliminating the odd order unknowns (for details, see Ballestra, 2002). The advantage of the method is to allow the use of a non uniform grid. For computational efficiency, the derivatives of the Laplacian operator are discretized using a second order centered scheme.

(C) Corrector step: After solving the Poisson equation (2.21), the projection equation (2.20) is used to compute the corrected divergence free field u^{i+1}. The pressure for the next step is obtained by subtracting (2.18) from the same equation with implicit pressure term (Gp^{i+1}); using the projection equation (2.20) we obtain the following update for the pressure:

$$p^{i+1} = p^i + \phi. \tag{2.22}$$

(D) Temperature update: The computed divergence free field is finally used to compute the temperature distribution from (2.14). This equation is discretized following the same time integration scheme as for momentum equations. A particular care is devoted to the discretization of convective terms using a TVD (Total Variation Diminishing) scheme described in detail below.

2.3.2. Spatial discretization

The computational grid is rectangular (fig.2.1), using Cartesian coordinates. The grid is generated separately following each space direction (x, y, z) by choosing ether a uniform distribution or a stretched mesh. The grid refinement is used only with second-order finite-difference schemes. Compact sixth-order schemes require uniform meshes in all space directions.

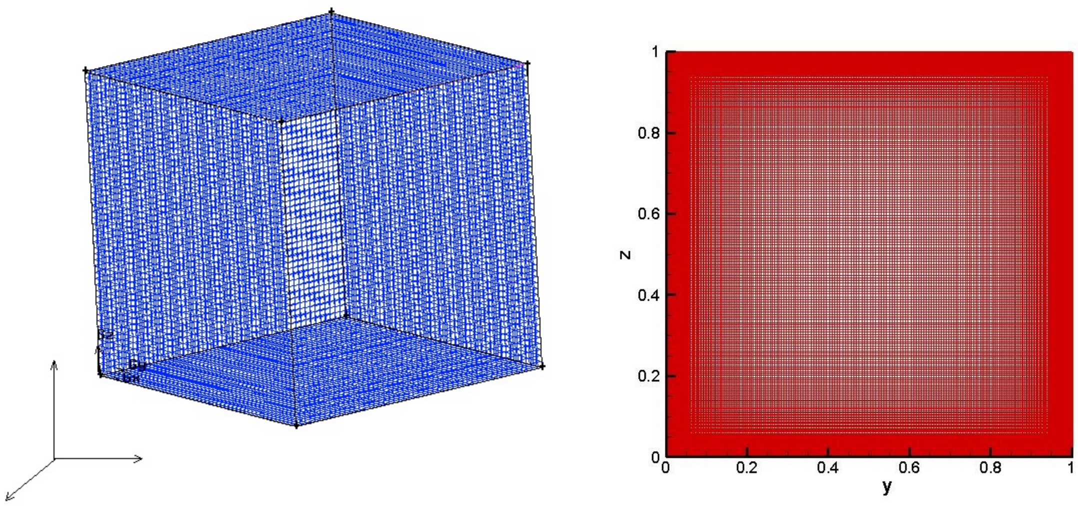

Figure 2.1.: Three-dimensional computational domain (left) and refined mesh near the walls in the (y, z) section (right).

We consider a staggered grid with the scalar variables (pressure, temperature) computed in the cell center and the velocity components on the cell faces (see fig. 2.2). The advantage of the staggered grids is that it avoids the decoupling between pressure and velocity, and border pressure problems that may occur in the cases of collocated variables. This type of grid was first used by Harlow and Welch (1965) in their MAC method. The staggered grid is efficient for the computations, it respects conservation properties and needs a small amount of memory space.

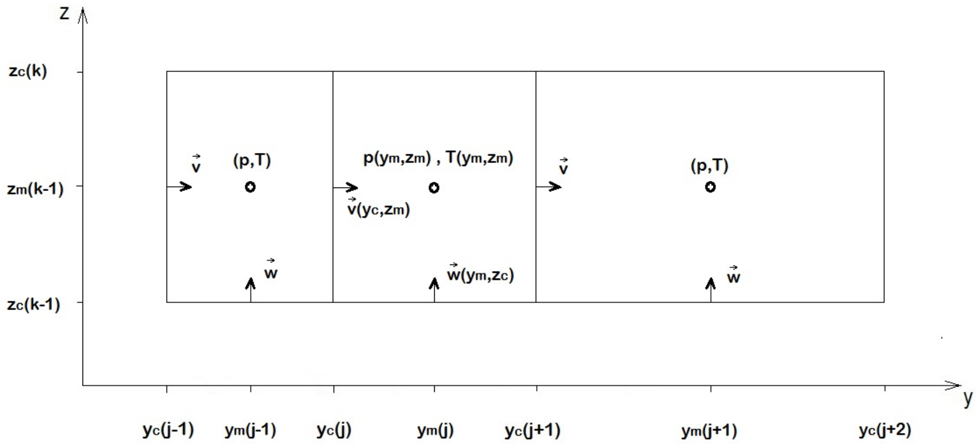

Figure 2.2.: Illustration of the staggered arrangement of variables following the y direction.

The three-dimensional computational domain Ω of dimension $L_x \times L_y \times L_z$ is discretized using $N_1 \times N_2 \times N_3$ grid points. At each node (i, j, k) we associate the corresponding (i, j, k) primary cell, defined by $[x_c(i), x_c(i+1)] \times [y_c(j), y_c(j+1)] \times [z_c(k), z_c(k+1)]$ for $i = 1, ...N_1 - 1; j = 1, ...N_2 - 1; k = 1, ...N_3 - 1$. For the case of a uniform grid

$$x_c(i) = (i-1)\delta x, \quad i = 1, ...N_1, \quad \delta x = L_x/(N_1 - 1), \tag{2.23}$$
$$y_c(j) = (j-1)\delta y, \quad j = 1, ...N_2, \quad \delta y = L_y/(N_2 - 1), \tag{2.24}$$
$$z_c(k) = (k-1)\delta z, \quad k = 1, ...N_3, \quad \delta z = L_z/(N_3 - 1). \tag{2.25}$$

The secondary grid (for scalar variables) is defined by cell centers, located at coordinates:

$$x_m(i) = [x_c(i) + x_c(i+1)]/2, \quad i = 1, ...N_1 - 1, \tag{2.26}$$
$$y_m(j) = [y_c(j) + y_c(j+1)]/2, \quad j = 1, ...N_2 - 1, \tag{2.27}$$
$$z_m(k) = [z_c(k) + z_c(k+1)]/2, \quad k = 1, ...N_3 - 1. \tag{2.28}$$

The grid refinement procedure is based on analytical coordinate transforms. It can be used with second-order finite-difference schemes to increase the grid resolution in the vicinity of heated obstacles, or near the walls where strong gradients are present. Let us consider only the y direction (as in fig. 2.2) and set a generic coordinate transform $y_c = f(\xi)$, where ξ maps the unitary interval:

$$\xi(j) = (j-1)\delta\xi, \quad j = 1, ...N_2, \quad \delta\xi = 1/(N_2 - 1). \tag{2.29}$$

The function f is a combination of hyperbolic-tangent functions with tuning parameters that allow to refine the mesh at different positions (the middle, one border or both borders of the interval $[0, L_y]$). We have used different analytical functions proposed by Orlandi (2000) with optimal parameters suggested by Ballestra (2002); Benteboula (2006). Once the primary mesh is computed, we use (2.26) to determine the secondary mesh.

The derivatives for the stretched mesh will be computed using the chain rule. For example, the first derivative of a generic quantity ψ with respect to x will be computed as

$$\frac{\partial \psi}{\partial y} = \frac{d\xi}{dy}\frac{\partial \psi}{\partial \xi} = \frac{1}{\frac{dy}{d\xi}}\frac{\partial u}{\partial \xi}. \tag{2.30}$$

It was shown Orlandi (2000) (see also Ballestra, 2002) that a discrete computation of the metrics $dy/d\xi$ reduces the approximation error, when compared to the use of their analytical formula. Consequently, we use for the metric evaluation the following second order schemes:

$$\left(\frac{dy}{d\xi}\right)(j) \approx dcy(j) = \frac{y_c(j+1) - y_c(j-1)}{2\,\delta\xi}, \quad j = 2, N_2 - 1, \tag{2.31}$$

$$dcy(1) = \frac{y_c(2) - y_c(1)}{\delta\xi}, \tag{2.32}$$

$$dcy(N_2) = \frac{y_c(N_1) - y_c(N_2 - 1)}{\delta\xi}, \tag{2.33}$$

and for cell centers:

$$\left(\frac{dy}{d\xi}\right)_{j+\frac{1}{2}} \approx dmy(i) = \frac{y_c(i+1) - y_c(i)}{\delta\xi}, \quad i = 1, N_2 - 1. \tag{2.34}$$

We shall see in the following how these metrics are used in computing different terms of the Navier-Stokes-Boussinesq equations when second-order finite difference schemes are used.

2.3.3. Discrete formulation of momentum equations: second and sixth-order schemes

We illustrate here the discretization of the momentum equations on the staggered grid. In the integration scheme (2.18), the explicit term H contains the convective, diffusive and buoyancy terms:

$$H_x = -\frac{\partial u^2}{\partial x} - \frac{\partial vu}{\partial y} - \frac{\partial wu}{\partial z} + \frac{1}{\mathcal{R}e}\left(\frac{\partial^2 u}{\partial x^2} + \frac{\partial^2 u}{\partial y^2} + \frac{\partial^2 u}{\partial z^2}\right), \tag{2.35}$$

$$H_y = -\frac{\partial uv}{\partial x} - \frac{\partial v^2}{\partial y} - \frac{\partial wv}{\partial z} + \frac{1}{Re}\left(\frac{\partial^2 v}{\partial x^2} + \frac{\partial^2 v}{\partial y^2} + \frac{\partial^2 v}{\partial z^2}\right), \tag{2.36}$$

$$H_z = -\frac{\partial uw}{\partial x} - \frac{\partial vw}{\partial y} - \frac{\partial w^2}{\partial z} + \frac{1}{Re}\left(\frac{\partial^2 w}{\partial x^2} + \frac{\partial^2 w}{\partial y^2} + \frac{\partial^2 w}{\partial z^2}\right) + \frac{\mathcal{R}a}{\mathcal{R}e^2\mathcal{P}r}T. \tag{2.37}$$

Following the staggered arrangement (fig. 2.2), these terms will be computed at different locations, corresponding to computational nodes for velocities. More precisely, we compute
H_x at $(i, j+1/2, k+1/2)$, *i. e.* $(x_c(i), y_m(j), z_m(k))$,
H_y at $(i+1/2, j, k+1/2)$, *i. e.* $(x_m(i), y_c(j), z_m(k))$,
H_z at $(i+1/2, j+1/2, k)$, *i. e.* $(x_m(i), y_m(j), z_c(k))$.
The staggered arrangement implies the use of interpolation of variables, with different procedures depending on the order of finite-difference scheme.

Second-order centered schemes

For a mesh generated by a coordinate transform, as described previously, we will need, following (2.30), to interpolate and derive variables with respect to the uniform coordinate ξ. For a uniform mesh, the interpolation operator for a centered position is

$$\overline{\psi}(\xi_i) = \frac{1}{2}\left[\psi(\xi_i + \frac{\delta\xi}{2}) + \psi(\xi_i - \frac{\delta\xi}{2})\right] = \psi_i + \mathcal{O}(\delta\xi)^2, \quad \psi_i = \psi(\xi_i), \tag{2.38}$$

and for a shifted position

$$\overline{\psi}^{\pm}(\xi_i) = \frac{1}{2}\left[\psi(\xi_i \pm \delta\xi) + \psi(\xi_i)\right] = \psi_{i\pm\frac{1}{2}} + \mathcal{O}(\delta\xi). \tag{2.39}$$

The first derivative is discretized following a centered second order scheme

$$\psi_\xi(\xi_i) = \frac{1}{\delta\xi}\left[\psi(\xi_i + \frac{\delta\xi}{2}) - \psi(\xi_i - \frac{\delta\xi}{2})\right] = \frac{d\psi}{d\xi}\Big|_i + \mathcal{O}(\delta\xi)^2, \tag{2.40}$$

and the second derivative operator will be obtain by two successive application of the first derivative:

$$\psi_{\xi\xi}(\xi_i) = \frac{1}{\delta\xi}\left[\psi_\xi(\xi_i + \delta\xi/2) - \psi_\xi(\xi_i - \delta\xi/2),\right] \tag{2.41}$$

leading to the well-known centered scheme:

$$\psi_{\xi\xi(\xi_i)} = \frac{1}{\delta\xi^2}\left[\psi(\xi_i + \delta\xi) - 2\psi(\xi_i) - \psi(\xi_i - \delta\xi)\right] = \frac{d^2u}{d\xi^2}\Big|_i + \mathcal{O}(\delta\xi)^2. \tag{2.42}$$

It is important to note that for the evaluation of the second derivatives, the formula (2.41) has better approximation properties on stretched meshes than (2.42) (Orlandi, 2000) (see also Ballestra, 2002). We shall use in the following the formula (2.40) for the first derivative and (2.41) for the second derivative and illustrate the discretization principle by considering the terms of the momentum equation following the direction y (since the arrangement of variables could be followed from fig. 2.2).

- Convective terms following the y-direction computed at $(i + 1/2, j, k + 1/2)$:

$$\frac{\partial v^2}{\partial y} = \frac{1}{\delta\xi_y\, dcy(j)}\left[\left(\frac{v_{i,j,k} + v_{i,j+1,k}}{2}\right)^2 - \left(\frac{v_{i,j,k} + v_{i,j-1,k}}{2}\right)^2\right]$$

$$\frac{\partial uv}{\partial x} = \frac{1}{\delta\xi_x\, dmx(i)}\left[\frac{v_{i,j,k} + v_{i+1,j,k}}{2}\frac{u_{i+1,j,k} + u_{i+1,j-1,k}}{2} - \frac{v_{i,j,k} + v_{i-1,j,k}}{2}\frac{u_{i,j,k} + u_{i,j-1,k}}{2}\right]$$

$$\frac{\partial wv}{\partial z} = \frac{1}{\delta\xi_z\, dmz(k)}\left[\frac{v_{i,j,k} + v_{i,j,k+1}}{2}\frac{w_{i,j,k+1} - w_{i,j-1,k+1}}{2} - \frac{v_{i,j,k} + v_{i,j,k-1}}{2}\frac{w_{i,j,k} + w_{i,j-1,k}}{2}\right]$$

where $\delta\xi_x = 1/(N_1 - 1), \delta\xi_y = 1/(N_2 - 1), \delta\xi_z = 1/(N_3 - 1)$ and $dmx(i), dcx(i), dmy(j), dcy(j), dmz(k), dcz(k)$ are the metrics defined previously.

Note that the uniform grid discretization is recovered when all the metrics are equal to 1.

- Diffusive terms following the y-direction computed at $(i + 1/2, j, k + 1/2)$:

$$\frac{\partial^2 v}{\partial y^2} = \frac{1}{\delta\xi_y\, dcy(j)}\left[\frac{v_{i,j+1,k} - v_{i,j,k}}{\delta\xi_y\, dmy(j)} - \frac{v_{i,j,k} - v_{i,j-1,k}}{\delta\xi_y\, dmy(j-1)}\right]$$

$$\frac{\partial^2 v}{\partial x^2} = \frac{1}{\delta\xi_x\, dmx(i)} \left[\frac{v_{i+1,j,k} - v_{i,j,k}}{\delta\xi_x\, dcx(i+1)} - \frac{v_{i,j,k} - v_{i-1,j,k}}{\delta\xi_x\, dcx(i)} \right]$$
$$\frac{\partial^2 v}{\partial z^2} = \frac{1}{\delta\xi_z\, dmz(k)} \left[\frac{v_{i,j,k+1} - v_{i,j,k}}{\delta\xi_z\, dcz(k+1)} - \frac{v_{i,j,k} - v_{i,j,k-1}}{\delta\xi_z\, dcz(k)} \right]$$

Sixth-order compact schemes

Compact schemes are based on implicit relationships between the discrete values of derivatives. These values are computed for all grid points in one direction by inverting a linear system. The main advantages of these schemes are their spectral-like behavior (no numerical dissipation and good spectral resolution) and a better representation of small scales, when compared to classical explicit schemes (usually second or fourth order centered schemes).

We consider for this study compact schemes for uniform grids (for streched grids, see for example Gamet et al., 1999). The general idea in deriving compact schemes is to consider linear relationships between the values of the function and its derivative for a given stencil. Several families of compact implicit finite differences schemes were derived by Lele (1992) and became very popular because of the use of a three-point stencil only. For example, let us consider a function $f(x)$ of class C^∞, discretized on a uniform grid of stepsize h and denote by f_i the value $f(x_i)$.

For the first derivative Lele (1992) considered the general formula:

$$\begin{aligned} &\beta f'_{i-2} + \alpha f'_{i-1} + f'_i + \alpha f'_{i+1} + \beta f'_{i+2} = \\ &= c\frac{f_{i+3} - f_{i-3}}{6h} + b\frac{f_{i+2} - f_{i-2}}{4h} + a\frac{f_{i+1} - f_{i-1}}{2h}, \end{aligned} \tag{2.43}$$

and derived the following linear system for the coefficients in order to obtain a sixth-order truncation error:

$$a + b + c = 1 + 2\alpha + 2\beta \tag{2.44}$$
$$a + 2^2 b + 3^2 c = 2\frac{3!}{2!}\left(\alpha + 2^2\beta\right) \tag{2.45}$$
$$a + 2^4 b + 3^4 c = 2\frac{5!}{4!}\left(\alpha + 2^4\beta\right) \tag{2.46}$$

For $\beta = c = 0$ a family of a three-point stencil schemes is obtained. For this study we have chosen the following scheme (largely used in the literature):

$$\beta = 0, \quad c = 0, \quad \alpha = \frac{1}{3}, \quad a = \frac{14}{9}, \quad b = \frac{1}{9}, \tag{2.47}$$

with the truncation error $T = \frac{4}{7!} h^6 f^{(7)}$.

For non-periodic meshes, different schemes are necessary for the nodes near the boundary. For the first grid point $i = 1$, Lele (1992) considered for the first derivative a family of schemes of the form:

$$f'_1 + \alpha f'_2 = \frac{1}{h}\left(a f_1 + b f_2 + c f_3 + d f_4\right). \tag{2.48}$$

For $i = 1$, we have chosen the third-order scheme with:

$$d = 0, \quad \alpha = 2, \quad a = -\frac{5}{2}, \quad b = 2, \quad c = \frac{1}{2}. \tag{2.49}$$

For $i = 2$ we apply the general three-point stencil scheme (2.43), but only with a forth-order accuracy since necessarily $\beta = c = b = 0$:

$$\beta = 0, \quad c = 0, \quad \alpha = \frac{1}{4}, \quad a = \frac{1}{4}, \quad b = 0. \tag{2.50}$$

For the second derivative, the same procedure is applied. The general formula is:

$$\beta f''_{i-2} + \alpha f''_{i-1} + f'_i + \alpha f''_{i+1} + \beta f''_{i+2} = \tag{2.51}$$
$$= c\frac{f_{i+3} - 2f_i + f_{i-3}}{9h^2} + b\frac{f_{i+2} - 2f_i + f_{i-2}}{4h^2} + a\frac{f_{i+1} - 2f_i + f_{i-1}}{h^2} \tag{2.52}$$

with the corresponding linear system for the coefficients for a sixth-order truncation error:

$$a + b + c = 1 + 2\alpha + 2\beta \tag{2.53}$$
$$a + 2^2 b + 3^2 c = \frac{4!}{2!}\left(\alpha + 2^2\beta\right) \tag{2.54}$$
$$a + 2^4 b + 3^4 c = \frac{6!}{4!}\left(\alpha + 2^4\beta\right) \tag{2.55}$$

We also considered a three-point stencil scheme for the second derivative, defined by:

$$\beta = 0, \quad c = 0, \quad \alpha = \frac{2}{11}, \quad a = \frac{12}{11}, \quad b = \frac{3}{11}, \tag{2.56}$$

and truncation error $T = -\frac{8\cdot 23}{11\cdot 8!}h^6 f^{(8)}$.

For the boundary node $i = 2$ we use the same scheme (2.52) but with forth-order accuracy:

$$\beta = 0, \quad c = 0, \quad \alpha = \frac{1}{10}, \quad a = \frac{6}{5}, \quad b = 0, \tag{2.57}$$

and for $i = 1$ we use a scheme of the form

$$f''_1 + \alpha f''_2 = \frac{1}{h^2}\left(a f_1 + b f_2 + c f_3 + d f_4\right) \tag{2.58}$$

with the following coefficients for a third-order accuracy:

$$\alpha = 11, \quad a = 13, \quad b = -27, \quad c = 15, \quad d = -1. \tag{2.59}$$

It is important to note the chosen schemes use a three-point stencil (even for boundary nodes) and imply the resolution of a linear system with tridiagonal matrix. This is done in a very efficient matter using the Thomas algorithm (a version of the LU decomposition) adapted to compute the derivatives for the nodes of an entire plane (y, z). The additional time necessary to compute the derivatives is thus very low.

Since we use a staggered grid, an high-order interpolation procedure is necessary. The principle is the same and described by Boersma (2005). We have chosen method which has the same formal accuracy as the one for the derivatives. The compact interpolation rule is the following:

$$f_i + a(f_{i+1} + f_{i-1}) = b(f_{i+1/2} + f_{i-1/2}) + c(f_{i+3/2} + f_{i-3/2}) + d(f_{i+5/2} + f_{i-5/2}) + e(f_{i+7/2} + f_{i-7/2}). \tag{2.60}$$

The values of the coefficients a, b, c, d, e for the sixth order accuracy are:

$$a = 3/10, b = 3/4, c = 1/20, d = 0, e = 0. \tag{2.61}$$

Closer to the boundary the stencil is smaller and a fourth order interpolation is obtained for:

$$a = 1/6, b = 2/3. \tag{2.62}$$

At the boundary a third order accurate extrapolation is used for the first grid point:

$$f_i = \frac{15}{8} f_{i+1/2} - \frac{5}{4} f_{i+3/2} + \frac{3}{8} f_{i+5/2}. \tag{2.63}$$

Formulas (2.60) to (2.62) form a tridiagonal system which is solved using the Thomas algorithm.

The same interpolation rules are used for the interpolation following the perpendicular direction, by shifting the data over a half grid cell from f_i to $f_{i+1/2}$, obtaining $n-1$ points instead of n. At the borders, the interpolation scheme is (Nagarajan et al., 2003):

$$f_{1/2} = a' f_1 + b' f_2 + c' f_3 + d' f_4, \tag{2.64}$$

and a forth order accuracy formulation is obtained for:

$$a' = 5/16, b' = 15/16, c' = 5/16, d' = 1/16. \tag{2.65}$$

The discretization of the momentum equations using compact schemes on a staggered grid will follow a different procedure than for second-order schemes. We consider the same illustration of this calculation, using the momentum equation following the y direction. The convective terms are rewritten here in a non-conservative form.

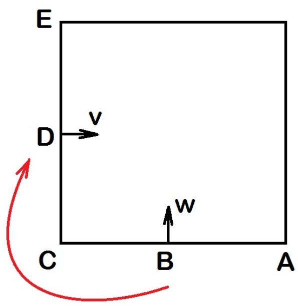

Figure 2.3.: Illustration of the interpolation scheme on the staggered grid: following the y-direction, the velocity w must be interpolated at point D.

Following fig. 2.3, the velocities u and w are first interpolated at point D. Each term is then obtained by multiplying the interpolated velocity (obtained with 2.60) and the sixth order derivative (2.43) as follows:

- Convective terms following the y-direction computed at $(i+1/2, j, k+1/2)$

$$\begin{aligned}
v\frac{\partial v}{\partial y} &= v(i,j,k) \quad \frac{\partial v}{\partial y}(i,j,k), \\
u\frac{\partial v}{\partial x} &= u(i,j,k)|_D \; \frac{\partial v}{\partial x}(i,j,k), \\
w\frac{\partial v}{\partial z} &= w(i,j,k)|_D \; \frac{\partial v}{\partial z}(i,j,k).
\end{aligned}$$

The diffusive terms at $(i+1/2, j, k+1/2)$ are obtained simply by applying the sixth-order scheme (2.52) (the interpolation is not needed) as:

$$
\begin{aligned}
\frac{\partial^2 v}{\partial y^2} &= \frac{\partial^2 v}{\partial y^2}(i,j,k),\\
\frac{\partial^2 v}{\partial x^2} &= \frac{\partial^2 v}{\partial x^2}(i,j,k),\\
\frac{\partial^2 v}{\partial z^2} &= \frac{\partial^2 v}{\partial z^2}(i,j,k).
\end{aligned}
$$

2.3.4. Discrete formulation of the temperature equation: TVD scheme

The use of the centered second order finite difference scheme may introduce oscillations when discontinuities are present. The concept of a total variation diminishing method was introduced by Harten (1983) and allows the capture of steep temperature gradients, while avoiding localized oscillations. The TVD scheme preserves the monotonicity of the numerical solution. This propriety ensures that the local augmentation of a gradient during the time integration is compensated by the diminishing of a gradient at a different location within the domain.

In our case, TVD schemes are necessary to treat convective terms in the temperature equation (2.14) in order to keep the values of the temperature between a minimum and a maximal value fixed by the initial conditions. In Cartesian coordinates this equation reads:

$$
\frac{\partial T}{\partial t} + \frac{\partial Tu}{\partial x} + \frac{\partial Tv}{\partial y} + \frac{\partial Tw}{\partial z} = \frac{1}{\mathcal{R}e\mathcal{P}r}\left(\frac{\partial^2 T}{\partial x^2} + \frac{\partial^2 T}{\partial y^2} + \frac{\partial^2 T}{\partial z^2}\right) \tag{2.66}
$$

The convective terms are computed after a general scheme proposed by Vreugdenhil and Koren (1993):

$$
\frac{\partial Tu}{\partial x} = \frac{F_{i+\frac{1}{2}} - F_{i-\frac{1}{2}}}{\delta x}, \tag{2.67}
$$

where:
- for $u_{i+\frac{1}{2}} > 0$ the flux at the face $i + \frac{1}{2}$ is:

$$
F_{i+\frac{1}{2}} = \left[T_i + \frac{1}{2}\Phi(c_{i+\frac{1}{2}})(T_i - T_{i-1})\right] u_{i+\frac{1}{2}}, \tag{2.68}
$$

$$
c_{i+\frac{1}{2}} = \frac{T_{i+1} - T_i + \varepsilon}{T_i - T_{i-1} + \varepsilon}, \tag{2.69}
$$

- for $u_{i+\frac{1}{2}} < 0$ the same flux is computed as:

$$
F_{i+\frac{1}{2}} = \left[T_i + \frac{1}{2}\Phi(c_{i+\frac{1}{2}})(T_{i+1} - T_{i+2})\right] u_{i+\frac{1}{2}}, \tag{2.70}
$$

$$
c_{i+\frac{1}{2}} = \frac{T_i - T_{i+1} + \varepsilon}{T_{i+1} - T_{i+2} + \varepsilon}, \tag{2.71}
$$

where $\varepsilon = 10^{-11}$ and the limiter:

$$
\Phi(c) = max\left[0, min\left(2c, min\left(\frac{1}{3} + \frac{2}{3}c, 2\right)\right)\right] \tag{2.72}
$$

The diffusive terms in the temperature equation are treated similarly to the momentum equation.

2.3.5. Boundary conditions

For simulating flows inside a cavity, non-slip wall (zero velocity) boundary conditions have to be imposed. We made use of ghost cells which are defined as an additional cells beyond the border (with the index 0 and $N+1$). The velocities inside the ghost cell are computed by linear interpolation between the first point inside the domain and the zero value imposed on the boundary. If we consider the same illustration following the y direction the non-slip wall conditions were imposed as follows:

$$\begin{aligned}
u(i,0,k) &= -u(i,1,k), \\
w(i,0,k) &= -w(i,1,k), \\
\\
u(i,n2,k) &= -u(i,n2-1,k), \\
w(i,n2,k) &= -w(i,n2-1,k), \\
\\
v(i,0,k) &= -v(i,2,k), \\
v(i,1,k) &= 0, \\
v(i,n2,k) &= 0.
\end{aligned} \tag{2.73}$$

The same procedure is applied for the intermediate velocities of the predictor step, since we impose $\widetilde{u} = \widetilde{v} = \widetilde{w} = 0$ on the boundary of the computational domain.

The same ghost cells are used to impose the boundary conditions for the temperature. We may consider Dirichlet or Neumann boundary conditions. For the same direction y, if $T = T_h$ for $y = 0$ and $T = T_c$ for $y = L_y$ (Dirichlet conditions for the Rayleigh-Bénard case), then

$$\begin{aligned}
T(i,0,k) &= 2T_h - T(i,1,k), \\
T(i,n2,k) &= 2T_c - T(i,n2-1,k),
\end{aligned}$$

and if $\partial T/\partial n = 0$ for both $y = 0$ and $y = L_y$ (Neumann conditions for the temperature driven cavity), then

$$\begin{aligned}
T(i,0,k) &= T(i,1,k), \\
T(i,n2,k) &= T(i,n2-1,k).
\end{aligned}$$

Finally, we recall that for solving the Poisson equation (2.21), Neumann boundary conditions are applied everywhere to ensure the compatibility with the boundary conditions on the velocity. The procedure for solving the Poisson equation takes into account these conditions implicitly, without using the ghost cells.

2.4. Structure of the Fortran90 simulation code

The numerical method presented below was implemented in Fortran 90. The structure of the code is presented in figure 2.4 showing the main modules.

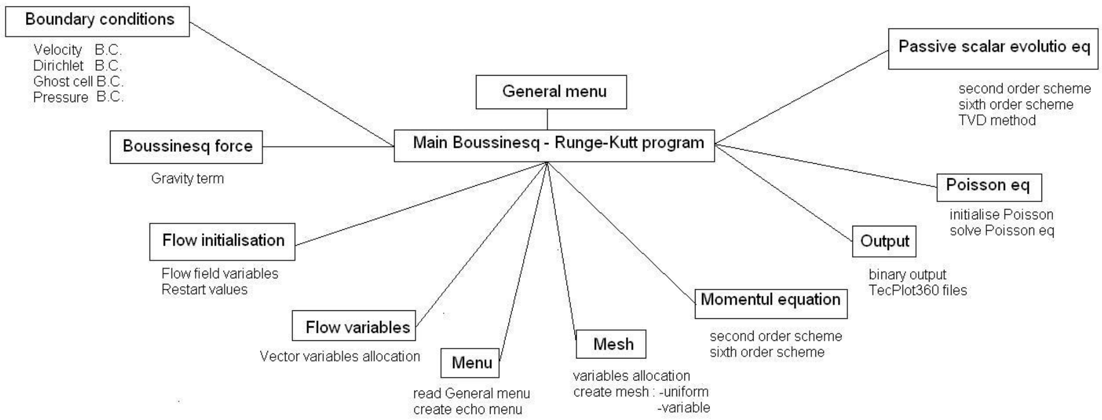

Figure 2.4.: Navier-Stokes-Boussinesq numerical code: general structure with modules in Fortran 90.

The code is structured in independent modules, with dynamic allocation of arrays, which make it very flexible in setting computational configurations and/or different mathematical models. The main parameters of the simulation are set by the user via a **general menu**; it is possible to define values for:
- domain dimensions, number of grid points,
- Reynolds, Rayleigh, Prandtl numbers,
- type of mesh for each direction (uniform or stretched),
- type of boundary conditions for velocity (periodic or slip-wall or non-slip wall),
- type of boundary conditions for temperature (Dirichlet or Neumann) and their localization,
- time integration scheme (Euler, Adams-Bashforth, Runge-Kutta),
- time integration parameters (final time, time step, etc),
- save and restart options with prescribed names for the files, etc.

In the main program there are several steps followed as:

(1) The initialization phase: a lecture of the general menu is made and all the parameters of the simulation set. The dynamic allocation of the variables is also done in order to save time and computer memory. The mesh is generated by calling the mesh module. Further the initial flow field values are set, together with boundary conditions imposed for the velocity, temperature and pressure field. The Boussinesq gravity term is also computed and an initialization of the Poisson solver is done before the time loop.

(2) The main time advancement loop: the main loop begins by saving the previous velocity and temperature values, at previous time step. The time advancement step is adapted to the type of integration scheme: one-step first-order Euler, one-step second Adams-Bashforth scheme and three-step Runge-Kutta scheme. Within this loop : the boundary conditions are imposed; the gravity term computed; the momentum equation, Poisson equation and passive scalar evolution equation are solved. As discussed in the previous section, after the momentum equation is solved a correction is made by solving the Poisson equation. The Poisson solver is

implemented into an independent module and make use of FFT libraries and FISHPACK.

After the time loop is finished the total divergence of the velocity filed is computed, the values of the flow filed are update. When a stationary state is searched, we monitor the Euclidean norm of the variation of velocities and temperature from one step to another.

(3) Final phase : save files with flow field variables and print the computing time.

The **main program** makes use of several modules. Each module is specific to a certain task and is called when needed. We give here a short description of the role of each module.

The **menu** module reads the values from the general menu, discussed before, and creates an echo of the parameters.

The **flow variables** module allocates each vector to the estimated size used in the computations.

The **mesh** module, generates the uniform or variable grids; different subroutines implementing transform coordinates for stretched meshes are present; the different metrics are also computed.

The **initial flow** module initialize the flow field variables (from a prescribed initial condition or from a restart file).

The **boundary conditions** module contains several subroutines, each with a particular task:
• the first one is used to impose the velocity boundary conditions; for each direction the boundary values are evaluated separately;
• the second one imposes the Dirichlet type boundary conditions and it is called specifically for the direction where we wish to enforce these values;
• the third one is used to set the values of variables of ghost cells, as function of the adjacent cells inside the flow field;
• the fourth subroutine evaluates the boundary conditions for the pressure for all three directions.

The **boussinesq force** module evaluates the value of the body-force terms for each direction. In our applications, only the gravity is present and we make a single call of this subroutine, following the z-direction.

The **momentum equation** the momentum equation using either second order or sixth order finite difference schemes.

The **Poisson** module solves the projection equation at each time step. It has different subroutines for 2D and 3D cases as well as the possibility to change between a periodical flow after the x direction (Fourier series development) and a non-periodical case (cosine series).

The **passive scalar** module computes the explicit terms of the temperature equation using either a second order scheme, or the TVD scheme or a sixth order compact scheme, depending on the initial choice.

The **output** module is set to produce either binary files for post-processing or directly files adapted for a Tecplot360 visualization of the flow field variables. It produces three-dimensional files as well as two dimensional sections within the cavity.

2.5. Study of the order of the numerical method

Compact schemes are derived to formally obtain low truncation errors, $calO(h^p)$, with h the grid size and p the order of the scheme. However, when non-periodic domains are used, the order of the method has to be decreased at the boundaries in order to maintain the band-structure of the matrix defining the scheme. For the sixth-order scheme used here, we formally have $p = 6$ for inner points, and near the boundaries $p = 4$ for $i = 2$ (or $i = N - 1$) and $p = 3$ for $i = 1$ (or $i = N$). Since we deal with an implicit scheme, all the linear equations giving the values of the derivatives are coupled and the global accuracy of the scheme is affected by the order decrease near the boundaries.

It was emphasized in previous studies (Lele, 1992) that the most appealing feature of compact schemes is the accurate representation of large range of wave numbers, rather than the resolution of a single wave. Nevertheless, we consider that it could be useful to estimate the global accuracy of the scheme when non-periodic boundaries are used. For this purpose, we undertake in this section some simple academic tests to measure the overall order of the derivation scheme: the derivation of a given analytical function (1D test) and the computation of the 2D Burggraf flow, which is an analytical, manufactured solution of the Naviers-Stokes equations. For both cases, the exact solution is known and could be used to compute the order of the method using the following classical indicators:

- Estimation of the approximation error: if the exact solution Φ is represented on the grid h by the numerical solution ϕ_h as

$$\Phi = \phi_h + C\, h^p + \mathcal{O}(h^{p+1}), \tag{2.74}$$

we can compute the approximation (or discretization) error $\varepsilon_h = \Phi - \phi_h$. We can measure ε_h for a given point of the computational domain (local error estimator) or compute various norms $\|\varepsilon_h\|$ (global error estimator). We use the following general definition of functional norms:

$$\begin{aligned}
\|v(x)\|_\infty &= \sup_x |v(x)| && \Longrightarrow && \|V\|_\infty = \sup_i |V_i|, \\
\|v(x)\|_1 &= \int_0^L |v(x)|dx && \Longrightarrow && \|V\|_1 = h \sum_{i=1}^{N} |V_i|, \\
\|v(x)\|_2 &= \left[\int_0^L v^2(x)dx\right]^{1/2} && \Longrightarrow && \|V\|_2 = h^{1/2} \left[\sum_{i=1}^{N} (V_i)^2\right]^{1/2}.
\end{aligned} \tag{2.75}$$

By computing $\|\varepsilon_h\|$ for different fine grids, we can represent $\|\varepsilon_h(h)\|$ in logarithmic coordinates and measure the slope of this curve, which gives an estimation of p.

- Estimation of the order of convergence by Richardson method: if (2.74) is also written for two other coarser grids $(2h)$ and $(4h)$

$$\Phi = \phi_{4h} + C\,(4h)^p + \mathcal{O}(h^{p+1}), \tag{2.76}$$
$$\Phi = \phi_{2h} + C\,(2h)^p + \mathcal{O}(h^{p+1}), \tag{2.77}$$

we obtain, by neglecting higher orders than p,

$$p = \frac{\ln\left(\dfrac{\phi_{2h} - \phi_{4h}}{\phi_h - \phi_{2h}}\right)}{\ln 2}. \tag{2.78}$$

From (2.74) and (2.77), we can estimate the approximation (discretization) error:

$$\varepsilon_h = \Phi - \phi_h = \frac{\phi_h - \phi_{2h}}{2^p - 1}, \tag{2.79}$$

and use $\phi_h + \varepsilon_h$ as a better estimation of the solution Φ. This is the Richardson extrapolation method - it implicitly assumes that the discretization error is monotonically decreasing and the grid is sufficiently refined. This method is often used as a tool for code validation, or an indicator of the grid convergence (local estimation of p could provide indication of the need of mesh refinement in that zone).

2.5.1. One dimensional case: derivation of an analytical function

We first consider a single wave function over a domain $L = 2\pi$:

$$f(x) = \sin(ax), \quad f'(x) = a\cos(x), \quad f''(x) = -a^2 \sin(ax). \tag{2.80}$$

and use second and sixth order finite difference schemes to compute the first and second derivative. At the boundaries ($i = 1$ and $i = N$), the centered second order scheme degenerates into a first order scheme. Figure 2.5 displays the approximation error ε_h.

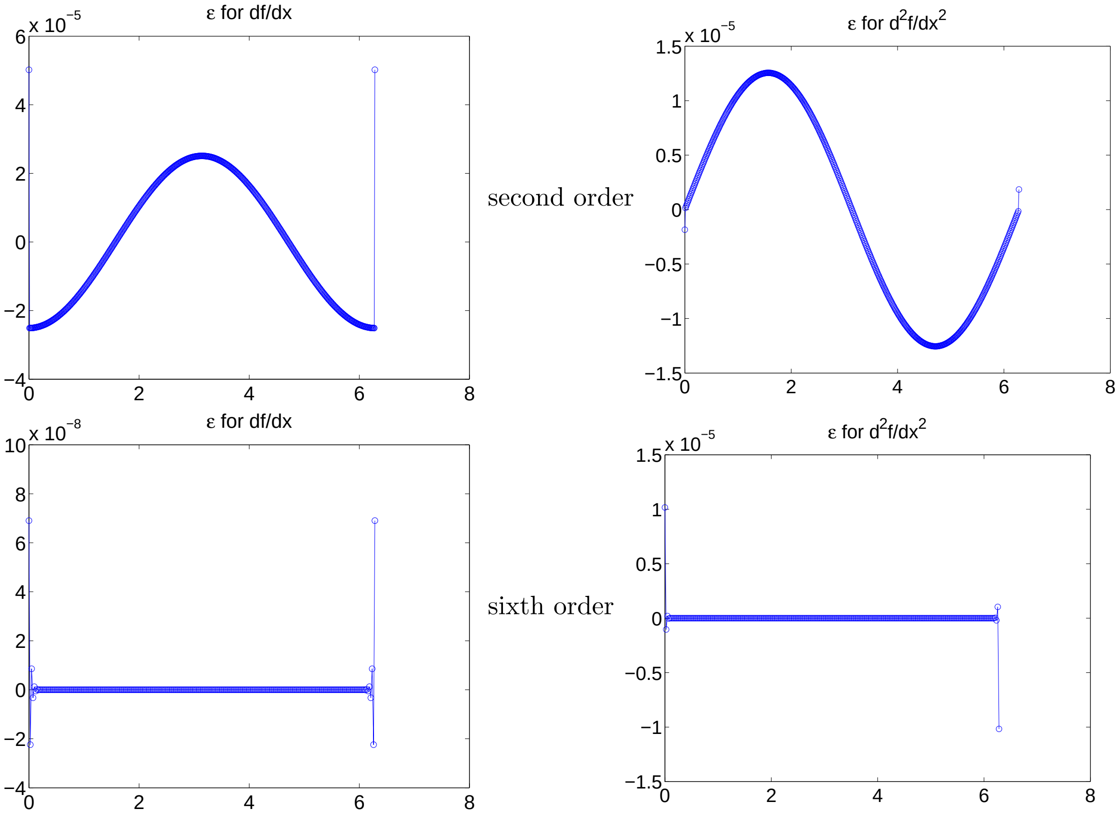

Figure 2.5.: Derivation of a single wave (sine) function. Approximation error ε_h for $N = 512$ discretization points.

We first note that the discretization error for the sixth-order scheme is several orders of magnitude lower than for the second order method. However, for both second and sixth order approximations, we can see the influence of the degeneracy of the accuracy of the scheme near the boundaries. We also notice that ε_h/h^p is not constant, which makes questionable the assumption (2.74) (C depends in fact on some derivative of the function). These observation suggests that global estimations of the order of accuracy (based on norm or Richardson analysis) has to be considered very carefully.

The global error estimation in fig. 2.6 is based on different norms. The slope of the curves $\|\varepsilon\|(h)$ is directly computed by a linear least-squares method. As expected, for the second order method the influence of the first grid point is not visible and $p = 2$ is obtained for both first and second derivative. For the sixth-order method, the influence of the border points is expected to bee more important, and, indeed, an order p between 3 and 6 is obtained, depending on the norm considered. The particular form of the function f makes the order p different for the first and second derivatives (super-convergence of the first derivative). We have checked that by changing f to a cosine function instead of the considered sine function, the results for the first and second derivative are symmetrically switched.

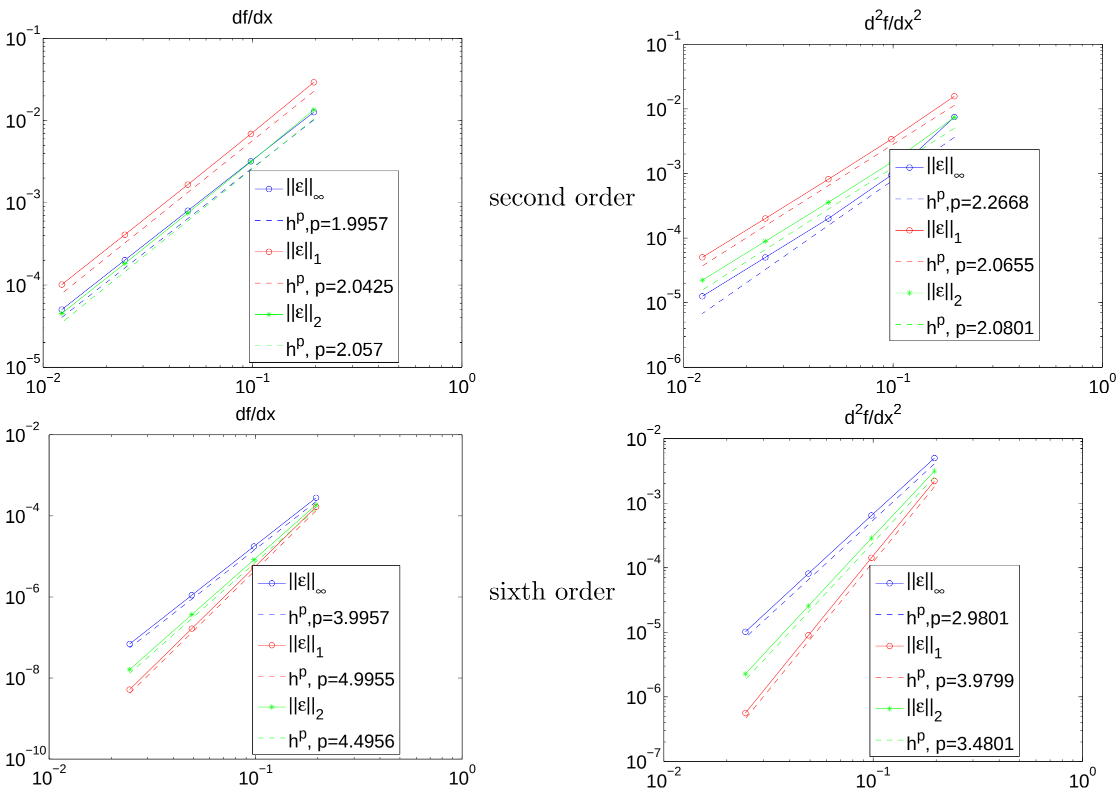

Figure 2.6.: Derivation of a single wave (sine) function. Global error estimation plotting $\|\varepsilon_h\|$ versus the grid size h. The order p of the method is computed for different norms using a linear least-squares method.

We look now at the local error estimator, considering the first grid point ($x = 0$) and the middle point ($x = L/2$). The modulus of the discretization error ε for these points is represented in fig. 2.7. For the second order method, $p = 2$ is again obtained for both points. For the second derivative, we note a super-convergence effect for the first point. Also, the order p of the second derivative could not be estimated for the middle point, since the discretization errors are very low, ranging in the round-off error domain; this is also the case for the sixth-order method and is due to the particular form of the function ($d^2f/dx^2(L/2) = 0$).

For the sixth-order method, we focus on the first derivative and notice that for the middle point the theoretical value $p = 6$ is obtained. For the first point, $p = 4$ shows a super-convergence for the first derivative, while the theoretical $p = 3$ is obtained for the second derivative. We notice again the much lower orders of magnitude of the discretization error when sixth-order schemes are used.

As a last remark for this case of derivation of a single wave (sine) function, we mention that the same study using periodic boundary conditions showed that the theoretical order $p = 2$ for the second order method and $p = 6$ for the sixth-order scheme are exactly found from computations.

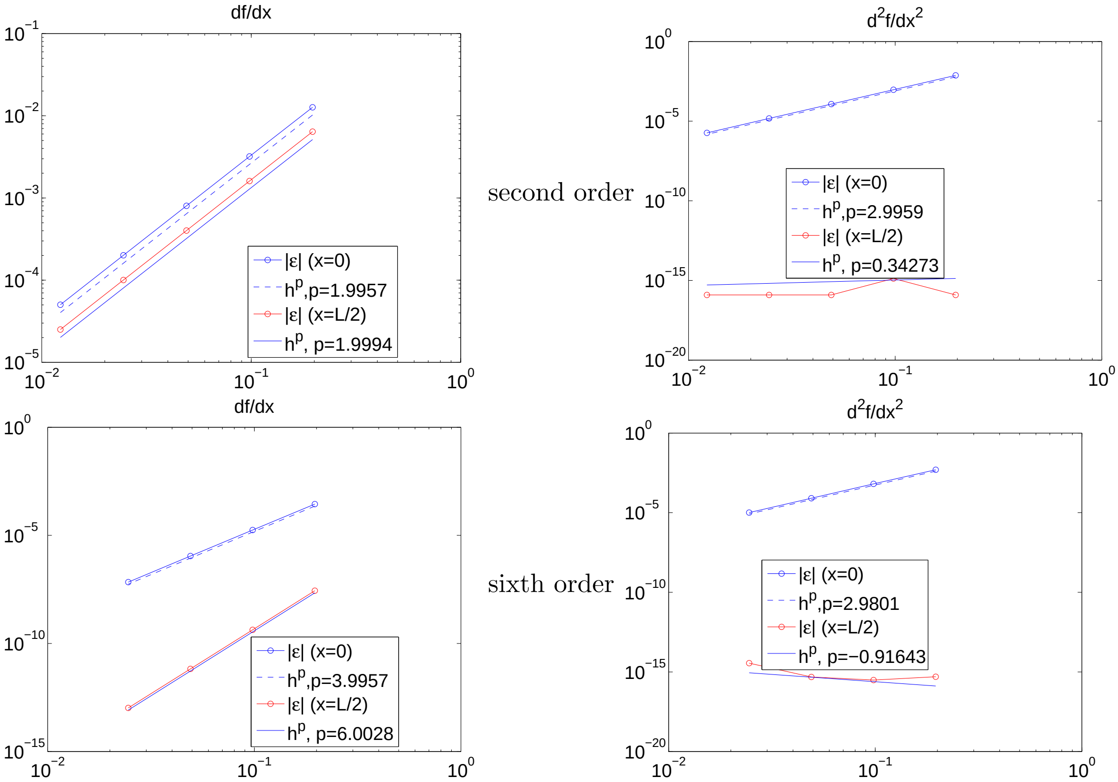

Figure 2.7.: Derivation of a single wave (sine) function. Local error estimation plotting $\|\varepsilon_h\|$ versus the grid size h for fixed points ($x = 0$ and $x = L/2$). The order p of the method is computed for different norms using a linear least-squares regression.

For the same exercise of the derivation of an analytical function, we take a second case considering a **polynomial function** from Laizet and Lamballais (2009):

$$f(x) = \frac{x^7}{7} - \frac{x^6}{2} + \frac{17x^5}{25} - \frac{9x^4}{20} + \frac{274x^3}{1875} - \frac{12x^2}{625} \tag{2.81}$$

The function is neither periodical nor symmetrical. Its boundary conditions are: $f'(0) = 0$ and $f'(L) = 0$. The computations of its first and second derivative can be compared with exact values:

$$f'(x) = (x-1)\left(x - \frac{4}{5}\right)\left(x - \frac{3}{5}\right)\left(x - \frac{2}{5}\right)\left(x - \frac{1}{5}\right)x, \tag{2.82}$$

$$f''(x) = 6x^5 - 15x^4 + \frac{68}{5}x^3 - \frac{27}{5}x^2 + \frac{548}{625}x - \frac{24}{625}. \tag{2.83}$$

Global error estimation in displayed in fig. 2.8. We notice again the boundary effects and the lower order of the discretization error when sixth-order schemes are used. The boundary discretization effects do not affect the global precision of the second order method; in exchange, they are critical for the sixth-order schemes since the global order is reduced to $p = 3$ (the discretization order of the first and last points).

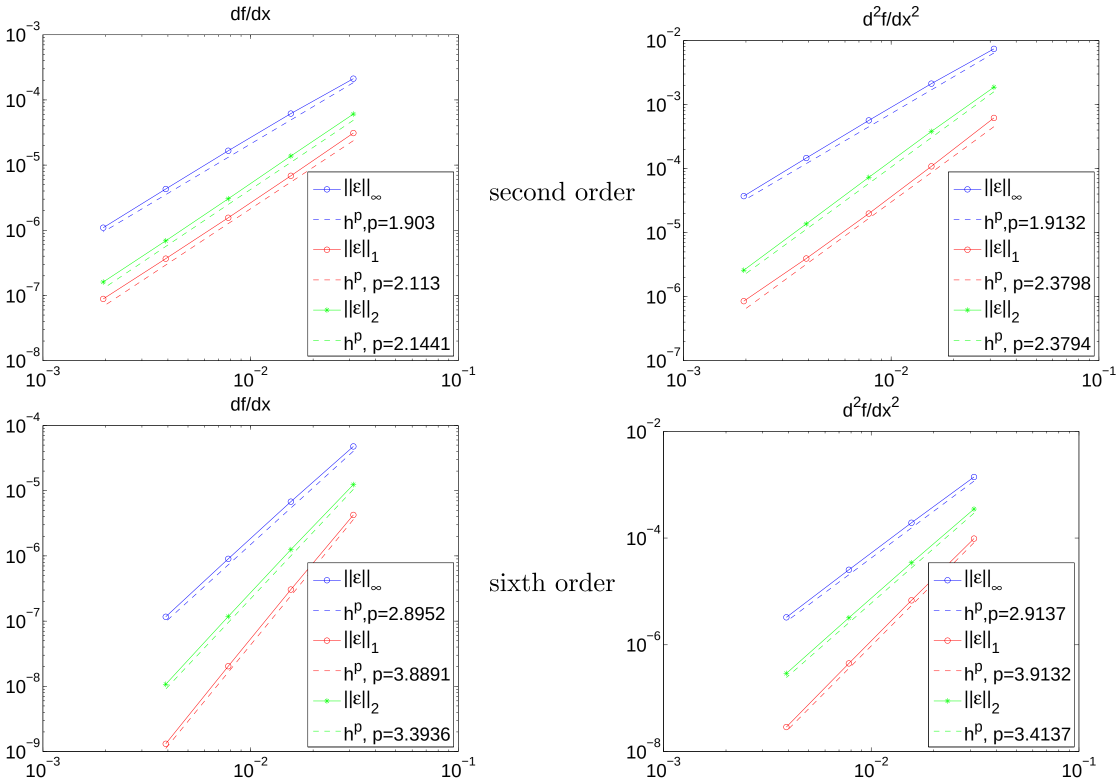

Figure 2.8.: Derivation of a polynomial function. Global error estimation plotting $\|\varepsilon_h\|$ versus the grid size h. The order p of the method is computed for different norms using a linear least-squares method.

Since the global error estimator is not appropriate to assess for the features of the scheme, we look in fig. 2.9 at particular points of the domain, the first point ($x = 0$) and the middle point ($x = L$), as in Laizet and Lamballais (2009). For the first derivative, $p = 2$ is obtained for the second order scheme and both derivatives. Again, for the middle point the discretization errors are very small for the second derivative and the order of both methods could not be determined accurately. For the sixth-order method, we notice the expected $p = 3$ for the first point and $p = 6$ for the middle point when the first derivative is considered. Also, $p = 3$ is obtained for the first point when the second derivative is computed.

It is important to emphasize that in our sixth-order scheme, the ghost cells are not used. In Laizet and Lamballais (2009) it was reported that the use of ghost cells together with the sixth-order scheme can decrease dramatically the order of convergence: $p = 2$ was obtained when a simple linear interpolation was used for the ghost cells. A special treatment of the ghost cells was proposed by Laizet and Lamballais (2009) to restore the sixth-order convergence for inner points of the domain. In our case, we prefer to use the sixth-order scheme without ghost cells since the computational effort is exactly the same.

Finally, we note that the results for the polynomial function are consistent with those obtained for the trigonometrical one. Both function were chosen to respect the symmetrical conditions $f' = 0$ for ($x = 0$ and $x = L$). The accuracy of the sixth-order order is significantly improved compared to the second-order scheme when inner points are considered. That emphasizes the fact that a global error estimator is not always appropriate to characterize compact schemes since discretization errors are dominated by the boundary treatment.

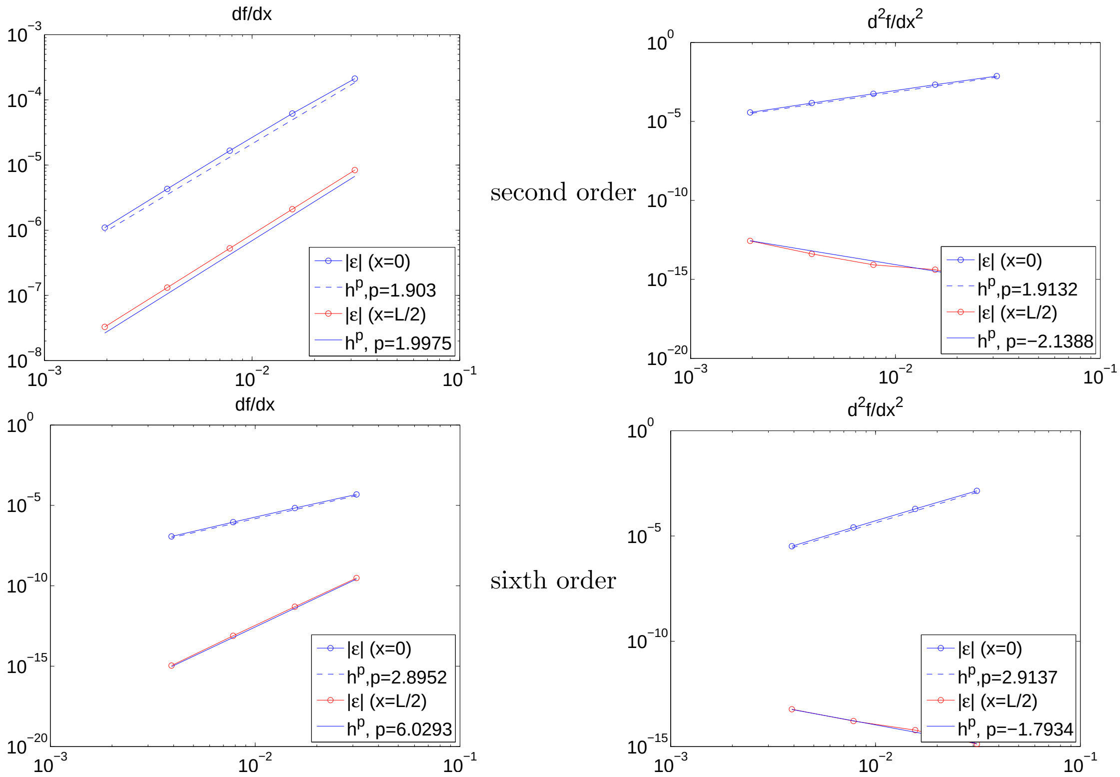

Figure 2.9.: Derivation of a polynomial function. Local error estimation plotting $\|\varepsilon_h\|$ versus the grid size h for fixed points ($x = 0$ and $x = L/2$). The order p of the method is computed for different norms using a linear least-squares regression.

Following this conclusion, another interesting question is how many points inside the computational domain will display a sixth order convergence rate? To answer this question, we consider the Richardson analysis (2.78) explained above. Figure 2.10 shows the results for the first derivative only: the discretization error ε is plotted first, followed by the computed values of p for each grid point, using (2.78). For both second and sixth order schemes, the three meshes have $N = 32, 64$ and 128 points, respectively. When $\varepsilon < 10^{-12}$ we discard the calculated values of p, since we are in the round-off errors domain and the method is not reliable.

For the second order method, all the grid points display the expected convergence rate $p = 2$. For the sixth order scheme we notice that the middle zone of the domain ($0.4 < x < 0.6$) displays the theoretical convergence rate $p = 6$. This zone corresponds to a monotonic decrease of the discretization error ε with the grid resolution. Near the locations $x = L/4$ and $x = 3L/4$, since ε decreases not uniformly, the calculated value of p exceed 6 and goes up to 15. This is explained by the faster reduction of the discretization error for $N = 128$ (the plateau with low discretization errors is larger and larger when the resolution is increased). When going near the boundaries, the value of p decreases again and reaches the theoretical value $p = 3$.

This variation of the convergence order p, not seen in previous publications, which suggest that the Richardson method should be used with caution when compact implicit schemes are used.

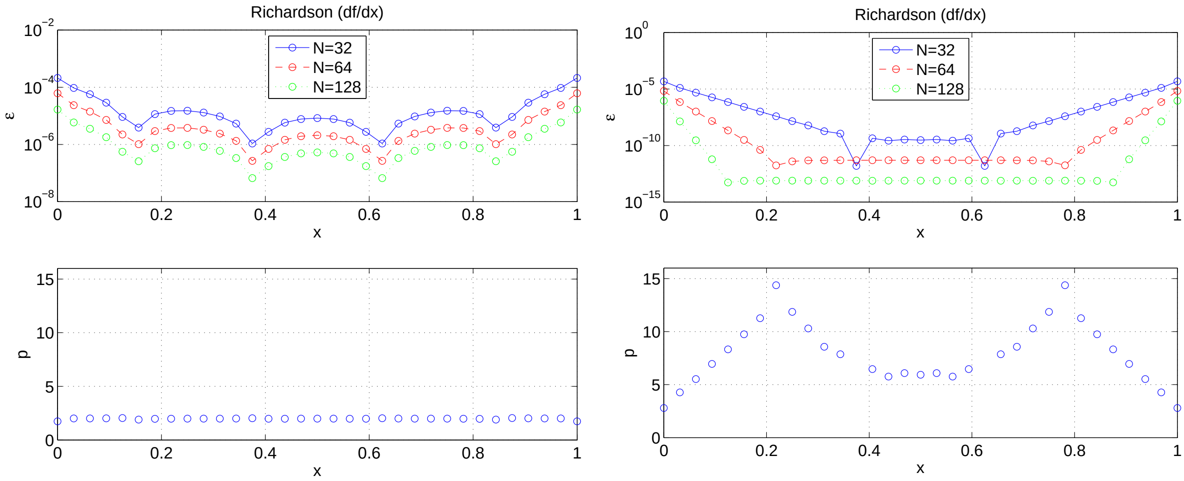

second order scheme

sixth-order scheme

Figure 2.10.: Derivation of a polynomial function (first derivative). Estimation of the convergence rate by the Richardson method. Discretization errors for the three grids considered (up) and calculated values of p for the grid points of the coarse grid (down).

2.5.2. Two-dimensional case: Burggraf flow

To test the accuracy of the Navier-Stokes solver we use the well-known (Shih et al., 1989; Sheu and Lin, 2004; Laizet and Lamballais, 2009) analytical solution called the Burggraf flow. It is in fact a manufactured solution, obtained by introducing an artificial force term in the momentum equations in order to get the prescribed solution. The Burggraf flow is a steady recirculating flow inside a square cavity $L_x = L_y = 1$, with non-slip wall conditions at the boundaries:

$$u(x, 0) = u(0, y) = u(1, y) = 0, \tag{2.84}$$

excepting for the top boundary, where the flow is entrained by a horizontal velocity:

$$u(x, 1) = 16(x^4 - 2x^3 + x^2). \tag{2.85}$$

It should be noted that this form of the velocity avoids discontinuities at the corners of the cavity, which is the case for the classical lid driven flow.

The exact solution of this flow is

$$\begin{aligned} u(x, y) &= 8(x^4 - 2x^3 + x^2)(4y^3 - 2y), && (2.86)\\ v(x, y) &= -8(4x^3 - 6x^2 + 2x)(y^4 - y^2), && (2.87) \end{aligned}$$

and corresponds to a y-direction forcing:

$$f_y = \left(\frac{8}{Re}[24g + 2g''h'' + g^{(4)}h] + 64\left(\frac{g'^2}{2}(hh''' - h'h'') - hh'(g'g''' - g''^2)\right)\right) e_y, \tag{2.88}$$

with:

$$g(x) = \frac{x^5}{5} - \frac{x^4}{2} + \frac{x^3}{3}, \quad h(y) = y^4 - y^2. \tag{2.89}$$

We used the second order solver for 40, 120 and 360 grid points, while for the sixth order we considered 20, 60 and 180 grid points. For the sixth-order a coarser grid offers the same accuracy as a more refined mesh for the second-order. In both cases staggered mesh is considered and we recall that the sixth order interpolation was used with the compact scheme. The computations were done for a Rayleigh number $Ra = 10^6$ and Prandtl number $Pr = 0.71$.

Figure 2.11 shows the streamlines obtained by the second order solver. We also show the decrease of the global discretization error $\|\varepsilon\|_2$ with the grid size. The equivalent definition for a 2D domain of the L^2 norm (2.75) was used. The expected second order convergence is obtained for both horizontal and vertical velocities.

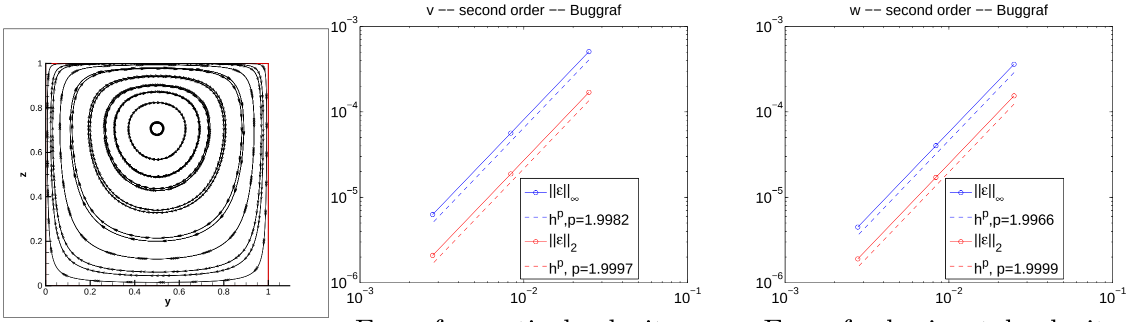

Error for vertical velocity   Error for horizontal velocity

Figure 2.11.: Burggraf flow computed with the second order solver. Streamlines and global discretization error $\|\varepsilon\|_2$ for the vertical and horizontal velocities.

For the sixth-order method the streamlines and decrease of the global error $\|\varepsilon\|_2$ are presented in figure 2.12. The results obtained state that despite the higher order used for velocities derivatives, only a second order ($p = 2.5$) accuracy is obtained. This behaviour was expected from the previous 1D study showing that global error estimates are greatly affected by the lower order of the scheme near the boundaries. We also recall that the Poisson solver used a second order discretization of the derivatives. A similar result ($p = 2$) for the Burggraf flow was reported by Laizet and Lamballais (2009); they claimed that the low order accuracy of the Poisson solver was responsible for this result. We can see now that this is not the only cause, and the global error estimates when the sixth order scheme is used could be misleading. We note in passing that a fully sixth order Poisson solver will allow to increase the global precision of the flow solver (Boersma, 2011).

At a first glance, the global accuracy for velocity and pressure is only slightly better for the sixth-order method, than for the second order one. It is interesting to compare in the following the grid resolution necessary to obtain the same level of the discretization error. Figure 2.13 presents the vertical and horizontal velocity profiles, following the centerlines. We note that

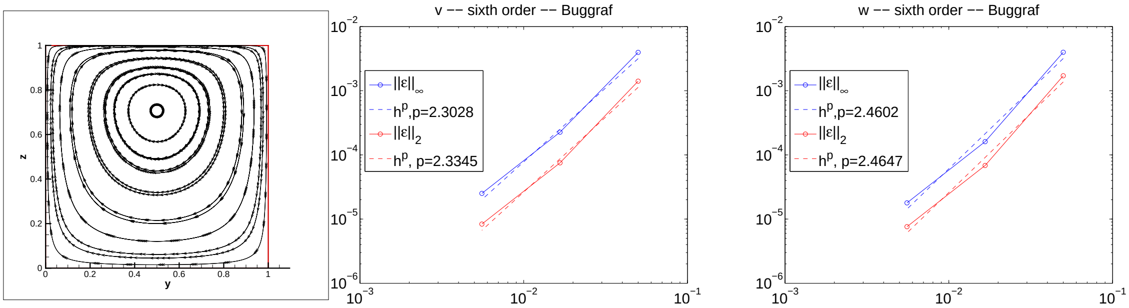

Streamlines　Error for vertical velocity　Error for horizontal velocity

Figure 2.12.: Burggraf flow computed with the sixth order solver. Streamlines and global discretization error $||\varepsilon||_2$ for the vertical and horizontal velocities.

the accuracy obtained with the finner grid for the second order solver (360×360) is attained by using the sixth-order solver with only (180×180) grid cells.

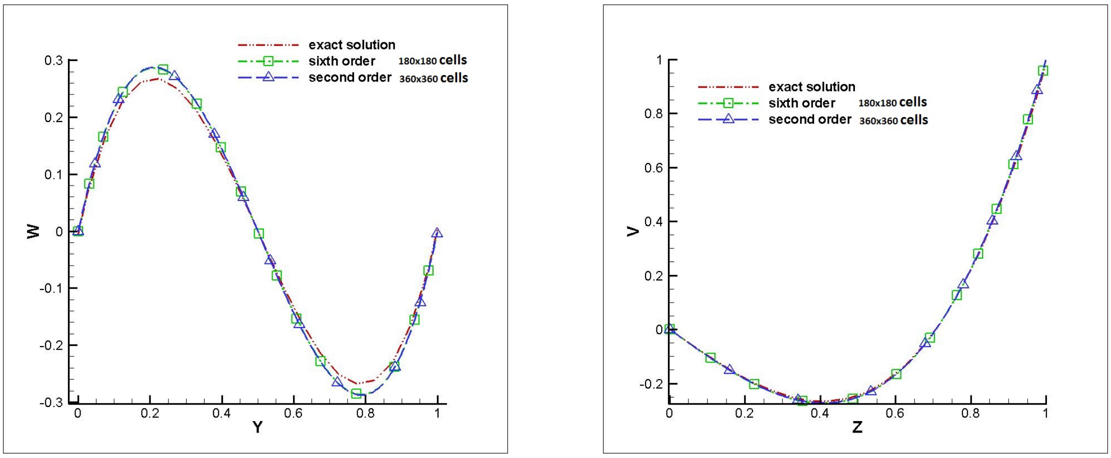

Figure 2.13.: Burggraf flow. Profiles following the centerline of the cavity for the vertical and horizontal velocities.

Even though the number of computational nodes could be divided by 4 when sixth order schemes are used, the computation of the derivatives in implicit schemes requires addition CPU time. From figure 2.14 it can be noted that while the computational time for an individual time step is higher for the sixth order than for the second-order accuracy, the overall global convergence time is lower since the sixth-order scheme reaches convergence in fewer steps than the second order scheme. This provides faster computational times for the sixth order to reach the stationary solution, for cases where the same number of grid points were considered.

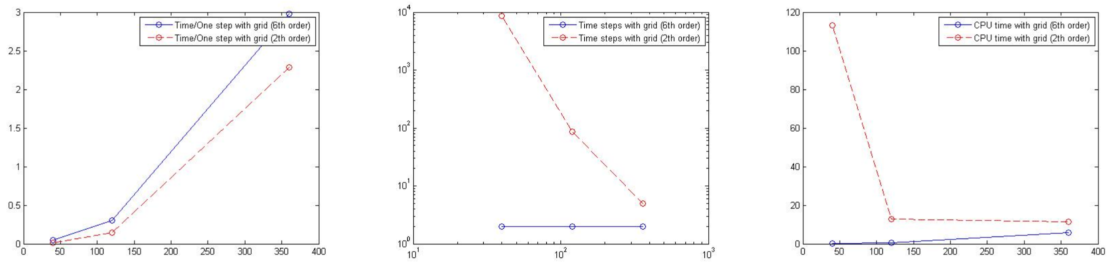

a) b) c)

Figure 2.14.: Burggraf flow. Variation with grid resolution N of a) the computational time for one time step, b) the total number of steps necessary for convergence to the steady state ; c) the total computational time to reach the stationary state.

3. Numerical simulation of natural convection flows

The most relevant fundamental problem for our configuration is the natural convection in cavities with obstacles. Natural convection inside enclosures is one of the most widely studied configurations in thermodynamics due to the large number of applications, such as electronic cooling, solar collectors, energy transfer, fluid filled storage, etc. A good knowledge of the natural convection flow provides a valuable starting point for testing and validating our numerical simulations.

3.1. Physical problem

Fundamental natural convection problems can be classified into two cases: the Rayleigh-Bénard case and the differentially heated cavity case (fig. 3.1). For both cases, a large number of benchmark numerical solutions exists for both two-dimensional (2D) and three-dimensional (3D) configurations. We shall use numerical data from well-known benchmarks to validate our simulations.

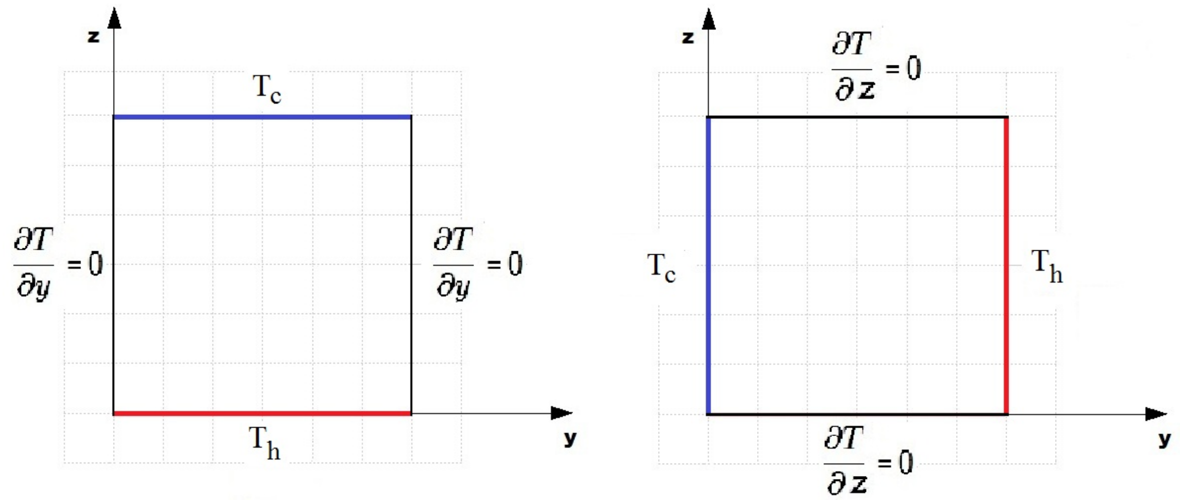

Figure 3.1.: Fundamental problems for natural convection in a cavity, driven by the temperature gradient between the hot (T_h) and cold (T_c) isothermal walls: Rayleigh-Bénard problem (left) and differentially heated cavity problem (right).

For both convection problems the fluid considered is air with $\mathcal{P}r = 0.71$. The dimension of the cavity is $L = 1$ and dimensionless temperatures are taken as $T_h = 0.5$ and $T_c = -0.5$.

It is important to note that these fundamental cases display distinctive behaviour which represent starting points for the study of natural convection in more complicated geometries.

Every cavity that contains a heat source can ultimately be striped down to a very simple case whose dynamics is described by one of the two families of fundamental problems. As a result, flows inside cavities can be divided in such a manner as to distinguish the simultaneous occurrence of both Rayleigh-Bénard and differentially heated cavity flows.

3.1.1. Rayleigh-Bénard convection

A schematic representation of Rayleigh-Bénard flow, for a square cavity, is depicted in figure 3.1 (left). The cavity is cooled form above and heated from below. The sidewalls are considered adiabatic.

The thermal instability of a fluid layer cooled form above and heated from below represents the basis of known convection flows. It appears for a very large number of space scales, starting from very small ones as those present in cooling systems for electronic components, to very large planetary ones. If the temperature difference is relatively small, the transfer is made by diffusion from below upwards. Otherwise, if the temperature difference is equal to the critical value, the flow becomes unstable and the fluid is set in motion, forming convection cells. The adjacent cells are counter-rotating (figure 3.2) and their geometry depends on the boundary conditions. Further increase of the temperature difference destabilize the flow in a periodical manner. The width and depth of the cavity have an important impact on the structure of the flow.

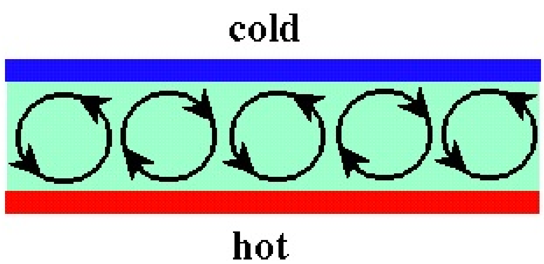

Figure 3.2.: Rayleigh-Bénard convection cells.

Busse (1978) defined four types of characteristic flow behavior depending on the Rayleigh number. The value of the $\mathcal{R}a$ number, relative to its critical value($\mathcal{R}a_c$), allows to distinguish between the following regimes:

- $\mathcal{R}a < \mathcal{R}a_c$, the conductive case where the fluid is stationary and the temperature field is linear between the two walls;
- $\mathcal{R}a > \mathcal{R}a_c$, the laminar case where counter-rotating cells appear;
- $\mathcal{R}a = 10\mathcal{R}a_c$, the flow becomes complex and the 2D cells are divided into 3D cells;
- $\mathcal{R}a >> \mathcal{R}a_c$, the flow becomes turbulent.

3.1.2. Differentially heated cavity

Flows inside differentially heated cavities are considered more stable than Rayleigh-Bénard flows. As shown in figure 3.1 (right), the cavity is heated from the left wall and cooled from the right one; the upper and lower walls are adiabatic.

Along the heated wall, the fluid temperature rises and its density decreases. Due to the density decrease, the fluid rises up to the point where it reaches the cold wall, where the reverse process occurs. This two simultaneous opposing effects create a recirculation cell. In the center of the cell, a stationary zone can be observed.

3.2. Previous numerical studies of natural convection flows

Numerous studies were done in the past for the square cavity, beginning with de Vahl Davis (1983); Mallinson and de Vahl Davis (1977) and de Vahl Davis and Jones (1983), who proposed one of the first two-dimensional (2D) computational benchmarks for the laminar regime, at Rayleigh numbers up to 10^6, using second-order centered finite difference schemes. Later, forth-order accuracy benchmarks were proposed by Saitoh and Hirose (1989), for Rayleigh numbers up to 10^4. Hortmann et al. (1990) used a multigrid finite volume method with refined grids and assembled a benchmark for Rayleigh numbers up to 10^6. Among the first numerical studies of natural convection flows in cavities we can also recall Bilski et al. (1986); Jia et al. (1990); Okanaga and Tanahashi (1990). Important studies to determine the critical Rayleigh number in air-filled cavity with adiabatic horizontal walls, such as Paolucci and Chenoweth (1990); Janssen and Henkes (1995); Xin et al. (1997); Le Quéré and Behnia (1998) were done. They used a spectral Chebyshev method with a velocity pressure coupling for $\mathcal{R}a$ up to 10^8.

For the turbulent regime, 2D DNS (direct numerical simulation) solutions were provided by Paolucci (1990) for $\mathcal{R}a = 10^{10}$ and Xin and Le Quéré (1995) for $\mathcal{R}a = 10^9$. Following these studies, the results based on RANS (Reynolds Averaged Navier Stokes) models of turbulence display a large scattering.

Three-dimensional (3D) benchmark numerical solutions were also proposed, beginning with study of Mallinson and de Vahl Davis (1977) for Rayleigh numbers up to 10^6 on coarse grids. Fusegi et al. (1991) calculated the flow inside an air filled cavity for $\mathcal{R}a = 10^4$ and $\mathcal{R}a = 10^6$ respectively, using a QUICK scheme on fine and non-uniform grids and compared the results to experimental ones. Using a second-order finite volume method and uniform and non-uniform grids, Janssen et al. (1993) conducted tests for the steady case with $\mathcal{R}a = 10^6$. Wakashima and Saitoh (2004) proposed a benchmark solution using a high-order time and space method for Rayleigh numbers varying between 10^4 and 10^6.

Different formulations of the governing equations were used in previous studies. Angirasa et al. (1995) used a vorticity-stream function formulation of the Navier-Stokes-Boussinesq model for the simulation natural convection in a square isothermal open cavity. The Boussinesq approximation was also previously used by Hinojosa and de Gortari (2010) for simulating the steady-state and transient heat transfer by natural convection in a horizontal isothermal open cubic cavity. They have validated their simulations for Rayleigh numbers from 10^4 to 10^7. Temperature-dependent fluid properties were taken into account in the Boussinesq approximation by Juárez et al. (2011); they used a finite-volume method to simulate an open cavity for Rayleigh numbers between 10^4 and 10^7. The laminar natural convection within an open cavity was also studied using the Boussinesq approximation by Mohamad (1995); Sezai and Mohamad (1998); Polat and Bilgen (2003) and Hinojosa et al. (2006). Chan and Tien (1985) investigated the laminar steady-state natural convection in a two-dimensional rectangular open cavity. Thermal radiation on the surface of the cavity was considered in the Boussinesq assumption by Lage et al. (1992) for the numerical study of the heat transfer by natural convection in a 2D open top cavity under. Balaji and Venkateshan (2008) conducted a numerical study of combined conduction, natural convection and surface thermal radiation in an open top cavity, also using the Boussinesq approximation.

Most of the numerical studies in the literature use the Navier-Stokes-Boussinesq model and classical numerical methods (finite difference, elements, of volume methods, or spectral methods). Recently, Lattice Boltzmann Methods (LBM) were proposed for these cases. Mohamad et al. (2009) simulated natural convection in an open cavity and demonstrated that open boundary conditions used at the opening of the cavity were reliable, and the predicted results were similar to conventional CFD method. Other results using LMBM methods for the square or inclined cavity in the laminar regime were reported by Huelsz and Rechtman (2013); Barrios et al. (2005).

Concerning the geometry of the problem, the cavity problem can be classified as: problems in cubic cavities, rectangular, square and cylindrical cavities. Extensive research can be found throughout literature for each of these cases. Pallares et al. (2002) discuss flow structures and heat transfer rates generated by Rayleigh-Bénard convective motions of a Boussinesq approximated laminar flow in the range of Rayleigh numbers $7 \times 10^3 \leq \mathcal{R}a \leq 10^5$. They also used a large-eddy simulation (LES) technique for simulations at two high Rayleigh numbers $\mathcal{R}a = 10^6$ and $\mathcal{R}a = 10^8$.

Fusegi et al. (1992) tested a high-resolution, finite-difference numerical scheme of three-dimensional natural convection in a cubic enclosure with differentially heated side walls and an internal partition located at the mid-plane. Sedelnikov et al. (2012) implemented a three-dimensional method for natural convection in a cubic cavity heated from below and rotating about its vertical axis of symmetry with two horizontal isothermal boundaries and the four insulated vertical walls. Other examples of cubic cavities are Valencia et al. (2007); Mamun et al. (2003); Pallaras et al. (1996); Leong et al. (1998); Hess and Henze (1984); Clausing et al. (1987); M.D. Pavlović and (1991); Jr. and Newell (2007).

Warrington and Powe (1985) investigated natural convection between concentrically located inner bodies and their isothermal cubic enclosures.

For the rectangular cavity study, a reference study is due to Wang and Hamed (2006); they used a SIMPLE algorithm for the flow simulations with Rayleigh numbers in the range between 10^3 and 10^4 with aspect ratio 4, and angle of inclination between 0 and 90. Shati et al. (2013) studied the effects of natural turbulent convection with the interaction of surface radiation and provide an empirical solution for the case of radiation and natural convection. Nithyadevi et al. (2007) performed a numerical study to investigate the effect of aspect ratio on the natural convection of a fluid with partially thermally active side walls. In the case of rectangular open cavity we can mention studies by Chen et al. (1983); Clausing (1982); Chen et al. (1985); Chan and Tien (1985, 1986); Comini et al. (1996); Chakroun et al. (1997); Elsayed and Chakroun (1999); Chakroun (2004).

Square cavity cases with enclosures were investigated by Wu and Ching (2010) for laminar natural convection, Park et al. (2012) for the natural convection in a square enclosure with hot and cold cylinders, Butler et al. (2013); Huelsz and Rechtman (2013); Quéré et al. (1981); Penot (1982); Angirasa et al. (1992), etc..

The case of cylindrical cavities was less studied than the ones before, but as a reference we can mention Prakash et al. (2009); Leibfried and Ortjohann (1995).

3.3. Validations for 2D convection problems

In this section, we consider two-dimensional benchmarks for laminar natural convection: the Rayleigh-Bénard convection and the differentially heated cavity (see fig. 3.1). For both cases, we present the benchmark (steady) solution followed by a quantitative and a qualitative analysis of each numerical model considered (for space discretization and time advancement). A table is provided for each of these cases that estimates the error between the benchmark and our solution, thus making clear the choice made for further simulations.

For the Rayleigh-Bénard benchmark we have considered the results proposed by Ouertatani et al. (2008) while for the differentially heated cavity we compared our results with those of Wakashima and Saitoh (2004).

All the results presented here are for a $Pr = 0.71$ and Ra numbers varying form 10^4 to 10^6, on a staggered uniform or variable grid. We have considered grids form 32×32 cells up to 512×512 and the comparisons with the benchmarks were made using the same grid resolution as the respective studies. The horizontal and vertical velocity distributions are extracted at mid-plane ($y = 0.5$) and mid-height ($z = 0.5$) and compared to available data from benchmarks. Initially the fluid is considered at rest and all the flow variables are set as to zero. The steady state is reached when $\max\limits_{\phi=v,w,T} \|\phi^{n+1} - \phi^n\|_2 < 10^{-7}$.

As general features for both cases, we can observe that for $Ra = 10^4$ the flow is symmetrical and presents a recirculation cell in the core region. With the increase of the $\mathcal{R}a$ number, two secondary cells appear, at the top left and bottom right corners, and are more and more prominent. It is similar for the isotherms, they are symmetrical for small $\mathcal{R}a$ numbers and the convection motion begins to be more intense as the $\mathcal{R}a$ increases.

We present the two types of grids considered, respectively the uniform and variable (stretched) one, as depicted in figure 3.3. For this particular situation, as there are no immersed objects, there is no need to use a grid refinement inside the cavity. Thus the refinement is applied in the vicinity of the walls to better capture the recirculation zones and the boundary layers, which become thinner when increasing the $\mathcal{R}a$ numbers. Second-order finite difference schemes are used for both uniform and variables meshes, while sixth-order compact schemes are used only with uniform grids.

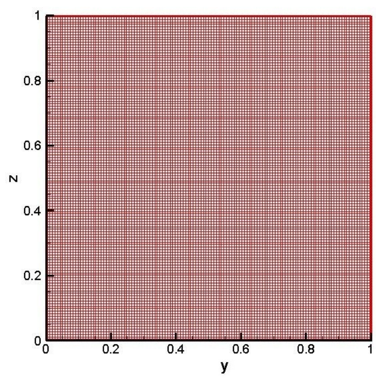

uniform grid

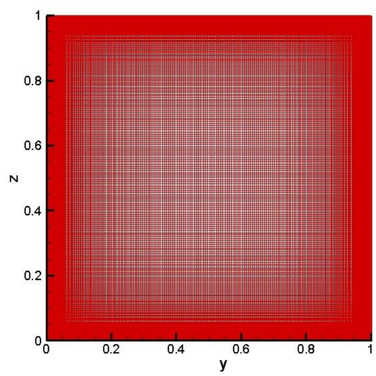

variable grid

Figure 3.3.: Grids considered for our simulations of natural convection.

3.3.1. Rayleigh-Bénard (vertical ∇T) case

Streamlines and isotherms reported by Ouertatani et al. (2008) are displayed in figure 3.4. Their numerical approach is based on a finite volume method and a full multigrid acceleration, applied on a fine grid with 256 × 256 nodes.

The expected feature of the flow for $Ra = 10^4$ is to be symmetrical and dominated by a single recirculation cell in the middle of the domain. Two very small eddies can be noticed in the top left corner and bottom right corner. By increasing the Rayleigh number to $Ra = 10^5$, the two secondary vortices increase in size. The isotherms are symmetrical and the beginning of a convective motion can be observed. As we further increase the Rayleigh number to 10^6, the eddies in the corners also expand and the isotherms contours are more distorted.

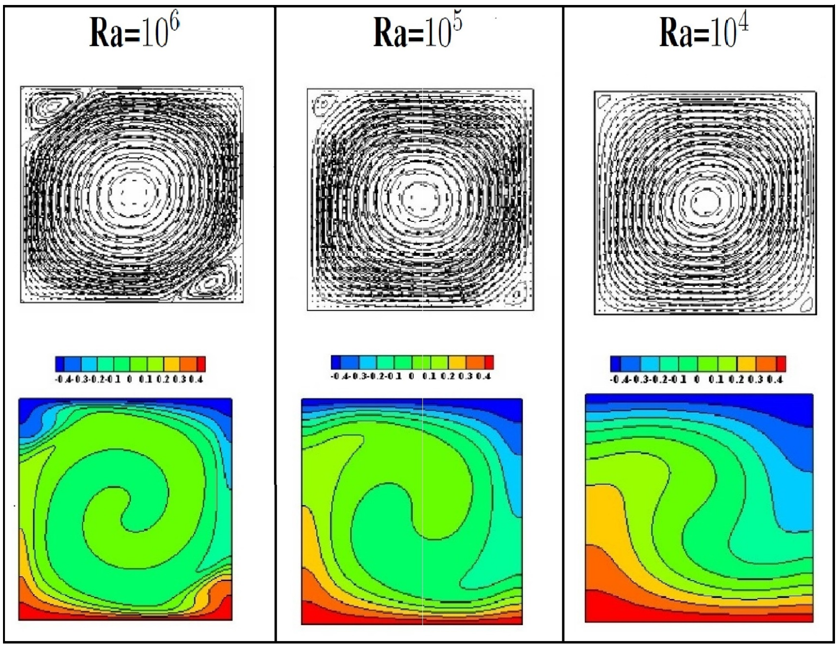

Figure 3.4.: Rayleigh-Bénard convection in a square cavity. Benchmark solution by Ouertatani et al. (2008).

We start by assessing the influence of the time-integration scheme on the accuracy of the results. The following simulations use second order finite difference schemes on the uniform grid with the same number of nodes as the test case, respectively 256 × 256. The time step is the same for all integration methods, $\delta t = 1.e-4$.

(1) Euler method

The isotherms and temperature fields are represented in figure 3.5. For $Ra = 10^4$ the presence of the three vortices can be seen: the dominant one in the center of the domain and two very small ones in the corners. With the increase of the Rayleigh number, the two secondary vortices also grow. These conclusions are in very good agreement with the ones drawn from the test case (figure 3.4).

The horizontal and vertical velocity distributions at the mid-width ($y = 0.5$) and at the mid-height ($z = 0.5$) and the variation of the Nusselt number on the hot wall, are presented in figure 3.6, for Rayleigh numbers between 10^4 and 10^6. As indicated by the velocity distribution, the increase of the Rayleigh number determines a confinement of the boundary layer to the walls.

The increase of the velocity norm indicates that convection becomes dominant.

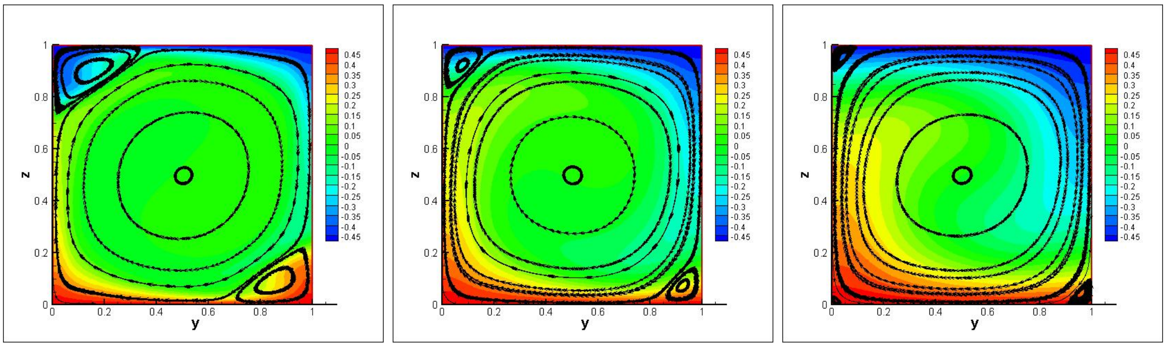

$Ra = 10^6$ $Ra = 10^5$ $Ra = 10^4$

Figure 3.5.: **Euler method**. Finite difference simulation of the Rayleigh-Bénard convection. Streamlines and temperature fields for different Rayleigh numbers.

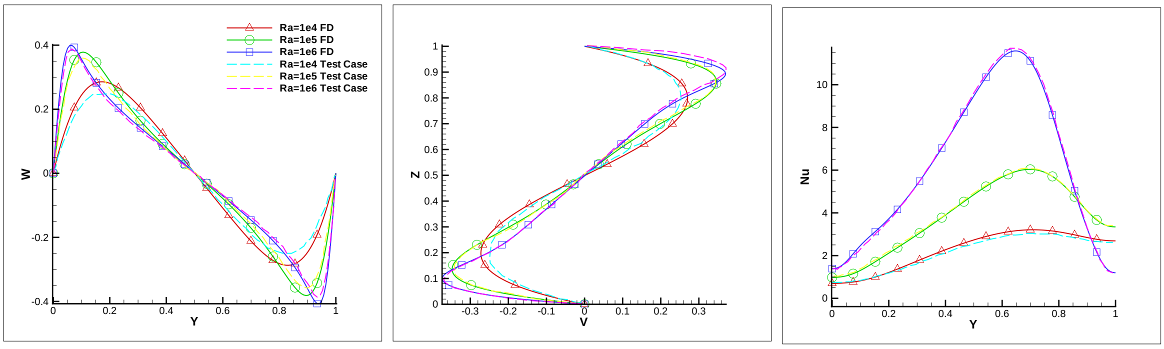

W velocity V velocity Nusselt number

Figure 3.6.: **Euler method**. Finite difference simulation of the Rayleigh-Bénard convection. Velocity profiles following horizontal and vertical centerlines: comparison with benchmark solution (dashed lines) from Ouertatani et al. (2008).

Rayleigh no.		Value (Position)	$U_{error}\%$ ($X_{error}\%$)
$Ra = 10^4$	$v_{max}(z)$	0.2705(0.8007)	7.2229%(−0.1894%)
	$w_{max}(y)$	0.2870(0.8320)	8.8706%(0.6935%)
	$Nu_{max(y)}$	3.2087(0.7070)	6.1432%(−1.5688%)
$Ra = 10^5$	$v_{max}(z)$	0.3463(0.8647)	0.5703%(0.1280%)
	$w_{max}(y)$	0.3814(0.8945)	1.5299%(−0.3085%)
	$Nu_{max}(y)$	6.0377(0.7)	−0.4496%(0.1001%)
$Ra = 10^6$	$v_{max}(z)$	0.3680(0.8945)	−0.7668%(−1.0036%)
	$w_{max}(y)$	0.4092(0.941406)	0.8039%(0.5883%)
	$Nu_{max}(y)$	11.8072(0.6529)	1.0025%(1.2625%)

Table 3.1.: **Euler method**. Finite difference simulation of the Rayleigh-Bénard convection. Maximum horizontal and vertical velocities along centerlines and their locations. Comparison with benchmark solution.

A quantitative comparison is offered in Table 3.1. The maximal values of the horizontal and vertical velocities and their locations, as well as the maximum Nusselt number, are extracted.

The relative error in % is computed with respect to the results presented by Ouertatani et al. (2008). A very good agreement with the considered benchmark is obtained. We can observe a diminution of the error with the increase of Rayleigh number. For $Ra = 10^4$ a maximum error of approximately 7% is obtained while for $Ra = 10^6$ an error within 0.8% difference is obtained.

(2) Adams-Bashforth method

A second time integration method considered is the Adams-Bashforth model. As it will soon be shown, this proves to be more accurate than the previous method (Euler). This an intermediate scheme, from the accuracy and time consuming point of view, between Euler and third order Runge-Kutta. In figure 3.7 we can observe the temperature field and isotherms for the three different Rayleigh numbers. This is qualitative comparison, that shows a good agreement to the benchmark solution. For all Rayleigh numbers considered, the same vortices appear as in the test case model.

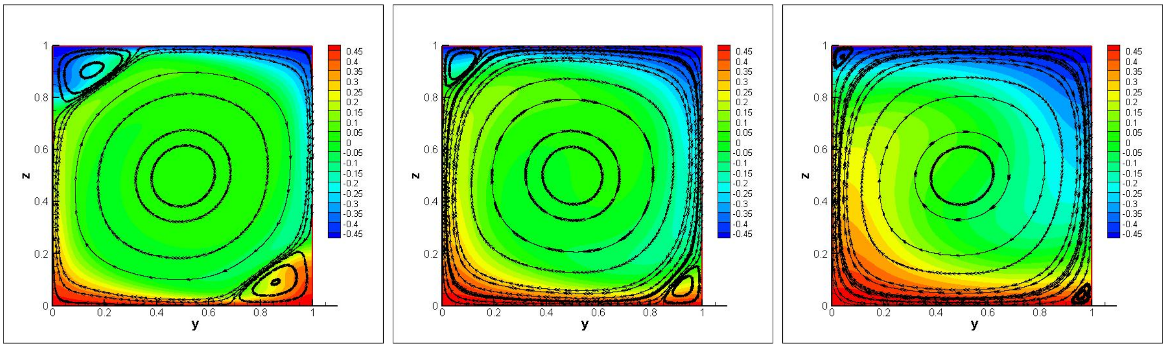

$Ra = 10^6$ $Ra = 10^5$ $Ra = 10^4$

Figure 3.7.: **Adams-Bashforth method**. Finite difference simulation of the Rayleigh-Bénard convection. Streamlines and temperature fields for different Rayleigh numbers.

Moving on to a quantitative comparison, the horizontal and vertical velocity distributions at the mid-width ($y = 0.5$) and at the mid-height ($z = 0.5$), as well as the Nusselt number on the hot wall, are presented in figure 3.6. A good agreement with Ouertatani et al. (2008) is obtained.

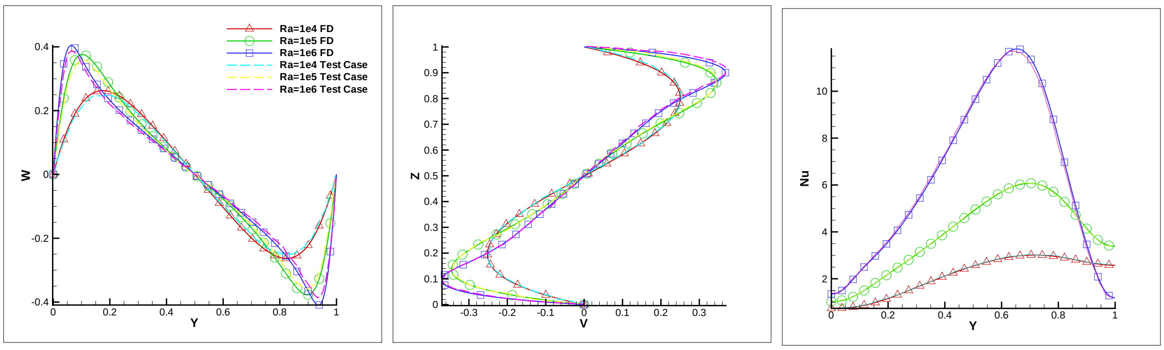

W velocity V velocity Nusselt number

Figure 3.8.: **Adams-Bashforth method**. Finite difference simulation of the Rayleigh-Bénard convection. Velocity profiles following horizontal and vertical centerlines: comparison with benchmark solution from Ouertatani et al. (2008).

The results from figure 3.6 are represented in Table 3.2. The relative error is shown and we can conclude that these results provide an improvement with respect to the previous ones. For $Ra = 10^4$ a decrease of 5% in error is noted, and the results are now within a 2% difference with Ouertatani et al. (2008). Also, considerable improvement can be noted for $Ra = 10^5$ and $Ra = 10^6$, where the global error for velocities, as well as for their position, is bellow 1%.

Rayleigh no.		Value (Position)	$U_{error}\%$ ($X_{error}\%$)
$Ra = 10^4$	$v_{max}(z)$	0.2569(0.8015)	1.881%(−0.091302%)
	$w_{max}(y)$	0.2711(0.8276)	2.8156%(−0.1284%)
	$Nu_{max}(y)$	3.0775(0.7127)	1.8054%(−0.7655%)
$Ra = 10^5$	$v_{max}(z)$	0.3452(0.8642)	0.2615%(0.073021%)
	$w_{max}(y)$	0.3787(0.8955)	0.8257%(−0.1935%)
	$Nu_{max}(y)$	6.0613(0.6997)	0.2348%(0.062872%)
$Ra = 10^6$	$v_{max}(z)$	0.3694(0.8981)	−0.3724%(−0.6001%)
	$w_{max}(y)$	0.4086(0.9372)	0.659%(0.1529%)
	$Nu_{max}(y)$	11.6564(0.6473)	0.9551%(0.4486%)

Table 3.2.: **Adams-Bashforth method**. Finite difference simulation of the Rayleigh-Bénard convection. Maximum horizontal and vertical velocities along centerlines and their locations. Comparison with benchmark solution from Ouertatani et al. (2008).

(3) Third order Runge-Kutta method

Moving forward to the third order Runge-Kutta method, we show the isotherms and temperature filed in figure 3.9, for the three Rayleigh numbers 10^6, 10^5 and 10^4. From a qualitative point of view, the results are again in good agreement with the test cases. However, we shall see below that this time integration method is more accurate than the two previously discussed.

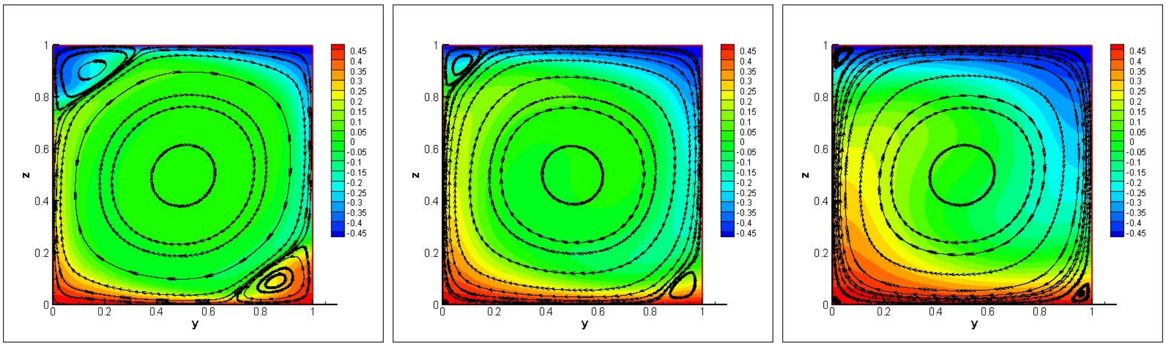

$Ra = 10^4$ $Ra = 10^5$ $Ra = 10^6$

Figure 3.9.: **Third order Runge-Kutta**. Finite difference simulation of the Rayleigh-Bénard convection. Streamlines and temperature fields for different Rayleigh numbers.

Figure 3.10, depicts a qualitative comparison, of velocities at mid-width ($y = 0.5$) and mid-height ($z = 0.5$) and Nusselt number on the hot wall, with the test case for the three $\mathcal{R}a$ considered. A good agreement is obtained.

From the profiles presented in figure 3.10, the maximum velocity value at mid-width and at mid-height are extracted in Table 3.3. A very good agreement is obtained, which consists of very low error with respect to the results proposed by Ouertatani et al. (2008).

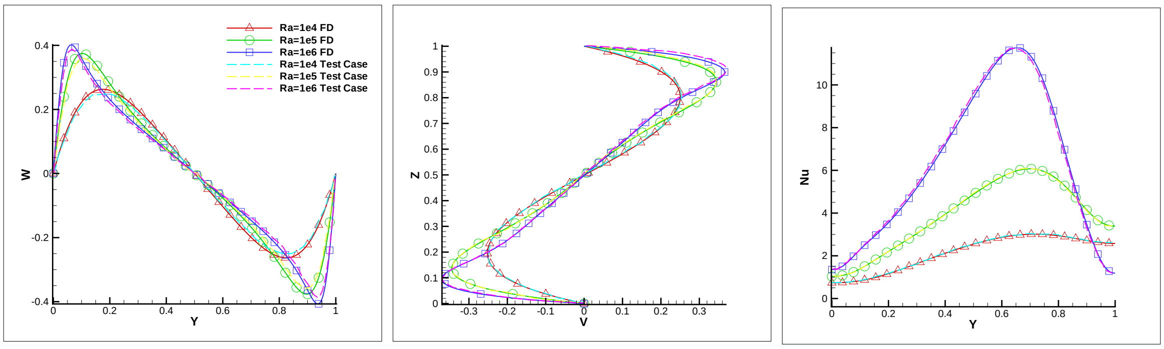

W velocity V velocity Nusselt number

Figure 3.10.: **Third order Runge-Kutta**. Finite difference simulation of the Rayleigh-Bénard convection. Velocity profiles following horizontal and vertical centerlines: comparison with benchmark solution from Ouertatani et al. (2008).

Rayleigh no.		Value (Position)	$U_{error}\%$ ($X_{error}\%$)
$Ra = 10^4$	$v_{max}(z)$	0.2502(0.8019)	$-0.7899\%(-0.04225\%)$
	$w_{max}(y)$	0.2631(0.8254)	$-0.2119\%(-0.098027\%)$
	$Nu_{max}(y)$	3.0120(0.7156)	$-0.3635\%(-0.3639\%)$
$Ra = 10^5$	$v_{max}(z)$	0.3447(0.8632)	$0.1071\%(-0.036938\%)$
	$w_{max}(y)$	0.3774(0.8960)	$0.4737\%(-0.1360\%)$
	$Nu_{max}(y)$	6.07318(0.6992)	$0.1348\%(-0.01158\%)$
$Ra = 10^6$	$v_{max}(z)$	0.370230(0.900)	$-0.1752\%(-0.3984\%)$
	$w_{max}(y)$	0.4075(0.9352)	$0.3692\%(-0.064750\%)$
	$Nu_{max}(y)$	11.581(0.644531)	$-0.9315\%(-0.041718\%)$

Table 3.3.: **Third order Runge-Kutta**. Finite difference simulation of the Rayleigh-Bénard convection. Maximum horizontal and vertical velocities along centerlines and their locations. Comparison with benchmark solution.

(4) Comparison between the three time integration methods

A comparison for the three time-integration methods is shown in figure 3.11. The velocity profiles at mid-width (fig. 3.11a) and mid-height (fig. 3.11c), are zoomed in figures (b) and (d) in the vicinity of the maximum. The dashed line in figure 3.11 represents the test case proposed by Ouertatani et al. (2008). We can clearly see that the third order Runge-Kutta method is more precise that the other two.

The same conclusion for the maximum velocities can be drawn from tables 3.1, 3.2 and 3.3. From the same tables, if we look at the Nusselt error variation between the three time integration schemes at $\mathcal{R}a = 10^4$, we can observe a reduction from 6.1432% (Euler) to 1.8054% (Adams-Bashforth) and further more to 0.3635% (Runge-Kutta). This represents a very important improvement. For $\mathcal{R}a = 10^5$ the difference is smaller, from -0.4496% (Euler) to 0.2348% (Adams-Bashforth) and 0.1348% (Runge-Kutta). The Euler approximation was already precise enough for this case and thus the improvement is not considerable. The same observation is valid for the case $\mathcal{R}a = 10^6$. The error variations for the vertical and horizontal velocity maximums are similar to the Nusselt error variation.

We can conclude that the third order Runge-Kutta method is, as expected, the most accurate. The drawback of this scheme is a larger computational (CPU) time. The convergence time increases from the Euler method to the third order Runge-Kutta by approximately 50%.

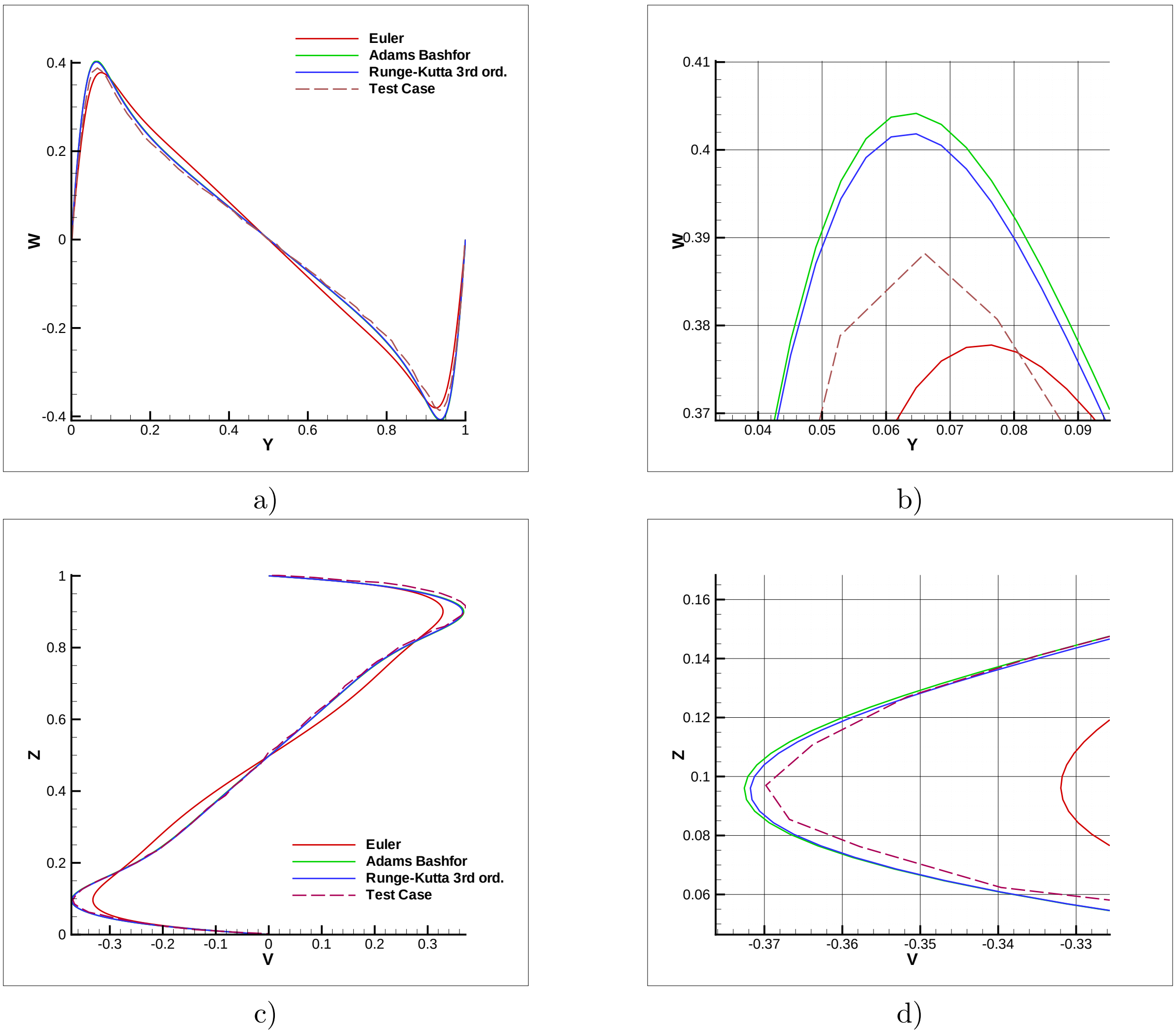

Figure 3.11.: Finite difference simulation of the Rayleigh-Bénard convection. Comparison between the three time integration methods and results of Ouertatani et al. (2008)

3.3.2. Differentially heated cavity (horizontal ∇T) case

For the differentially heated cavity, we have chosen as reference the results of Wakashima and Saitoh (2004) and Barakos et al. (1994). Figure 3.12 depicts the isotherms they have obtained for three Rayleigh number. We have simulated the same case using our finite difference code.

The expected flow behavior when increasing the Rayleigh number is the following. For low Rayleigh numbers ($\mathcal{R}a = 10^4$) a central vortex is dominant and characteristic of the flow. Going to $\mathcal{R}a = 10^5$, the vortex becomes elliptic and breaks up into two vortices. The two vortices shift towards the horizontal walls at $\mathcal{R}a = 10^6$. This gives rise to a third central vortex, which is very weak in comparison to the other two. The rotation is clockwise owing to a very small temperature gradient in the center of the cavity.

In the same order as before we shall present the results of the three time integration methods.

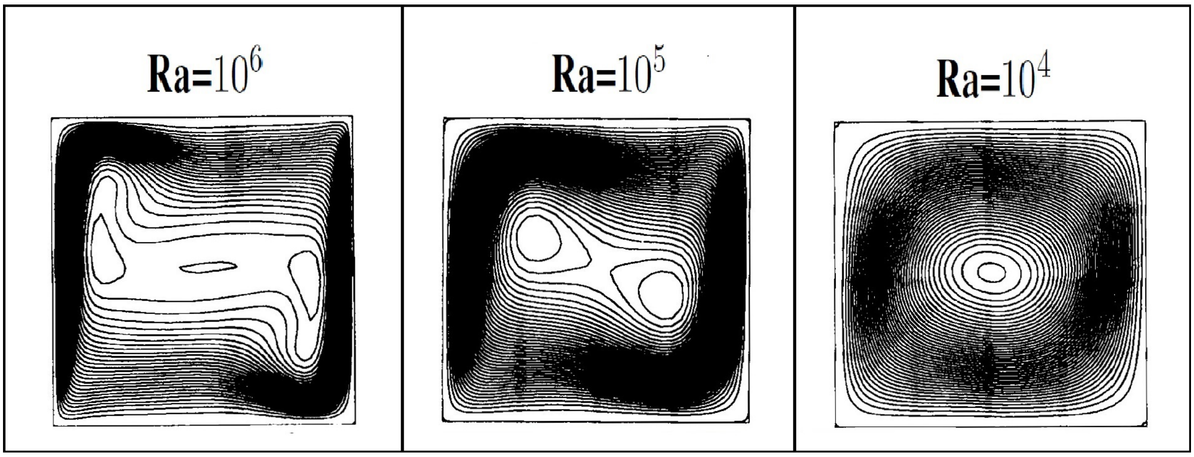

Figure 3.12.: Benchmark solution for the differentially heated cavity from Wakashima and Saitoh (2004).

The following simulations use second order finite difference schemes on the uniform grid with the same number of nodes as the test case, respectively 256×256. The time step is the same for all integration methods, $\delta t = 1.e - 4$.

(1) Euler method

For the Euler time integration method, we give a qualitative comparison for the isotherms and temperature fields in figure 3.13. From the left to the right of figure 3.13, we have $\mathcal{R}a = 10^6$, 10^5 and 10^4. For low Rayleigh numbers, $\mathcal{R}a = 10^4$, the profiles follow the same pattern as in the test case, while for $\mathcal{R}a = 10^5$ and $\mathcal{R}a = 10^6$ the streamlines are clearly distorted. For $\mathcal{R}a = 10^5$, the elliptic vortex is deformed and breaks into two other vortices that have slightly different form with respect to the benchmark. Even more, for $\mathcal{R}a = 10^6$ the three vortices seem to occupy a much larger space within the domain, and the central eddy is larger that expected and almost equal to the other two.

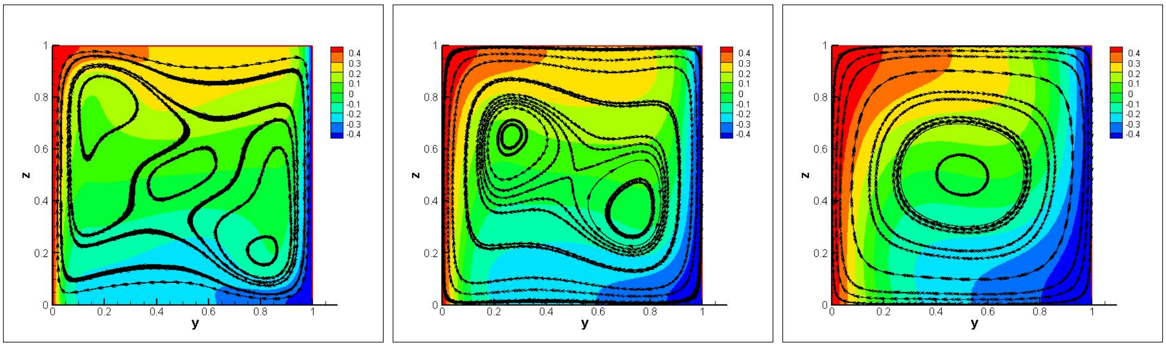

$Ra = 10^6$ $\qquad$ $Ra = 10^5$ $\qquad$ $Ra = 10^4$

Figure 3.13.: **Euler method**. Finite difference simulation of the differentially heated cavity case. Streamlines and temperature fields for different Rayleigh numbers.

We can draw a similar conclusion from velocity profiles are presented in figure 3.14. A clear difference between the obtained results and the results by Wakashima and Saitoh (2004) can be seen. Numerical profiles obtained with the Euler method have a slightly different form.

The maximum velocities and their positions are presented in Table 3.4. The error is com-

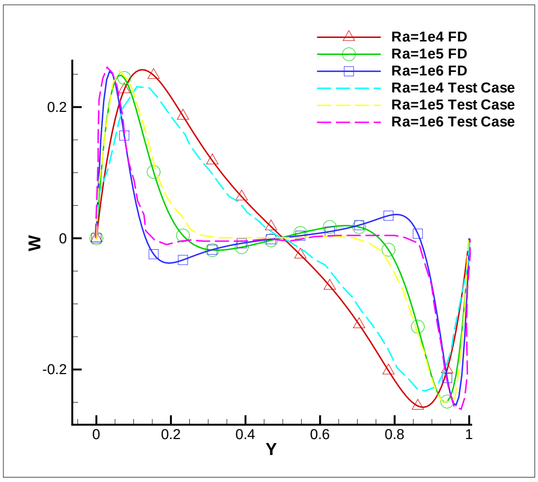

W velocity

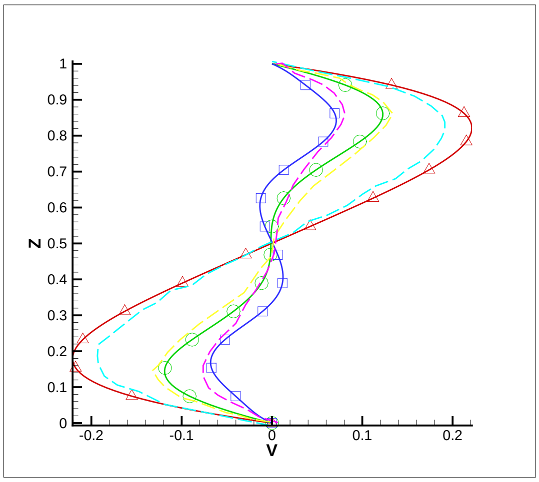

V velocity

Figure 3.14.: **Euler method**. Finite difference simulation of the differentially heated cavity case. Velocity profiles following horizontal and vertical centerlines: comparison with benchmark solution from Wakashima and Saitoh (2004).

puted with respect to the results reported by Wakashima and Saitoh (2004). A fairly good global accuracy is obtained, with an error diminishing for $Ra = 10^5$ and $Ra = 10^4$.

Rayleigh no.		Value (Position)	$U_{error}\%$ ($X_{error}\%$)
$Ra = 10^4$	$v_{max}(z)$	0.2213(0.8228)	11.3146%(−0.2624%)
	$w_{max}(y)$	0.2568(0.1220)	15.9273%(4.5818%)
$Ra = 10^5$	$v_{max}(z)$	0.1227(0.8622)	−13.3241%(1.4358%)
	$w_{max}(y)$	0.2483(0.0669)	4.5863%(3.8830%)
$Ra = 10^6$	$v_{max}(z)$	0.0711(0.8385)	−12.2646%(−2.2972%)
	$w_{max}(y)$	0.2541(0.0354)	−1.7398%(6.4057%)

Table 3.4.: **Euler method**. Finite difference simulation of the differentially heated cavity case. Maximum horizontal and vertical velocities along centerlines and their locations. Comparison with benchmark solution from Wakashima and Saitoh (2004).

(2) Adams-Bashforth method

The results obtained with the Adams-Bashforth time integration method are presented in figure 3.15. The aspect of the streamlines and temperature filed is consistent with the test case results. For $\mathcal{R}a = 10^5$ we can see the elliptic vortex that separated into two eddies. At $\mathcal{R}a = 10^6$ the two vortices shift towards the horizontal walls and a smaller central vortex can be seen. These results are in good agreement with Wakashima and Saitoh (2004).

Figure 3.16, represents the velocity profiles following the centerlines for each Rayleigh number. The velocity profiles following the horizontal and vertical centerlines are in very good agreement with the test case results. The maximum values of the horizontal and vertical velocities and their locations are extracted in table 3.5 and compared to the maximal values obtained by Wakashima and Saitoh (2004). A considerable improvement is observed by comparing to the results obtained with the Euler time integration scheme (table 3.4).

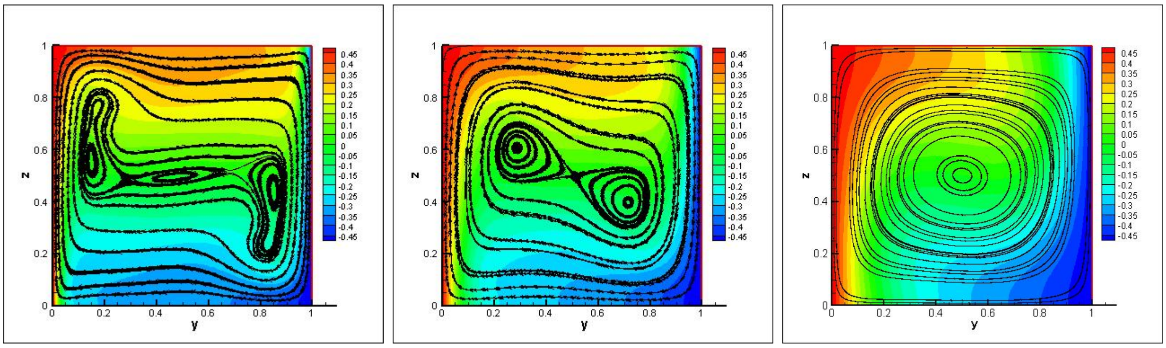

$Ra = 10^6$ $Ra = 10^5$ $Ra = 10^4$

Figure 3.15.: **Adams-Bashforth method**. Finite difference simulation of the differentially heated cavity case. Streamlines and temperature fields for different Rayleigh numbers.

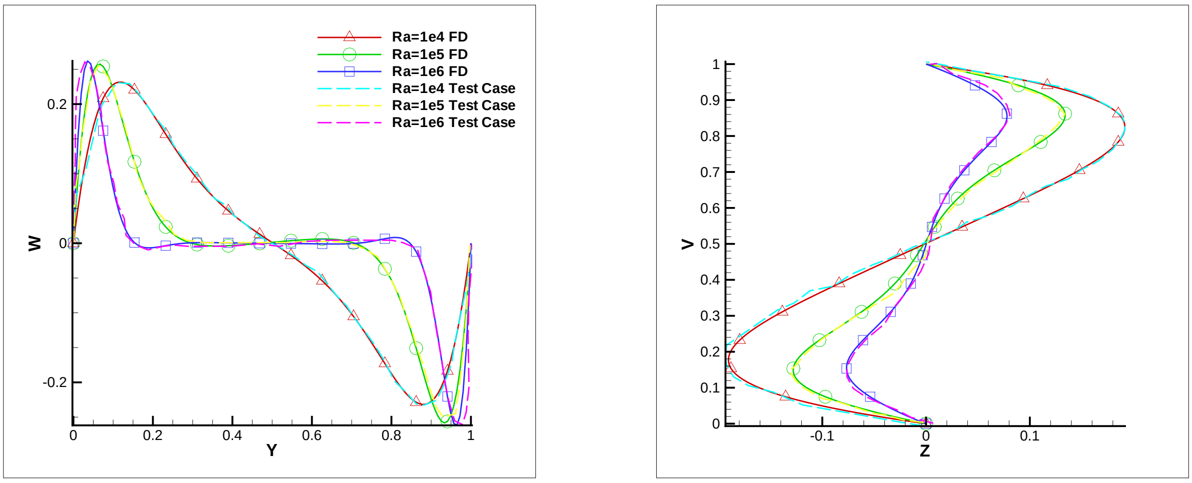

W velocity V velocity

Figure 3.16.: **Adams-Bashforth method**. Finite difference simulation of the differentially heated cavity case. Velocity profiles following horizontal and vertical centerlines: comparison with benchmark solution from Wakashima and Saitoh (2004).

Rayleigh no.		Value (Position)	$U_{error}\%$ ($X_{error}\%$)
$Ra = 10^4$	$v_{max}(z)$	0.2015(0.8228)	1.3710%(−0.2624%)
	$w_{max}(y)$	0.2399(0.1167)	8.3093%(2.9708%)
$Ra = 10^5$	$v_{max}(z)$	0.1338(0.8543)	−5.5084%(0.5058%)
	$w_{max}(y)$	0.2574(0.0669)	4.5916%(0.3298%)
$Ra = 10^6$	$v_{max}(z)$	0.0788(0.8543)	−2.7524%(−0.4660%)
	$w_{max}(y)$	0.2623(0.0354)	−1.7394%(6.3963%)

Table 3.5.: **Adams-Bashforth method**. Finite difference simulation of the differentially heated cavity case. Maximum horizontal and vertical velocities along centerlines and their locations. Comparison with benchmark solution.

(3) Third order Runge-Kutta method

In figure 3.17 the temperature profiles and isotherms are presented for the third order Runge-Kutta time integration scheme. From a qualitative point of view the results are in good agreement to the test cases. This time integration method proved to be more accurate than the two previously discussed.

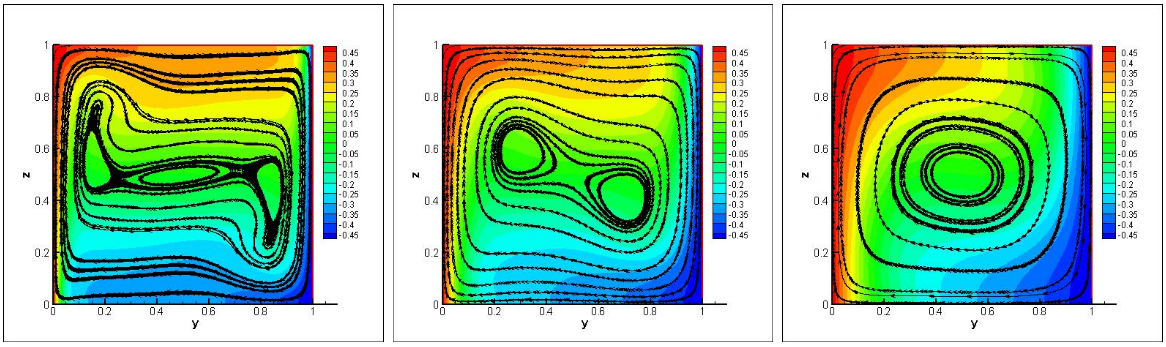

$Ra = 10^6$ $Ra = 10^5$ $Ra = 10^4$

Figure 3.17.: **Third order Runge-Kutta**. Finite difference simulation of the differentially heated cavity case. Streamlines and temperature fields for different Rayleigh numbers.

Figure 3.18 represents the velocity profiles at mid-width ($y = 0.5$) and mid-height ($z = 0.5$) following the centerlines. Again, a good agreement with Wakashima and Saitoh (2004) is obtained.

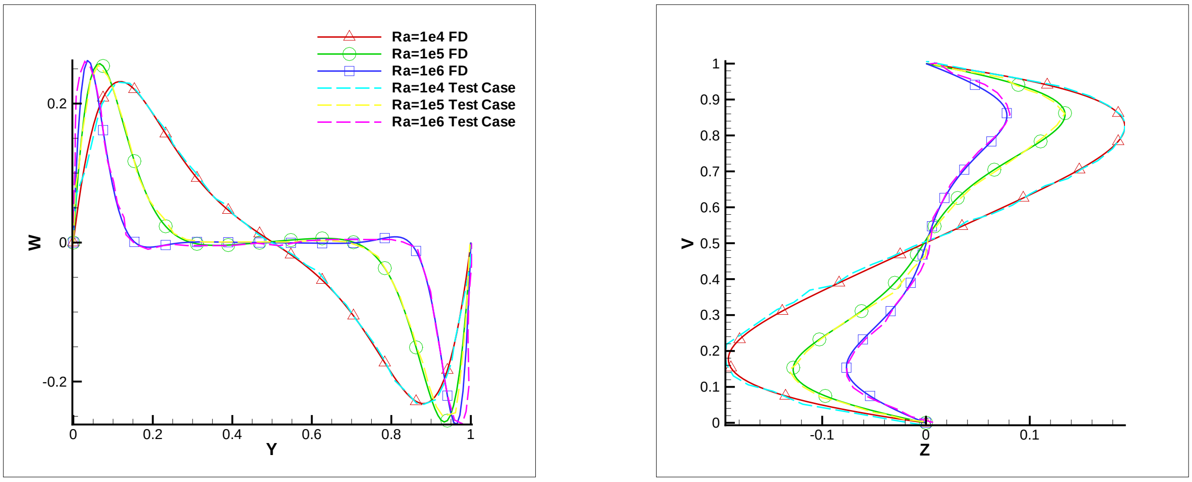

W velocity V velocity

Figure 3.18.: **Third order Runge-Kutta**. Finite difference simulation of the differentially heated cavity case. Velocity profiles following horizontal and vertical centerlines: comparison with benchmark solution from Wakashima and Saitoh (2004).

The maximum velocity values are extracted in Table 3.6. A very good agreement is obtained, which consists of very low error with respect to the results proposed by Wakashima and Saitoh (2004).

Rayleigh no.		Value (Position)	$U_{error}\%$ ($X_{error}\%$)
$Ra = 10^4$	$v_{max}(z)$	0.1916(0.8228)	−3.6008%(−0.2624%)
	$w_{max}(y)$	0.2315(0.1141)	4.5004%(−2.1653%)
$Ra = 10^5$	$v_{max}(z)$	0.1339(0.8543)	−5.3891%(0.5095%)
	$w_{max}(y)$	0.2573(0.0692)	0.9158%(0.3433%)
$Ra = 10^6$	$v_{max}(z)$	0.0780(0.8543)	−3.7942%(−0.4624%)
	$w_{max}(y)$	0.2620(0.0354)	1.3022%(6.4054%)

Table 3.6.: **Third order Runge-Kutta**. Finite difference simulation of the differentially heated cavity case. Maximum horizontal and vertical velocities along centerlines and their locations. Comparison with benchmark solution proposed by Wakashima and Saitoh (2004).

Form the two test cases presented for natural convection it is clear that the third order Runge-Kutta method is the most well suited. The following simulations from this chapter, as well as for the following chapters, will be performed using the third-order Runge-Kutta time integration scheme.

3.3.3. Comparison with the results obtained with a spectral code

In this section we investigate the influence of the accuracy of the finite difference scheme (second or sixth order) on the obtained results. For this purpose, we compare our results with the results of Xin et al. (1997) for the differentially heated cavity case. They used a spectral Chebyshev collocation method for spatial discretization and a direct Uzawa method for velocity-pressure coupling. As far as we know, these results are considered to be one of the most accurate in the literature.

The methodology for these comparisons is the following. We first use the classical second-order finite difference method and compare the uniform and variable mesh results. After the most accurate solution between these two is determined, it will be further compared to the results obtained with a sixth-order compact scheme. All computations are performed with the third-order Runge-Kutta method for the time integration.

For the classical second order finite-difference method we compare the horizontal and vertical velocity distributions at the mid-width ($y = 0.5$) and at the mid-height ($z = 0.5$) in figure 3.19. Grids of 128^2 cells are considered. A very good agreement is obtained for both cases.

Figure 3.20 compares the results obtained with the classical second order finite difference method with those obtained with a compact six order scheme. From the velocity profiles following the horizontal and vertical centerlines we can only conclude that both cases are in very good agreement with the results proposed by Xin et al. (1997). Note that for the sixth-order scheme a coarser mesh was used, with two time less grid points.

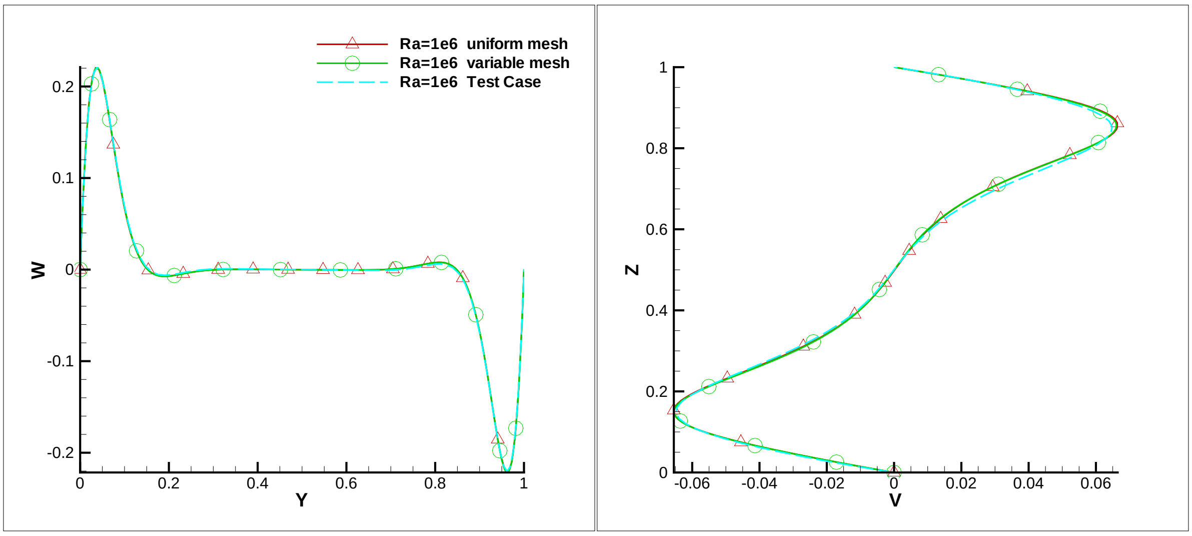

W velocity V velocity

Figure 3.19.: Differentially heated cavity case for $\mathcal{R}a = 10^6$. **Variable versus uniform grid** for second-order scheme. Velocity profiles following horizontal and vertical centerlines: comparison with benchmark solution from Xin et al. (1997).

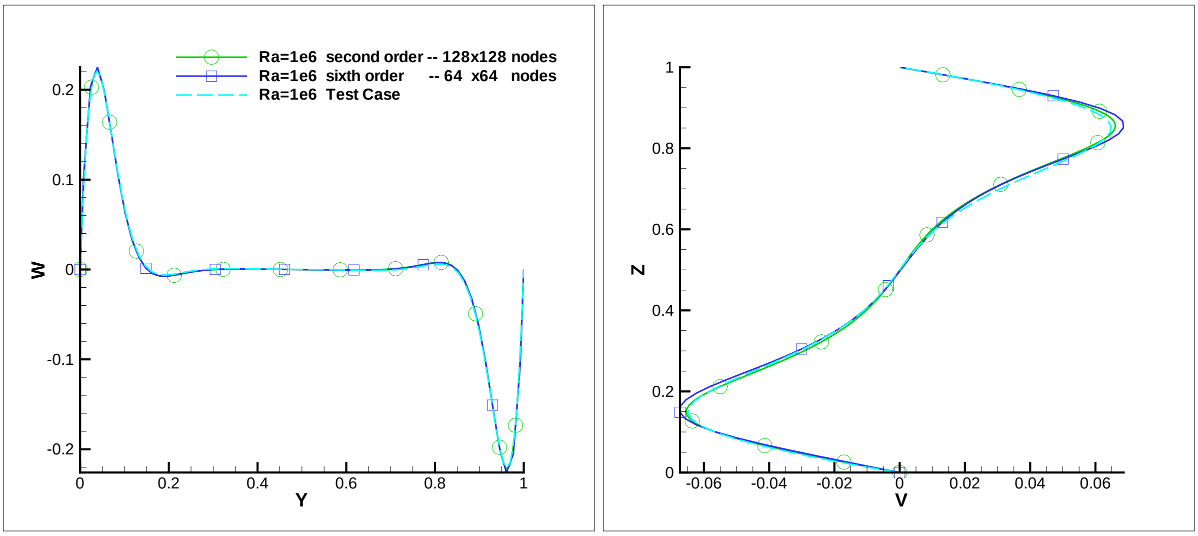

W velocity V velocity

Figure 3.20.: Differentially heated cavity case for $\mathcal{R}a = 10^6$. **Sixth-order versus second order schemes**. Velocity profiles following horizontal and vertical centerlines: comparison with benchmark solution from Xin et al. (1997).

A detailed analysis of the cases considered is presented in Tables 3.7, 3.8 and 3.9. Table 3.7 presents the maximum velocity values and their corresponding location obtained for a uniform mesh. Table 3.7 provides the same results for a variable grid. From the first two tables we can see that, while the maximal velocity value remains within the same % difference, the error for the location is lower for the variable mesh. Globally the variable mesh is more accurate than the uniform one and is thus preferred when second-order schemes are used. Both cases provide a good agreement with the benchmark.

Rayleigh no.		Value (Position)	$U_{error}\%$ ($X_{error}\%$)
$Ra = 10^4$	$v_{max}(z)$	0.1616(0.8188)	−0.1259%(−0.7064%)
	$w_{max}(y)$	0.1952(0.1181)	−0.5341%(−1.4080%)
$Ra = 10^5$	$v_{max}(z)$	0.1127(0.8503)	2.6299%(−0.3701%)
	$w_{max}(y)$	0.2168(0.0629)	−0.0007%(−1.1919%)
$Ra = 10^6$	$v_{max}(z)$	0.0664(0.8503)	2.5623%(−1.1485%)
	$w_{max}(y)$	0.2210(0.03149)	0.2392%(−17.2467%)

Table 3.7.: **Second order FD (128x128 nodes)– Uniform mesh**. Maximum horizontal and vertical velocities along centerlines and their locations. Comparison with benchmark solution.

Rayleigh no.		Value (Position)	$U_{error}\%$ ($X_{error}\%$)
$Ra = 10^4$	$v_{max}(z)$	0.1615(0.8185)	−0.1422%(−0.7454%)
	$w_{max}(y)$	0.1950(0.1164)	−0.6340%(−2.7868%)
$Ra = 10^5$	$v_{max}(z)$	0.1123(0.8520)	2.2789%(−0.1783%)
	$w_{max}(y)$	0.2167(0.0639)	−0.0841%(0.3249%)
$Ra = 10^6$	$v_{max}(z)$	0.0612(0.8520)	2.05687%(−0.1783%)
	$w_{max}(y)$	0.2204(0.0342)	−0.355%(−10.0497%)

Table 3.8.: **Second order FD (128x128 nodes)– Variable mesh**. Maximum horizontal and vertical velocities along centerlines and their locations. Comparison with benchmark solution.

Rayleigh no.		Value (Position)	$U_{error}\%$ ($X_{error}\%$)
$Ra = 10^4$	$v_{max}(z)$	0.1619(0.8125)	0.0778%(−1.482%)
	$w_{max}(y)$	0.1951(0.1093)	−0.5966%(−8.699%)
$Ra = 10^5$	$v_{max}(z)$	0.1134(0.8437)	3.2861%(−1.1485%)
	$w_{max}(y)$	0.2169(0.0625)	0.03601%(−1.9638%)
$Ra = 10^6$	$v_{max}(z)$	0.0660(0.8515)	2.7977%(−0.2332%)
	$w_{max}(y)$	0.2213(0.0312)	0.3688%(−17.893%)

Table 3.9.: **Sith order FD (64x64 nodes)**. Maximum horizontal and vertical velocities along centerlines and their locations. Comparison with benchmark solution.

Table 3.9 presents the results obtained for the compact six order finite difference method. We can observe a small increase in error for the location of the maximal velocities, caused by smaller grid employed. Even though the grid is half than the one used for the second order the velocity value error is within the same % difference and also presents an improvement.

Finally, we display in figure 3.21 the streamlines and temperature fields reported by Xin et al. (1997) (first row), the solution obtained with the second order finite difference method (second row) on a 128^2 nodes grid and the solution obtained with the sixth-order compact schemes on a 64^2 nodes grid. For all three Rayleigh numbers a good agreement is observed for the temperature field and vortices shape and position.

a) Xin et al. (1997)

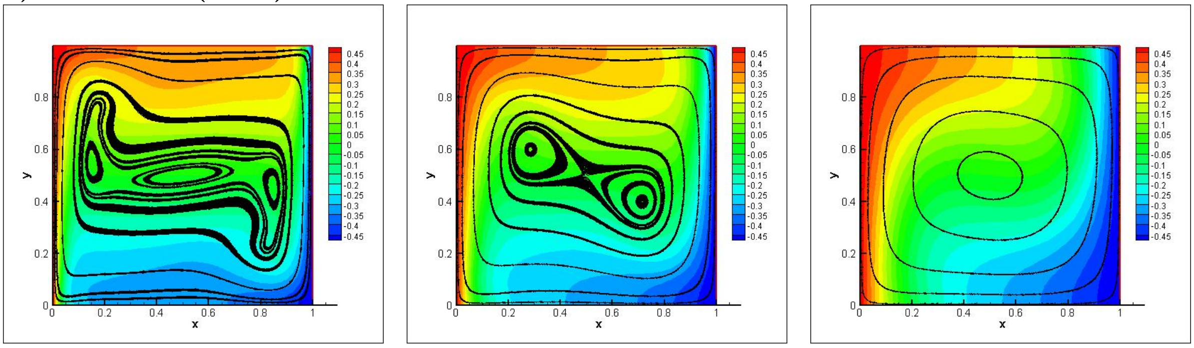

$Ra = 10^6$ $Ra = 10^5$ $Ra = 10^4$

b) Second-order finite difference method (128x128 nodes)– Variable mesh

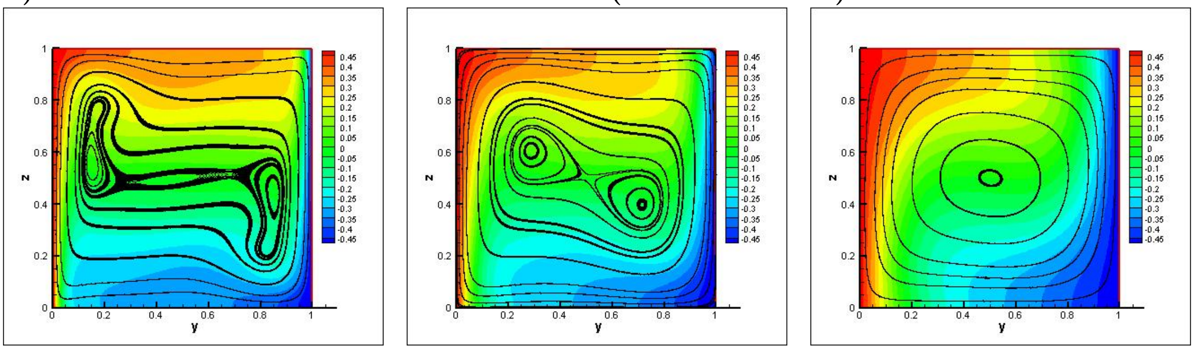

$Ra = 10^6$ $Ra = 10^5$ $Ra = 10^4$

c) Sixth order compact scheme (64x64 nodes)

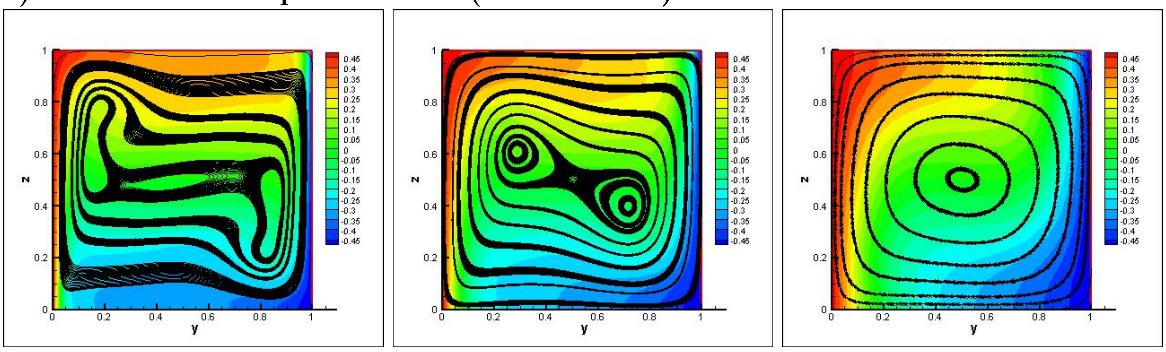

$Ra = 10^6$ $Ra = 10^5$ $Ra = 10^4$

Figure 3.21.: Differentially heated cavity case. Streamlines and temperature fields for different Rayleigh numbers. a) Benchmark solution of Xin et al. (1997); b) Classical second-order finite difference method; c) Sixth order compact scheme.

3.3.4. Conclusion

As a conclusion for this part of the numerical study of natural convection flows, we can say that the numerical code provides a good agreement to several 2D benchmarks presented in literature, for both the Rayleigh-Bénard convection and the differentially heated cavity. A variable mesh in the vicinity of the walls ensures a good capture of the recirculation cells, and a general mesh resolution of 128×128 is sufficient for rendering good results for the second order finite difference scheme. For the sixth order compact scheme a 64×64 nodes mesh proved to be just as accurate. In addition to this, as discussed in the previous chapter 2, the sixth order method ensures lower time steps for convergence, when the same number of grid nodes is considered.

3.4. Validations for 3D convection problems

The numerical model was further tested for the simulation of a three-dimensional (3D) cavity. A schematic model of the problem is displayed in figure 3.22 a). The Prandtl number is 0.71 and three Rayleigh numbers are considered: $\mathcal{R}a = 10^4$, $\mathcal{R}a = 10^5$, $\mathcal{R}a = 10^6$. The walls are rigid and impermeable. The vertical walls at $x = 0$ and $x = 1$ are isothermal and have different temperatures $T_h = 1$ and $T_c = 0$ respectively. The remaining walls are considered adiabatic. Figure 3.22 b) shows the present three dimensional grid.

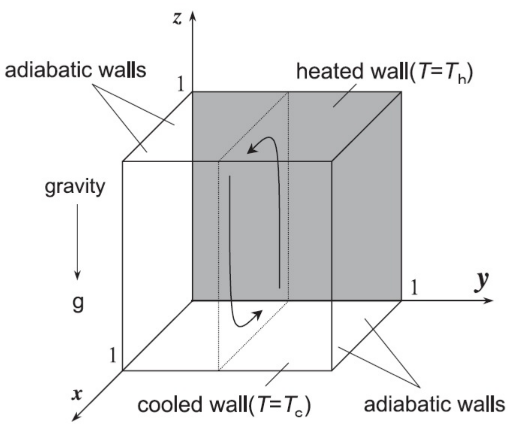

a)

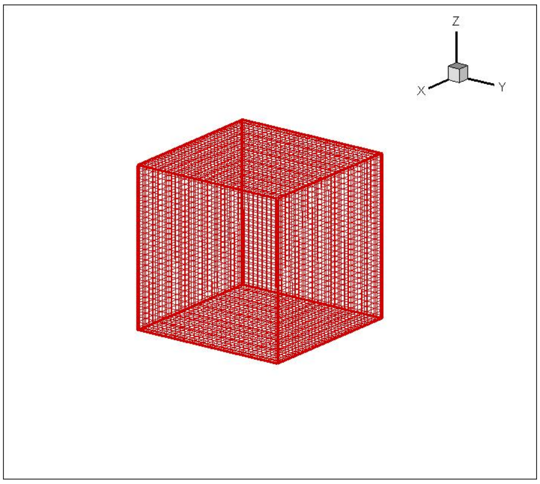

b)

Figure 3.22.: (a) Schematic model for the natural convection in a cubic cavity; (b) present 3D uniform mesh.

For this test case, Wakashima and Saitoh (2004) used a forth order finite difference method, with a vorticity-stream function formulation with different uniform meshes of $120 \times 120 \times 120 \times 10$ grid nodes. Our results were obtained for two grids of $32 \times 32 \times 32$ and $64 \times 64 \times 64$ nodes, using a second-order finite difference scheme on a uniform mesh. A third order Runge-Kutta method is used for time integration.

Figure 3.23 shows four lateral walls of each case, with the (x_{max}, y) being the cold wall and (x_{min}, y) the hot wall. The converged flow pattern and temperature distributions are symmetrical with respect to the center of the cavity for all cases.

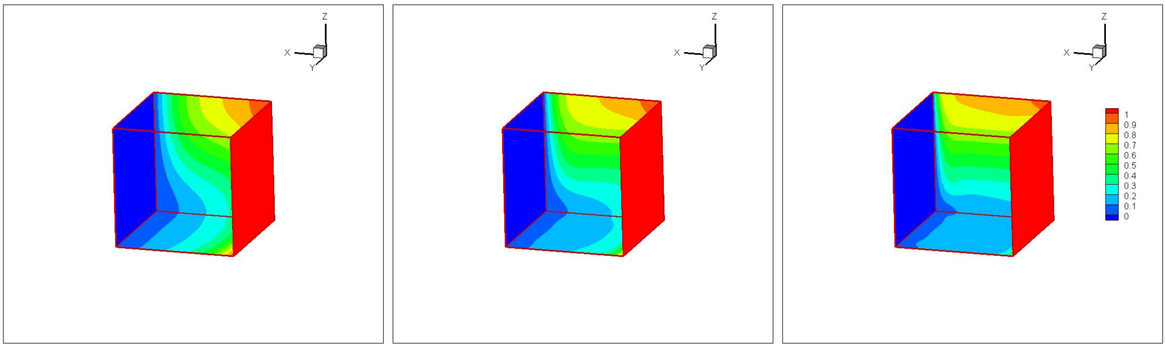

$Ra = 10^4$ $\quad$ $Ra = 10^5$ $\quad$ $Ra = 10^6$

Figure 3.23.: Three dimensional temperature profiles for the 3D differentially heated cavity.

As a consequence, we consider the mid section ($y = 0.5$) for comparison. Temperature contours (between 0 and 1, with increment 0.1) at the mid-plane $y = 0.5$ of the cavity are shown in figure 3.24. On the left we display the test cases, as presented by Wakashima and Saitoh (2004), and on the right our results, varying form first to last from $\mathcal{R}a = 10^4$ to $\mathcal{R}a = 10^6$. The results show a good agreement with the benchmark solution.

Velocity distribution for u and w at mid-plane $y = 0.5$ are presented in figure 3.25. On the left we display the test case result, while on the right the present results. From figure (a) to (c), we have the cases of the three different Rayleigh numbers. (1) and (2) represent the velocities u and w respectively. Boundary layers near the vertical walls get thinner with the increase of the Rayleigh number. In the vicinity of the lower walls the boundary layers are thicker. Our results are thus in very good agreement with the considered test case.

Velocity contours of u at the cross-section $x = 0.5$, and w at $z = 0.5$ are presented in figure 3.26. For the u velocity at $\mathcal{R}a = 10^4$ a single extrema point is present at the mid plane $y = 0.5$; when increasing the Rayleigh number to 10^5 and 10^6, two extrema appear neat the corners. For $\mathcal{R}a = 10^6$, the profiles are symmetrical with respect to the center. The figures for w show that two extrema appear at $\mathcal{R}a = 10^4$. With the increase of Rayleigh number the peaks move toward the corners. A good agreement between our results and the results of Wakashima and Saitoh (2004) was again established.

Table 3.10 provides a comparison between present results and numerical results from literature. The comparison concerns the maximum and minimum velocity values and their corresponding location. An excellent agreement is found for all values of the Rayleigh number.

For the case of $\mathcal{R}a = 10^4$, the solution shows a good convergence on a mesh 2.35 times denser than the one proposed by Wakashima and Saitoh (2004), and 3.54 times denser than the one considered by Fusegi et al. (1991). Table 3.10 shows that our results for u_{max} are smaller than those considered, within a 5% difference, and the ones for w_{max} are within a 0.7% difference. The locations of the velocities at the mid plane can also be found within a 1% difference. In the case of $\mathcal{R}a = 10^5$, our results are between those proposed by Wakashima and Saitoh (2004) and Fusegi et al. (1991), within a 0.5% difference from the latter. For $\mathcal{R}a = 10^6$, the results are in good agreement.

Benchmark **Present results**

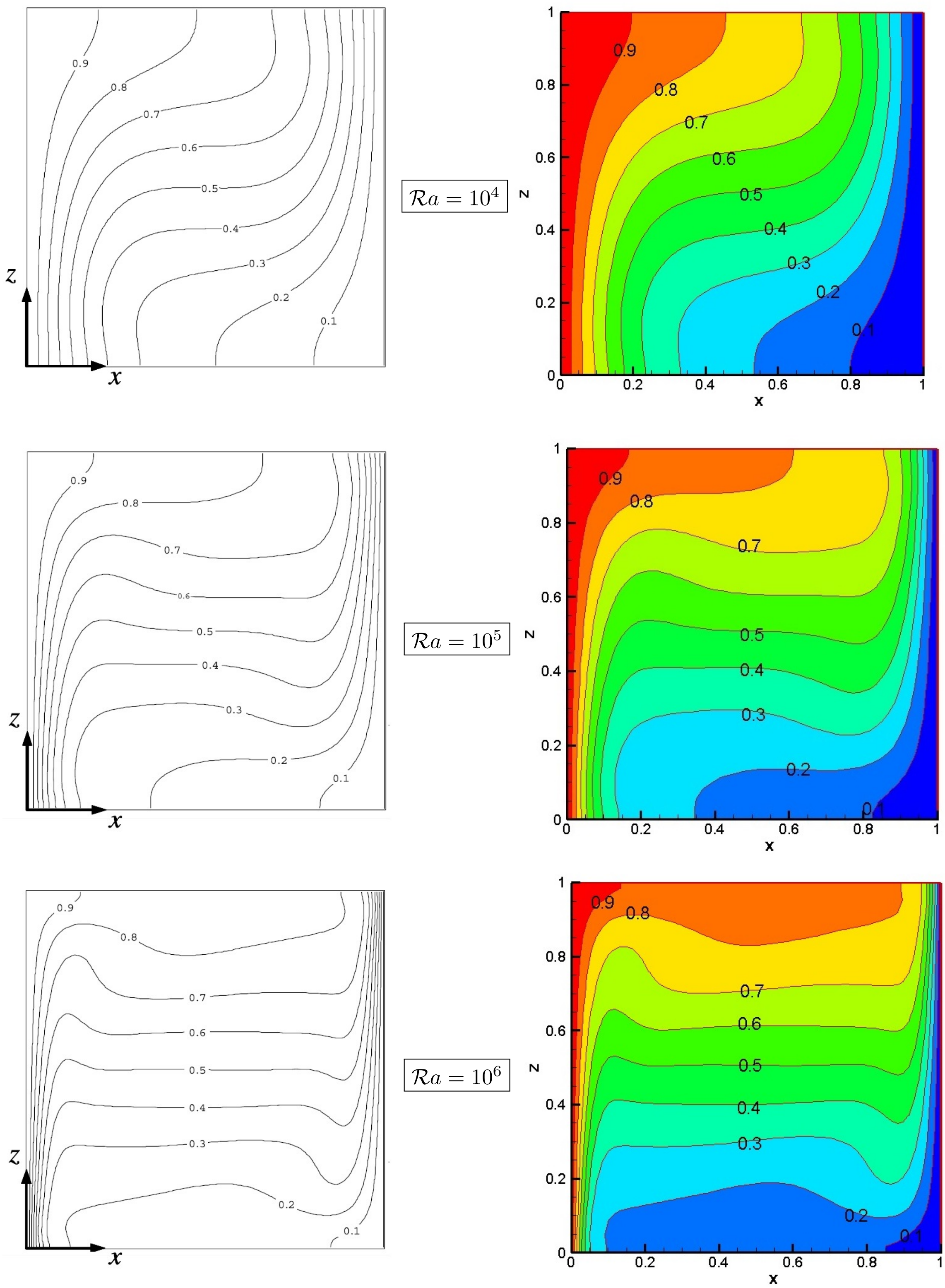

Figure 3.24.: 3D differentially heated cavity. Temperature contours at the mid-plane of ($y = 0.5$); comparison with the results of Wakashima and Saitoh (2004) (left images).

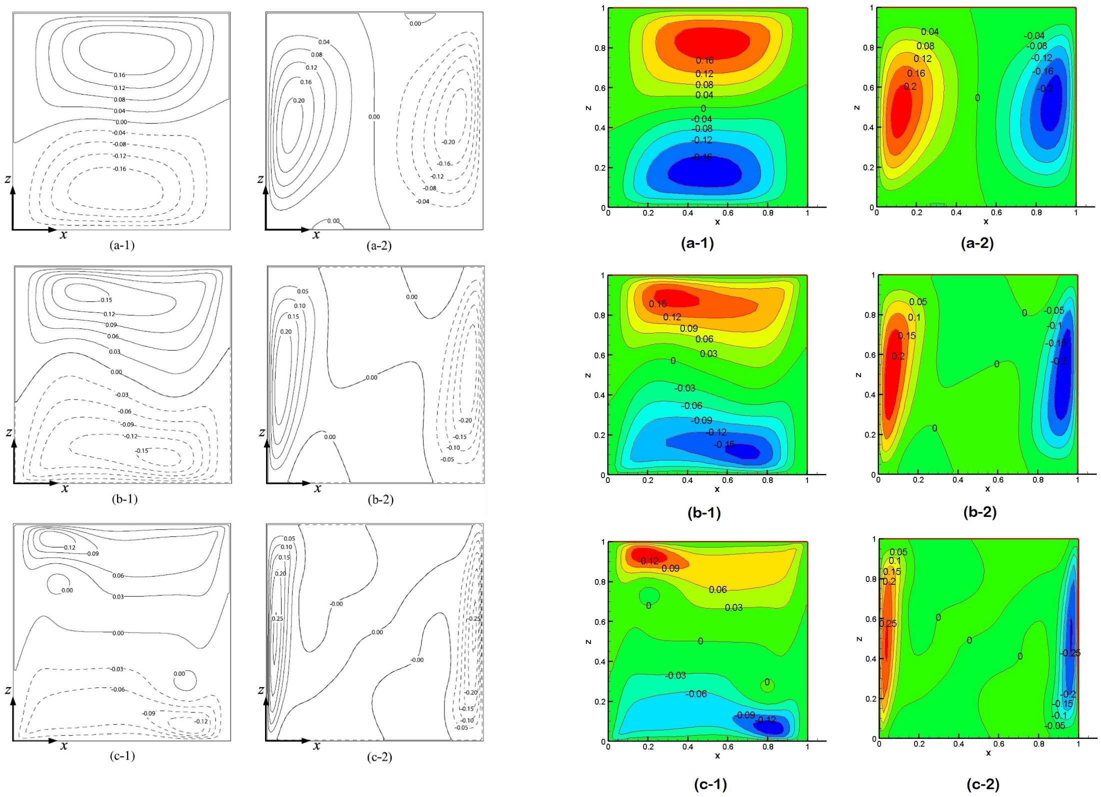

Benchmark **Present results**

Figure 3.25.: 3D differentially heated cavity. Velocity contours of u and w at the mid-plane $y = 0.5$. $\mathcal{R}a = 10^4$: (a-1) u contours; (a-2) w contours. $\mathcal{R}a = 10^5$: (b-1) u contours; (b-2) w contours. $\mathcal{R}a = 10^6$: (c-1) u contours; (c-2) w contours. Comparison with the results of Wakashima and Saitoh (2004) (left images).

Rayleigh no.	Grid size	$u_{max}(z)$	$w_{max}(x)$
$Ra = 10^4$	0.0294	0.1859(0.8230)	0.2234(0.1172)
Wakashima and Saitoh (2004)	0.0125	0.1985(0.8250)	0.2218(0.1125)
Fusegi et al. (1991)	0.0083	0.2013(0.8167)	0.2252(0.1167)
$Ra = 10^5$	0.0294	0.1461(0.8540)	0.2459(0.0703)
Wakashima and Saitoh (2004)	0.0125	0.1418(0.8500)	0.2450(0.0625)
Fusegi et al. (1991)	0.0083	0.1468(0.8547)	0.2471(0.0647)
$Ra = 10^6$	0.0294	0.0830(0.8550)	0.2553(0.3905)
Wakashima and Saitoh (2004)	0.0125	0.08105(0.8500)	0.2606(0.0375)
Fusegi et al. (1991)	0.0083	0.08416(0.8557)	0.2588(0.0331)

Table 3.10.: 3D differentially heated cavity. Comparison with benchmark solutions for $\mathcal{R}a = 10^4$, $\mathcal{R}a = 10^5$, $\mathcal{R}a = 10^6$.

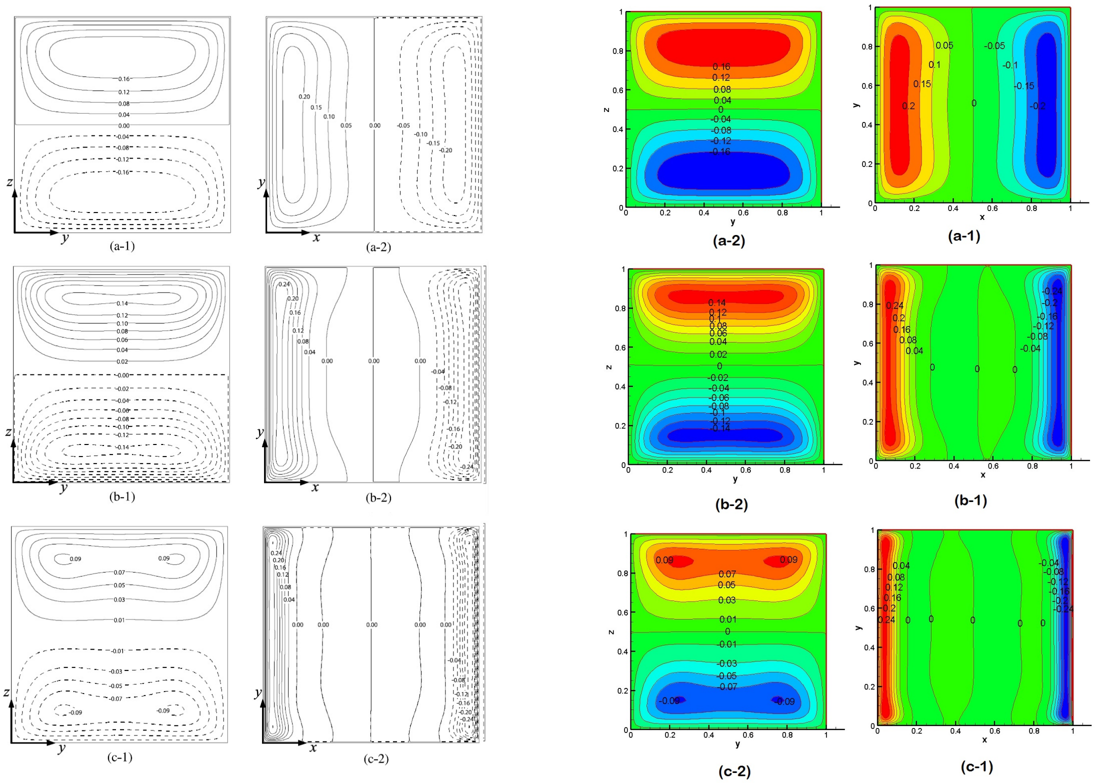

Benchmark **Present results**

Figure 3.26.: 3D differentially heated cavity. Contours of the cross-sectional velocity vertical to the mid-planes $x = 0.5$ and $z = 0.5$. $\mathcal{R}a = 10^4$: (a-1) u contours; (a-2) w contours. $\mathcal{R}a = 10^5$: (b-1) u contours; (b-2) w contours. $\mathcal{R}a = 10^6$: (c-1) u contours; (c-2) w contours. Comparison with the results of Wakashima and Saitoh (2004) (left images).

3.5. Conclusion

Most of the natural convection simulations in the literature consider 2D problems. Compared to the 2D case, the flow inside a 3D differentially heated cavity is complex: the fluid moves in spiral tubes along the walls and the heat transfer takes place in the same region. Our numerical code allows to capture this physics and provides results in very good agreement with previously reported numerical results.

As a general conclusion of this chapter, we can say that the finite difference solver for the Navier-Stokes-Boussinesq equations was validated for both two-dimensional and three-dimensional cases. The proposed numerical schemes are efficient and accurate. After this validation, our solver will be used for the simulation of convection flows in cavities with immersed boundaries.

4. Finite element approach for the Navier-Stokes-Boussinesq model

We develop in this chapter an alternative finite element (FE) algorithm for solving the 2D Navier-Stokes-Boussinesq equations. The idea behind this new development is to use the capability of the FE discretization to cope with complex geometries; the FE code will be used latter to validate computations of configurations with obstacles using the finite difference (FD) method in conjunction with the immersed boundary method (IBM). The development of the FE code was greatly simplified by the use of the FreeFem++ software, offering a friendly environment to work with different types of finite elements.

We start by presenting in this chapter the main Newton algorithm to solve the Navier-Stokes-Boussinesq equations and its validation for natural convection flows. In the next chapter we shall use this code to deal with complex geometries, with obstacles inside a cavity. In chapter 7 the Newton algorithm will be extended to deal with new nonlinearities, appearing in the models for the simulation of phase-change problems.

4.1. Characteristics of the FreeFem++ software

FreeFem++ Hecht et al. (2012) is high level integrated development environment for numerically solving partial differential equations in two and three dimensions using finite elements. The FreeFem++ language is a C++ based idiom. This free software represents a tool for research, allowing to quickly test algorithms and models, but also to simulate complex applications. It runs on Macs, Windows, Unix machines.

FreeFem++ is adapted and used to solve many problems starting from physics, engineering, mathematics and even finance, that are modeled by one or several partial differential equations. The main advantage of this software is that it is highly adaptive. Many problems involve several coupled systems that require different finite element approximations and polynomial degrees and even interpolations on multiple meshes. The language is set in such a manner as to easily handle all these requirements.

To be solved with FreeFem++, problems must be described by their variational formulation. For multi-variables, multi-equations, two-dimensional and three-dimensional steady or time dependent, linear or nonlinear coupled systems, the user is can easily implement the numerical algorithm and select the type of the finite element discretization. The geometric input must be done by an analytic description of the boundaries.

Another advantage of FreeFem++ is its automatic mesh generator, based on the Delaunay-Voronoi algorithm (the inner point density is proportional to the density of points on the boundaries). Metric-based anisotropic mesh adaptation is also taken into account. The interpolations between multiple element meshes is automatic. It also covers a large variety of triangular finite elements (linear, quadratic Lagrangian elements etc.) and of linear direct and iterative solvers (LU, Cholesky, Crout, CG, GMRES, UMFPACK, MUMPS, SuperLU etc.). The software also has a tool for the definition of discontinuous Galerkin finite element formulations.

4.2. Variational formulation

We start by recalling the two-dimensional Navier-Stokes-Boussinesq equations, using here a slightly different notation for vectorial quantities:

$$\begin{aligned} \nabla\cdot\mathbf{u} &= 0,\\ \frac{\partial\mathbf{u}}{\partial t}+(\mathbf{u}\cdot\nabla)\mathbf{u}+\nabla p-\frac{1}{\mathcal{R}e}\Delta\mathbf{u}-f_B(\theta)\mathbf{e}_y &= 0,\\ \frac{\partial\theta}{\partial t}+\nabla\cdot(\theta\mathbf{u})-\frac{1}{\mathcal{R}e\mathcal{P}r}\Delta\theta &= 0, \end{aligned} \tag{4.1}$$

where $\mathbf{u}(y,z)$ is the velocity vector and the buoyancy force is denoted by $f_B(\theta)=\dfrac{\mathcal{R}a}{\mathcal{P}r\,\mathcal{R}e^2}\theta$. We also use in the following a different scaling, expressed by (2.16) and resulting in $\mathcal{R}e=1$. This scaling will also be used for phase-change problems.

Finite element methods for the discretization of the Navier-Stokes equations are based on the weak (or variational) formulation of the partial differential equations. Weak formulations for this case are based on a separate discretization of the temporal derivative and the generalization of the Stokes problem for the resulting system. We consider a backward implicit Euler scheme for the time advancement from t_n to t_{n+1} and a classical penalty method for the diverge free constraint for the velocity field. The resulting equation system obtained is:

$$\begin{aligned} \nabla\cdot\mathbf{u}^{n+1}+\varepsilon p^{n+1} &= 0,\\ \frac{\mathbf{u}^{n+1}}{\delta t}+(\mathbf{u}^{n+1}\cdot\nabla)\mathbf{u}^{n+1}+\nabla p^{n+1}-\Delta\mathbf{u}^{n+1}-f_B\theta^{n+1}\mathbf{e}_y &= \frac{\mathbf{u}^n}{\delta t},\\ \frac{\theta^{n+1}}{\delta t}+\nabla\cdot\left(\mathbf{u}^{n+1}\theta^{n+1}\right)-\nabla\cdot\left(\frac{1}{\mathcal{P}r}\nabla\theta^{n+1}\right) &= \frac{\theta^n}{\delta t}, \end{aligned} \tag{4.2}$$

with $\varepsilon>0$ the penalty parameter.

We consider the problem of the cavity, with homogeneous Dirichlet boundary conditions for the velocity: $\mathbf{u}=0$ on $\partial\Omega$. For the velocity and pressure we set the classical Hilbert spaces:

$$\mathbf{V}=V\times V,\, V=H_0^1(\Omega),\quad Q=\left\{q\in L^2(\Omega)\,\middle|\,\int_\Omega q=0\right\} \tag{4.3}$$

Following the generalization of the Stokes problem, the variational formulation of the system (4.2) can be expressed as: find $(\mathbf{u}^{n+1},p^{n+1},\theta^{n+1})\in\mathbf{V}\times Q\times V$, such that:

$$\begin{aligned} b\left(\mathbf{u}^{n+1},q\right)-\varepsilon(p^{n+1},q) &= 0,\ \forall\, q\in Q\\ \frac{1}{\delta t}\left(\mathbf{u}^{n+1},\mathbf{v}\right)+c\left(\mathbf{u}^{n+1};\mathbf{u}^{n+1},\mathbf{v}\right)+a\left(\mathbf{u}^{n+1},\mathbf{v}\right) & \\ +b\left(\mathbf{v},p^{n+1}\right)-f_B\theta^{n+1}\left(\mathbf{e}_y,\mathbf{v}\right) &= \frac{1}{\delta t}\left(\mathbf{u}^n,\mathbf{v}\right),\ \forall\,\mathbf{v}\in\mathbf{V}\\ \frac{1}{\delta t}\left(\theta^{n+1},\phi\right)-\left(\mathbf{u}^{n+1}\cdot\nabla\phi,\theta^{n+1}\right)+\left(\frac{1}{Pr}\nabla\theta^{n+1},\nabla\phi\right) &= \frac{1}{\delta t}\left(\theta^n,\phi\right),\ \forall\,\phi\in V, \end{aligned} \tag{4.4}$$

where $(.,.)$ denotes the scalar product in $L^2(\Omega)$ or $\left(L^2(\Omega)\right)^2$; the bilinear forms a, b and trilinear form c are defined as:

$$
\begin{aligned}
a : \mathbf{V} \times \mathbf{V} \to \Re, &\qquad a(\mathbf{u}, \mathbf{v}) = \int_\Omega \nabla \mathbf{u} \cdot \nabla \mathbf{v} = \sum_{i=1}^{2} \int_\Omega \nabla u_i \cdot \nabla v_i \\
b : \mathbf{V} \times Q \to \Re, &\qquad b(\mathbf{u}, q) = -\int_\Omega \nabla \cdot \mathbf{u}\, q = -\sum_{i=1}^{2} \int_\Omega \partial_i u_i \cdot q \\
c : \mathbf{V} \times \mathbf{V} \times \mathbf{V} \to \Re, &\qquad c(\mathbf{w}; \mathbf{z}, \mathbf{v}) = \int_\Omega \left[(\mathbf{w} \cdot \nabla)\, \mathbf{z}\right] \cdot \mathbf{v} = \sum_{i,j=1}^{2} \int_\Omega w_j (\partial_j z_i) v_i.
\end{aligned}
\tag{4.5}
$$

4.3. Newton algorithm

The discretized equations (4.4) are solved using a Newton iterative algorithm. The space discretization is based on a P2-P1 Taylor-Hood finite elements and mesh adaptivity. The Newton linearization method has been successfully applied for fluid dynamics (Dennis and Schnabel, 1983). It has the advantage of rapid computations due to its quadratic convergence. For the incompressible Navier-Stokes equations, classical or high-order Newton methods were proposed by Sheu and Lin (2004) and Sheu and Lin (2005). They applied it to finite-difference methods on non staggered grids. The drawback of the Newton method is that the convergence is obtained only if the guess for the initial solution is sufficiently close to the final state and if critical point of the derivatives are avoided.

We recall the classical Newton method to solve a scalar equation $F(u) = 0$: starting from an initial guess u_0, iterate following

$$
u^{n+1} = u^n - \left[\frac{\partial F}{\partial u}\right]^{-1} F(u^n). \tag{4.6}
$$

It we denote by

$$
w^n = u^n - u^{n+1}, \tag{4.7}
$$

then the system becomes:

$$
\left[\frac{\partial F}{\partial u}\right] w^n = F(u^n). \tag{4.8}
$$

After solving this equation, the solution is updated: $u^{n+1} = u^n - w^n$. Convergence is reached when the variation of w^n is lower than $\epsilon = 10^{-10}$.

In order to apply the Newton method for the Boussinesq system, the system of equations (4.4) is regarded as $\mathcal{F}(w) = 0$, with $w = (\mathbf{u}^{n+1}, p^{n+1}, \theta^{n+1}) \in W = \vec{V} \times Q \times V$, and $\mathcal{F} : W \to W$ a differentiable mapping. The classical Newton algorithm is then used to advance the solution from time t_n to t_{n+1}: starting from an initial guess $w^0 = (\mathbf{u}^n, p^n, \theta^n)$ (which is the solution at t_n), construct the sequence (w^k) by solving for each inner iteration k:

$$
D_w \mathcal{F}(w^k) \left(w^k - w^{k+1}\right) = \mathcal{F}(w^k), \tag{4.9}
$$

where $D_w \mathcal{F}$ is the linear operator representing the differential of $\mathcal{F}$.

Denoting by $(\mathbf{u}_w, p_w, \theta_w) = w^k - w^{k+1}$, and after differentiating (4.4), the system of equations (4.9) can be explicitly written as:

$$
\begin{aligned}
b(\mathbf{u}_w, q) - \varepsilon(p_w, q) = b\left(\mathbf{u}^k, q\right) - \varepsilon(p^k, q),\\
\frac{1}{\delta t}(\mathbf{u}_w, \mathbf{v}) + c\left(\mathbf{u}_w; \mathbf{u}^k, \mathbf{v}\right) + c\left(\mathbf{u}^k; \mathbf{u}_w, \mathbf{v}\right) + a(\mathbf{u}_w, \mathbf{v}) + b(\mathbf{v}, p_w) - \frac{df_B}{d\theta}\theta_w(\mathbf{e}_y, \mathbf{v}) =\\
\frac{1}{\delta t}\left(\mathbf{u}^k - \mathbf{u}^n, \mathbf{v}\right) + c\left(\mathbf{u}^k; \mathbf{u}^k, \mathbf{v}\right) + a(\mathbf{u}_k, \mathbf{v}) + b\left(\mathbf{v}, p^k\right) - f_B\theta^k(\mathbf{e}_y, \mathbf{v}),\\
\frac{1}{\delta t}(\theta_w, \phi) - \left(\mathbf{u}^k \cdot \nabla\phi, \theta_w\right) - \left(\mathbf{u}_w \cdot \nabla\phi, \theta^k\right) + \left(\frac{1}{\mathcal{P}r}\nabla\theta_w, \nabla\phi\right) =\\
\frac{1}{\delta t}\left(\theta^k - \theta^n, \phi\right) - \left(\mathbf{u}^k \cdot \nabla\phi, \theta^k\right) + \left(\frac{1}{\mathcal{P}r}\nabla\theta^k, \nabla\phi\right).
\end{aligned}
\tag{4.10}
$$

We impose homogeneous Dirichlet boundary conditions $(\mathbf{u}_w; p_w; \theta_w) = 0$ for this system. The Newton loop (following k) has to be iterated until convergence for each time step. The algorithm is written as:

$$
\left\|\begin{array}{l}
\text{Navier-Stokes time loop following } n\\
\text{set } w^0 = (\mathbf{u}^n, p^n, \theta^n)\\
\left\|\begin{array}{l}
\text{Newton iterations following } k\\
\quad \text{solve (4.10) to get } (\mathbf{u}_w, p_w, \theta_w)\\
\quad \text{actualize } w^{k+1} = w^k - (\mathbf{u}_w, p_w, \theta_w)\\
\text{stop when } \|w^{k+1} - w^k\| < \epsilon
\end{array}\right.\\
\text{actualize } (\mathbf{u}^{n+1}, p^{n+1}, \theta^{n+1}) = w^k
\end{array}\right.
\tag{4.11}
$$

4.4. Implementation in FreeFem++ and validations

For the space discretization of system (4.10) we use standard Taylor-Hood finite elements (Taylor and Hood, 1973), approximating the velocity with P_2 finite elements and the pressure with the P_1. We present in the following the validation of finite element code written with FreeFem++.

Similarly to the validation of the finite difference method (see previous chapter 3) we consider the two most studied cases in literature for the temperature driven cavity: the vertical (Rayleigh-Bénard convection) and horizontal (temperature driven cavity) temperature gradient problems. For the Rayleigh-Bénard benchmark we have considered the results reported by Ouertatani et al. (2008), while for the differentially heated cavity we compared our results with those of Wakashima and Saitoh (2004). An additional comparison is made with the results published by Xin et al. (1997). For each case, qualitative and quantitative analysis of the results are presented below.

All the results presented here are for $Pr = 0.71$ and Ra numbers varying form 10^4 to 10^6. The finite element grid is depicted in figure 4.1. The horizontal and vertical velocity distributions are considered at mid-plane ($y = 0.5$) and mid-height($z = 0.5$). The computational time needed for these simulations is low and the finite element code provides a very good agreement to each of the tests considered.

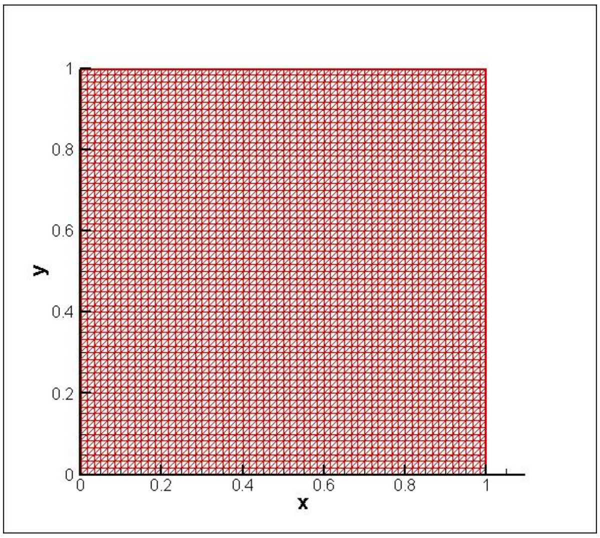

Figure 4.1.: FreeFem++ finite element grid for natural convection problems (60 points are used for each side of the square cavity).

4.4.1. Rayleigh-Bénard (vertical ∇T) case

Reference results were presented in the previous chapter 3 (see fig 3.4).
We show in figure 4.2 the temperature field, for the three Rayleigh numbers: 10^6, 10^5 and 10^4. On the top of each figure we represent the temperature variation, keeping in mind that all the variables are dimensionless and the temperatures on the opposed walls are $T_h = 0.5$ (top) and $T_c = -0.5$ (bottom), respectively. A very good qualitative agreement with the results of Ouertatani et al. (2008) is obtained for the streamlines and temperature shape. The finite element results are also similar to the results obtained in the previous chapter with the finite difference code.

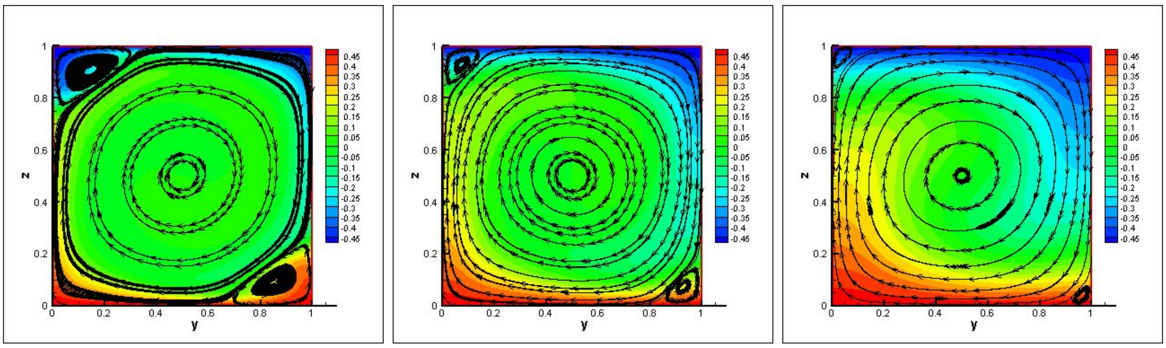

$Ra = 10^6$ $Ra = 10^5$ $Ra = 10^4$

Figure 4.2.: FreeFem++ simulation of the Rayleigh-Bénard convection. Streamlines and temperature fields for different Rayleigh numbers.

For a more quantitative comparison, we represent in fig. 4.3 velocity profiles along centerline sections of the cavity. Again, a good agreement with Ouertatani et al. (2008) is obtained. This is also confirmed in table 4.1 by extracting from these profiles the maximum horizontal and vertical velocities along centerlines and their locations.

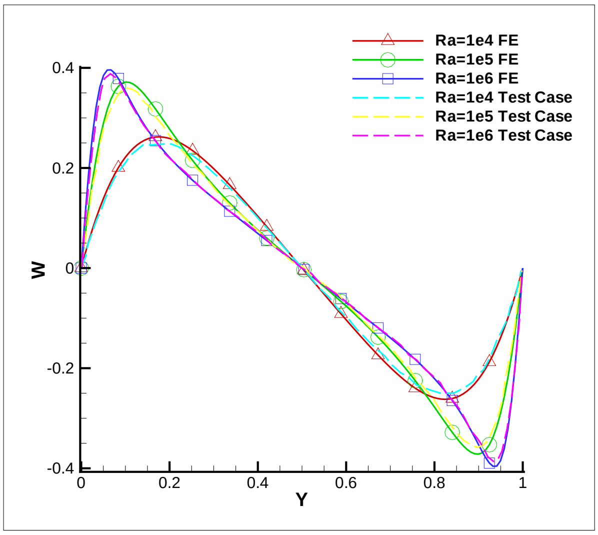

W velocity

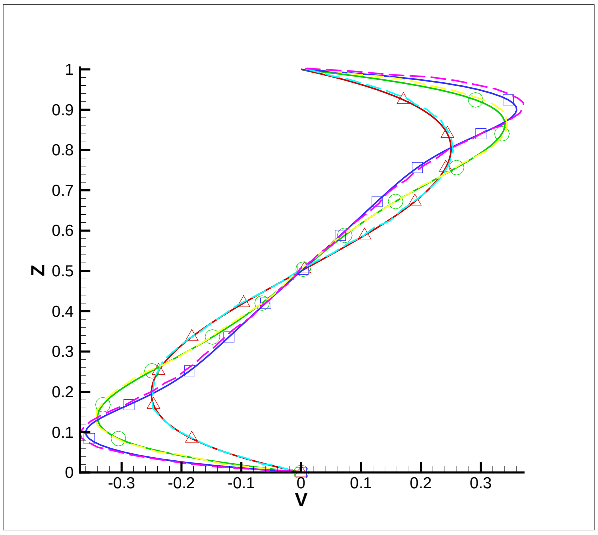

V velocity

Figure 4.3.: FreeFem++ simulation of the Rayleigh-Bénard convection. Velocity profiles following horizontal and vertical centerlines: comparison with benchmark solution from Ouertatani et al. (2008).

$\mathcal{R}a$	Grid	$V_{max}\,(z)$	$W_{max}\,(y)$
$Ra = 10^4$	40	0.2504 (0.8067)	0.2622 (0.824)
Ouertatani et al. (2008)	256	0.25228 (0.8023)	0.2636 (0.8263)
$Ra = 10^5$	40	0.341 (0.8651)	0.3723 (0.8991)
Ouertatani et al. (2008)	256	0.3443 (0.8636)	0.3756 (0.8973)
$Ra = 10^6$	40	0.3601 (0.8991)	0.3962 (0.9328)
Ouertatani et al. (2008)	256	0.3788 (0.9036)	0.406 (0.9359)

Table 4.1.: FreeFem++ simulation of the Rayleigh-Bénard convection. Maximum horizontal and vertical velocities along centerlines and their locations (see fig. 4.3). Comparison with benchmark solution.

4.4.2. Differentially heated cavity (horizontal ∇T) case

Reference results for were presented in the previous chapter (see fig 3.12). For quantitative comparisons, we use the results of Wakashima and Saitoh (2004) and Barakos et al. (1994). Figure 4.4 depicts the obtained streamlines and temperature fields they for three Rayleigh numbers: 10^6, 10^5 and 10^4. We notice a good agreement with previously obtained results using the finite difference method and with pictures of Wakashima and Saitoh (2004).

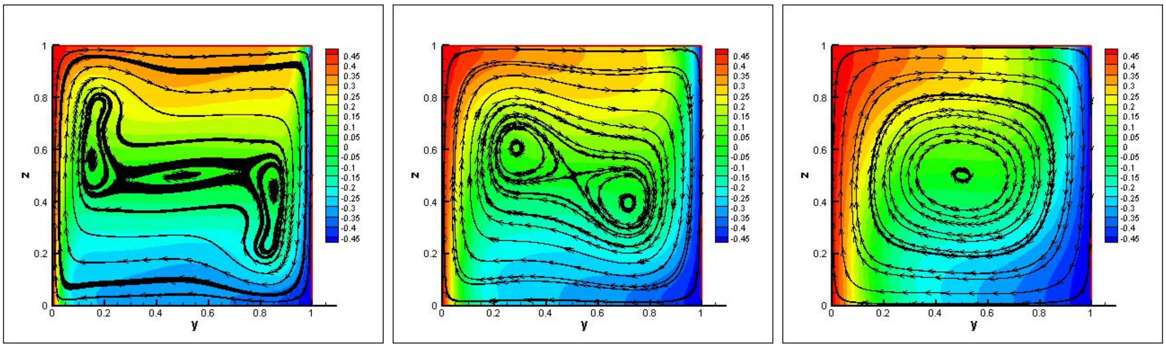

$Ra = 10^6$ $Ra = 10^5$ $Ra = 10^4$

Figure 4.4.: FreeFem++ simulation of the differentially heated cavity. Streamlines and temperature fields for different Rayleigh numbers.

Figure 4.5 represents the velocity profiles following the centrelines. Quantitative comparisons following figure 4.5, is presented in Table 4.2 showing maximum velocities for these profiles. A very good agreement is also obtained for this test case.

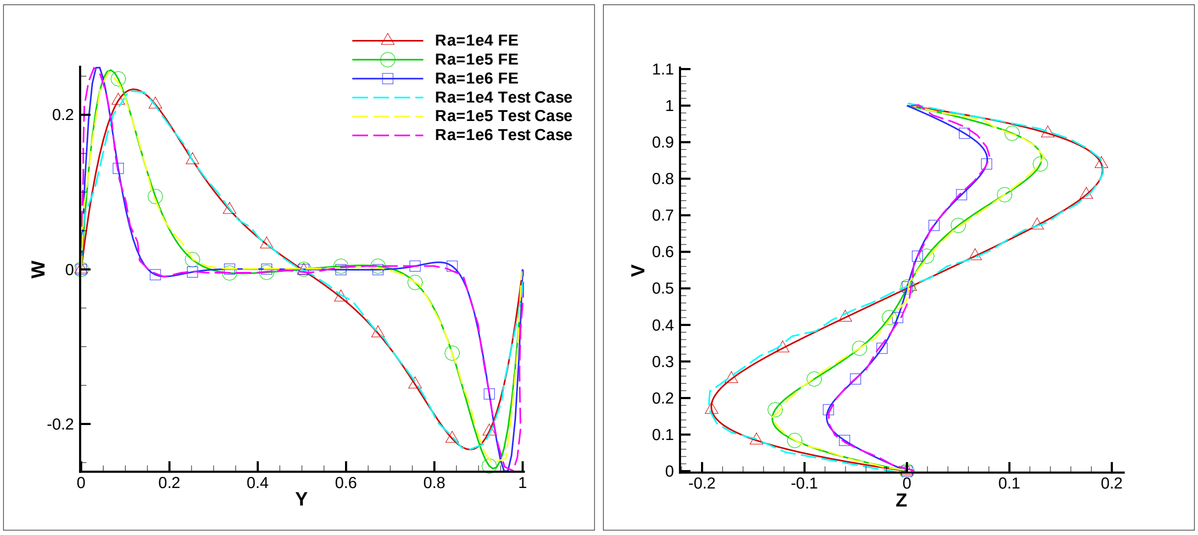

W velocity V velocity

Figure 4.5.: FreeFem++ simulation of the differentially heated cavity. Velocity profiles following horizontal and vertical centerlines: comparison with benchmark solution from Wakashima and Saitoh (2004).

Rayleigh no.	Grid size	$V_{max}(z)$	$W_{max}(y)$
$Ra = 10^4$	0.025	0.1910(0.8235)	0.2330(0.1176)
Wakashima and Saitoh (2004)	0.0125	0.1985(0.8250)	0.2218(0.1125)
Fusegi et al. (1991)	0.0083	0.2013(0.8167)	0.2252(0.1167)
$Ra = 10^5$	0.025	0.1355(0.8514))	0.2578(0.0672)
Wakashima and Saitoh (2004)	0.0125	0.1418(0.8500)	0.2450(0.0625)
Fusegi et al. (1991)	0.0083	0.1468(0.8547)	0.2471(0.0647)
$Ra = 10^6$	0.025	0.07833(0.856))	0.2610(0.0335)
Wakashima and Saitoh (2004)	0.0125	0.08105(0.8500)	0.2606(0.0375)
Fusegi et al. (1991)	0.0083	0.08416(0.8557)	0.2588(0.0331)

Table 4.2.: FreeFem++ simulation of the Rayleigh-Bénard convection. Maximum horizontal and vertical velocities along centerlines and their locations (see fig. 4.5). Comparison with benchmark solutions.

4.5. Comparison with the results obtained with a spectral code

For a more precise quantitative comparison with previously published results, we consider the results of Xin et al. (1997). They used a spectral Chebyshev collocation method for spatial discretization and a direct Uzawa method for velocity-pressure coupling. As far as we know, there results are considered to be one of the most precise.

Figure 4.6 depict the temperature field and streamlines for Rayleigh numbers form 10^4 to 10^6. For all three Rayleigh numbers a good conformity appears in what regard the aspect of the temperature field and vortexes formation. At $Ra = 10^4$ a central vortex is present and dominant. Increasing to $Ra = 10^5$ the recirculation cell becomes elliptic and breaks in two. The two vortices shift towards the horizontal walls at $Ra = 10^6$, an a third small central vortex appears.

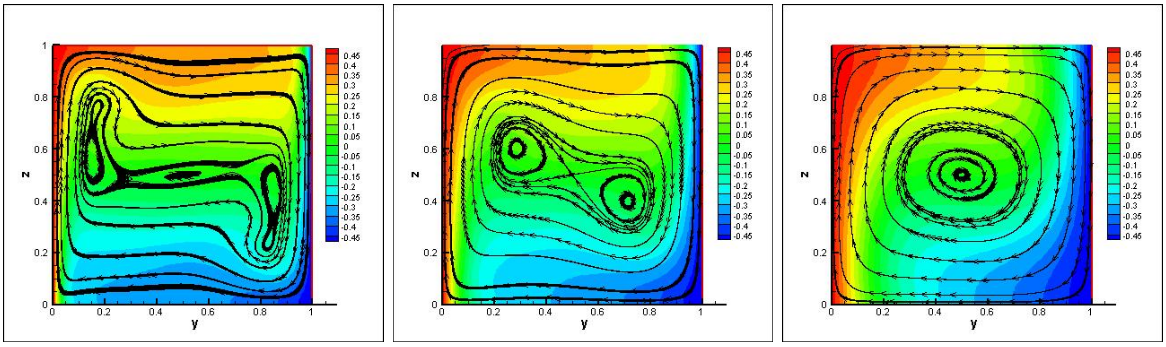

$Ra = 10^6$ $\quad$ $Ra = 10^5$ $\quad$ $Ra = 10^4$

Figure 4.6.: FE isotherms and temperature fields.

The horizontal and vertical velocity distributions at the mid-width $y = 0.5$ and at the mid-height $z = 0.5$ are presented in figure 4.7 (first row), for Rayleigh numbers between 10^4 and 10^6. The increase of the velocity norms with Rayleigh number indicates that convection becomes dominant. A very good agreement is obtained. The second row from figure 4.7 represents a comparison if the temperature distribution at mid-width and mid-height. The profiles show a good concordance with the test case.

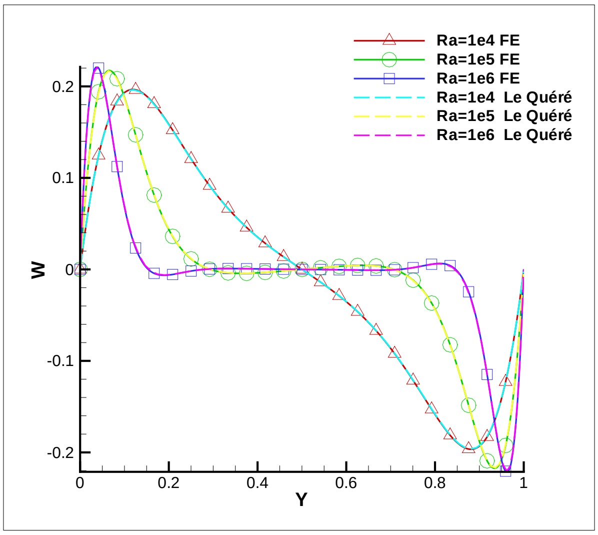

W velocity

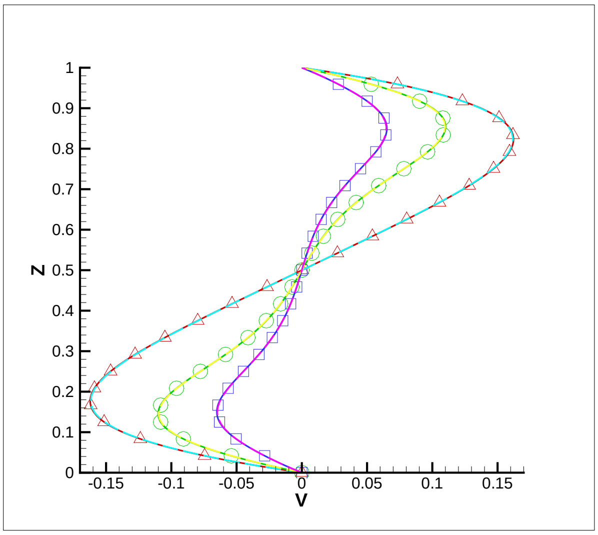

V velocity

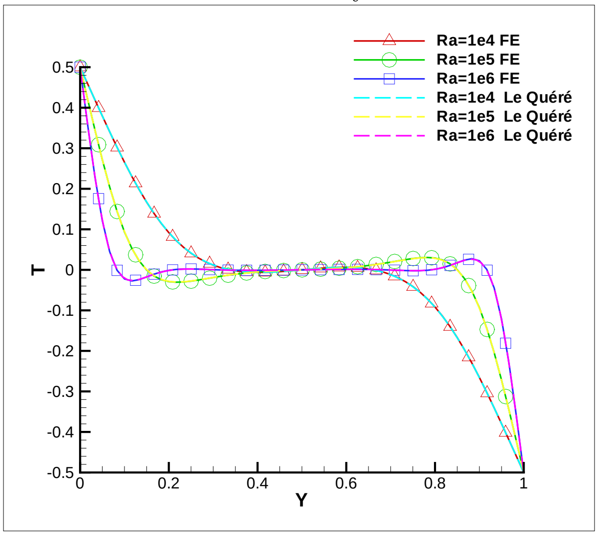

Temperature after y-direction

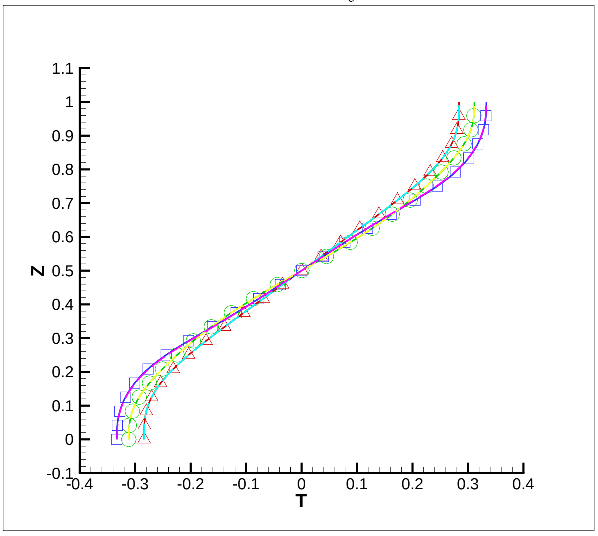

Temperature after z-direction

Figure 4.7.: Profiles following centerlines

Table 4.3 provides a comparison between present results and numerical results proposed by Xin et al. (1997). The comparison concerns the maximum velocity values and there corresponding location. An excellent agreement is found for all values of Rayleigh. The present results were obtained on a 60^2 grid nodes, white the test case solution was computed on a 80^2 grid nodes.

For the case of $Ra = 10^4$ Table 4.3 shows that our results for v_{max} and w_{max} are grater that those considered within a 0.2% difference. The locations of the velocities at the mid plane can also be found within a -0.18% difference and -1.1% respectively. In the case of $Ra = 10^5$ our results present a good agreement and are within the same % difference. When $Ra = 10^6$ the results are again in very good agreement and within a 0.5% difference with respect to the results proposed by Xin et al. (1997).

Rayleigh no.		Value (Position)	$Value_{error}\%$ ($Possition_{error}\%$)
$Ra = 10^4$	$v_{max}(z)$	0.1621(0.8231)	0.2246%(−0.1864%)
	$w_{max}(y)$	0.1965(0.1184)	0.1617%(−1.1394%)
$Ra = 10^5$	$v_{max}(z)$	0.1102(0.8548)	0.2405%(0.1553%)
	$w_{max}(y)$	0.2173(0.06588)	0.2289%(3.3508%)
$Ra = 10^6$	$v_{max}(z)$	0.06512(0.8498)	0.4985%(−0.4309%)
	$w_{max}(y)$	0.2212(0.0383)	0.3162%(0.8015%)

Table 4.3.: Comparison with the results proposed by Xin et al. (1997).

4.6. Conclusion

The finite element solver for the Navier-Stokes-Boussinesq equations was validated in this chapter against classical benchmarks for natural convection flows. The proposed Newton algorithm proved very efficient in solving the discretized equations following an implicit Euler scheme. The Taylor-Hood finite elements (quadratic for velocities and linear for pressure) offer sufficient precision to accurately simulate these flows with reasonable grid densities (60^2 nodes) and low computational cost.

After this necessary validation, the solver will be used in the next chapters for more complex problems: convection within a cavity with obstacles and convection with phase-change phenomena.

5. Navier-Stokes Boussinesq model and immersed boundary method

We recall that our starting problem concerns the study of the flow developing inside a telecommunication cabinet. Inside the outdoor cabinet we can find electronic equipments that, when active, generate heat. The geometry and properties of these components can be simplified under the form of geometrical immersed bodies inside the flow. These immersed objects can produce either high or low temperatures, that may vary in time, depending on the internal operating conditions.

The simplified model adopted in this chapter to simulate outdoor cabinets is a cavity with rectangular obstacles inside. We develop in the following a numerical model based upon the Immersed Boundary Method (IBM) to simulate flows in complex geometries using rectangular finite difference grids. The IBM method will be implemented in the Navier-Stokes-Boussinesq finite difference code presented and validated in previous chapters.

The first section presents the existing literature and will explain the principle of the IBM method, together with its advantages and disadvantages. The second section describes the IBM method implemented in our code. Afterwards, extensive validations are presented, using as reference the finite element code and previous studies in literature. The finite element approach, presented in chapter 4, has the advantage of rendering an exact solution, as no approximation is used for obstacles.

5.1. Immersed Boundary Method: principle and existing studies

Natural and forced convection within complex domains is a widely spread problem in engineering applications. The notion of ”immersed boundary method” was introduced by Peskin (1972) in reference to a method used to simulate cardiac mechanics and associated blood flow. The novelty of the method consisted in the use of a Cartesian grid which did not conform to the geometry of the simulated object. Peskins formulated a procedure for modeling the effect of the immersed boundary on the flow. Since the method was introduced, numerous modifications and refinements were made for it’s improvement and a large number of variants now exist (for a review, see Mittal and Iaccarino, 2005b).

Let us consider the model problem depicted in figure 5.1. The fluid region is denoted by Ω_f where the solid immersed object occupies the domain Ω_s with boundary Γ_s. The flow inside the domain is governed by the incompressible Navier-Stokes equations:

$$\frac{\partial \vec{u}}{\partial t} + \vec{u} \cdot \nabla \vec{u} + \nabla p - \Delta \vec{u} = 0 \tag{5.1}$$

$$\nabla \cdot \vec{u} = 0 \text{ in } \Omega_f \text{ and}$$

$$\vec{u} = \vec{u}_s \text{ on } \Gamma_s, \ \vec{u} = 0 \text{ on } \Gamma_f.$$

For the immersed boundary method the first (momentum) equation is discretized on a non-boundary conforming grid and the boundary conditions (BC) are imposed through modifications of the last equation. The most common manipulation is the through the use of a forcing function in the momentum equation that reproduces the effect on the flow of a solid body. Another approach would be the so called cut-cell approach. Depending on the way the forcing term is introduced in the equations, Mittal and Iaccarino (2005b) divide the immersed boundary into two categories : continuous forcing and discrete forcing approach.

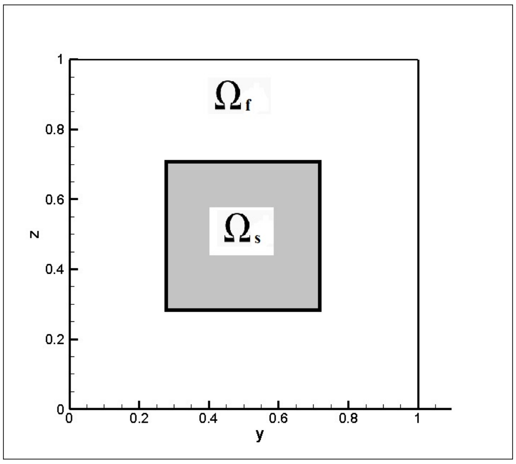

Figure 5.1.: Model problem for the Immersed Boundary Method (IBM).

In the continuous forcing approach, the forcing term is included in the momentum equations and the system becomes:

$$\frac{\partial \vec{u}}{\partial t} + \vec{u} \cdot \nabla \vec{u} + \nabla p - \Delta \vec{u} = \vec{f}, \tag{5.2}$$

and the equations are afterwards discretized. This method was fist introduced by Peskin (1972), for flows with elastic boundaries and afterwards extended in numerous studies, *e. g.* Goldstein et al. (1993); Saiki and Biringen (1996); Lai and Peskin (2000); Silva et al. (2003), to model rigid boundary flows using a feedback forcing strategy. The main disadvantage of this approach is that the smoothing of the forcing function prohibits sharp representation of the boundary and restricts the time step. To improve numerical stability, a solution was proposed that replaced the feedback forcing method with a direct forcing strategy on the Lagrangian markers (Su et al., 2007; Zhang and Zheng, 2007; Chen et al., 2007; Le et al., 2008).

In the discrete forcing approach, the equations are first discretized on a Cartesian grid, without taking into account the body, and only afterwards the forcing term is introduced with a discrete value for each grid cell. This approach explicitly enforces boundary conditions and has the advantage that the stability constraint of the time-integration scheme is not degraded as shown in several studies (J., 2001; Fadlun et al., 2000; Kim et al., 2001; Tseng and Ferziger, 2003; Balaras, 2004; Kim and Choi, 2006; Yang and Balaras, 2006).

The cut-cell approach does not introduce a forcing function but is based on a truncation of the Cartesian cells at the border of the immersed body to create a new cell which conforms to the shape of the body surface. This reshaping may lead to a very small cells, which has a negative impact on the numerical stability, and may be corrected by a cell-merging strategy. The cut-cell method is mostly associated with the finite volume simulation of flow; it also appears in finite difference methods (Udaykumar et al., 1999). This method was applied for both stationary and moving boundary.

Although a second-order accuracy in the discretization is generally achieved for the interior cells, the accuracy of the discretization for the boundary cells is usually decreased to a first-order accuracy, see (see Pember and Bell, 1995; Popinet, 2003). Second-order accurate interpolation schemes, as the one proposed by Ji et al. (2010b), were developed for application to inviscid compressible flow problems. They made use of a cell-merging approach to ensure the stability. Ingram et al. (2003) developed a cut-cell method for both moving bodies and moving material interfaces. Hartmann et al. (2011), proposed such a method for two- and three-dimensional viscous, compressible flow problems on arbitrarily refined graded meshes.

Bouchon et al. (2012) presented a second-order IBM method, based on the MAC scheme on Cartesian grids, for simulation of two-dimensional incompressible flows past immersed bodies. Two-dimensional unsteady viscous incompressible two-phase flows with embedded moving solid boundaries were simulated by Chung (2013). They treated the fluid-fluid interface by the level set method. Schneiders et al. (2013) studied a way to eliminate oscillations occurring in Cartesian grid methods extended to moving-boundary problems. Other similar studies can be mentioned, *e. g.* Fidkowski and Darmofal (2007); Causon et al. (2001); Ji et al. (2008, 2010a).

The main disadvantage of the immersed boundary method is that the piecewise solution across the boundary is perturbed by the distribution of the singular forces over multiple grid nodes, which generates a reduced spatial resolution and accuracy in the vicinity of the boundary. A solution was proposed by Leveque and Li (1994), that was supposed to maintain the sharpness of the result near the boundary. This method was named the *Immersed Interface*: the governing equation at the interface was modified by adding a forcing function designed to enforce appropriate jump conditions at the interface. Studies that used this approach were also reported by Li and Lai (2001); Lai and Peskin (2000); Xu et al. (2006). Several jump conditions at the interface for the three dimensional have also been presented by Xu and Wang (2006a,b).

In the *Sharp Interface Method*, the boundary is tracked by identifying the cells that are cut by the immersed boundary (Ye et al., 1999). Consequently, as shown by several studies (Udaykumar et al., 1999, 2001; Marella et al., 2005), the irregular shapes of cut cells result in a need for complicated interpolation procedures to approximate fluxes, and this affects computational efficiency of the solvers. Other examples of sharp interfaces are those proposed by Mittal et al. (2008), which makes use of a ghost cell technique to satisfy the boundary conditions on the immersed boundary. This method was developed for stationary interfaces in fluid structure interactions. The same principle was also used by Ghias et al. (2007); Luo et al. (2008). Later Zhao et al. (2008); Taira and Colonius (2007) maintained a sharp interface by a boundary body force with projection-based method which satisfies the non-slip boundary condition, and thus ensuring the momentum conservation.

Wang et al. (2010b) presented a hybrid meshfree-and-Cartesian grid method, for incompressible 3D flows with moving boundary, that combines a finite difference approximations on Cartesian grids with generalized finite difference (GFD) approximations on meshfree grids. The meshfree method was proposed by Liszka and Orkisz (1980), and further developed by Liszka (1984); Liszka et al. (1996); Ding et al. (2004a,b); it was also extended to solve incompressible fluid flow problems in the stream function-vorticity formulation (Chew et al., 2006).

A study of the satisfaction of the boundary conditions in the presence of immersed bodies was performed by Domenichini (2008). They concluded that the direct forcing scheme in combination with the fractional step method is not able to satisfy the impenetrability condition and offered some solutions. Liao et al. (2010) proposed an immersed-boundary method, based on the direct momentum and energy forcing, for the simulation of natural and forced convection at low Reynolds numbers.

Calhoun (2002) developed a method based on an underlying uniform Cartesian grid and second-order finite-difference/finite-volume discretizations of the stream function-vorticity equations. Another example of rigid boundary is the one proposed by Le et al. (2008) who used a finite difference method on a uniform Cartesian grid, singular forces are applied at the rigid boundaries to impose the no-slip conditions.

The immersed boundary method has been used in a variety of problems, including modeling the flow of blood in the heart (Peskin, 1977, 1981; Peskin and McQueen, 1989), aquatic locomotion (Fauci and Peskin, 1988), blood clotting (Fogelson, 1984), (Fogelson and Peskin, 1988), and wave motion in the cochlea (Beyer, 1992).

Present approach

In this study, we chose to use a direct-forcing approach that explicitly enforces boundary conditions near the immersed boundary. J. (2001) proposed a direct-forcing method that introduces a body force such that the desired velocity distribution is obtained at the boundary. Fadlun et al. (2000) extended this approach to a finite-difference formulation on a staggered grid, where direct forcing is applied at the first grid points external to the immersed boundary. It was concluded that the stability of the time integration scheme is not altered and good agreement with experimental measurements is obtained.

Generally, the implementation of such immersed boundary methods is based on explicit schemes for time-advancement of the solution. Some methods that use the semi-implicit time-integration technique are proposed by Fadlun et al. (2000). An explicit calculation of the forcing terms in conjunction with a semi-implicit solver was studied by Kim et al. (2001). However, this requires an additional resolution of the momentum equation, once for the forcing field and the second one for the time advancement of the solution. Other direct forcing formulations are proposed by Tseng and Ferziger (2003); Balaras (2004); Kim and Choi (2006); Su et al. (2007); Zhang and Zheng (2007); Choi et al. (2007).

The direct forcing approach partially alleviates the problem of the stability limits, as shown by Verzicco (2005); Cristallo and Verzicco (2006). This is done by the use of interpolation procedures, that enforce the desired solution at the immersed boundary, as the position of the unknown on the grid does not usually coincide with that of the boundary.

Interpolation procedures were successively improved in a series of articles proposed by Kim et al. (2001); Gilmanov et al. (2003); Balaras (2004). The latter provided a method that interpolates the velocity along lines normal to the body surface and thus improves the quality of the results in the near body region. This methodology has been extended to cases of compressible flows, as the ones studied by De Palma et al. (2006); de Tullio et al. (2007). The technique was also extended to Navier-Stokes solvers with curvilinear-coordinate, structured grids by Kim et al. (2001); Moin (2002); Roman et al. (2009). Their use remains restricted to the study of a relatively small class of problems, where bulk cylindrical geometry is combined with obstacles and thus give an overall complex shape.

5.2. Implementation of an IBM method in the finite difference code

We are interested in implementing an IBM method for an incompressible fluid with thermal convection, governed by the Navier-Stokes equations under the Boussinesq approximation. Within the flow we have a rectangular immersed body that generates heat. The influence of the immersed boundary on the fluid is represented by two types of forces: the body-force due to the position of the body and the buoyancy force due to temperature difference.

The IBM method we have used is based on a direct momentum forcing on a Cartesian grid; it can also be viewed as a discrete forcing approach. The governing Navier-Stokes-Boussinesq equations, modified accordingly to the IBM method, are the following:
Continuity equation:

$$\nabla \cdot \vec{u} = 0 \tag{5.3}$$

Momentum equation:

$$\frac{\partial \vec{u}}{\partial t} + (\vec{u}\nabla)\vec{u} = -\nabla p + \frac{1}{\mathcal{R}e}\Delta\vec{u} + \frac{\mathcal{R}a}{\mathcal{R}e^2\mathcal{P}r}T\vec{e}_z + \vec{f}_m \tag{5.4}$$

Temperature (passive scalar) equation:

$$\frac{\partial T}{\partial t} + (\vec{u}\nabla)T = \frac{1}{\mathcal{R}e\mathcal{P}r}\Delta T + f_e \tag{5.5}$$

Compared to the already discussed Navier-Stokes-Boussinesq equations, two forcing terms are added: $\vec{f}_m$ and f_e. The discrete-time momentum forcing $\vec{f}_m$ is applied to satisfy the no-slip conditions on the immersed boundaries, and the discrete-time passive scalar forcing f_e is used to satisfy the prescribed temperature conditions on the body. Both the momentum forcing and passive scalar forcing were applied at the nodes adjacent to the immersed boundary.

The numerical procedure consist on applying the method proposed by Liao et al. (2010) to our finite difference code. The discrete form of the algorithm for solving the governing equations is as follows:

(1) Compute the non-solenoidal velocity field following a generic time advancement method of substeps $i = 1, 2, \ldots, l$:

$$\frac{\hat{\vec{u}} - \vec{u}^i}{\delta t} = \left[\gamma_i \vec{H}^i + \rho_i \vec{H}^{i-1} - \alpha_i \vec{G}^i\right] + \vec{f}_m^{i+1}, \tag{5.6}$$

with $\vec{G} = \nabla p$ and $\vec{H} = -(\vec{u}\nabla)\vec{u} + \frac{1}{\mathcal{R}e}\Delta\vec{u} + \frac{\mathcal{R}a}{\mathcal{R}e^2\mathcal{P}r}T\vec{e}_z$.

(3) Solve the discrete Poisson equation:

$$\Delta\phi = \frac{1}{\alpha_i \cdot \delta t}\nabla.\hat{\vec{u}} \tag{5.7}$$

(4) Apply the velocity and pressure corrections:

$$\vec{u}^{i+1} = \hat{u} - \alpha_i\, \delta t \nabla\phi \tag{5.8}$$

$$p^{i+1} = p^i + \phi. \tag{5.9}$$

(5) Solve the temperature equation:

$$\frac{T^{i+1}-T^i}{\delta t} = \gamma_i Q^i + \rho_i Q^{i-1} + f_e^{i+1}, \quad Q = -\nabla(\vec{u}T) + \frac{1}{\mathcal{R}e\mathcal{P}r}\Delta T. \tag{5.10}$$

The force applied to the nodes due to the presence of an immersed body are computed at an advanced level before the solution procedure begins. We denote by $\tilde{\vec{u}}$ and $\widetilde{T}$ the estimates of the velocity and, respectively, temperature, at time level $i+1$, in the absence of a body. These values are obtained from (5.6) and (5.10), respectively, by setting the force terms to zero:

$$\frac{\tilde{\vec{u}} - \vec{u}^i}{\delta t} = \left[\gamma_i \vec{H}^i + \rho_i \vec{H}^{i-1} - \alpha_i \vec{G}^i\right], \tag{5.11}$$

$$\frac{\widetilde{T} - T^i}{\delta t} = \gamma_i Q^i + \rho_i Q^{i-1}. \tag{5.12}$$

If $\vec{u}_F$ and T_F are the velocity and temperature values in the presence of the body, the forcing terms for the momentum equation are expressed by a simple Newton acceleration (Liao et al., 2010):

$$\vec{f}_m^{i+1} = \frac{\vec{u}_F - \tilde{\vec{u}}}{\delta t} = \frac{\vec{u}_F - \vec{u}^i}{\delta t} - \left[\gamma_i \vec{H}^i + \rho_i \vec{H}^{i-1} - \alpha_i \vec{G}^i\right], \tag{5.13}$$

where (5.11) was used to replace $\tilde{\vec{u}}$. We apply for the temperature equation a similar forcing term and use (5.12) to derive its final expression:

$$f_e^{i+1} = \frac{T_F - \widetilde{T}}{\delta t} = \frac{T_F - T^i}{\delta t} - \left[\gamma_i Q^i + \rho_i Q^{i-1}\right]. \tag{5.14}$$

The values of $\vec{u}_F$ and T_F are obtained by linear interpolation between adjacent points lying on the same grid line. Figure 5.2 illustrates the interpolation scheme near the body for one component of the velocity vector.

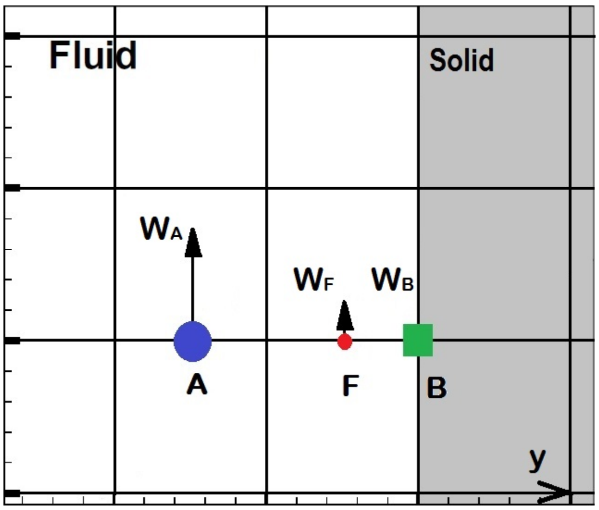

Figure 5.2.: Interpolation scheme for the IBM method.

For the vertical velocity forcing we have:

$$w_F = \widetilde{w}_A - \frac{\widetilde{w}_A - \widetilde{w}_B}{y_A - y_B}(y_A - y_F) \tag{5.15}$$

Similar linear interpolation is applied for the other two components of the velocity vector. For temperature we also use a linear interpolation scheme:

$$T_F = \widetilde{T}_A - \frac{\widetilde{T}_A - \widetilde{T}_B}{y_A - y_B}(y_A - y_B) \tag{5.16}$$

For the cases where the temperature is previously know, as for the situation of imposing a measured temperature, we substitute the interpolation T_F, with the prescribed value. This case was used in the next chapter for the comparison between the numerical solution and the experimental part.

Finally, the numerical algorithm consists in the following steps:

- Identify (flag) grid points inside the solid domain and identify the immersed boundary location.
- Compute $\tilde{\vec{u}}$ from (5.11) and and $\widetilde{T}$ from (5.12).
- Obtain $\vec{u}_F$ and T_F by linear interpolation in the vicinity of the body.
- Compute forcing terms using (5.13) for $\vec{f}_m^{i+1}$ and (5.14) for f_e^{i+1}.
- Compute the non-solenoidal velocity field $\hat{\vec{u}}$ from (5.6).
- Solve the Poisson equation (5.7).
- Compute the solenoidal velocity field $\vec{u}^{i+1}$ from (5.8) and update the pressure from (5.9).
- Compute the new temperature field T^{i+1} from (5.10).

5.3. Validation of the IBM method for 2D problems

The validation procedure starts by considering rectangular immersed objects. The results obtained by the finite difference (FD) code using the IBM method are compared with the results given by the finite element (FE) solver described and validated in the previous chapter. For the same geometries involving obstacles, the FE method offers the advantage of an exact representation of the obstacles. The second part of the validation contains comparisons with previously published results for cases with immersed circular geometries.

5.3.1. Square cavity with one immersed heated rectangular object

We consider the case of a differentially heated square cavity with $T_h = 0.5$, $T_c =_0 .5$ and $Pr = 0.71$ (see chapter 3). Inside the cavity we place a square obstacle heated at constant temperature $T_F = 0.8$. Simulations are performed for $\mathcal{R}a = 10^4$, $\mathcal{R}a = 10^5$, $\mathcal{R}a = 10^6$.

For $\mathcal{R}a = 10^4$, figure 5.3 shows the temperature field and isotherms of the FE simulation (on the left) and the FD+IBM case, (on the right). We find the same allure of the isotherms, with identical recirculation cells. We note that the immersed obstacle is not symmetrically represented inside the cavity but finds its self slightly shifted to the left. The convection is not yet fully dominant and a weak upward thermal plume forms on top of the square. Two small inner recirculation cells appear, one in the top left corner and one to the right of the cavity. The circulation around the immersed object is more active. The small eddy to the right of the square is also caused by the asymmetry of the geometry.

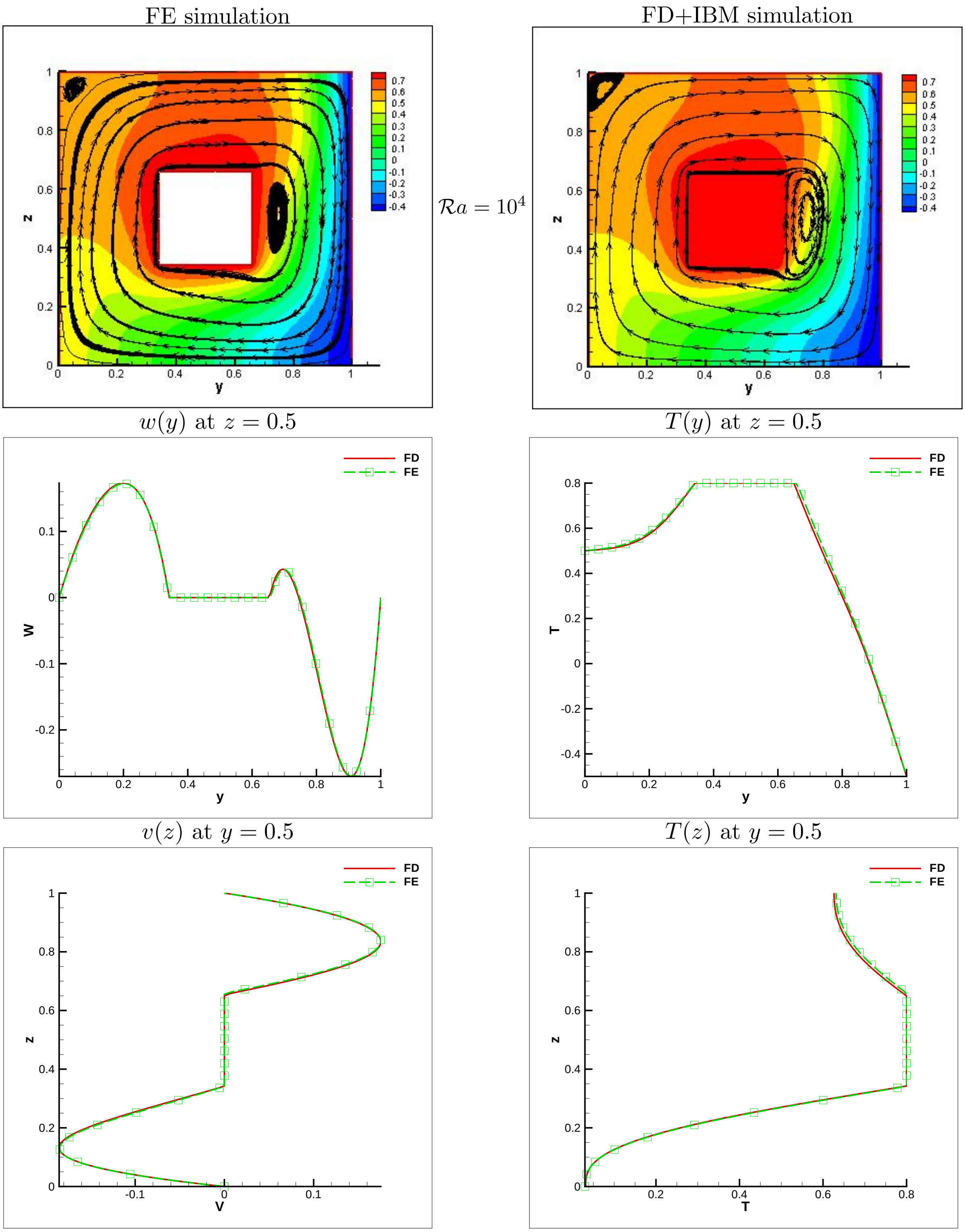

Figure 5.3.: $\mathcal{R}a = 10^4$. Differentially heated cavity case with one immersed heated object. Streamlines and temperature fields. Profiles of velocity and temperature following centerlines of the cavity.

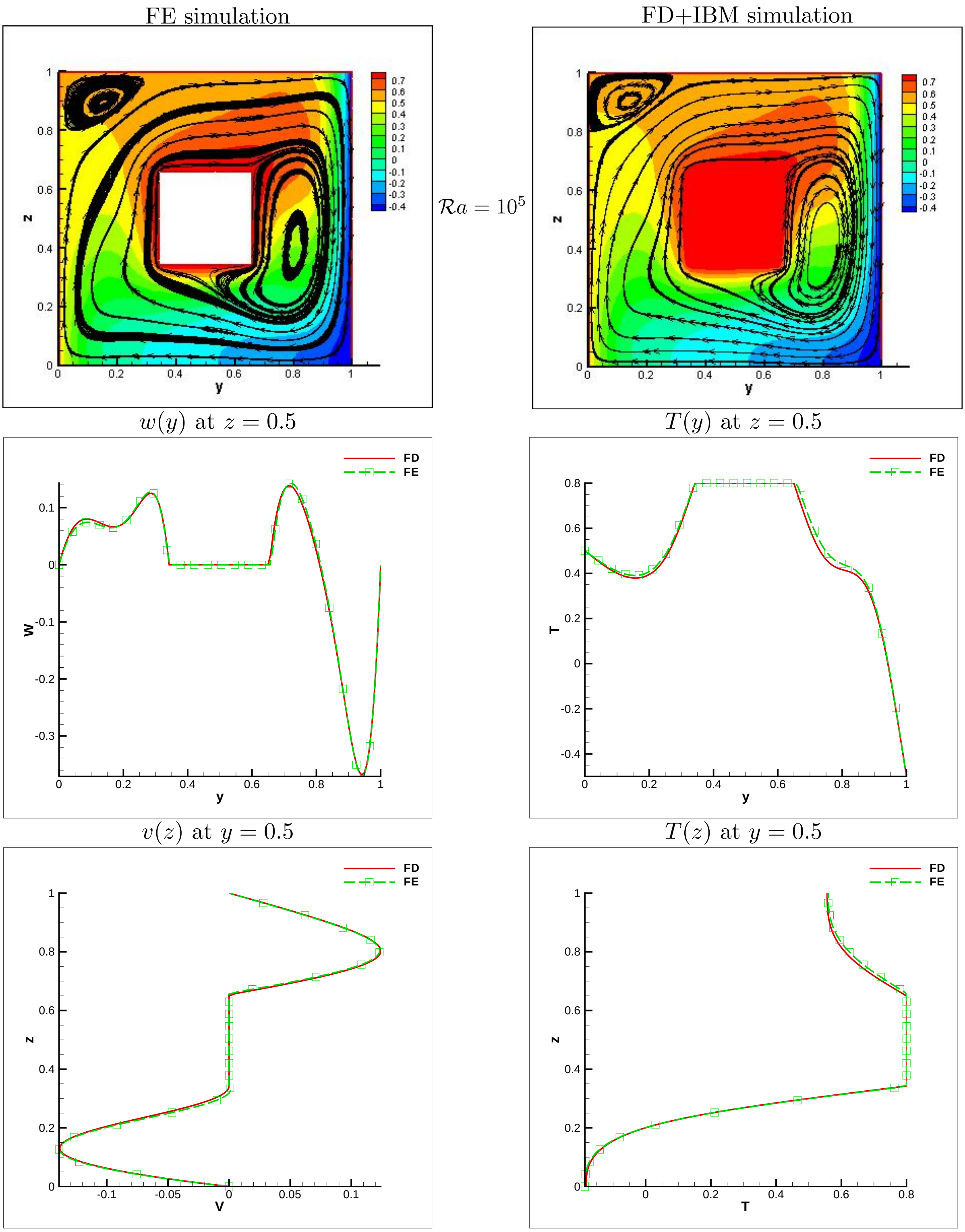

Figure 5.4.: $\mathcal{R}a = 10^5$. Differentially heated cavity case with one immersed heated object. Streamlines and temperature fields. Profiles of velocity and temperature following centerlines of the cavity.

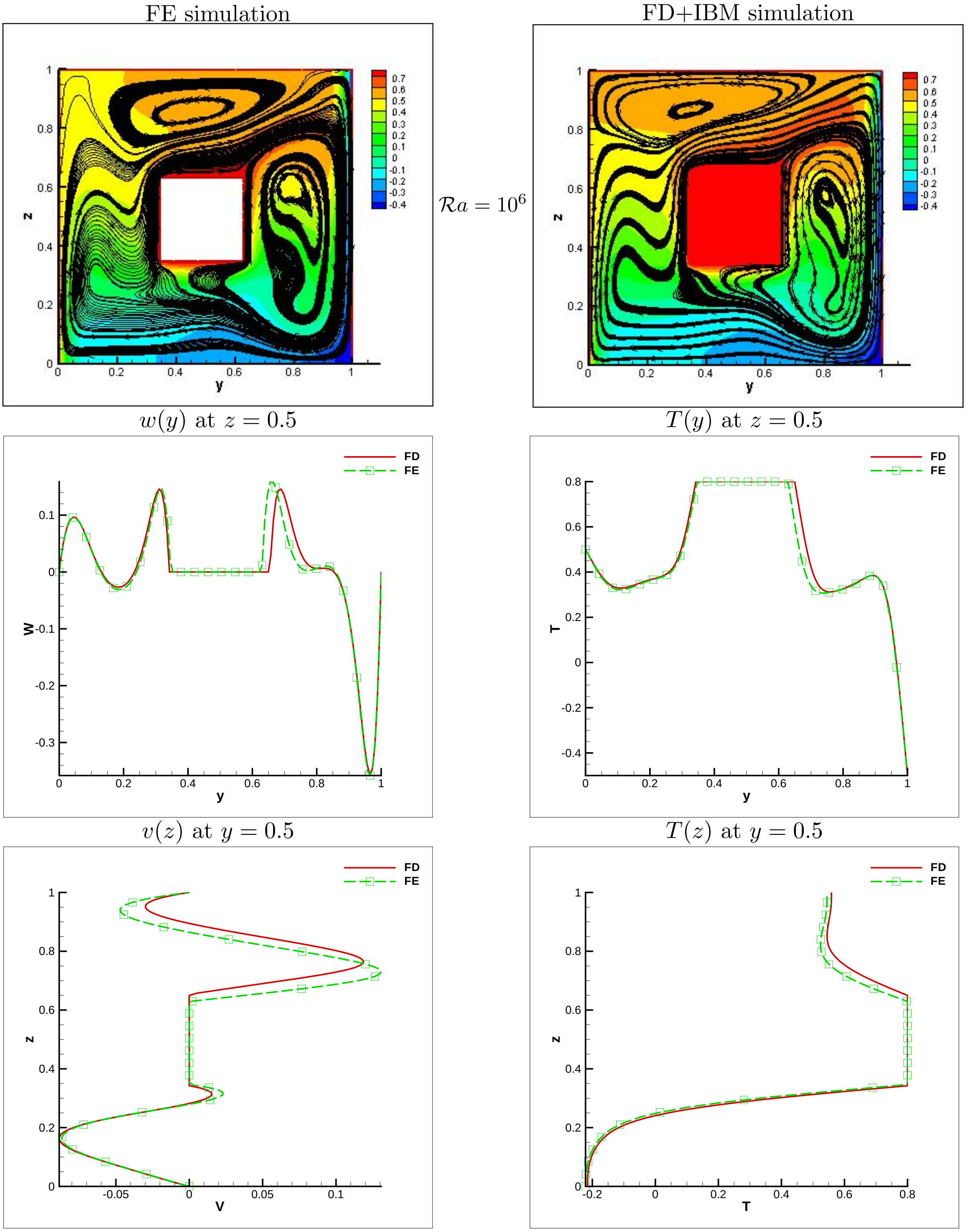

Figure 5.5.: $\mathcal{R}a = 10^6$. Differentially heated cavity case with one immersed heated object. Streamlines and temperature fields. Profiles of velocity and temperature following centerlines of the cavity.

Passing to a quantitative analysis, we also display in figure 5.3 the velocity and temperature profiles along centerlines. We notice the very good agreement between the two simulations. The velocity profiles superpose perfectly, while for the temperature profiles we can see a slight shift, to the right of the body.

As the Rayleigh number increases to $\mathcal{R}a = 10^5$ (figure 5.4), the convection becomes dominant and the thermal boundary layer becomes thinner. The plume rising from the square tilts to the right towards the cold wall. Consequently the size of the secondary inner recirculating cell to the right of the object increases. The thermal gradient at the left top corner also increases. The velocity and temperature profiles are again in good agreement, with the same slight shift for temperature, to the right of the boundary.

As we reach $\mathcal{R}a = 10^6$ (figure 5.5), the heat transfer is completely governed by convection. A strong plume is present and tilted to the right, towards the cold wall. The small left upper corner recirculation cell present at $\mathcal{R}a = 10^4$ and $\mathcal{R}a = 10^5$ grows in size and almost reaches the right wall. The eddy at the right side of the square also grows and extends towards the bottom left of the cavity. Overall the temperature field and isotherms are in good agreement. For this case the centreline profiles (velocities and temperature) present a small shift to the left with respect to the finite element method. This is due to the boundary approximations used. The measured maximal difference between the two simulations is 2.5%.

Another comparison considered for this case with a single obstacle is with the results reported by Leplat et al. (2009). A heated square of aspect ratio of 0.4 is placed inside the cavity. The upper and lower walls are isothermal and kept at a constant temperature of $T_c = 20\,°\mathrm{C}$, while the horizontal walls are adiabatic. The object is heated at $T_h = 30C$. The Rayleigh number is $2.3 \cdot 10^5$, determining a heat transfer mostly govern by convection. The temperature field and flow streamlines are plotted in figure 5.6. We can remark that our result seem closer to the experimental picture. Four distinct recirculation cells are formed. Two bigger ones to the left and right side of the cavity, and two smaller ones directly above the heated square.

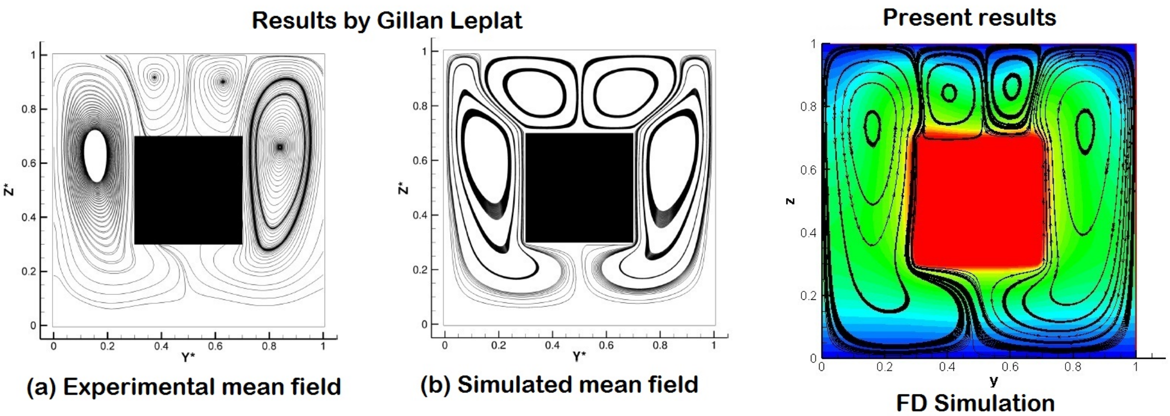

Figure 5.6.: Comparison with the results of Leplat et al. (2009). Left figure: experimental data by Leplat et al. (2009). Middle figure: numerical simulations by Leplat et al. (2009). Right: present simulation using FD+IBM.

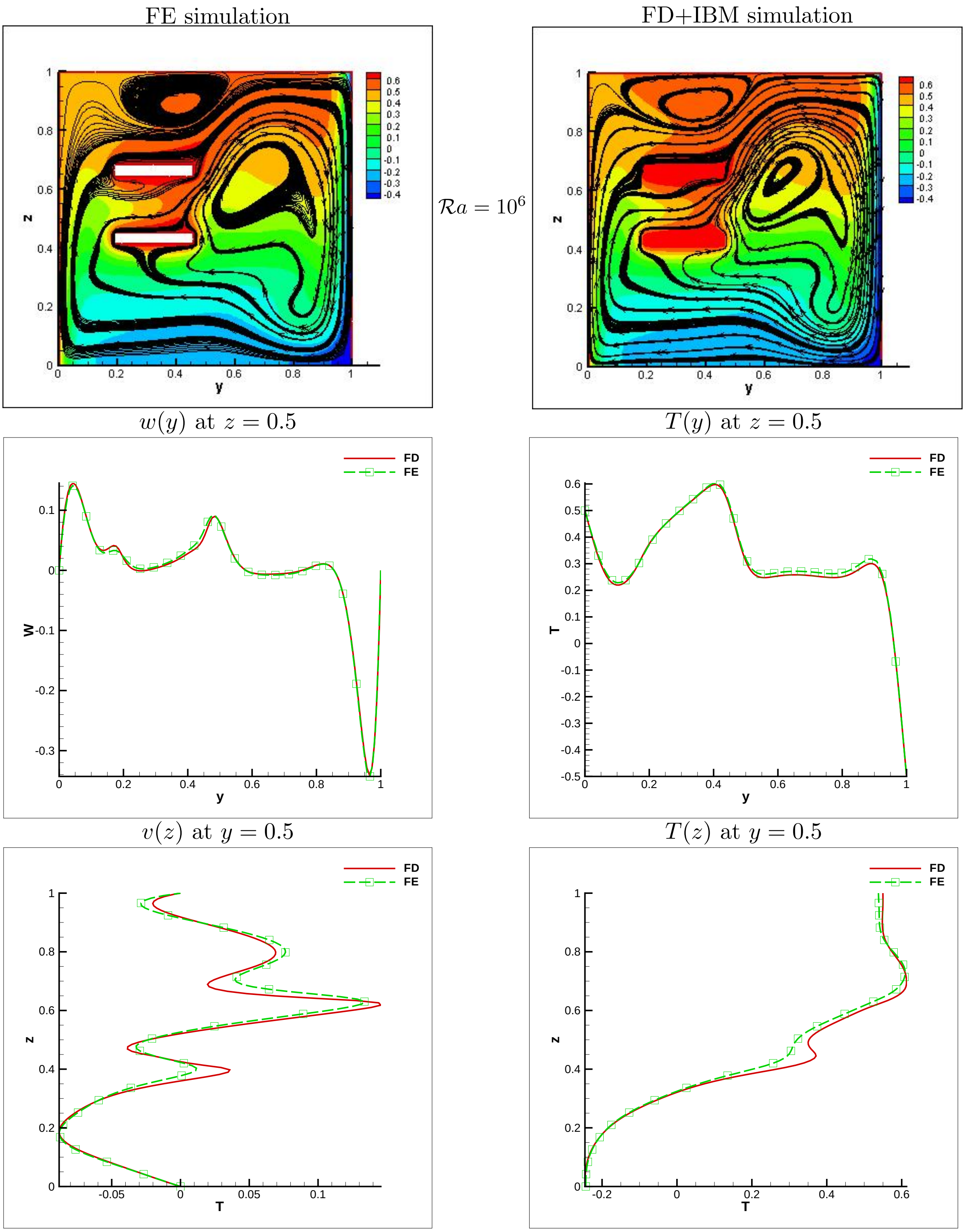

Figure 5.7.: $\mathcal{R}a = 10^6$. Differentially heated cavity case with two immersed heated objects. Streamlines and temperature fields. Profiles of velocity and temperature following centerlines of the cavity.

5.3.2. Square cavity with two immersed heated rectangular objects

A more complex case at a high $\mathcal{R}a = 10^6$ and thus a strong convective movement of the fluid, is presented in figure 5.7 for two immersed rectangular objects. A strong plume forms at top of the upper body, which also incorporates the plume formed on the lower body. The plume tilts to the right where more unoccupied space is available, towards the cold wall. Two recirculation cells can be noticed. One in the upper part of the cavity, considerably smaller in size, and one larger around the immersed objects.

A good agreement is obtained for the temperature field: the convection cells have the same shape, orientation and position. When extracting velocity and temperature profiles along centerlines (figure 5.7), we note a small displacement for the horizontal velocity and temperature lines, with a 2.0% maximal error.

5.3.3. Square cavity with an immersed heated circular cylinder

The representation of rectangular obstacles by the IBM method do not require interpolations, since the borders of the obstacles follow grid lines. To fully test the numerical system, further comparisons were made with respect to the results proposed by Kim et al. (2008). Inside a cubical cavity of width $L = 0.1$ an isothermal circular body ($R = 0.2L$) is placed. The walls of the cavity are also isothermal and have a temperature $T_c = 0$, while the temperature of the circular body is $T_h = 1$. The immersed obstacle is places in the middle of the domain. The Prandtl number considered is $\mathcal{P}r = 0.71$. For the velocity field, no-slip boundary conditions are imposed on the walls.

The flow for three different Rayleigh numbers is considered: $\mathcal{R}a = 10^6$, $\mathcal{R}a = 10^5$ and $\mathcal{R}a = 10^4$. Figure 5.8 shows a good agreement for the streamlines between the results of Kim et al. (2008) (first row) and the results obtained with our computational code (second row). In figure 5.9 the sae comparison is done for the isotherms of the flow.

At $\mathcal{R}a = 10^4$ the heat transfer in the cavity is dominated by conduction. The streamlines depict two rotating symmetric vortices with two inner recirculation cells. We can observe that the thermal boundary layer on the bottom of the cylinder is thinner than that on the upper side. The inner lower vortexes are slightly smaller in size and weaker in strength compared with the opposite ones.

With the increase of the Rayleigh number to 10^5, the role of convection in heat transfer becomes more significant. A plume forms on the top of the cylinder and defining a stronger thermal gradient in the upper section of the cavity and a lower gradient in the lower part. The dominant flow is present in the upper part of the enclosure and, the recirculation cells are located there as well. The two inner vortices merge and the flow at the bottom of the enclosure becomes weaker.

At $\mathcal{R}a = 10^6$, the heat transfer is governed by convection. A strong plume appears and separates as it reaches the top of the enclosure. The flow is dominant in the upper part of the cavity and two symmetrical recirculation cells form. Two small symmetric vortices appear on the bottom wall, caused by the separation of the boundary layer by the strong convective flow.

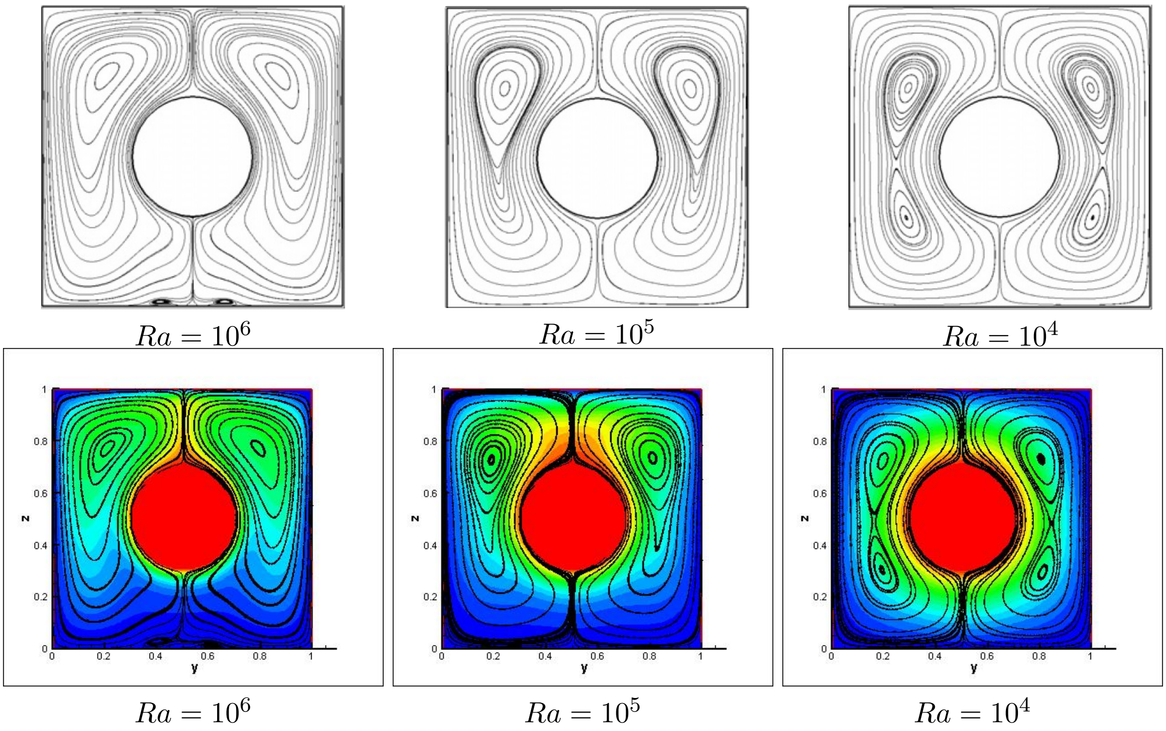

Figure 5.8.: Streamlines and temperature fields for a square cavity with an immersed heated circular cylinder. Results proposed by Kim et al. (2008) (first row). Present study results (second row).

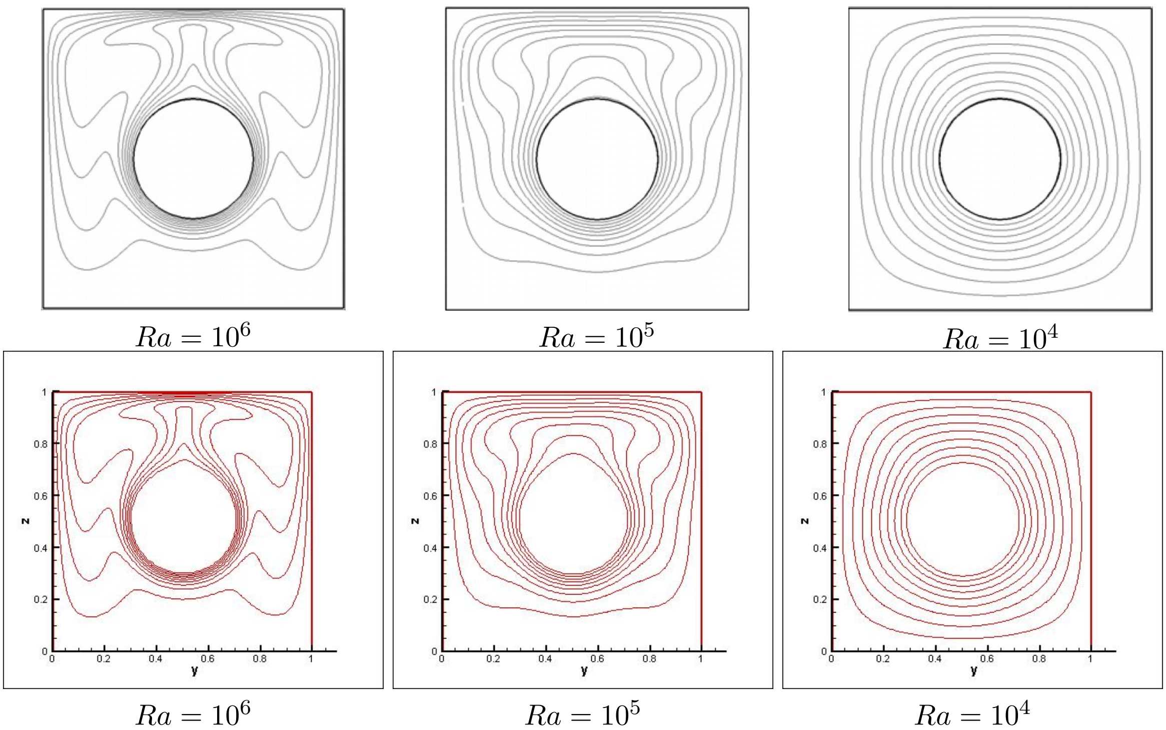

Figure 5.9.: Isotherms for a square cavity with an immersed heated circular cylinder. Results proposed by Kim et al. (2008) (first row). Present study results (second row).

After the velocity and temperature fields are obtained, the mean Nusselt number at the hot wall is computed. The calculated values for the test case are compared with the benchmark values in table 5.1.

	Mean Nu at hot wall	error %
$\mathcal{R}a = 10^4$	5.0914	0.3240
$\mathcal{R}a = 10^5$	7.7307	0.4673
$\mathcal{R}a = 10^6$	13.8972	1.5076

Table 5.1.: Square cavity with an immersed heated circular cylinder. Surface-averaged Nusselt number and relative error compared to results by Kim et al. (2008).

5.3.4. Square cavity with two immersed circular cylinders

A second test case is extracted from Park et al. (2012). It considers two isothermal cylinders inside an isothermal square cavity of length $L = 1$. The hot and cold cylinders of radius $R = 0.2L$ are located at $z = 0.25L$ and $z = 0.75L$, respectively, along the vertical centerline $y = 0.5L$. The walls of the square cavity are kept at a constant low temperature of $T_c = 0$, and the left hot and right cold cylinders within the enclosure were kept at constant high temperatures of $T_h = 1$ and $T_c = 0$, respectively.

Figure 5.10 shows the streamlines for three different Rayleigh numbers, form 10^4 to 10^6. The first rows represents the results obtained by Park et al. (2012), and the second row the present results. A good agreement is obtained.

In figure 5.11 the isotherms are shown, following the same order as for the streamlines.

For $\mathcal{R}a = 10^4$, the conduction is the dominant heat transfer mode and the effect of convection is weak. The flow is defined by two recirculation cells with two smaller inner vortices, positioned at the left and respectively right of the hot cylinder. The thermal boundary layer is thinner on the heated cylinder.

Increasing the Rayleigh to 10^5 a plume rising from the hot cylinder interacts with the cold cylinder and the enclosure. Convection is now dominant and plays an important role in the distributions of the fluid flow. The plume formed on the hot cylinder tilts to the right due to the greater surface area before reaching the right wall. As a consequence, the the sizes of the inner upper recirculation cells increases and they become stronger while the inner lower cells become weaker and smaller.

For $\mathcal{R}a = 10^6$, the strong plume rising from the hot cylinder shifts toward the upper right part of the enclosure. Consequently, the sizes of the inner upper recirculation cells increases and they become stronger while the inner lower cells become even weaker and smaller than for $Ra = 10^5$. The thermal gradient around the hot cylinder and top wall increases with the Rayleigh number while the gradient along the bottom wall decreases.

The variation of the local Nusselt number along the walls is presented in figure 5.12. A good agreement is obtained with respect to the result of Park et al. (2012).

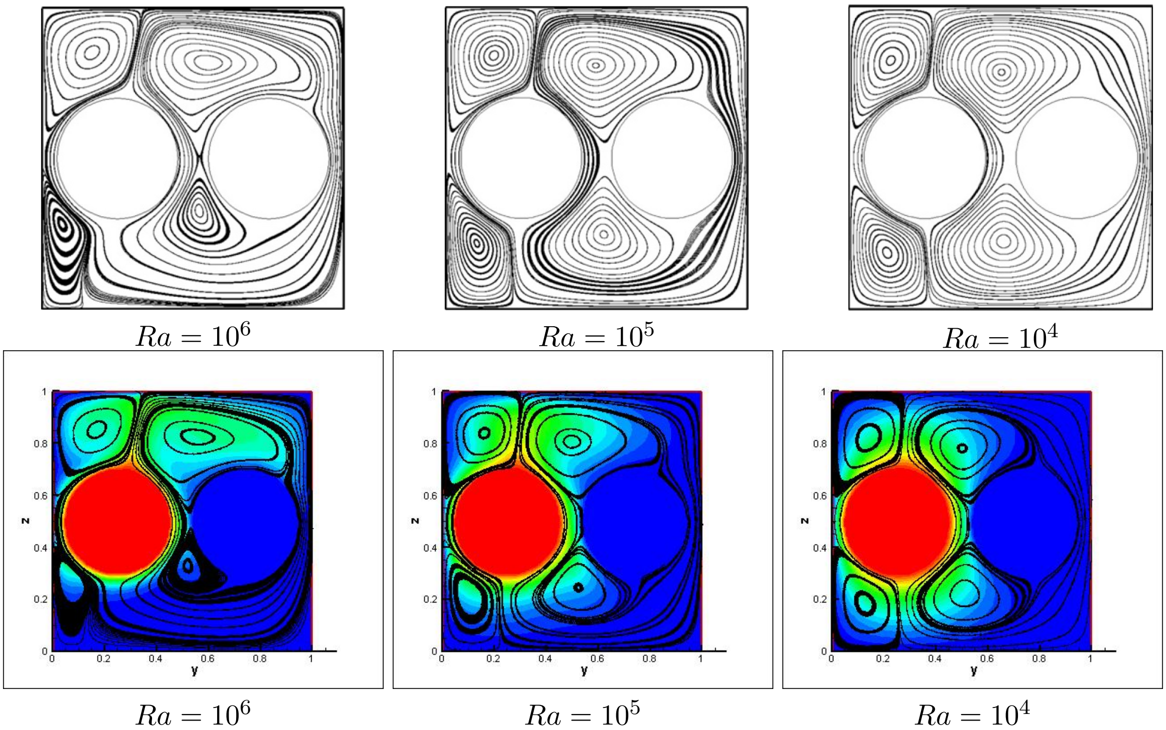

Figure 5.10.: Streamlines and temperature fields for a square cavity with two immersed circular cylinders. Results proposed by Park et al. (2012) (first row). Present study results (second row).

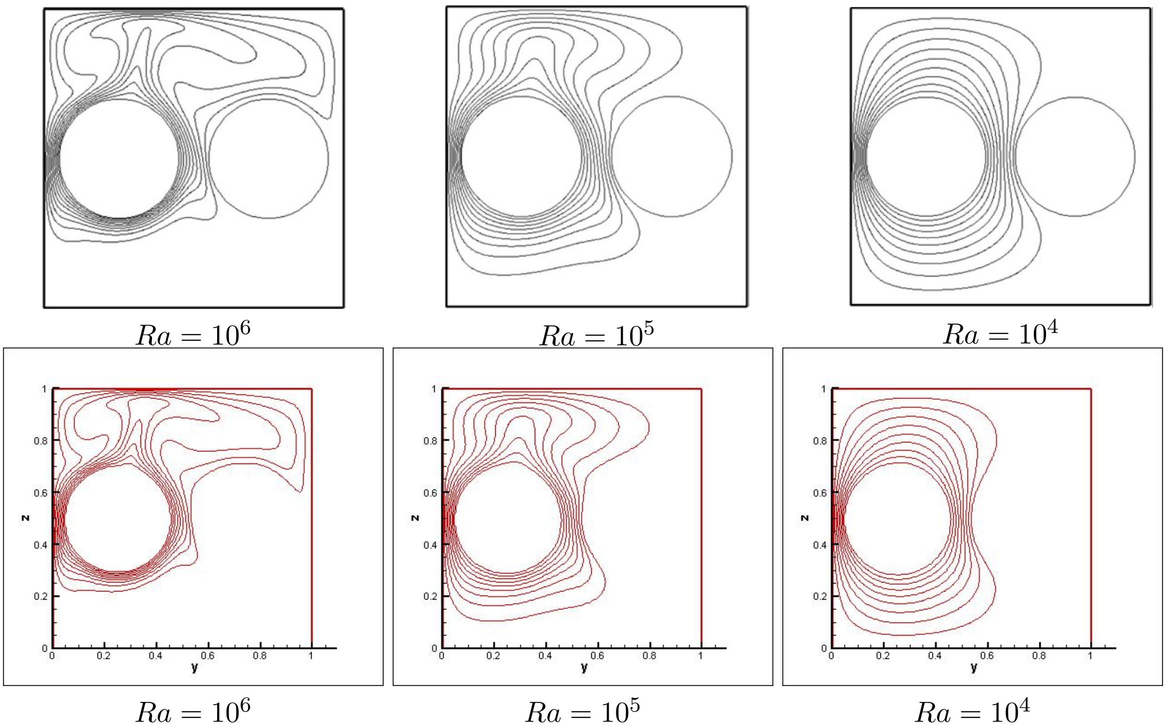

Figure 5.11.: Isotherms for a square cavity with two immersed circular cylinders. Results proposed by Park et al. (2012) (first row). Present study results (second row).

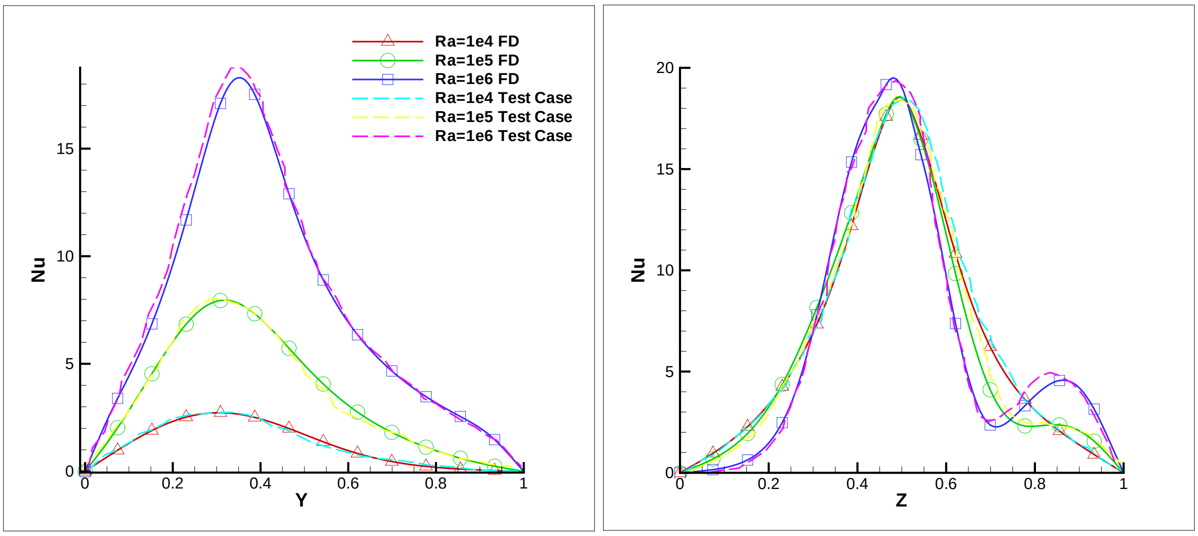

Nusselt number at $z = z_{max}$ Nusselt number at $y = y_0$

Figure 5.12.: Square cavity with two immersed circular cylinders. Distribution of local Nusselt number along two walls for different values of Rayleigh number. Comparison with Park et al. (2012).

5.4. Validation of the IBM method for 3D problems

The three-dimensional natural convection induced by a temperature difference between a cold outer cubic enclosure was also investigated. Simulations were run and compared to the results proposed by Yoon et al. (2010). They used a finite volume method with an IBM approach to model a sphere. Different Rayleigh numbers varying in the range of $10^4 - -10^6$ were considered. The study investigated the effect of the inner sphere location on the heat transfer and fluid flow. A schematic of the three-dimensional domain is presented in figure 5.13.

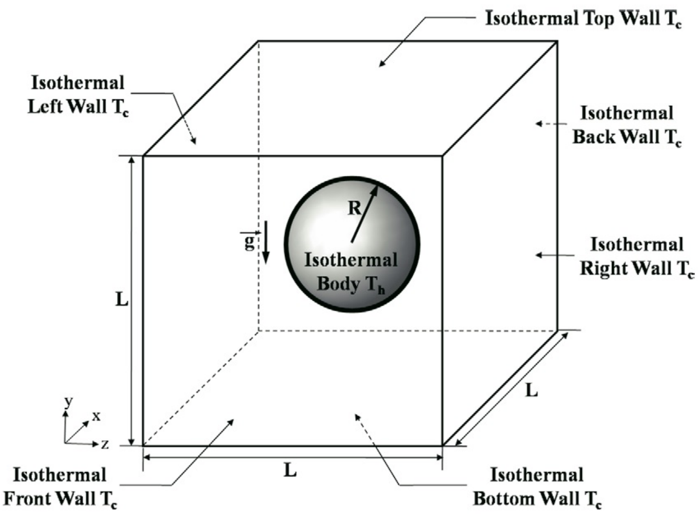

Figure 5.13.: Computational domain and boundary conditions for a 3D convection problem with a spherical obstacle.

No-slip boundary conditions are imposed on the walls for the velocity field. The walls are isothermal, of temperature $T = 0$, while the inner sphere temperature is $T = 1$. The flow and thermal fields converge towards a steady state for all Rayleigh numbers.

Figure 5.14 presents the isotherms and streamlines obtained by Yoon et al. (2010) for Rayleigh numbers varying from 10^4 to 10^6.

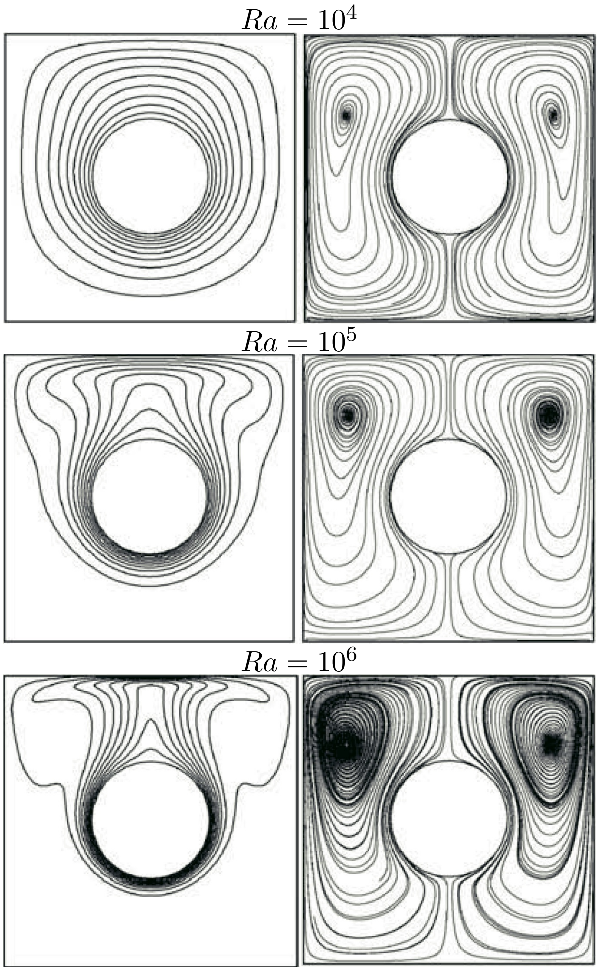

Figure 5.14.: 3D convection problem with a spherical obstacle. Isotherms and streamlines for three different Ra numbers. Results of Yoon et al. (2010).

Figure 5.15 shows the same maps obtained with our numerical code. For $\mathcal{R}a = 10^4$, the effect of convection on heat transfer is low forming a weak upward thermal plume on the top of the sphere. The thermal boundary layer on the bottom part of sphere is thinner than that on the upper side. The circulation in the upper part of the enclosure is more active, resulting in the formation of one inner recirculation cell.

For $Ra = 10^5$ convection is predominant with respect to conduction, as shown in figure 5.15. A plume forms on top of the inner sphere which gives rise to stronger thermal gradient on the top of the enclosure. The dominant flow is in the upper half of the enclosure, and correspondingly the center of the recirculating cell is located in the upper half.

For $\mathcal{R}a = 10^6$, the isotherms are distorted due to the stronger convection effects thus having a stable stratification of isotherms. The convection velocity increases with increasing Rayleigh number, the boundary layer behaviour can be seen in the lower part regions of the sphere and the upper part of the enclosure. The plume arising form the sphere separates as it reaches the top wall. The centres of the inner recirculation cells move toward the upper corners.

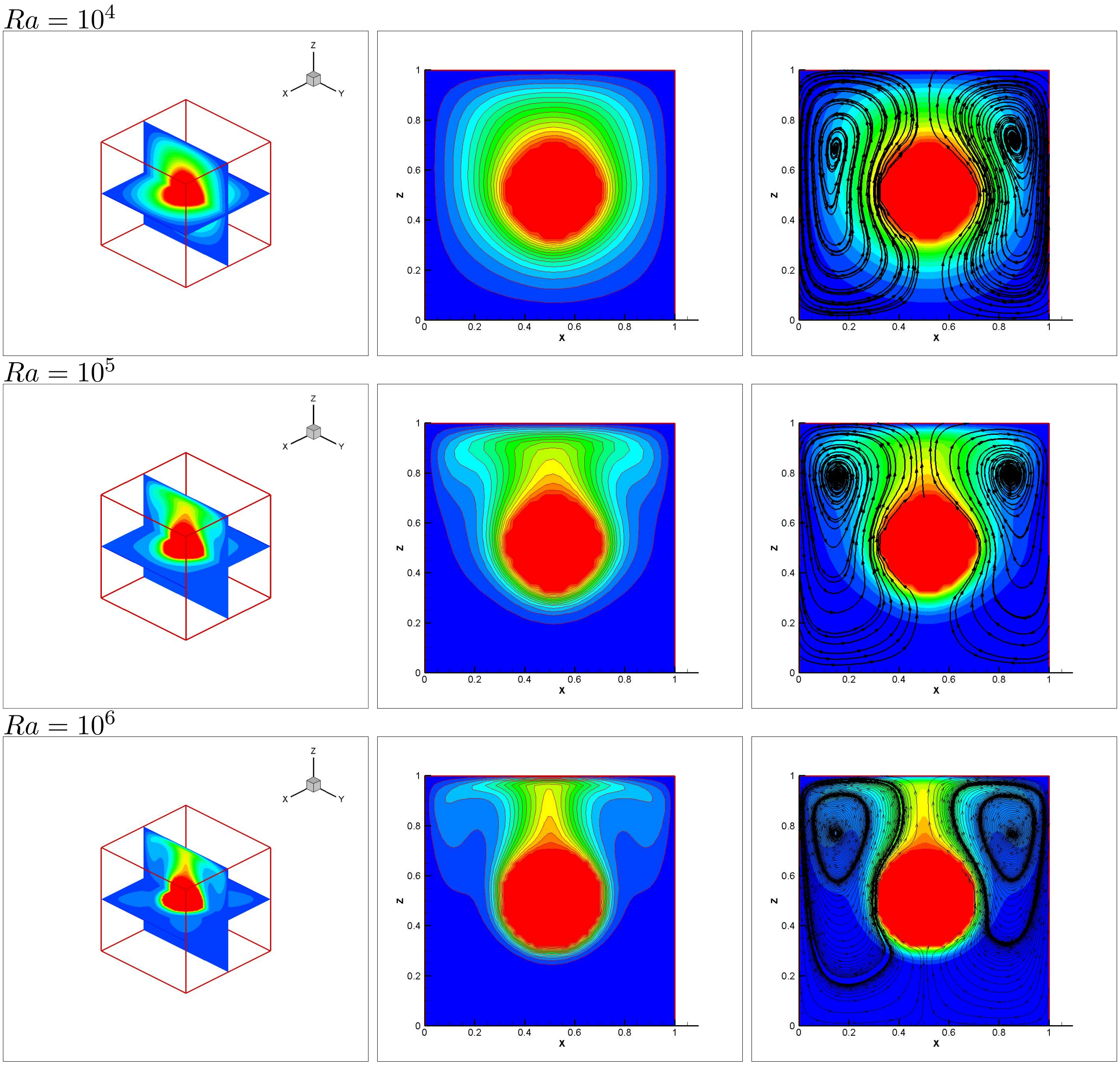

Figure 5.15.: 3D convection problem with a spherical obstacle. Present study. Isotherms and streamlines for different Rayleigh numbers.

We can conclude that the results obtained with our FD+IBM method for the 3D case are in good agreement with the test case considered, rendering possible the simulation of 3D configurations with obstacles of general geometries.

6. Experiments and configurations of outdoor cabinets

The sixth chapter of the thesis is a detailed description of the experimental approach for an outdoor telecommunication cabinet. A simplified geometry of the cabinet was taken into consideration and temperature measurement were made inside as well as outside. The cabinet was placed inside an thermal chamber, that allowed a good general control over the temperature and environmental air velocity. Several configurations were taken into account and temperature profiles were obtained. The objective of this part was to create a reference solution for comparison with the simulation code results.

Inside the cabinet we placed two metal boxes, and each of them contained several resistances powered by an electrical supply. These boxes were meant to simulate the electrical client cards which appear in the configurations of real telecommunication cabinets. Temperature were measured using type K thermocouples.

The first sub-chapter presents the experimental set-up and the instruments used. This is followed by a second sub-chapter containing a descriptions of the data gathered for different configurations and another one with preliminary result for the comparison between the experiments and the numerical simulations considered.

The main goal was the validation of the numerical code proposed. Such a tool proves to be very useful for a preconception design of cabinets. Generally the experimental set-up necessitates a great amount of time and material until an optimal configuration can be found, all of with can be greatly simplified by the use of a numerical software.

6.1. Introduction

Due to the rapid technology development a continuous increase of system power has emerged as well as a shrinkage of size. This has led inevitably to a thermal management challenge of electronics as to maintain the desirable operating temperature. Various methods of cooling have been proposed from experimental work on analysing different cooling techniques, numerical simulations, natural convection to advanced cooling. The component needed for the telecommunication cabinets are vulnerable to dust and humidity. This creates the necessity for the outdoor cabinets to be tightly sealed. Thus the ambient air cannot serve as a mean of cooling this equipments and hybrid coolers which combine several cooling solutions are researched.

The challenge of maintain the temperature between certain limits also includes maintaining the electronic equipments at low temperature values despite the high heat density, evacuating the heat flux in low power consuming manner and the global thermal management of the telecommunication outdoor cabinets. The main constraint for thermal management is cost, thus the technologies employed for cooling must be cost effective. This is why passive solutions are desired, or solutions that employ a minimal amount of energy and management. Additional important constraints are: simplicity, cost of maintenance and energy consumption.

Thermal management can be separated into two categories: active cooling techniques(which are mechanically assisted) and passive cooling techniques. Active methods offer high cooling capacity and a good control over the temperature domain but are not always cost effective and need periodical maintenance. Lately these methods have begun to relay less on cooling fans and more on systems as air/liquid, forced liquid convection, spray cooling thermoelectric coolers, refrigeration systems etc.. The passive cooling techniques on the other hand employ heat spreaders, heat sinks, phase change materials and so on. It is more cost effective but has achievement limitation.

Solutions are envisioned that employ both methods in an effective manner.

Depending on the element employed for cooling another classification has been made, that separates these methods as: air cooling, liquid cooling, heat pipes , refrigeration cooling, thermoelectric cooling, and phase change materials cooling. As an approach method either one of these techniques can be user or a combination of two or more at the same time.

The air cooling method is the simplest and most widely used, it's advantage being the ready availability and ease of application. The most common are based on the use of fans. Natural convection and radiation is mostly used for computer cooling of circuit boards and does not have the sufficient capacity for cooling large telecommunication cabinets. A few examples where such a method was used are presented by Cengel (2003), Florio and Harnoy (2007),Tso et al. (2004),Bhowmik and Tou (2005),Hamady et al. (1994),Tou and Zang (2003),Tso et al. (2004),Jin et al. (2005), Le Masson et al. (2012).

For the cases where natural convection is not enough, forced convection is implemented, such as fans, pumps, jet of air and so on. Examples of such solutions are proposed and detailed by:Yoo et al. (2000) ,Burmann et al. (2002), Acikalin et al. (2004).

Liquid cooling is more effective for high power electronic collections. Heat pipes are passive two phase devices that transfer large quantities of heat with a minimal temperature drop. Tuckerman and Pease (1981) first introduced the concept of micro-channel heat sink. Other studies such as Choi et al. (2007), Qu and Mudawar (2002), Gillot et al. (2000), Peng (1996), Samba et al. (2013) further developed the analysis of liquid cooling heat exchangers.

An example is the vapour compression, Schmidt and Shaukatullah (2003) proposed a review of the literature analysing, numerically and/or experimentally, various aspects of cooling schemes, energy saving schemes, and other related areas. Other studies were made as for: natural circulation systems such as solar water heater Zvirin et al. (1997), nuclear power plants Dimmick et al. (2002), gas-cooled fast reactors Malo et al. (2006), integral type reactors Chung et al. (2006), hybrid coolers combining vapour compression and natural circulation cycles Lee et al. (2009). Study such as those by Cinato et al. (1998) McGlen et al. (2004) focused on the performance of telecommunication equipments subjected to hot ambiental conditions and the improvement in performance of hybrid cooler systems.

Phase change material based cooling require massive equipment, the material have high latent heat of melting. PCM energy storage is based on the absorbed or released heat, the material changes the phase usually between solid and liquid states. It can reduce the size of cooling system and is fairly economic depending on the material used. This is usually used to absorb peak heat loads during the time when the system is most used and dissipates the heat when the temperature lowers. A few reference articles that take into consideration phase change materials are: Pal and Joshi (2000), O'Conner and Weber (1997), Zheng and Wirtz (2004), Lamberg and Siren (2003), Benard et al. (1986), Azzouz et al. (2008).

Other studies for the optimization of fanned heat sinks were conducted by Noda et al. (2005), Lin and Chou (2004). When the heat flux is to great or insufficient space is available at the heat source to mount a fanned heat sink, liquid cooling comes into play. Examples of studies for liquid based cooling schemes are Eason et al. (2005), Prasher and Mahajan (2005),Valenzuela et al. (2005), Walsh and Grimes (2007).

The heat sink is generally larger that the heat source and has a spreader, usually placed between the source and the sink, to uniformly distribute the heat flux. Zhang et al. (2008) proposes an two-phase thermosyphon spreader. Some examples of studies on cooling systems using heat pipes, are: McCreery (1994),Vafai and Wang (1992),Koito et al. (2006) and for mini/micro heat pipes we note Groll et al. (1998), Vasiliev (2005).

Pulsating Heat Pipes have been considered in studies such as Yang et al. (2009), Charoensawan et al. (2003), Lin (2001), Tong et al. (2003), Zhang and Faghri (2002), Cai et al. (2006), Khandekar and Groll (2004), Xu et al. (2005), Khandekar et al. (2003). They represent passive heat transfer devices consisting of meandering continuous flow passages in which a two-phase mixture of a working fluid exists. They are usually used for cooling applications of of power/microelectronic components.

Heat transfer enhancement techniques in combination with phase change material have also been considered. They include partitions/fins, graphite/metal matrices, dispersed high-conductivity particles in the PCM, and micro-encapsulation of PCM. A number of articles can be cited on this subject such as Velraj et al. (1999), Zalba et al. (2004), and Pal and Joshi (2000) for PCM-based heat sinks. Other studies using PCM were proposed by Tan and Tso (2004), Pal and Joshi (2000),Zheng and Wirtz (2004),Lamberg and Siren (2003) end so on.

Based on the above mentioned papers and so many other that exist in literature it is clear that the main focuses of research in cooling techniques are based on high performance heat pipe, thermoelectric coolers, low acoustical novel micro-fans for air cooling, and phase change materials. The goal is to obtain a low cost-high efficient system capable of keeping up with the technological advances.

6.2. Experimental set-up presentation

As mentioned before, a real configuration of an outdoor cabinet is very complex, from a geometrical point of view. The outside conditions also present a challenge in modelling of the thermal transfer within the cabinet and outside. The goal was to reduce and control the parameters of the experiments in order to have a better grasp of the problem. Two examples of completely equipped cabinets are shown in figure 6.1.

The first step considered was to simplify the geometry to a basic configuration. Thus striping down the cabinet to it's simplest form, we introduced two heated object inside. Each of them is powered individually. As figure 6.2 shows, the boxes are sported by two steel bars each and fixed in place using stainless steel nuts. The red wires, in figure 6.2 are connected to the power supply while the green ones are thermocouples placed inside the boxes.

The isometric view and three side views sections, providing the exact dimensions of the cabinet, are presented in 6.3. The wires, bars and bolts, sporting the boxes, are not represented. This scheme depicts the simplest configuration possible.

Figure 6.1.: Outdoor telecommunication cabinet

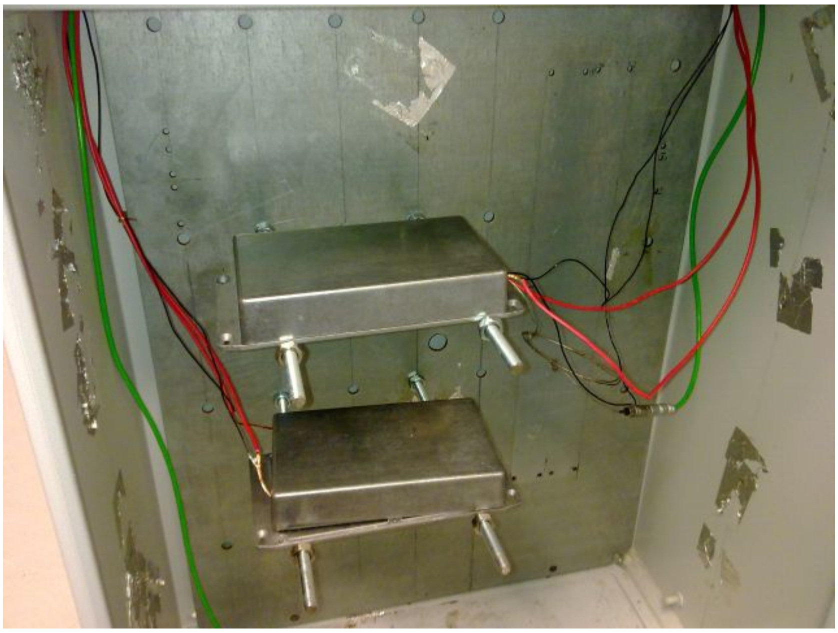

Figure 6.2.: Simplified cabinet

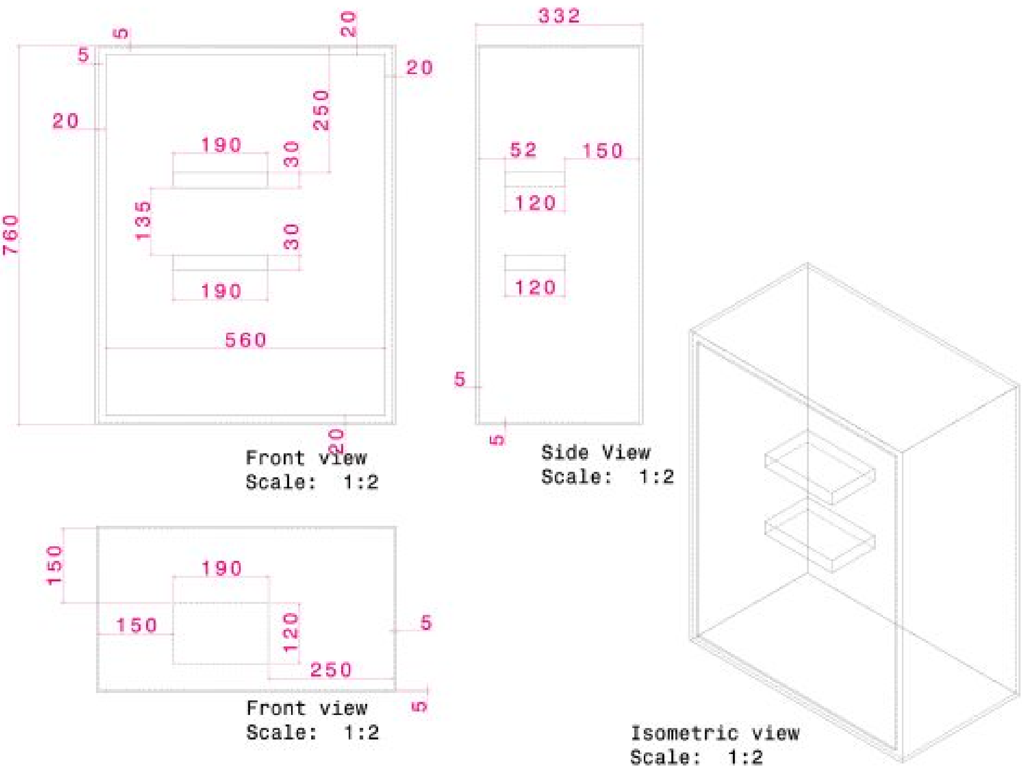

Figure 6.3.: Scheme of the cabinet

Inside the boxes fourteen resistances are placed and fixed on a metal grid. Figure 6.4 a) shows the bottom part of the box with the metal grid, and a resistance. Each resistance is fixed with bolts on the metal grid, after this the resistances are configured in a series circuit (6.4 b)) and the ensemble is placed in the box. Each box has a 3 mm hole, through witch the power supply cable and the thermocouple are inserted. The box is bolted shut and places within the cabinet.

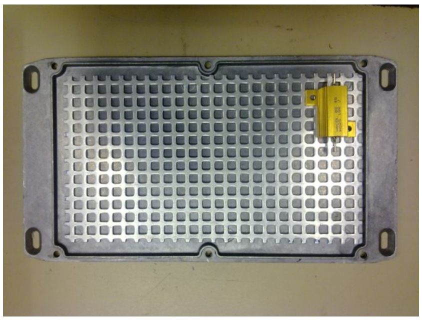

a)

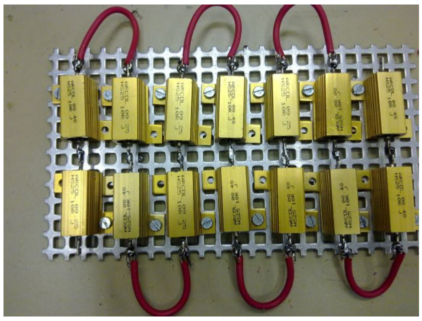

b)

Figure 6.4.: Resistances placed inside the box

A schematic of the interior circuit is presented in figure 6.5. Each resistance has 10Ω thus rendering a global resistance of 140Ω.

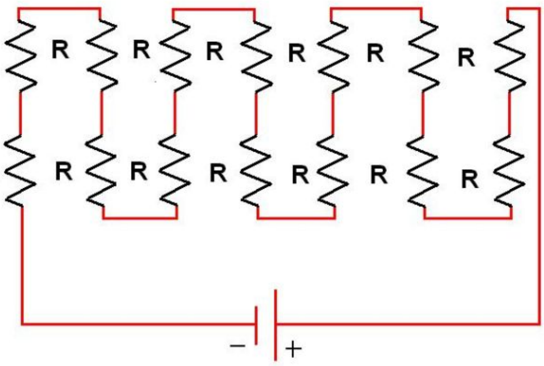

Figure 6.5.: Electric circuit scheme

The data is measured and recorded with Data Logger. They are instruments of acquisition and logging used to record and measure a wide variety of quantities. The graphical interface allows quick and easy basic measurements. The data can be extracted with a memory stick or downloaded using a web interface into files ready for import. Temperature, current and voltage were recorded with the help of this tool.

The temperatures were measured with type K thermocouples. They are the most common general purpose thermocouples with a sensitivity of approximately $41\mu V/\,°C$, cromel positive relative to alumel. The have a wide variety of probes in a range of $-200\,°C$ to $125\,°C$ and the wire diameter is $\phi = 75\mu m$

Before being included in the experimental set-up, the thermocouples accuracy was calibrated and a correction coefficient was obtained. We have had a total of 42 thermocouples placed as: 16 on the outdoor cabinets surfaces; 19 measuring the air temperature above, between and under the heated obstacles; 5 on the outside surfaces of the cabinet and 2 inside the object.

The placement of these thermocouples is shown in figure 6.6. With green (left figure) we have marked the thermocouples measuring the air temperature, and with red (right figure) the ones placed on the surfaces of the heated objects.

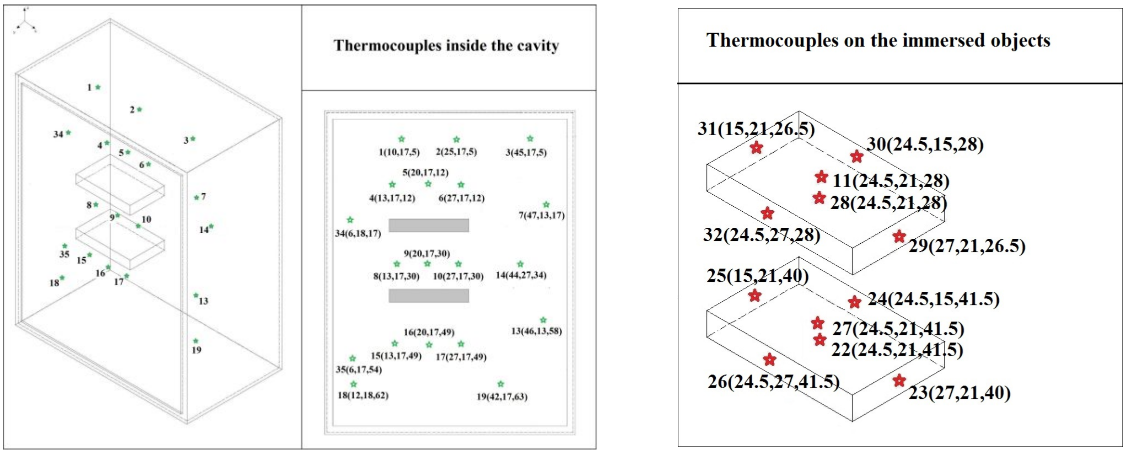

Figure 6.6.: Thermocouple placement

The cabinet is placed within a controlled environment, respectively a climatic test chamber. The Servathin climatic test chambers ensures a controlled climate with temperature ranges between $-50\,°C$ and $+80\,°C$. They are specially designed for thermal test, and have conditioning on the ceiling. The user interface provides local operator control and monitoring of the system. An embedded exterior panel permits the accurate control of temperature and temperature cycles. Our tests were performed for chamber temperatures of $20\,°C$ and $30\,°C$.

6.3. Measurements

For the measurements we have chosen to present three complementary cases. First only the upper box is heated, in a second case both are and last only the lower one is heated. We show the graphics of temperature variation for a few chosen thermocouples, respectively six that can be found above, between and below the head objects and two that are places directly on the surface of each box. As mentioned in the set-up section, the measurements were made using type K thermocouples.

Bases on the placement of the thermocouples 6.6, the air velocity and exterior conditions, the temperature values vary accordingly.

A. Case study 1: upper cavity heated.

For the case were only the upper body is heated measurement are made for two constant exterior temperatures, $20\,°C$ and $30\,°C$ respectively. Both cases are plotted on the same graphic as to denote the impact of different exterior values on the interior. In figure 6.7 temperature values of thermocouples no. 1, 3, 4 and 6 are presented. The green line represent the plateau at $20\,°C$ and the purple line the one at $30\,°C$. The red curve is the temperature variation inside the cabinet at an exterior temperature of $30\,°C$, and the blue curve for $20\,°C$ respectively.

A thermal plume forms on top of the heated object. As thermocouples no. 4 and 6 are right above it, the measured temperature is higher, compared to the one registered for thermocouples no. 1 and 3. Going higher inside the cavity, due to fluid movement and lower temperature of the boundaries, the temperature decreases. The supplied power variations between $1.8W$ and $29W$ can be seen in the four levels that appear for temperature. The 10 °C difference between the two cases considered (exterior temperature of 20 °C and 30 °C respectively) can be noted in the spacing between each set of curves, and is constant for all thermocouples.

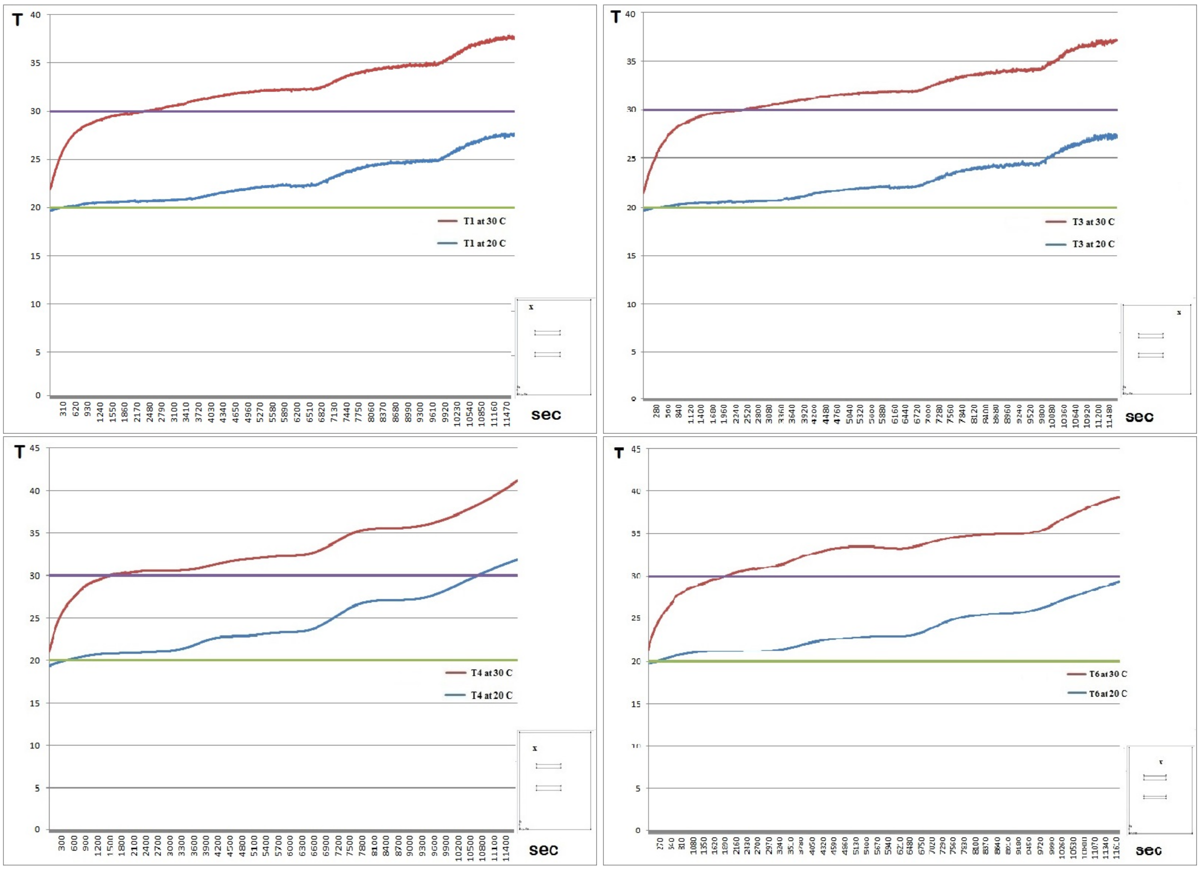

Figure 6.7.: Thermocouples 1, 3, 4 and 6

As the lower cavity is not heated, the temperature underneath it are lower. This can be seen in figure 6.8. The values slightly depasses the ambient temperature, and as we go further from the heated object, thermocouples 15 and 17, we can see that the difference, between the inside and outside temperature is even smaller.

For thermocouples placed on the surfaces of each immersed object, no. 11 and 22 respectively(figure 6.9), we can notice the fable increase in temperature for the lower cavity a) and the rapid one for the heated one b) respectively. For the object that is not heated the surface temperature has values in the vicinity of the exterior temperature. While for the heated object the temperature increases greatly.

The power varies between 1.8 W and 29 W in four plateaus. When the power is increased the temperature starts to augment until it reaches an equilibrium plateau value and starts rising again when the power is increased. This variations are stronger for the temperatures measured on the surfaces of the heated objects or in there vicinity.

B. Case study: both immersed objects heated.

For the case when both bodies are heated, we conducted two experiments at the same exterior temperature of 30 °C. We consider three power plateaus(1.8W, 7.5W, and 16.5W)

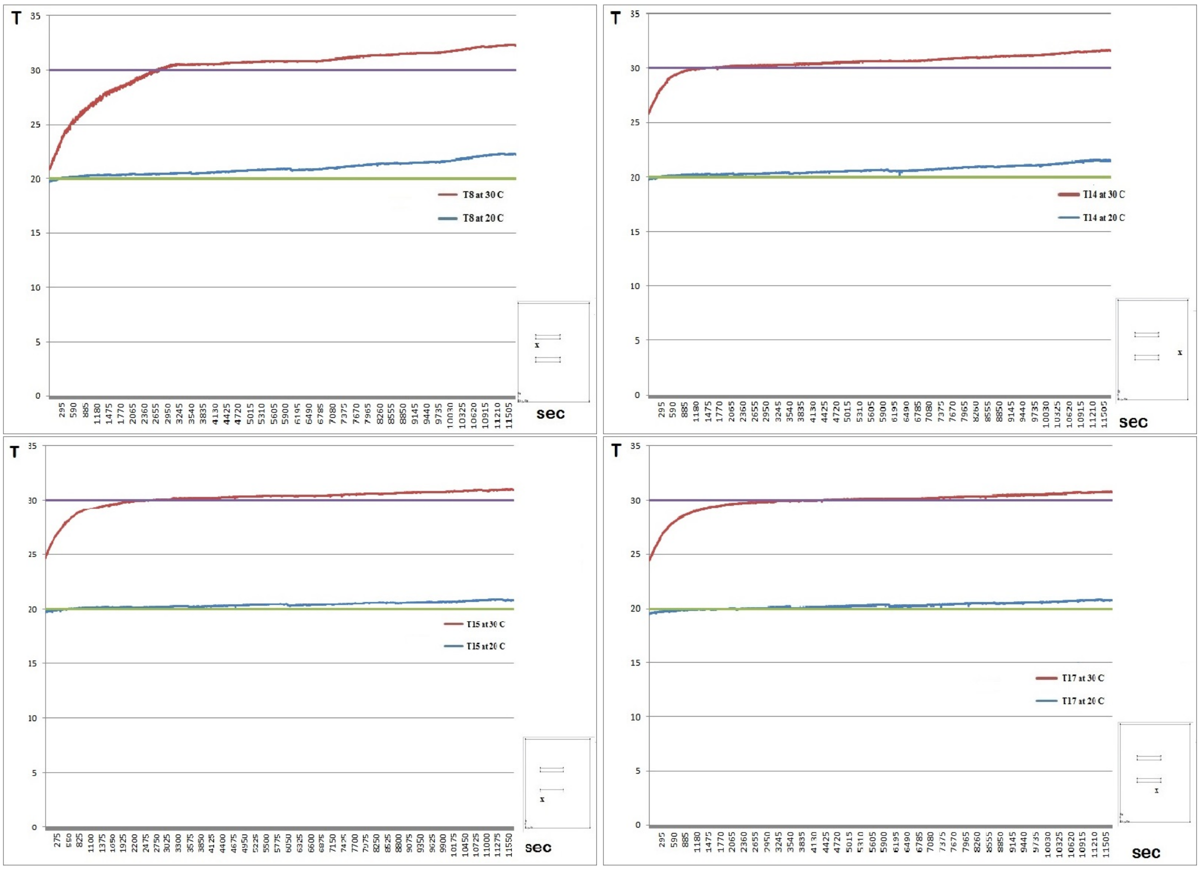

Figure 6.8.: Thermocouples 8, 14, 15 and 17

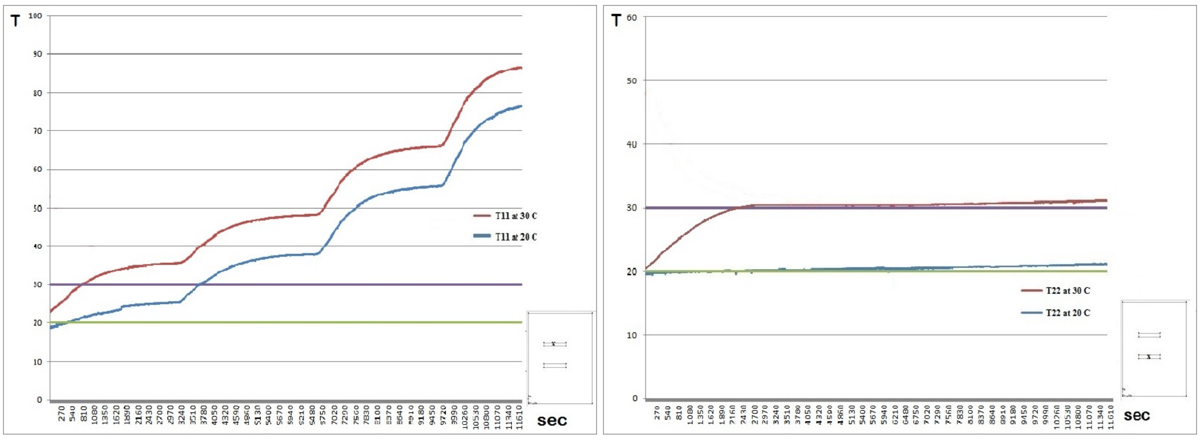

a) b)

Figure 6.9.: Thermocouples on the surfaces 11 and 22

which are visible from the temperature variations of each thermocouple. Both immersed object are heated at the same temperature. We took into account the same thermocouples as for the case presented above. Figure 6.10 shows the variations in temperature for thermocouples 1, 3, 4 and 6. They are placed above the higher body incorporating a part of the heat flux produced by the lower body and a part of the one from the upper box, thus increasing in temperature. The maximum temperature values are higher than for the first case.

For thermocouples no. 1 and 3 the measured values are within the same values as for thermocouples no. 4 and 6.

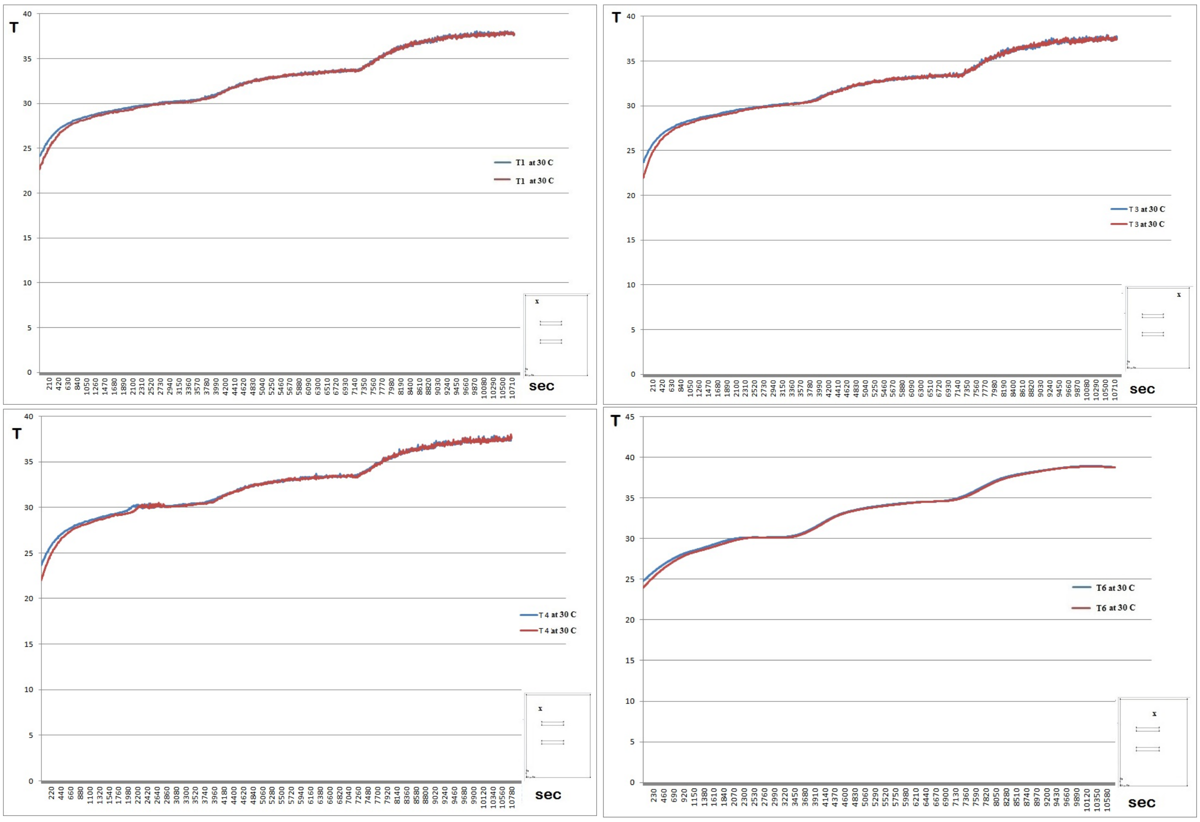

Figure 6.10.: Thermocouples 1, 3, 4 and 6

Figure 6.11 presents thermocouples no. 8, 14, 15 and 17. For this particular case the addition of a second heated obstacle induces a rise in temperature of 10 °C. The comparison between two different experimental cases under the same parameters also ensures the validity of the measurement. We found in each case the same the same variations, as expected.

The temperature variations measured by the thermocouples placed on the surfaces of the cavities, respectively no. 11 and 22 is shown in 6.12. Thermocouple 11 placed on the upper body shows a slightly higher temperature then thermocouple 22, which can be found on the lower body. The thermal plume formed on the lower object merges with the one formed on the upper one.

C.Case study 3: the lower cavity being heated.

For the case were only the bottom body is heated measurement were made for two constant exterior temperatures, 20 °C and 30 °C respectively. The green line depicts the 20 °C temperature limit while the purple line the 30 °C constant value. The red curve represent the measurement done, within the cabinet, for an exterior temperature of 20 °C and the blue curve

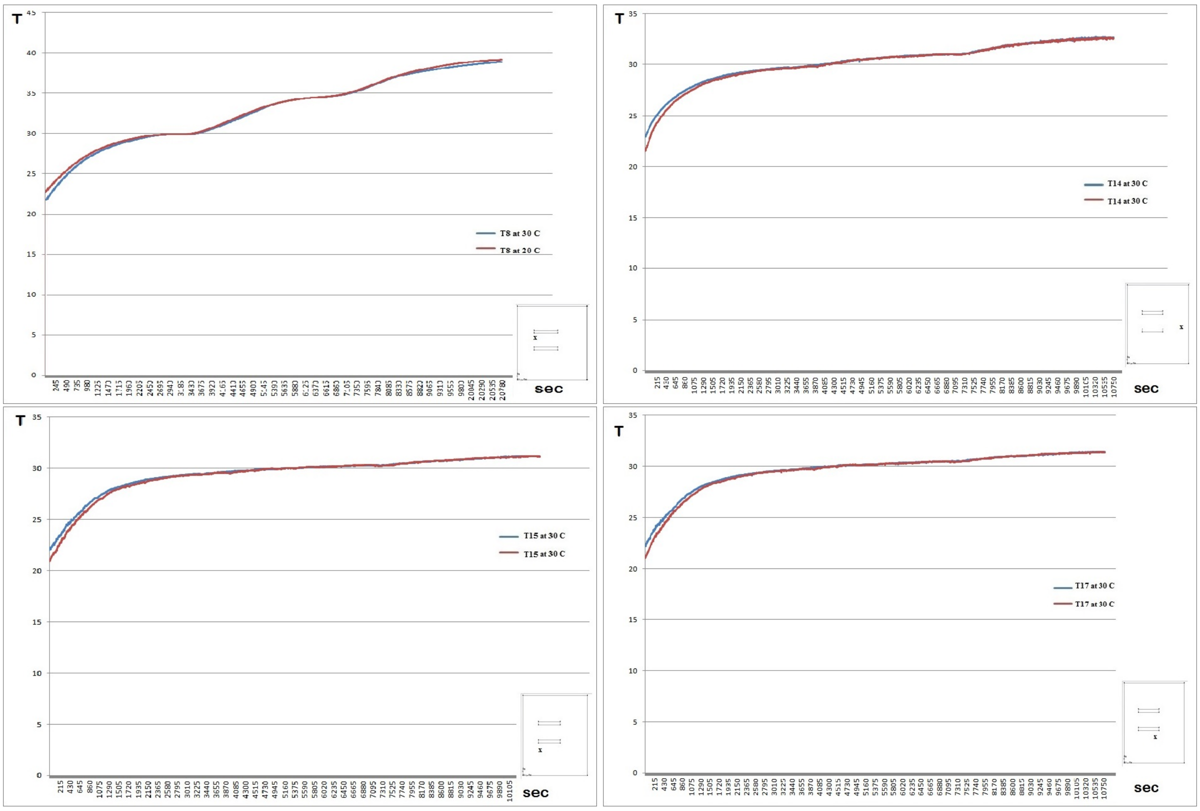

Figure 6.11.: Thermocouples 8, 14, 15 and 17

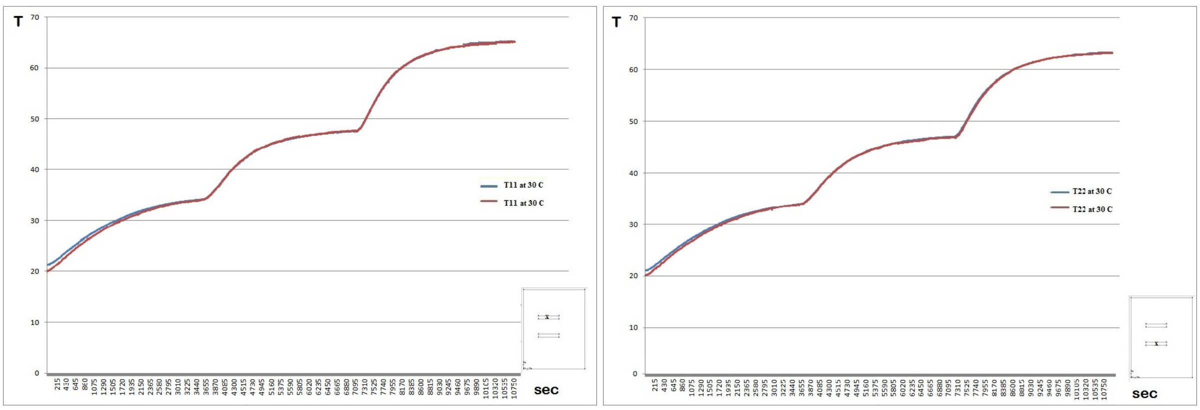

Figure 6.12.: Thermocouples on the surfaces 11 and 22

for 30 °C respectively. In figure 6.13 we can observe the temperature variation for thermocouples no. 1, 3, 4 and 6. We notice all these thermocouples are places above the upper obstacle, which is not heated. This explains the slow augmentation in temperature, the body acts as an obstacle in front of the heat wave generated by the lower body.

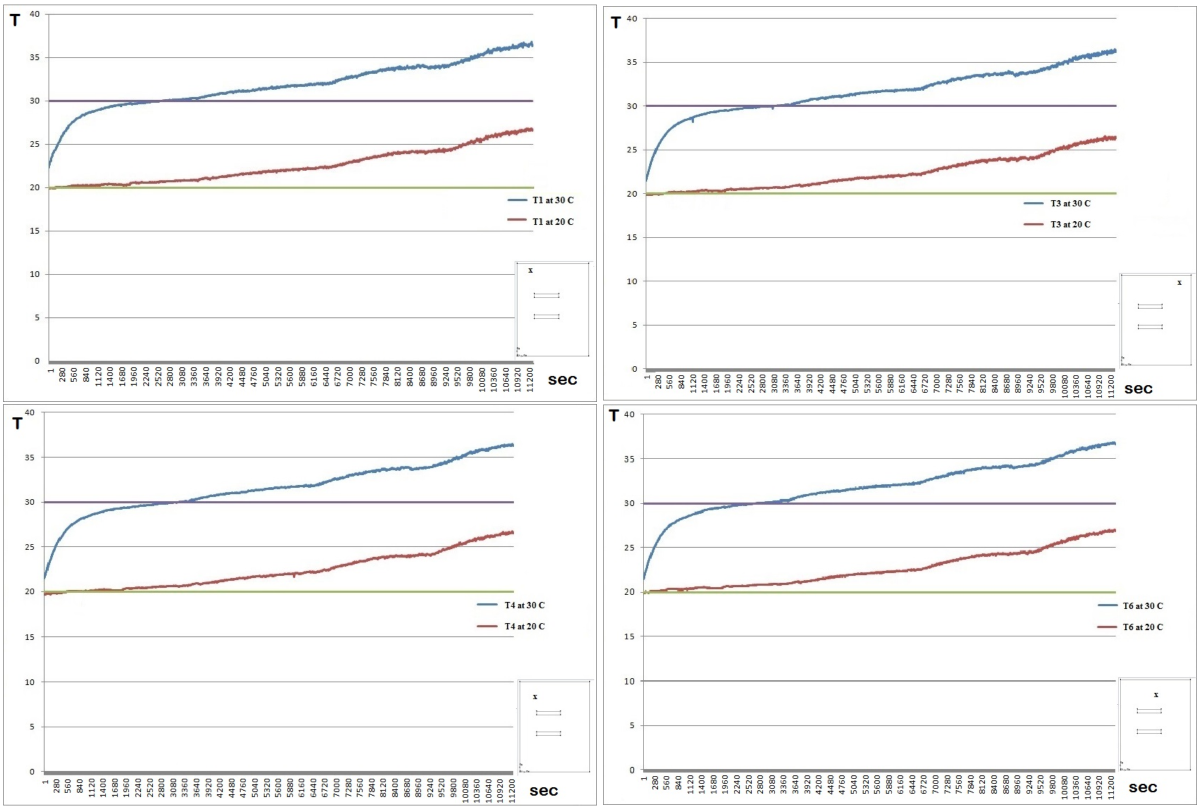

Figure 6.13.: Thermocouples 1, 3, 4 and 6

Figure 6.14 shows the behaviour of thermocouples no. 8, 14, 15 and 17. Thermocouple 8 is above the heated object, the temperature difference puts in motion the velocity field thus rendering instationary aspect of the values. Thermocouple 14 is on the left of the heated object and has a relatively slower evolution in temperature. We can see that thermocouple no. 8 registers values almost 10 °C higher that no. 14. Thermocouples 15 and 17 are under the heated object and measure lower temperatures.

Temperature variations measured by thermocouples no. 11 and 22 are shown in figure 6.15. Thermocouple 11 is placed on the surface of the of the upper body, which is not heated, this can be seen from the mild temperature variation. Thermocouple 22 is found on the surface of the lower cavity, the variations follow the power augmentation plateaus. The heated body reaches temperatures twice as high as the non-heated counterpart.

It is clear that with the augmentation of the exterior temperature an equal temperature increase appears inside the cabinet. The difference between the 20 °C exterior temperature and the 30 °C is constant with the power increase for all thermocouples.

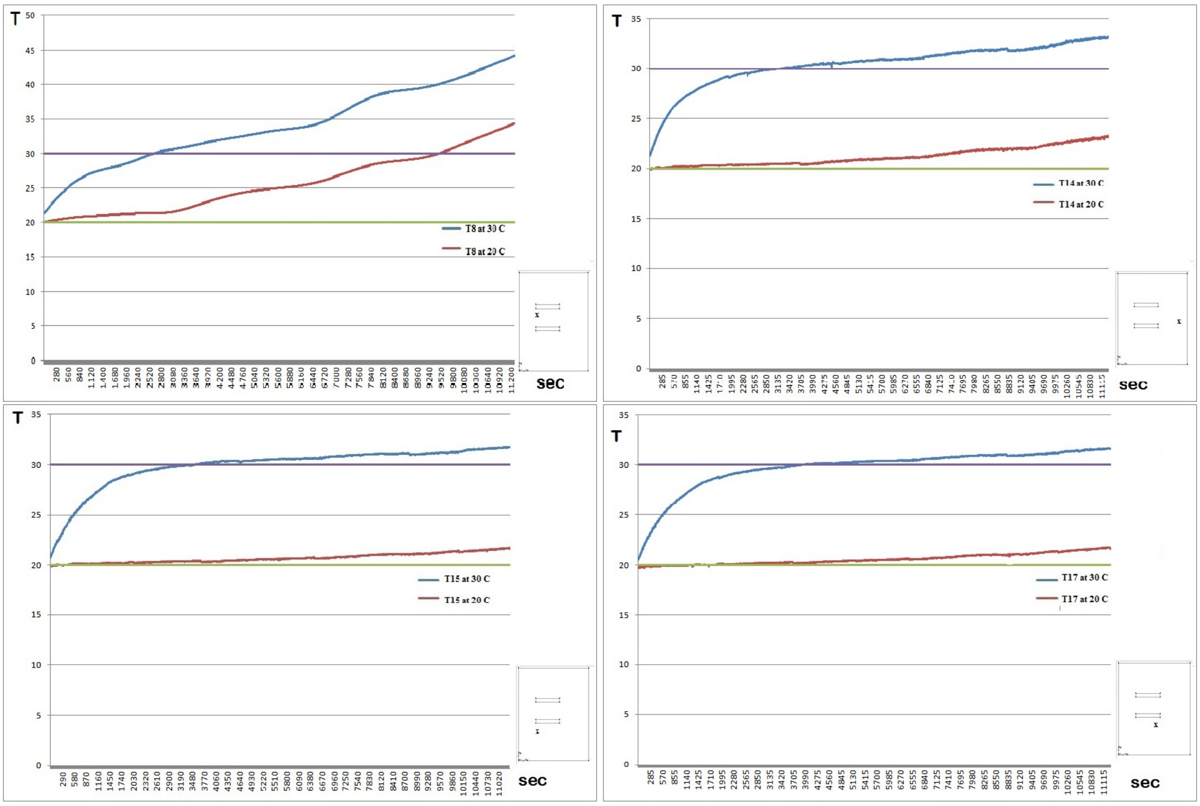

Figure 6.14.: Thermocouples 8, 14, 15 and 17

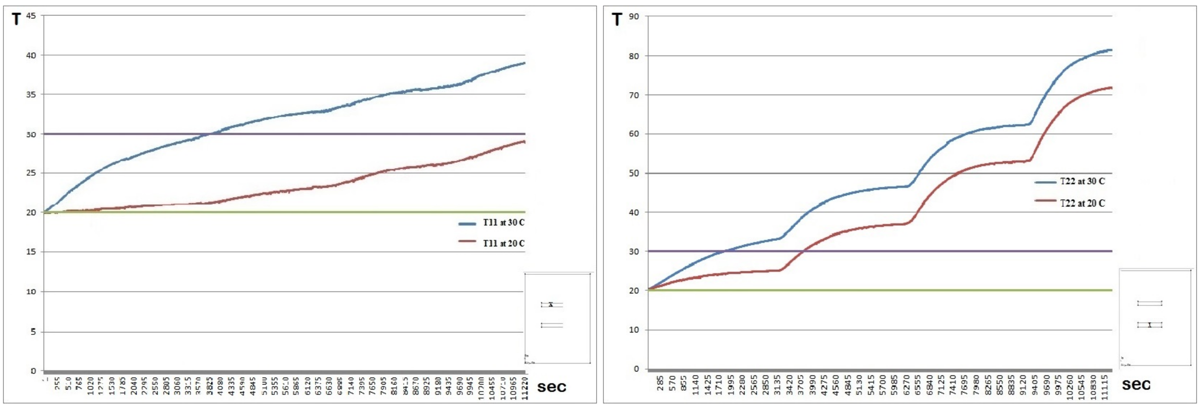

Figure 6.15.: Thermocouples on the surfaces 11 and 22

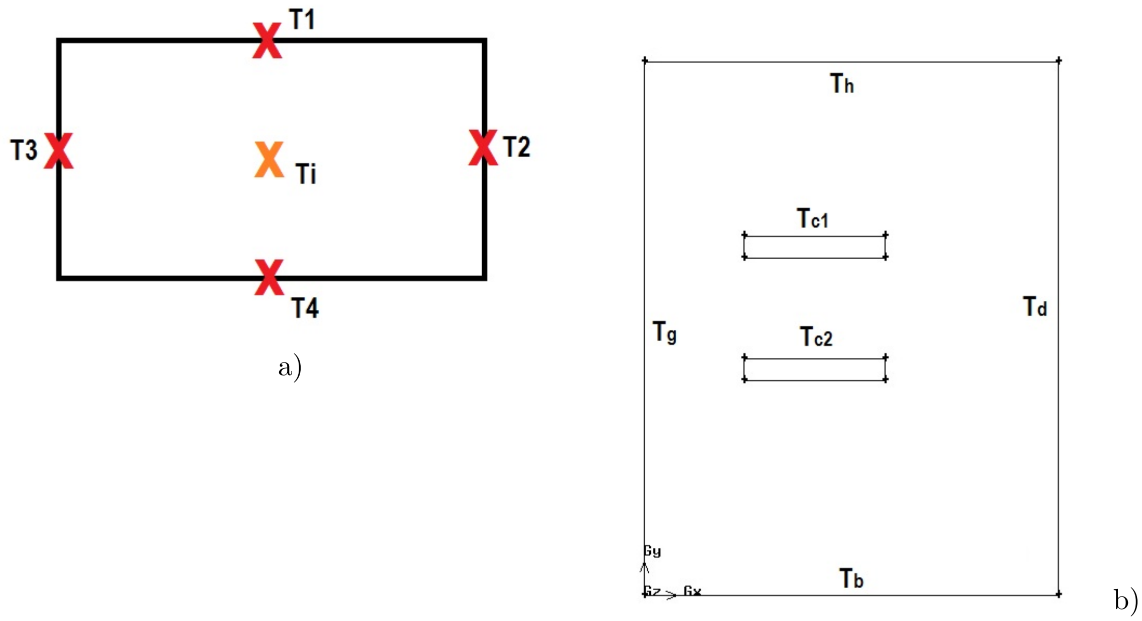

Figure 6.16.: Temperature measurement used as boundary conditions; T1,T2, T3, T4 - temperature measured on the surfaces, Ti- interior temperature; T_{c1}, T_{c2} - immersed boundary temperature, T_h,T_b,T_g,T_d - temperature on the cavity walls.

6.4. Experimental - Numerical Simulation Comparison

In this chapter we present a preliminary comparison between the numerical and experimental simulations. This analysis offers a validation of the simplifying hypothesis considered for the computations. For this case the temperature measured on the surfaces of the heated obstacles is used as a boundary condition for the numerical simulation.

The interior power that heats the objects varies from 1.8 W to 29 W following four plateaus. Different experimental flow topologies are compared to those obtained by the simulations.

Three cases were considered. First the case where only one obstacle is heated and the exterior temperature is 30 °C. For the second case the same object is heated following the same pattern but the exterior temperature is 20 °C. And for the third case we considered the two immersed objects as both being heated at an exterior temperature of 20 °C.

6.4.1. Comparison for one heated object

Before evaluating the effect of conductivity and introducing the heat flux generated by the objects, a preliminary comparison is made where the measured surface temperature is used as boundary conditions for the numerical simulation. These considered temperature measurements are presented in figure 6.16. We have considered the object on the bottom as being heated. The immersed object, that plays the role of the active equipment inside a real cabinet, is heated following four different temperature plateaus defined by the power supplied to the resistances.

As mentioned before, experimental tests were made for chamber temperatures of 20 °C and 30 °C. For each of these cases the temperature on the immersed boundary is as in figure 6.16.

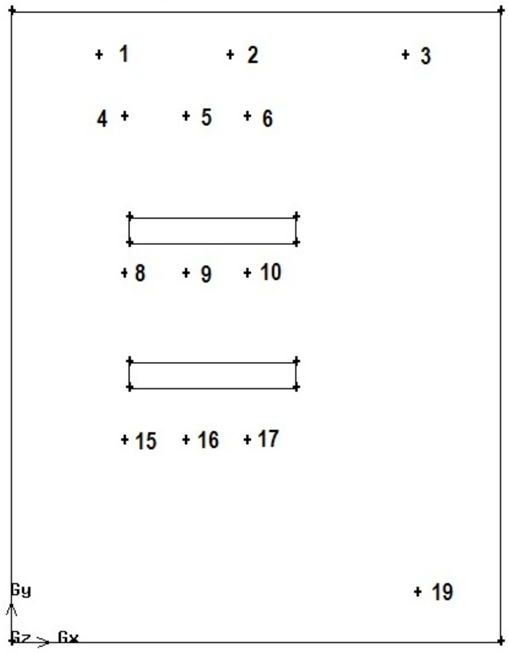

Figure 6.17.: Thermocouples placement

The average of T1,T2, T3, T4 and Ti is considered as the given body temperature.

6.4.2. Case of climate chamber temperature 30 °C

The test chamber temperature is maintained constant at 30 °C. The measured of surface temperature is taken into account as boundary conditions for the numerical simulations.

The flow inside a cavity presents two recirculation cells. The fluid heats along the source and has an ascendant trajectory around the second object, the one above and the re-descends along the vertical walls just to ascend again towards the lower heated object. The two recirculation cells engage a part of the air volume on the bottom of the cavity. In consequence the air cools along the vertical walls.

We can notice that the difference in temperature between the four wall is feeble. The difference in temperature between the immersed objects is induces by the lack of power feed for the upper object.

The measured temperature values are shown in table 6.1, they are further used as boundary conditions for the numerical simulation.

Power (W)	T_{c1} (°C)	T_{c2} (°C)	T_h (°C)	T_b (°C)	T_g (°C)	T_d (°C)
1,8	20,7	24,9	20,4	20,0	19,9	19,8
7,4	32,7	46,6	30,8	30,2	30,4	29,8
16,4	35,8	62,6	31,5	30,5	31,0	30,2
29,3	39,2	81,7	32,4	31,1	31,5	30,7

Table 6.1.: Boundary conditions imposed for the simulations(6.16); Temperature measurement for a chamber temperature of 30 °C.

As velocity boundary conditions for the immersed boundaries no-slip wall are considered.

Figure 6.18 depicts the temperature field and isotherms for a section inside the cabinet at the center of the x-axis. A thermal plume forms on the heated object. As it reaches the upper object the plume tilts to the right, where more space is available until reaching the wall. Two recirculation cells are formed. The counter-clockwise cell is small in size. The thermal boundary layer on the bottom of the heated object is smaller than on top.

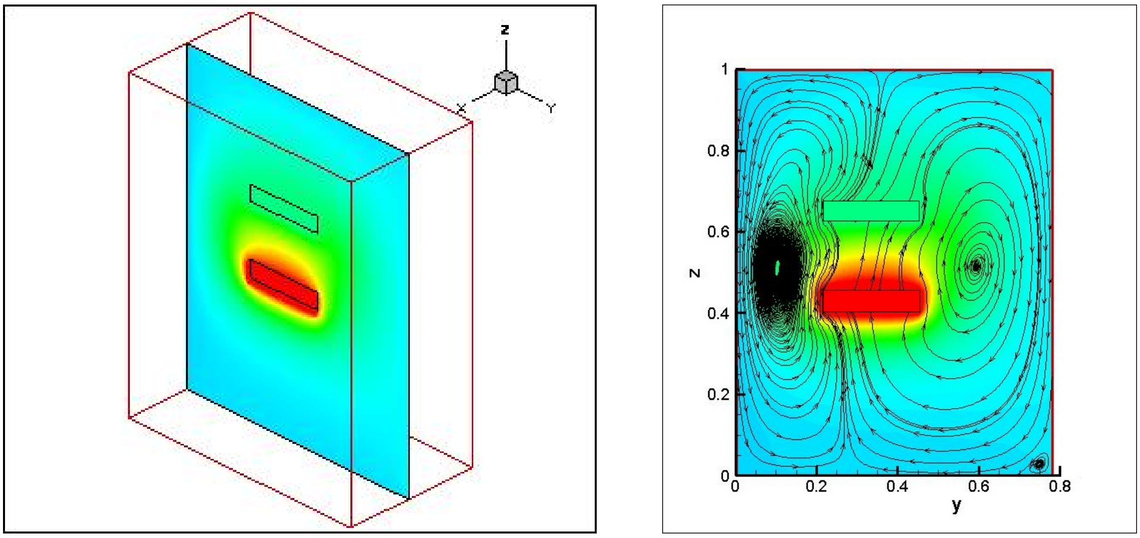

Figure 6.18.: Temperature field and isotherms for $x - axis$ section; At 30 °C.

In figure 6.19 we can see an acceptable agreement between the numerical and experimental results.

While most errors can be found within a difference of 1% to 3.5%, there are some exceptions. We notice a grater error for the last plateau, when the immersed component had the maximal temperature value. For T_3 the error for the last simulation is of 13.5%, for T_5 the error is 8.3%, for T_{16} a error of 21.8% was attained.

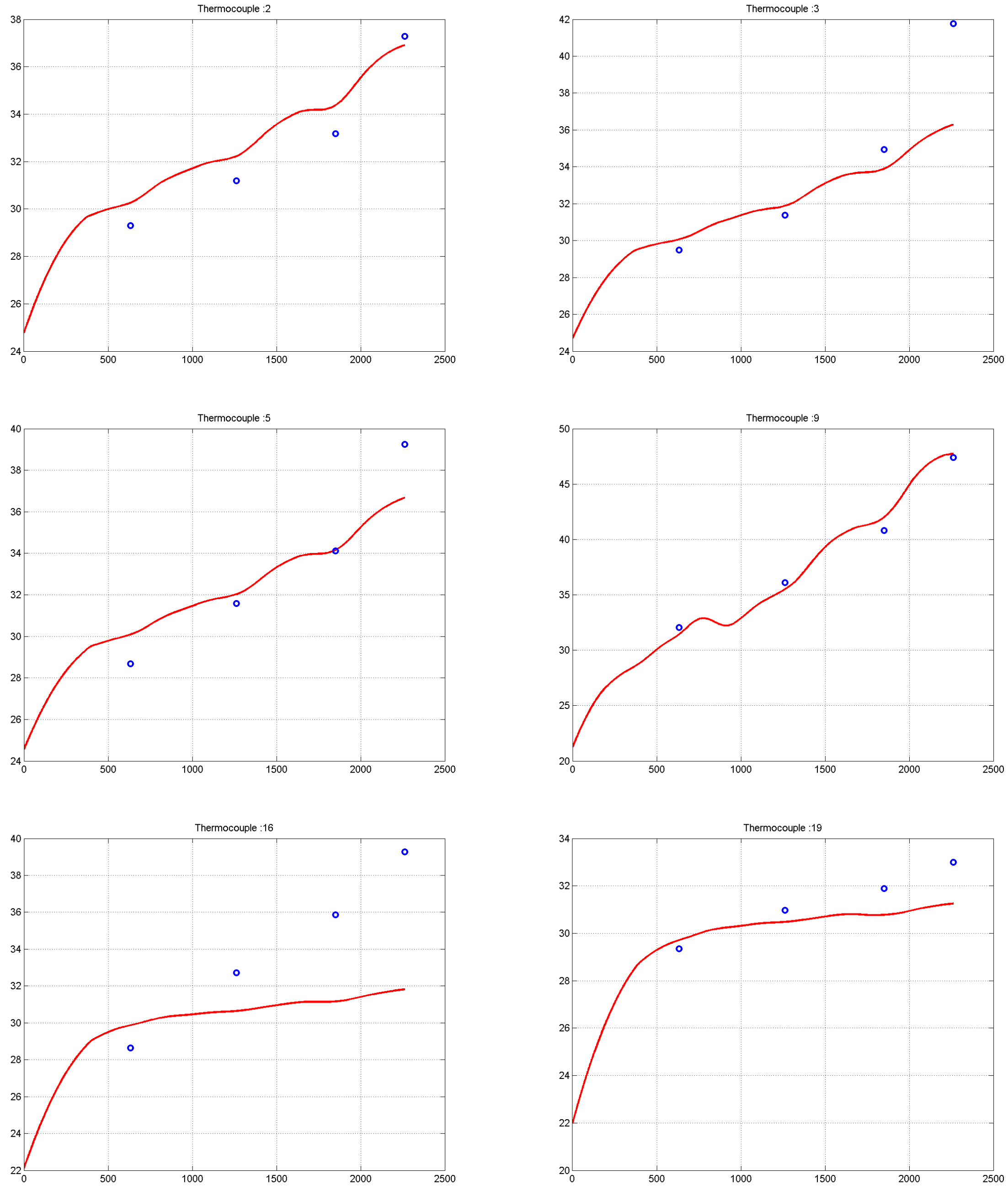

Figure 6.19.: Comparison between experimental results (red line) and numerical results (blue dot); At 30 °C.

6.4.3. Case of climate chamber temperature 20 °C

For the second case, of a test chamber temperature of 20 °C, as the exterior temperature is lower, we can see that the interior temperature decrease as well. Take for example the case of supplying the body with 29 W, it is clear by comparing the two cases that when the exterior temperature augments with 10 °C the temperature measured on the interior body also augments with an equivalent temperature of 9.6 °C, according to our measurement. The measured values of temperature are presented in tables 6.2.

Power (W)	T_{c1} (°C)	T_{c2} (°C)	T_h (°C)	T_b (°C)	T_g (°C)	T_d (°C)
1,8	20,8	25,0	20,4	20,0	19,9	19,8
7,4	23,0	36,8	20,8	20,2	20,2	19,8
16,4	26,2	53,2	21,4	20,5	20,6	19,8
29,3	29,2	72,1	22,1	20,8	21,1	19,7

Table 6.2.: Boundary conditions imposed for the simulations(6.16); Temperature measurement for a chamber temperature of 20 °C.

In figure 6.20 the temperature field and isotherms are presented for a section at $x = 0.5$. A thermal plume is forms on the lower body and as before it tilts to the right. The flow presents the same geometry as before, with two recirculation cell across the whole cavity.

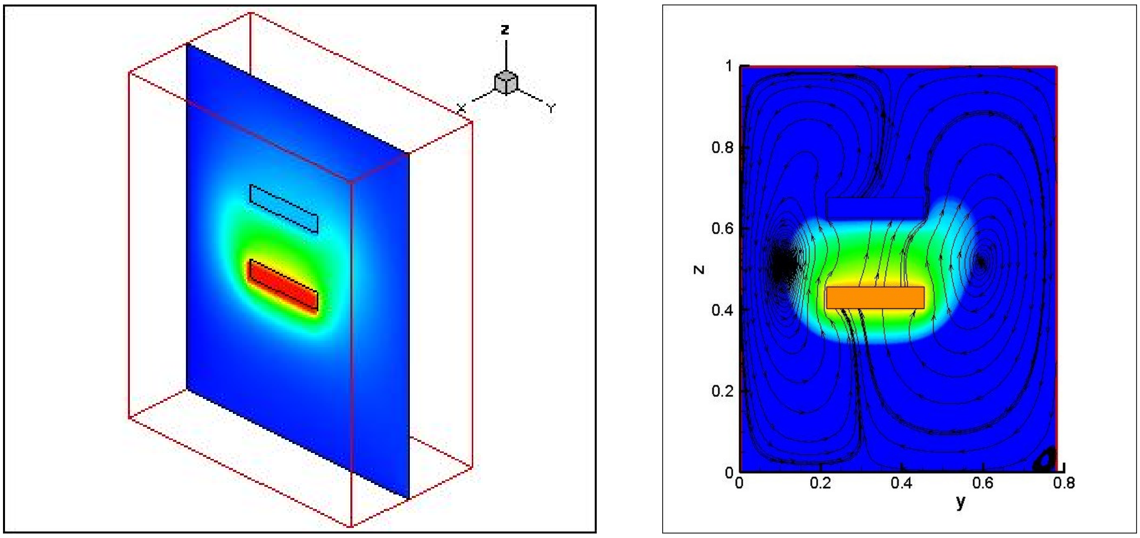

Figure 6.20.: Temperature field and isotherms for $x - axis$ section; At 20 °C.

The thermocouples used for measurement are on the same plane which is a transversal section plan, of the cavity. Figure 6.21 shows the comparison between the experimental (red line) and numerical (blue dots) results. The placement of these thermocouples is shown in figure 6.4.2.

We notice again the great error increase for T_{16}. Further analysis shows an increase of the error for the lower part of the cavity.

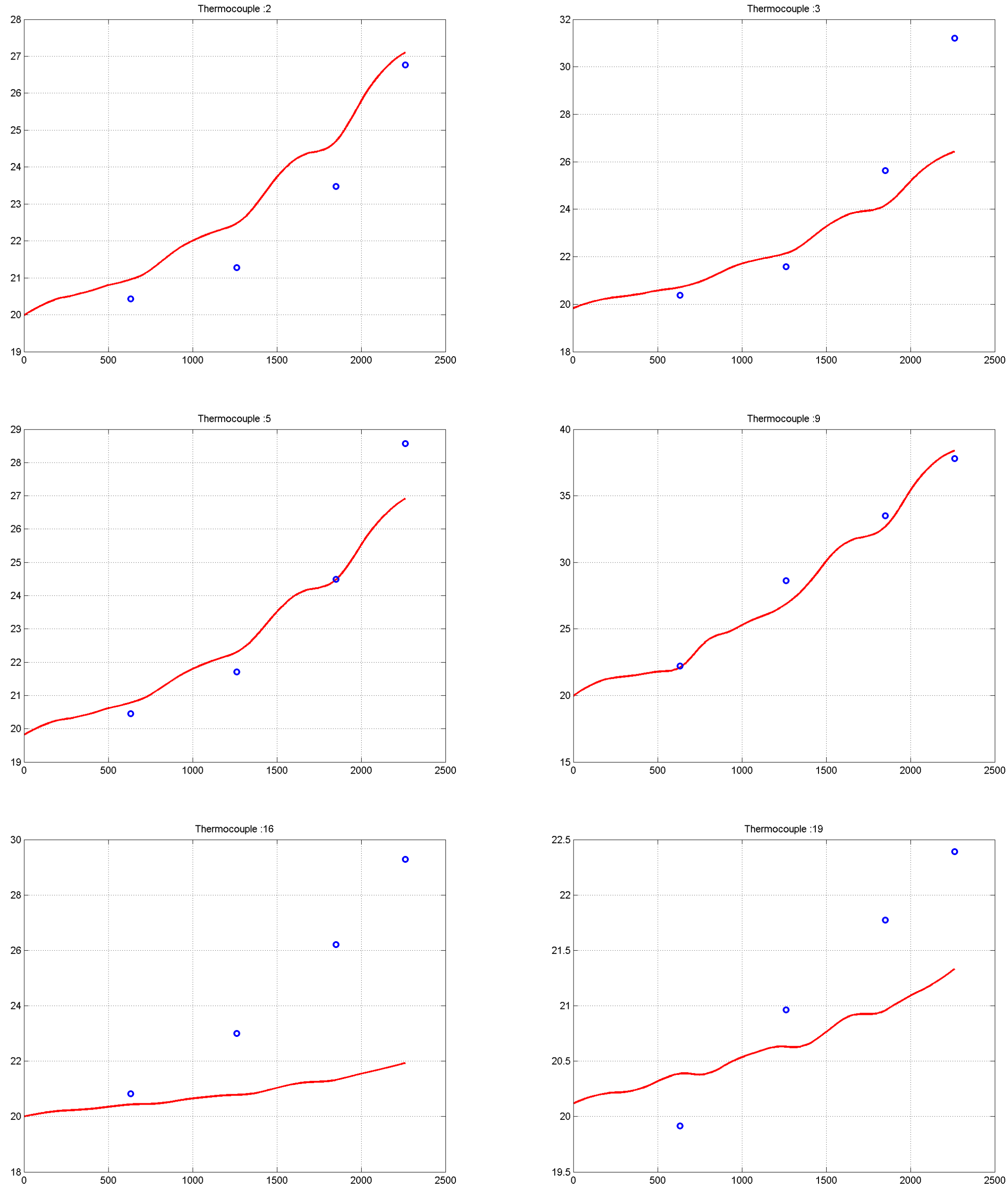

Figure 6.21.: Comparison between experimental results (red line) and numerical results (blue dot); At 20 °C.

6.4.4. Both immersed objects are heated

Another case considered is when both object are supplied with the same power, thus heated equally. Table 6.3 presents the temperature boundary conditions considered. Three power supply levels are taken into account.

Power (W)	T_{c1} (°C)	T_{c2} (°C)	T_h (°C)	T_b (°C)	T_g (°C)	T_d (°C)
1,8	34,3	33,9	30,5	29,6	30,2	29,9
7,4	35,7	46,9	31,8	30,3	30,7	30,4
16,4	64,3	63,3	33,7	30,6	31,4	31,1

Table 6.3.: Boundary conditions imposed for the simulations(6.16); Temperature measurement for a chamber temperature of 20 °C.

Figure 6.22 shows the comparison between the experimental (red line) and numerical (blue dots) results. Two smaller vortexes form in the lower corners of the cavity. The thermal gradient is stronger in the upper part of the cabinet.

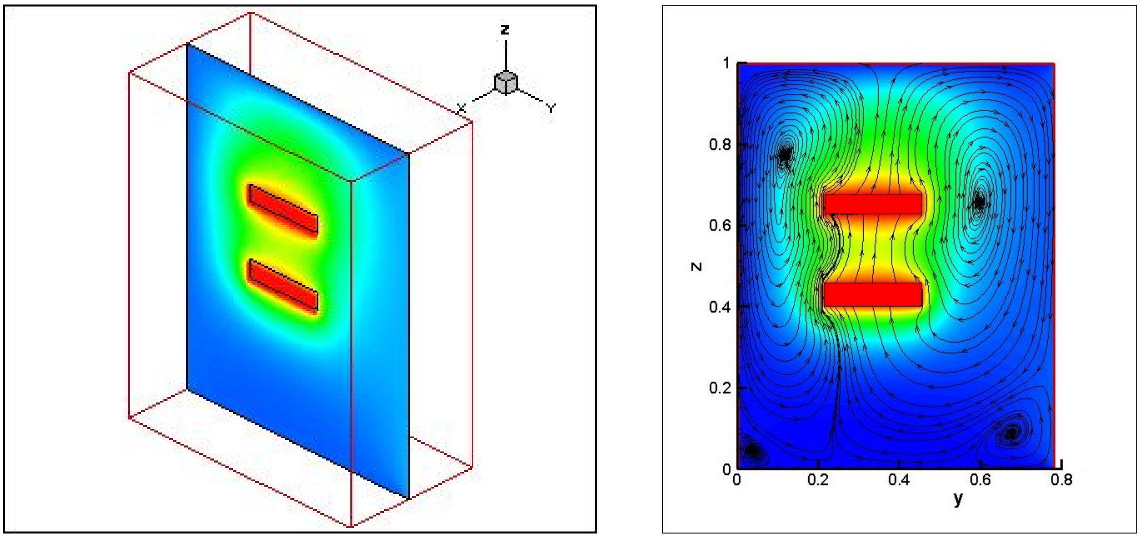

Figure 6.22.: Temperature field and isotherms for $x - axis$ section.

The upper obstacle receives an additional heat flux form the bottom body thus rising in temperature. An global good agreement is obtained for this preliminary comparison.

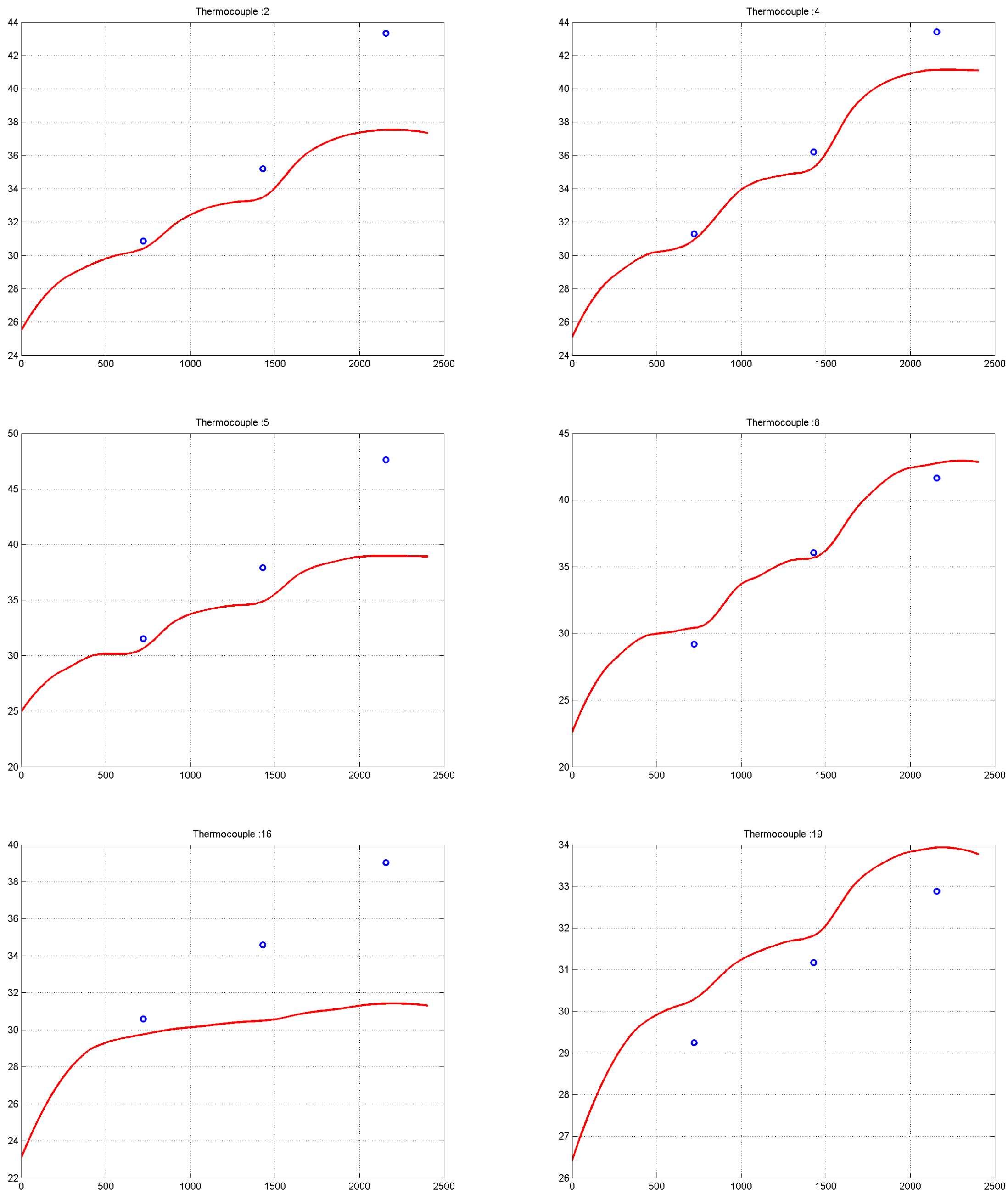

Figure 6.23.: Comparison between experimental results (red line) and numerical results (blue dot).

6.5. Conclusion

Given the complexity of the fluid low and the difficulties of the measurement we obtained a fair agreement. The discrepancies could be due to the relative small number of thermocouples used or to the low number of mesh nodes of the numerical simulation. We would recommend PIV measurement in order to obtain better variable fields. Further measurements should be done and analysed before drawing definite conclusions.

7. Modeling and simulation of phase-change materials

We extend in this chapter the finite element (FE) algorithm developed in chapter 4 for solving the 2D Navier-Stokes-Boussinesq equations to phase-change systems with convection. We use the flexibility of the proposed Newton algorithm to introduce new nonlinearities related to phase-change phenomena. The numerical system is validated against benchmarks for the melting of a paraffin phase-change material.

7.1. Phase-change materials (PCM)

7.1.1. PCM as passive heat storage device

One of the main problems that arise in cooling the outdoor cabinets is controlling the internal temperature, and simultaneously minimizing the overall energy consumption. The cabinets are under sever environmental conditions and the heat produced by the interior equipments contributes to the increase of temperature in the cabinet. In order to assure an efficient performance of these equipments the temperature should not exceed 55°C. Due to price reasons, a control system that requires very little maintenance and a limited, or none at all, energy consumption, would be optimal. A simple and promising idea of a passive cooling solution is the increase of the thermal inertia of walls by adding phase change materials (PCM). Latent thermal energy storage by PCMs may be an innovating technique which could provide a high energy storage density and has the advantage of storing energy as latent heat of fusion.

The materials added in sufficient quantities could limit the maximum temperature inside the outdoor cabinet. They also offer two means of energy stoking: sensible heat and latent heat which is the necessary energy, at the melting temperature, so the material could pass from solid to liquid and vice versa. Even though the principle of using PCMs for passive cooling might seems appealing, the lack of prediction tools for the thermal exchanges still poses a problem. Another issue of using PCMs is the optimal geometry for such devices. Two geometries are the most studied: a thin layer for the thermal storage in buildings and a very thin layer (from two to three centimeters) for diminishing the peak temperature variation for certain electronic components. PCMs could be encapsulated and placed as an exchanger with the heat transferring fluid in the air-conditioning systems and even micro-encapsulated in the coatings of the porous materials for energy storage in the power plants or thermal regulations of buildings.

7.1.2. Phase-change physical problem

We describe in the following how a PCM could be used as a heat storage device (see fig. 7.1).

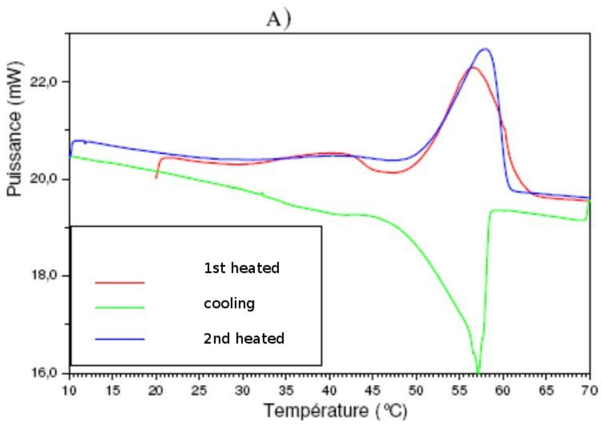

Figure 7.1.: Example of melting and solidification curves (absorbed power versus temperature for Rubitherm RT58 product) for a PCM.

In a first step, the material is heated until it reaches the melting point, where we can notice a heat flow peak; afterwards the heat flow decreases while the temperature still rises. The second step represents a cooling phase, when the material solidifies; we can observe the lowest peak of the heat flow that rises afterwards with the decrease of temperature. The red line in the figure represents a second heating that has slightly different value in comparison with the one before, but keep the same allure and thus validates the measurement.

During an experimental melting process the material is stabilized at a lower temperature in a solid state, a higher temperature constraint is imposed on one of the lateral walls. Figure 7.2 represents the liquid phase evolution in time, during the melting process. A first remark would be that the separation of the phase change front between solid and liquid is clear and no macroscopic thickness can be noticed. In this case the problem of a phase change front becomes one of a border between the two states. The convection within the fluid will establish latter the shape of the interface.

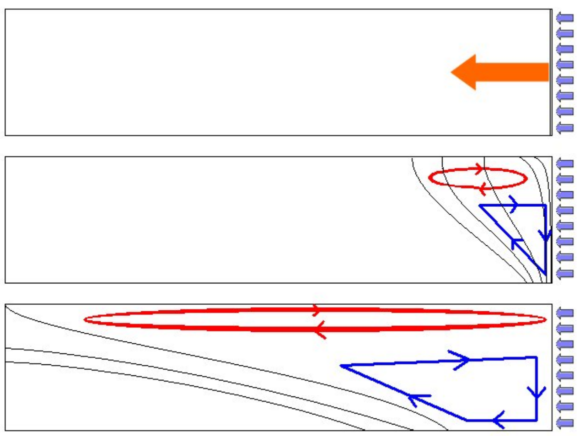

Figure 7.2.: Sketch of the melting process of a PCM. Convection flux in the liquid region.

The subsequent PCM behavior can be divided into three periods. The first period is relatively short and lasts for only a few minutes. It corresponds to the development of a thin boundary layer, close to the heated wall. The layer is vertical and the general energy transport method is conduction. In the second period, a natural convection regime is formed within the liquid. The phase change front presents two inflection points. At latter stages, convection becomes dominant and the liquid phase develops faster in the upper part of the system, while in the middle part the phase change front is almost horizontal. The hot liquid rises and enters into contact with the phase change interface, the material change from solid to liquid maintaining a temperature close to the phase change temperature. The cooler liquid descends along the boundary. The upper part of the system where the temperature is higher melts faster then the lower part.

The third period (not appearing in the figure) corresponds to the moment when the phase change front comes into contact with the opposing wall.

7.1.3. Physical models for phase-change systems

Phase change problems have been widely studied since Stefan in 1891. There are numerous applications, among which the melting domain, to liquefy the metal and control its behavior during solidification, and tissue conservation through freezing. The interest for such phenomenons has greatly increased in the '80s through the use of latent heat for energy storage. The first studies conducted for a liquid/solid phase change have neglected the fluid convection Longworth and Hartley (1978). This is described as the Stefan problem, the domain taken into account is semi-infinite, homogeneously heated on one extremity. An analytical solution is only possible for a one dimension problem Voller and Cross (1981).

In reality, the physical phenomena which arise during melting and solidification are numerous. One can observe various phenomena from conduction, to gravity, conduction in the liquid zone, recirculation of the fluid and phase change. Delaunay (1985) made a detailed analysis of different regimes during the melting phase in a square cavity. The first phase, which is very short, corresponds to the conduction phase; the solid liquid interface is rectilinear and parallel with the heated boundary. In the second phase, a transition one, conduction is still dominating. The third phase is the development of a boundary layer one in which convection is the main transport phenomenon; the solid-liquid interface shows a curved shape that increases with time, due to the presence of recirculation flows.

The influence of natural convection in the liquid phase is still little known. There are only few available visualizations of the liquid flux and the interface. In the case of melting with a uniform heated boundary several interpretations are developed. One of these takes into account the presence of several convection cells along the melting layer Hannoun et al. (2005), but the widest used interpretation proposes a single convection cell.

The phases for solidification differ from those for melting, conduction is preponderant during most of the process and the moving interface boundary is linear. These different stages can be defined through the Rayleigh number (Marshall and Chen, 1982) . The characteristic time for each of these stages can differ with the considered phase.

Another difficulty in modeling PCMs arises from the fact that the phase change is a problem with two scales, the microscopic and macroscopic. Such sort of problem can be decomposed into three regions: liquid, solid, and between them a region, also called *mushy* zone, that consists of both solid and liquid particles. This is due to the difference of temperature between the solidification and melting processes. The variations of the physical properties of this region are microscopic phenomena which depend on the nature and composition of the material. In this area, the presence of crystals are sometimes observed, with orientations and lengths that can vary with the macroscopic properties of the area Swaminathan and Voller (1997). During experimental trials of solidification on paraffins, the presence of long alcane fibres can be easily visualized. Thus the role of the mushy zone cannot be neglected, even though the transport phenomena for the solid and liquid phase are macroscopic.

7.1.4. Numerical studies of phase-change systems

From a numerical point of view most models consider the conduction as the basic mechanism for heat transfer during melting or solidification. Several other important physical phenomena, such as convection in the liquid phase, the presence of the *mushy* region at the interface between the two phases, gravity effects, variable material thermo-physical properties, etc. are only recently considered. For a comprehensive review of such models, see Faghri and Zhang (2006).

In the propagation of the melting/solidification front and the heat transfer between phases, natural convection plays an important role. Numerous studies that confirm this hypothesis were published, such as Morgan (1981); Voller (1987); Jany and Bejan (1988); Evans et al. (2006); Vidalain et al. (2009); Wang et al. (2010a).

A widely used numerical model is the single domain approach. In the liquid phase, the natural convection flow is simulated by solving the full incompressible Navier-Stokes equations with Boussinesq approximation. The same system of equations is solved in the solid phase by introducing a variable viscosity coefficient taking very large values in the solid (*e. g.* Ma and Zhang (2006)). This model allows the velocity to progressively vanish in the solid through a intermediate *mushy* region, defined accordingly to classical enthalpy methods (*e. g.* Voller (1987); Cao et al. (1989)). In enthalpy methods, the phase change is modelled by introducing an enthalpy source term in the heat equation. The phase-change is supposed to occur over a temperature interval setting the width of the mushy region. This temperature interval is also used to regularize discontinuous functions representing the variation of material constants (conductivity, specific heat, latent heat) across the solid-liquid interface.

The main advantage of the single domain approach is that the same system of equations is solved in both liquid and solid phase. In exchange, the numerical method has to tackle two important challenges: properly resolve the convection cells in the fluid region and accurately capture the solid-liquid interface.

7.2. Governing equations

A single domain approach to simulate phase-change systems with convection is used for the present study (see Danaila et al. (submitted)). The considered solid-liquid system is placed in a two dimensional cavity of width L and height H. The subscripts s and l make reference to the solid and respectively the liquid phase . The horizontal walls are considered adiabatic, while the vertical ones are isothermal of temperature T_h(hot) and T_c(cold). T_f is the fusion temperature. For obtaining the non-dimensional equations the reference length scale is $L_{ref} = H$ and the liquid reference state is $(\rho_{ref}, V_{ref}, T_{ref})$. The scaling values are :

$$\mathbf{x} = \frac{\mathbf{X}}{L_{ref}}, \ \mathbf{u} = \frac{\mathbf{U}}{V_{ref}}, \ \Theta = \frac{T - T_{ref}}{T_h - T_c}, \ t = \frac{\tau}{t_{ref}}, \ t_{ref} = \frac{L_{ref}}{V_{ref}} \tag{7.1}$$

In this setting, the incompressible Navier-Stokes equations with the Boussinesq approximation can be written under the form:

$$\begin{aligned} \nabla \cdot \mathbf{u} &= 0, \\ \frac{\partial \mathbf{u}}{\partial t} + (\mathbf{u} \cdot \nabla)\mathbf{u} + \nabla p - \frac{\mu_{ls}}{\mathcal{R}e} \Delta \mathbf{u} - f_B(\theta)\, \vec{e}_y &= 0, \end{aligned} \tag{7.2}$$

with $f_B = g(\rho_{ref} - \rho)/\rho_{ref}$ is the (non-dimensional) buoyancy force.

The dimensionless numbers that characterize the flow are:

$$\mathcal{R}e = \frac{\rho_{ref} V_{ref} L_{ref}}{\mu_l}, \ \mathcal{P}r = \frac{\nu_l}{\alpha_l}, \ \mathcal{R}a = \frac{g \beta L_{ref}^3 (T_h - T_c)}{\nu_l \alpha_l} \tag{7.3}$$

where μ represents the dynamic viscosity, ν the kinematic viscosity, α the thermal diffusivity, β the thermal expansion and g the gravitational acceleration.

For the energy equation an enthalpy transforming model Voller (1987); Cao et al. (1989) was used to obtain the following non-dimensional form:

$$\frac{\partial C\theta}{\partial t} + \nabla \cdot (C\theta \mathbf{u}) = \nabla \cdot \left(\frac{K}{Pr} \nabla \theta \right) - \frac{\partial CS}{\partial t} - \nabla \cdot (CS\mathbf{u}), \tag{7.4}$$

where the specific heat is $C = c_s/c_l$ and the conductivity $K = k_s/k_l$. The non-dimensional source term is defined as $S = s/(T_h - T_c)$ and takes into account the latent heat of fusion. The source term is theoretically a Heaviside function that is null in the solid phase and has a large value in the liquid phase. The basis of this model is that the change of phase occurs over an interval around the point of fusion $[\theta_f - \epsilon_1, \theta_f + \epsilon_2]$. The model adopted for S is:

$$S = \begin{cases} S_l, & \theta - \theta_f \geq \varepsilon_2 \\ F_S(\theta), & -\varepsilon_1 \leq \theta - \theta_f < \varepsilon_2 \\ S_s, & \theta - \theta_f < -\varepsilon_1 \end{cases} \tag{7.5}$$

The function $F_S(\theta)$ represents a regularization of the enthalpy variation in the mushy region. The regularization is done by a continuous and differentiable hyperbolic-tangent function with three parameters, defined for all θ:

$$F(\theta; a_s, \theta_s, R_s) = f_l + \frac{f_s - f_l}{2} \left\{ 1 + tanh \left(a_s \left(\frac{\theta_s - \theta}{R_s} \right) \right) . \right\} \tag{7.6}$$

f_l and f_s are imposed values in the liquid and solid phases, a_s is a smoothing parameter and θ_s the value around which the regularization is made. R_s represents the smoothing radius. The same function, but holding different parameters is used for the variations of the material properties.

The variable viscosity allowing the passage from liquid to solid will be also represented by this function.

A further simplification of the energy equations is obtained by supposing that the mushy region is very narrow and acts like a solid. As a consequence, the last (advection) term is neglected. The final system of equations is the following:

$$\begin{aligned} \nabla \cdot \mathbf{u} = 0, \\ \frac{\partial \mathbf{u}}{\partial t} + (\mathbf{u} \cdot \nabla)\mathbf{u} + \nabla p - \mu_{sl}(\theta) \Delta \mathbf{u} - f_B(\theta) \mathbf{e}_y = 0, \\ \frac{\partial (C\theta)}{\partial t} + \nabla \cdot (C\theta \mathbf{u}) - \nabla \cdot \left(\frac{K}{\mathcal{P}r} \nabla \theta \right) + \frac{\partial (CS)}{\partial t} = 0. \end{aligned} \tag{7.7}$$

7.3. FreeFem++ implementation and mesh adaptivity

In the system of equations (7.7) the difficulties encountered while implementing the algorithm are represented by two types of non-linearity : the variation of the viscosity $\mu_{sl}(\theta)$ (from 1 in the fluid to 10^8 in the solid) and the variation of the enthalpy function $S(\theta)$. In order to simplify the algorithm we have considered $K = C = 1$ (assumption valid for paraffin PCMs).

We use for this problem the Newton algorithm (4.10) developed in chapter 4 for the Navier-Stokes-Boussinesq equations. The following modified Newton algorithm proved very robust and effective for the phase-change systems:

$$
\begin{aligned}
b(\mathbf{u}_w, q) - \varepsilon(p_w, q) &= b(\mathbf{u}^k, q) - \varepsilon(p^k, q)\\
\frac{1}{\delta t}(\mathbf{u}_w, \mathbf{v}) + c(\mathbf{u}_w; \mathbf{u}^k, v) + c(\mathbf{u}^k; \mathbf{u}_w, v) &+\\
\mu_{sl}(\theta^k) a(\mathbf{u}_w, \mathbf{v}) + \left[\frac{d\mu_{ls}}{d\theta}\theta^k\right]\theta_w a(\mathbf{u}^k, v) + b(\mathbf{v}, p_w) - \frac{df_B}{d\theta}\theta^k\theta_w(\mathbf{e}_y, \mathbf{v}) &=\\
\frac{1}{\delta t}(\mathbf{u}^k - \mathbf{u}^n, \mathbf{v}) + c(\mathbf{u}^k; \mathbf{u}^k, v) + \mu_{sl}\theta^k a(\mathbf{u}^k, \mathbf{v}) + b(\mathbf{v}, p^k) - f_B(\theta^k)(\mathbf{e}_y, \mathbf{v}) &\\
\frac{1}{\delta t}(\theta_w, \phi) - (\mathbf{u}^k \cdot \nabla\phi, \theta^k) + \left(\frac{K}{\mathcal{P}r}\nabla\theta_w, \nabla\phi\right) + \frac{1}{\delta t}\left[\frac{dS}{d\theta}\theta^k\right]\theta_w\phi &=\\
\frac{1}{\delta t}(\theta^k - \theta^n, \phi) - (\mathbf{u}^k \cdot \nabla\phi, \theta^k) + \left(\frac{K}{\mathcal{P}r}\nabla\theta^k, \nabla\phi\right) + \frac{1}{\delta t}\Big(S(\theta^k) - S(\theta^n)\Big)\phi &
\end{aligned}
\tag{7.8}
$$

For the spatial discretization we use standard Taylor-Hood finite elements Taylor and Hood (1973): the velocity is approximated with P_2 finite elements and the the pressure with P_1 finite elements.+ Compared to natural convection problems, we shall use here mesh adaptivity in order to accurately track the interface between solid adn liquid.

Mesh adaptivity by metric control is a standard function in FreeFem++. Delaunay-type algorithms developed in George and Borouchaki (1998) are used for the mesh generator with the addition when the new mesh is generated of an extra criterion added to keep the new mesh nodes and connectivity maps unchanged as much as possible when the prescribed mesh by the new metric is similar to the previous mesh. This extra criterion reduces the perturbations when the solution is interpolated from the old mesh to the new one. The flexibility of the mesh adaptivity algorithm allows for simultaneously taking into account several metrics computed for different variables monitoring the evolution of the phase-change system. To accurately track the solid-liquid interface the variation of the enthalpy source term was added as an adaptivity criterion.

7.4. Simulations of phase-change systems

We consider as a validation test the case of the octadecane PCM, melting inside a square cavity. The results are compared with both experimental and numerical results presented by Okada (1984) and respectively Wang et al. (2010a); Ma and Zhang (2006).

Constant material characteristics (specific heat C and conductivity K) are considered, as in previous numerical studies Wang et al. (2010a); Ma and Zhang (2006). Figure 7.3 presents a schematic figure of the considered case. Initially, the material is solid and melts progressively starting from the left heated boundary, maintained at a hot temperature $\theta_h = 1$. The right boundary is also isothermal and kept at a cold temperature $\theta_c = -0.01$; the horizontal boundaries are adiabatic. The second image in figure 7.3 offers an image of the system evolution at time step $t = 78.7$, with the streamlines of the flow developing in the liquid phase and the liquid-solid interface.

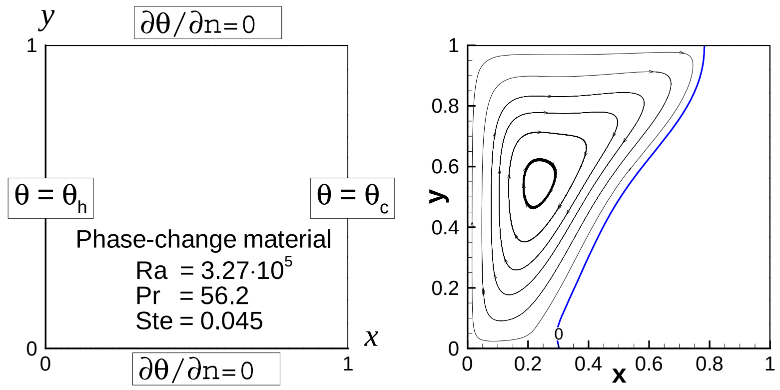

Figure 7.3.: Melting of a octadecane phase change material. Problem definition and streamlines of the flow developing in the liquid part at $t = 71$ and in blue the solid-liquid interface ($\theta = 0$).

In solving the system (7.9) it is necessary to model the variation of two nonlinear functions: μ_{sl} - the variable viscosity and S - the enthalpy source term. Both are regularized using the function (7.6), as shown in figure 7.4 for the viscosity. The mushy region is defined for $\theta \in [\theta_f - \varepsilon_1, \theta_f + \varepsilon_2]$ according to Wang et al. (2010a); for this computation $\theta_f = 0$ and $\varepsilon_1 = \varepsilon_2 = \varepsilon = 0.01$. The S term is regularized using the same function (7.6), with $S_s = 0$, $S_l = 1/Ste$, where Ste denotes the Stefan number.

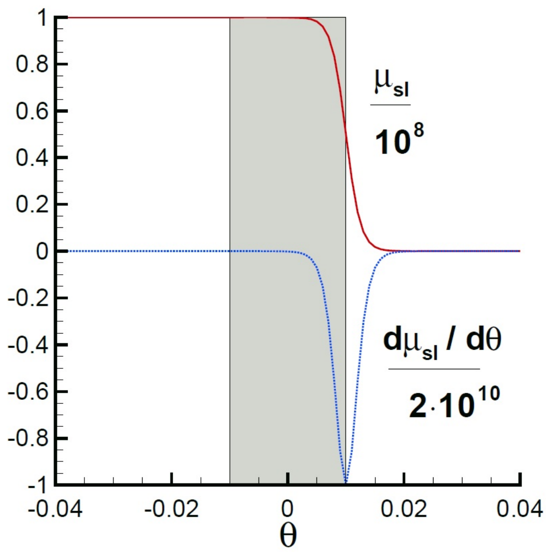

Figure 7.4.: Variation of the viscosity μ_{sl} and the derivative $d\mu_{sl}/d\theta$ for the single domain approach: $\mu_{sl} = 10^8$ in the solid and $\mu_{sl} = 1$ in the liquid region. Functions normalized with their maximum value (indicated on the graphs). The (grey) mushy region is defined as the temperature interval $[\theta_f - \varepsilon_1; \theta_f + \varepsilon_2]$, with $\theta_f = 0$ here. Case with $\varepsilon_1 = \varepsilon_1 = 0.01$ and $F(\theta; 2; \varepsilon_1; \varepsilon_1/2)$

The physical parameters describing the test case are: $Ra = 3.27 \cdot 10^5$, $Pr = 56.2$ and $Ste = 0.045$.

At time $t = 0$ when the computations starts we have a refined mesh near the boundary. Mesh adaptivity is used at each time step. The mesh is refined using metrics computed from three variables: the two fluid velocities and the enthalpy source term S. The resulting domain is well refined in the fluid part and the mushy region around the the liquid-solid interface. The mesh and corresponding temperature field are shown in figure 7.5. The smooth appearance of iso-lines for the temperature at the interface offers an improvement compared to the results proposed by Wang et al. (2010a); Ma and Zhang (2006).

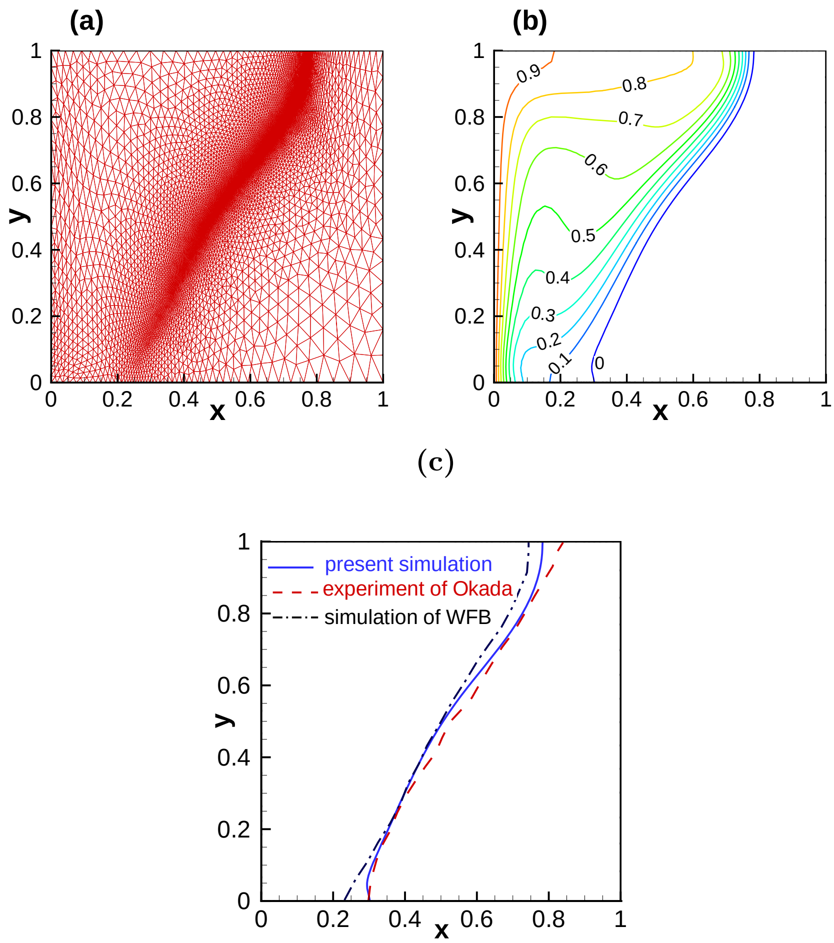

Figure 7.5.: Melting of a (PCM) phase change material (octadecane). Configuration at $t = 78.7$: (a) adapted finite-element mesh; (b) temperature iso-lines in the liquid phase (c) Solid-liquid interface at $t = 78.7$: comparison with numerical results of Wang, Faghri and Bergman Wang et al. (2010a) and experimental data of Okada (1984).

For a quantitative assessment, a comparison is made for the position of the liquid-solid interface at $t = 78.7$. Figure 7.5c compares our results with the experimental data by Okada (1984) and previously published numerical results by Wang et al. (2010a). The obtained shape and position of the liquid-solid interface is closer to experimental results than numerical results reported in Wang et al. (2010a). This is a direct consequence of the mesh adaptivity capabilities of our method.

A second computational case was designed to reproduce an experiment undergone at Orange Labs. An alcane material is placed inside a rectangular cavity, heated from the left side. The remaining three walls are considered adiabatic. The time evolution of the melting process is shown in figure 7.6. The process takes around 6 hours until the liquefied material reaches the right wall. The numerical simulation reproduces qualitatively the shape of the solid-liquid interface; no quantitative comparisons were made since detailed experimental data were not available.

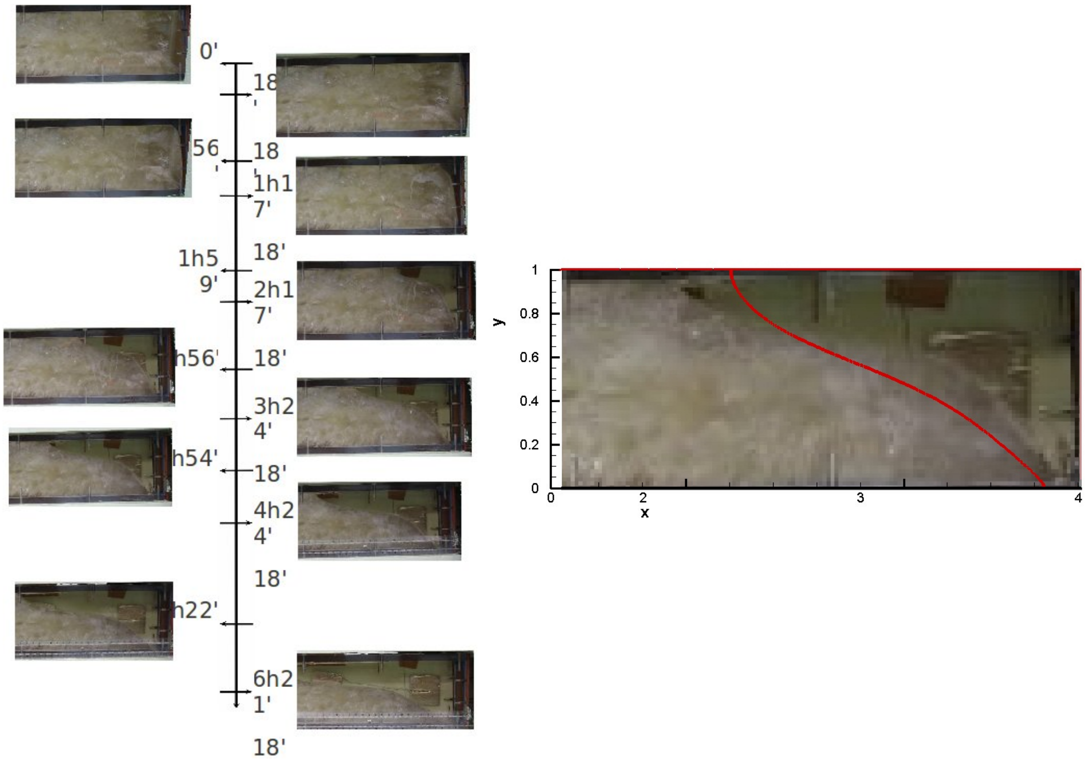

Figure 7.6.: Melting of a PCM alcane. Experimental images and comparison between experimental and numerical results (red line).

7.5. Conclusion

We can conclude that our FE solver provides accurate results. In particular, an accurate tracking of the solid-liquid interface is permitted by the use of mesh adaptivity by metric control. The Newton global formulation permits the implementation of different types of non-linearities in the system of equations and could be extended to other physical systems.

As possible future studies, we mention the simulation of more complicated configurations, with PCMs immersed in a cavity, or the continuous simulation of the melting followed by the solidification of the PCM. These are two new topics, not yet studied in the literature, that could be tackled in the future.

8. Conclusions

In this study we have addressed the problem of outdoor telecommunication cabinets cooling. We have mainly developed numerical investigation tools for simulating the flow and thermal effect inside cabinets. A complementary experimental study was also undertaken using a simplified configuration of an outdoor cabinet.

As a first purpose of the study, we have developed a state-of-the-art computer simulation code for outdoor telecommunication cabinets submitted to unsteady thermal effects due to internal heat sources. The code, written in Fortran90, solves numerically the incompressible Navier-Stokes equations, with the Boussinesq approximation for thermal effects. The novelty of our approach is to use sixth order compact finite difference schemes to discretize the 3D velocity-pressure description of Boussinesq flows. This high-order spatial discretization is combined with high order integration schemes (third order Runge-Kutta) and accurate (TVD) methods for capturing sharp temperature evolution.

Since most of the numerical codes used in numerical heat transfer community are based on (second-order) finite volumes codes, we started by investigating the benefits of the high-order discretization. Theoretical 1D (derivation of an analytical function) and 2D (simulation of the steady Burgraff flow) test cases were used to assess on the accuracy of the numerical system. These tests suggest that global estimations of the order of accuracy (based on global norms or Richardson analysis) has to be considered very carefully. Though the discretization error for the sixth-order scheme is several orders of magnitude lower than for the second order method, the influence of the degeneracy of the accuracy near the boundaries is of great influence. For the sixth-order method, the influence of the border points determines an order of accuracy p between 3 and 6, depending on the norm considered. The same study using periodic boundary conditions showed that the theoretical order $p = 6$ for the sixth-order scheme is found from computations.

The accuracy of the Navier-Stokes solver was tested using the well-known (Shih et al., 1989; Sheu and Lin, 2004; Laizet and Lamballais, 2009) analytical solution called the Burggraf flow. We can conclude that, despite the higher order used, only a second order convergence is obtained for the velocity field. This behavior was predicted by the results obtained for the 1D study. Laizet and Lamballais (2009) claimed that the low order accuracy of the Poisson solver is responsible for this result. We can see that this is not the only cause, and the global error estimates when the sixth order scheme is used could be misleading. By analyzing the grid resolution necessary to obtain the same level of the discretization error, we note that the accuracy of the sixth-order solver is attained with a two times denser grid when using classical second order schemes. We have also shown that the sixth-order scheme provides faster computational times than second-order methods to obtain stationary states, since high-order schemes give a better representation of small scales of the flow.

After these theoretical tests, the Navier-Stokes-Boussinesq solver was validated against classical benchmarks of classical convection. A study of different time integration schemes concluded that the most accurate results for the Navier-Stokes-Boussinesq solver are provided by the use of a third order Runge-Kutta method. This is the case for Rayleigh numbers greater than $\mathcal{R}a = 10^5$; for lower $\mathcal{R}a$ values, the Euler (first-order in time) scheme is precise enough to offer a good resolution of the steady flow. The drawback of the Runge-Kutta scheme is its larger computational (CPU) time. The convergence time increases from the Euler method to the third order Runge-Kutta by approximately 50%.

After a thorough investigation, considering the fundamental natural convection problems (Rayleigh-Bénard case and the differentially heated cavity), we could conclude that our solver provides a good agreement with the benchmarks presented in literature. A variable mesh in the vicinity of the walls ensures a good capture of the recirculation cells. The sixth-order schemes ensures a spectral-like resolution and more flexibility in modeling non-linear boundary conditions. Usually, natural convection simulations in the literature consider 2D problems. The flow inside a 3D differentially heated cavity is more complex. Our numerical code, for the case of a 3D Navier-Stokes-Boussinesq flow, proved efficient for this task and provided a very good agreement with previously reported numerical results.

The finite difference (FD) solver was further developed by implementing an immersed boundary method (IBM) to model heated obstacles inside the computational domain. This method is nowadays very popular to simulate flows in complex configurations without using cumbersome body-fitted grids. Suitable volume forces were numerically introduced as source terms in the Navier-Stokes-Boussinesq equations to take into account the influence of immersed boundaries on the velocity and temperature fields.

The second purpose of the study was to develop an alternative numerical solver for the Navier-Stokes-Boussinesq equations using the finite element method. Since the finite-element method offers an exact representation of immersed obstacles, this code was used to validate the results obtained with the FD code using an IBM method. This is an original validation approach, making possible not only qualitative, but also quantitative comparisons. A good agreement was obtained for all considered cases, rendering possible the simulation of complex configurations with obstacles of general shapes (rectangular, circular, etc).

For the finite element approach, a Newton algorithm system based on a penalty finite-element formulation of the Navier-Stokes equations was proposed and extensively tested. The development of the FE code was greatly simplified by the use of the FreeFem++ software. The advantage of this formulation was to permit a straightforward implementation of different types of non-linearities in the system of equations. As an original application of the method, we used this algorithm to simulate phase-change systems with convection. With this numerical system, we were able to tackle a large range of problems, from natural convection to melting and solidification. For difficult benchmarks of melting and, especially, solidification, we have obtained results that compare better with experiments that previously published numerical studies (see the submitted paper entitled *A Newton method with adaptive finite elements for solving phase-change problems with natural convection*).

The third purpose of the thesis was to conduct experimental measurements using a simplified configuration of an outdoor cabinet and compare experimental and numerical results. Experiments were conducted at the Orange Laboratories in Lannion, France. A preliminary comparison between the measured temperature field and the simulated one showed overall qualitative similarities, but a detailed analysis revealed important discrepancies for some regions of the flow. This suggested that a more successful comparison would need to consider 3D simulations with more refined grids, and also, more detailed measurements giving access to a better description of the experimental flow.

Future work

While the sixth-order scheme provides a spectral-like resolution and more flexibility in modeling immersed boundaries and non-linear boundary conditions, the computational cost is relatively high. We propose the development of a parallelized version of the solver which will greatly reduce the computational time. Considering the global accuracy of the code, a Poisson solver using also a sixth-order discretization (as in Boersma, 2011) would improve convergence properties. These are not easy tasks, since sixth-order discretization implies implicit coupling of computational nodes, and, thus, special parallel algorithms (*e. g.* byciclic methods for solving linear systems with tridiagonal matrices).

Concerning the Navier-Stokes-Boussinesq flow, new boundary conditions could further be developed to accommodate time variable boundary conditions. Time dependent boundary conditions are more realistic for the outdoor telecommunication cabinet, and they also represent one of the major problems that arise in the cooling issue. A more complex geometry should also be considered and tested.

A real telecommunication cabinet is quite complex; it contains many electronic components and wires that occupy more than 60% of the volume. Further and more thorough experiments should provide an estimate of what is to be expected from such a case. Also, for cooling purposes, an optimal estimation for the placement of each component should be considered. This would require optimization techniques (*e. g.* gradient or genetic algorithms), or simplified representations using advanced mathematics (*e. g.* reduced basis). Nowadays, most cabinets are cooled using ventilation systems; for these configurations, the code should be tested with respect to experimental results where forced convection is used.

In order to fully understand the impact of complex geometry and complex boundary condition on flows inside cabinets, an emphasis should be made on comparing more experimental and numerical results. PIV (Particle Image Velocimetry) experimental techniques giving access to a more detailed description of the flow (velocity vectors) could be very useful in validating the computational code.

Other cooling techniques should be tested. A promising path would be the use of phase-change materials (PCM), acting as a passive heat storage device. Our finite element solver proved effective in simulating the complex physics of such devices and could be further used in simulating more complex configurations (a PCM immersed into a differentially heated cavity).

A. Appendix

A.1. Experimental set-up presentation

The first step considered was to reduce the geometry to a basic configuration. Thus striping down the cabinet to it's simplest form, we introduced two heated object inside. Each of them is powered individually. As figure A.1 shows, the boxes are sported by two steel bars each and fixed in place using stainless steel nuts. The red wires, in figure A.1 are connected to the power supply while the green ones are thermocouples placed inside the boxes.

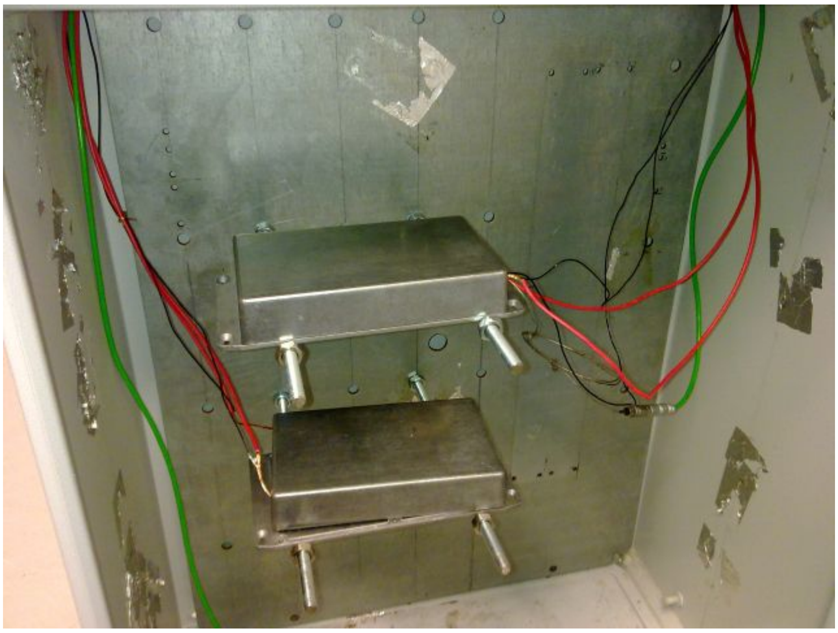

Figure A.1.: Simplified cabinet

The isometric view and three side views sections, providing the exact dimensions of the cabinet, are presented in A.2. The wires, bars and bolts, sporting the boxes, are not represented. This scheme depicts the simplest configuration possible.

Inside the boxes fourteen resistances were placed and fixed on a metal grid. Figure 6.4 a) shows the bottom part of the box with the metal grid, and a resistance. Each resistance is fixed with bolts on the metal grid, after this the resistances were configured in a series circuit (A.3 b)) and the ensemble was placed in the box. Each box has a 3 mm hole, through witch the power supply cable and the thermocouple were inserted. The box is bolted shut and places within the cabinet.

A schematic of the interior circuit is presented in figure A.4. Each resistance has 10Ω thus rendering a global resistance of 140Ω.

The box is heated using a Numeric-Lambda power supply (A.5). *Genesys*^{TM} are wide

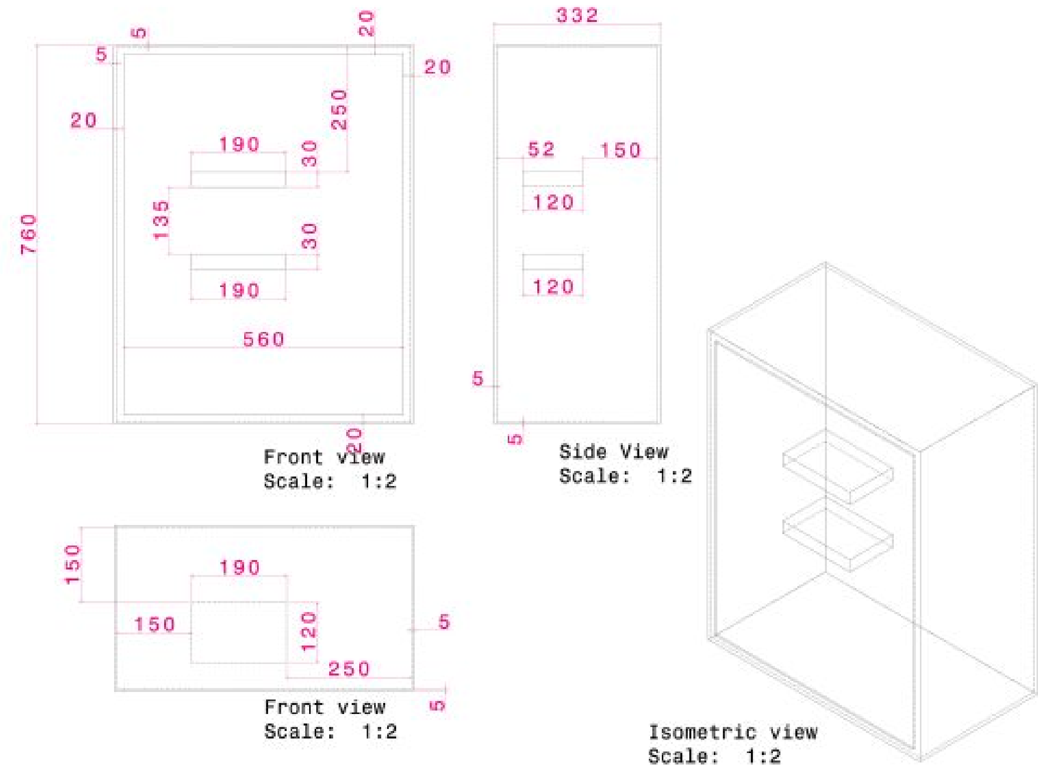

Figure A.2.: Scheme of the cabinet

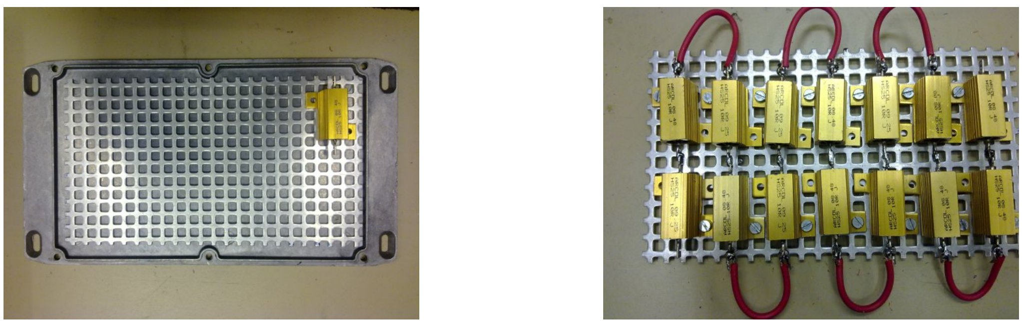

a) b)

Figure A.3.: Resistances placed inside the box

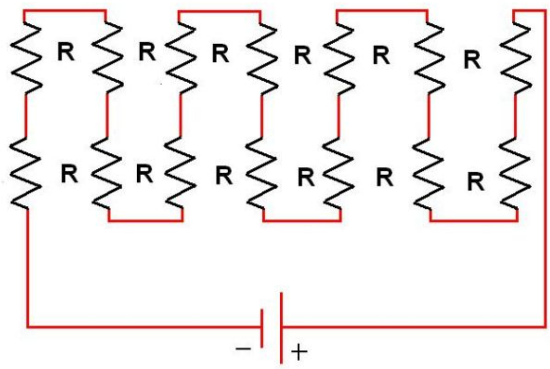

Figure A.4.: Electric circuit scheme

output rage power supplies with high performance switching. Output voltage and current are displayed and LED indicators show the complete operating status of the power supply. The front panel controls are for imposing the output parameters and preview the settings. The rear panel is composed of the necessary connectors to control and monitor the operation by remote analog signals or by built-in serial communication.

Figure A.5.: $Genesys^{TM}$ 1500 W power supply

The output voltage and current settings are programmed via a serial communication port. Analog inputs and outputs are provided at the rear panel for analog control of the power supply. The output voltage and current limit is programmed and can be monitored.

The rear panel is presented in figure A.6

The data is measured and recorded with Data Logger A.7. They are instruments of acquisition and logging used to record and measure a wide variety of quantities. The graphical interface allows quick and easy basic measurements. The data can be extracted with a memory stick or downloaded using a web interface into files ready for import. Temperature, current and voltage were recorded with the help of this tool.

The temperatures were measured with type K thermocouples A.8 (chromel90% nicked and 10% chromium - alumel 95% nickel,2% manganese, 2% aluminium and 1% silicon). They are the most common general purpose thermocouples with a sensitivity of approximately $41\mu V/C$, cromel positive relative to alumel. The have a wide variety of probes in a range of $-200C$ to $125C$ and the wire diameter is $\phi = 75\mu m$

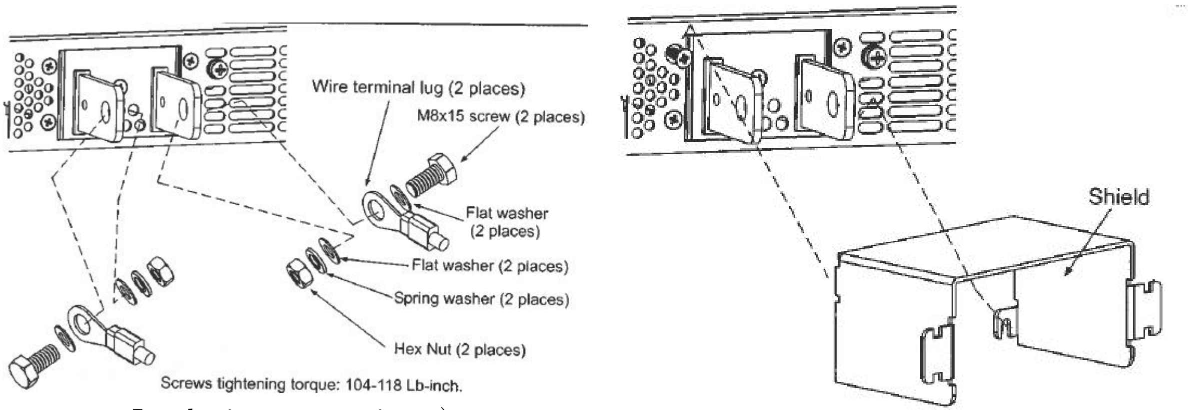

Load wires connection a)

Bus-bars shield mounting b)

Figure A.6.: Rear panel

Figure A.7.: Data Logger

Figure A.8.: Type K thermocouples

Before being included in the experimental set-up, the thermocouples accuracy was tested and a correction coefficient was obtained. We have had a total of 42 thermocouples placed as: 16 on the outdoor cabinets surfaces; 19 measuring the air temperature above, between and under the heated obstacles; 5 on the outside surfaces of the cabinet and 2 inside the object.

The placement of these thermocouples is shown in figure A.9. With green (left figure) we have marked the thermocouples measuring the air temperature, and with red (right figure) the ones placed on the surfaces of the heated objects.

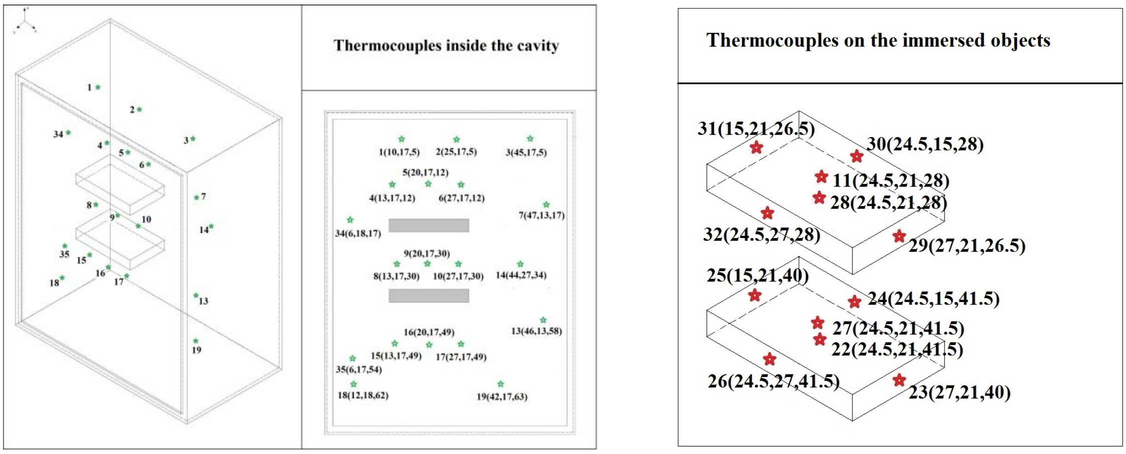

Figure A.9.: Thermocouple placement

The cabinet is placed within a controlled environment, respectively a climatic test chamber. The Servathin climatic test chambers ensures a controlled climate with temperature ranges between $-50C$ and $+80C$. They are specially designed for thermal test, and have conditioning on the ceiling A.10. The user interface provides local operator control and monitoring of the system. An embedded exterior panel permits the accurate control of temperature and temperature cycles. Our tests were performed for chamber temperatures of $20C$ and $30C$.

Figure A.10.: Climatic test chambers

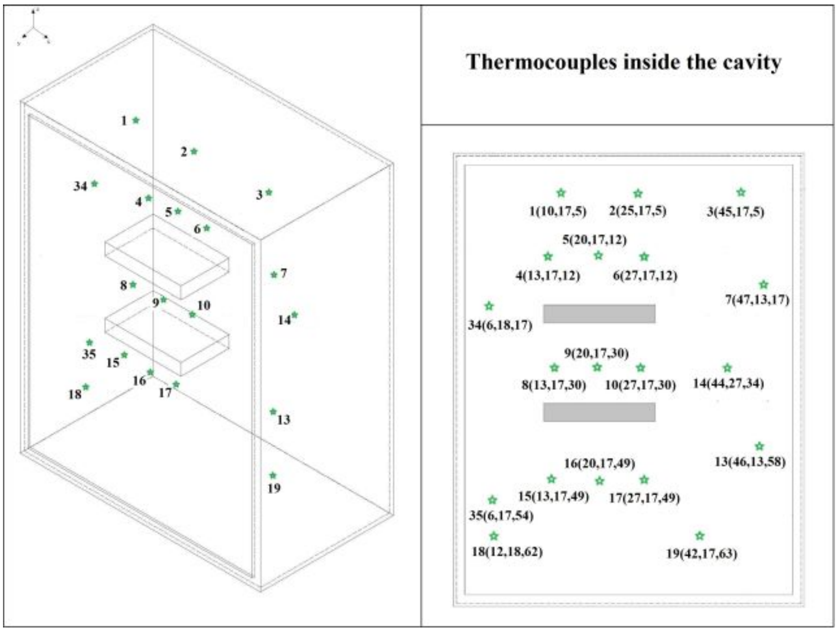

Figure A.11.: Thermocouple placement

A.2. Case of climate chamber temperature $30\,^{\circ}\mathrm{C}$

Further measurements:

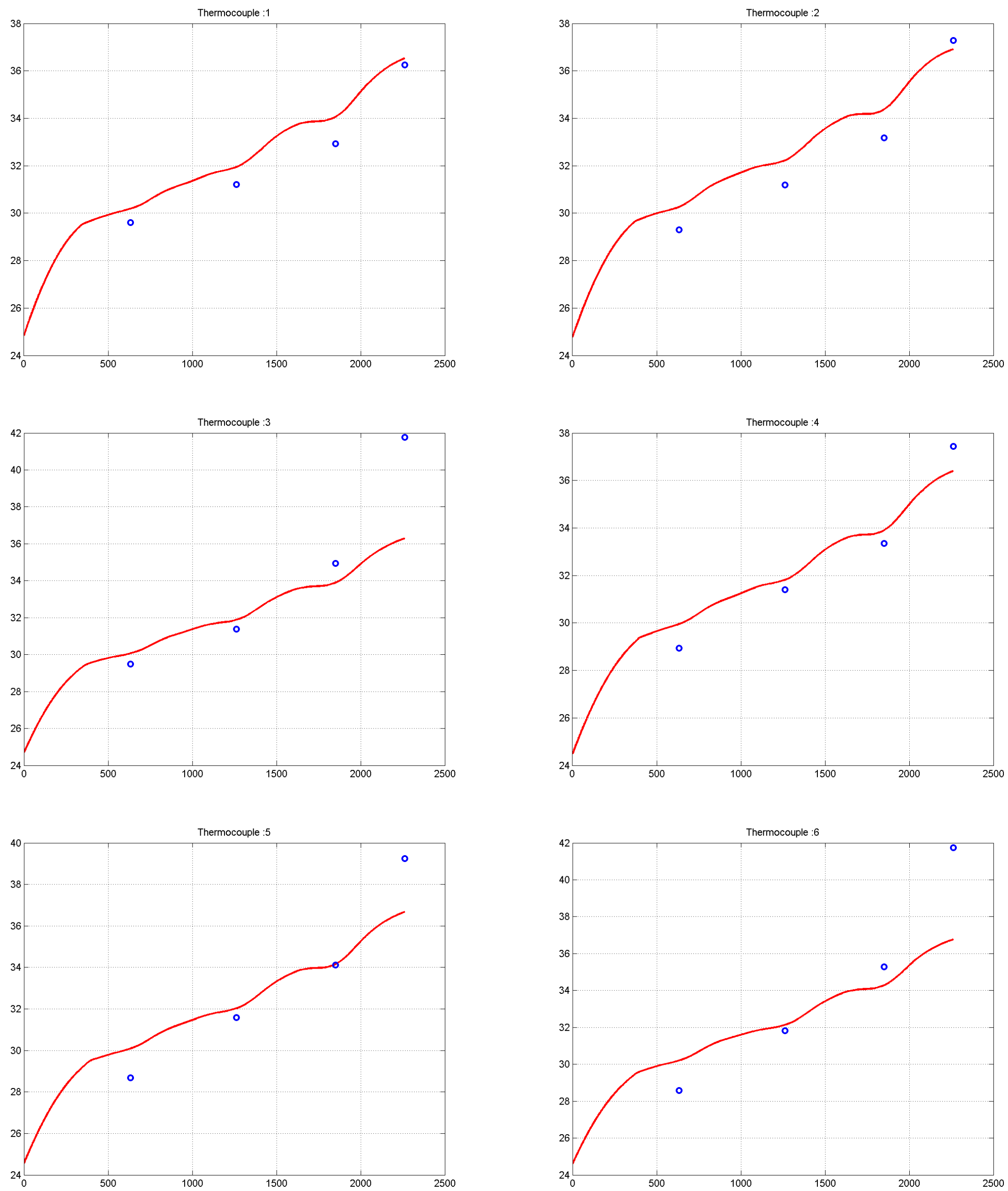

Figure A.12.: Comparison between experimental results (red line) and numerical results (blue dot); At 30 °C.

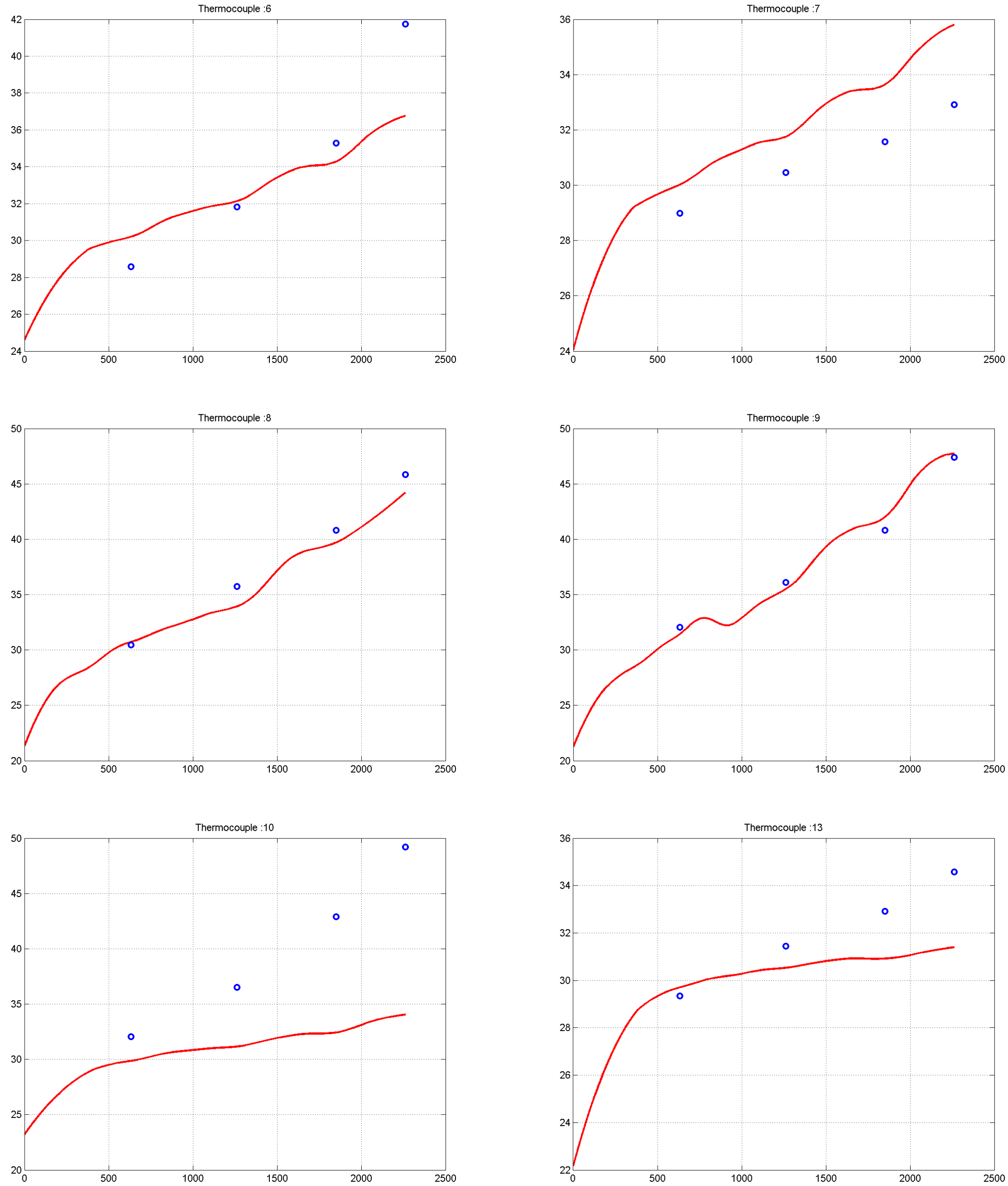

Figure A.13.: Comparison between experimental results (red line) and numerical results (blue dot); At 30 °C.

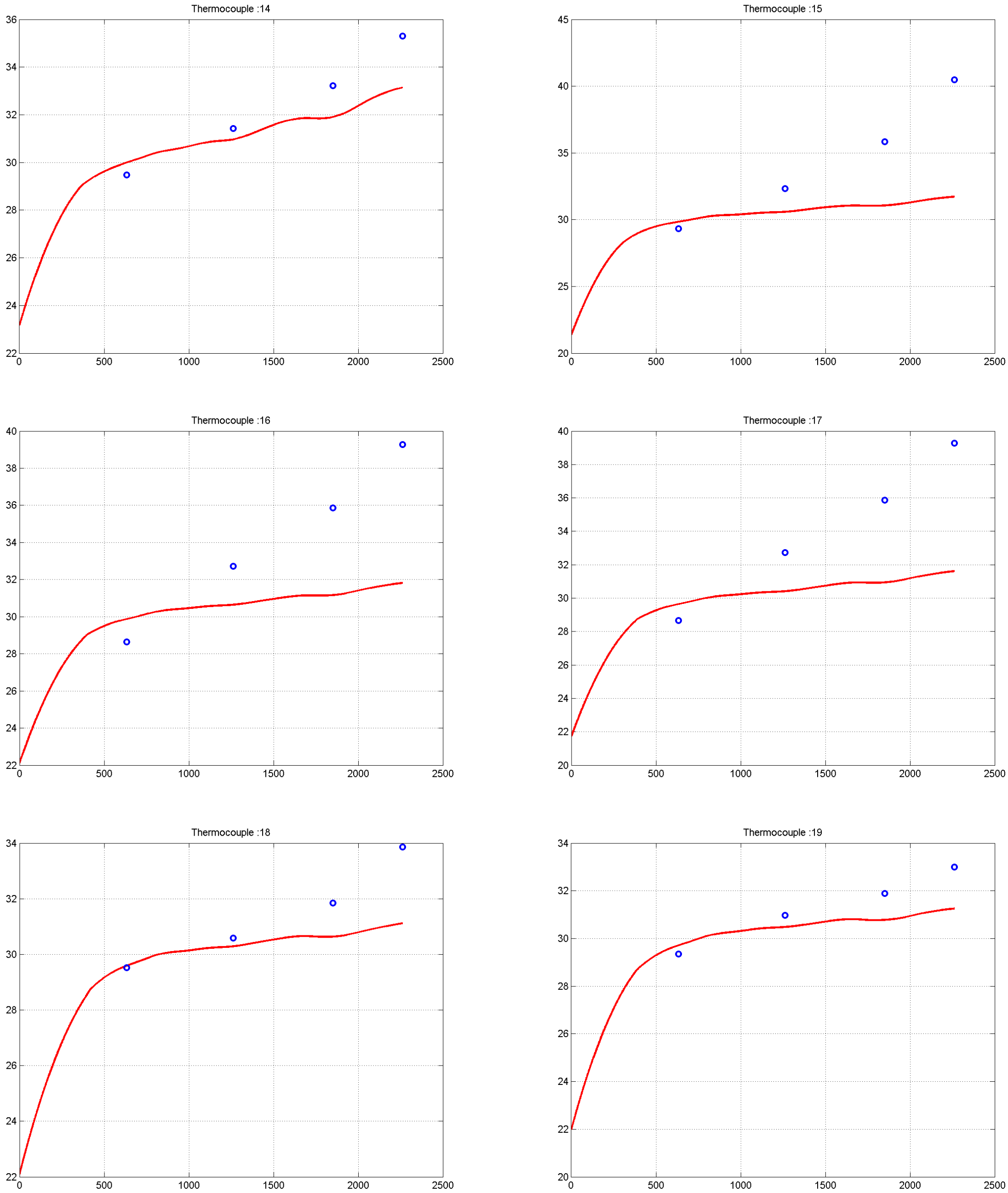

Figure A.14.: Comparison between experimental results (red line) and numerical results (blue dot); At 30 °C.

A.3. Case of climate chamber temperature $20\,^{\circ}\mathrm{C}$

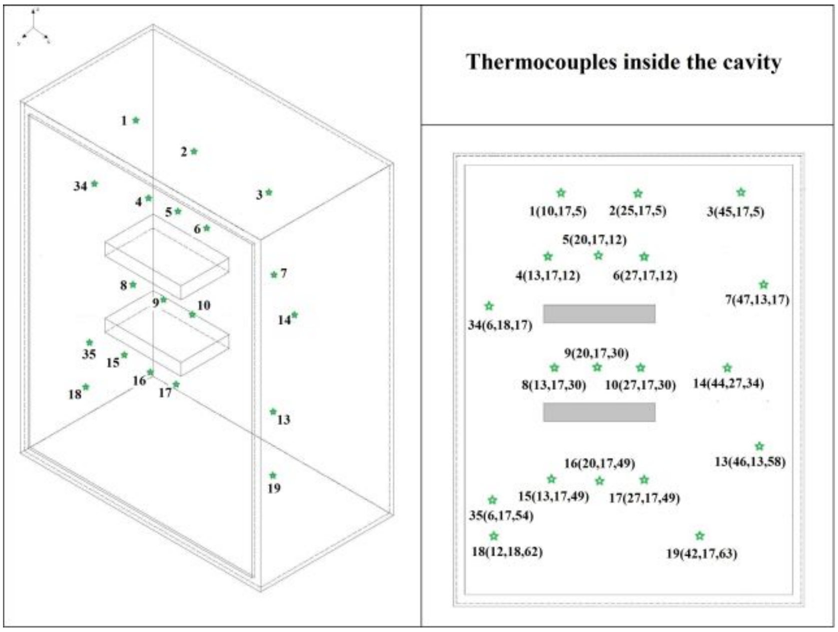

Figure A.15.: Thermocouple placement

Further measurements:

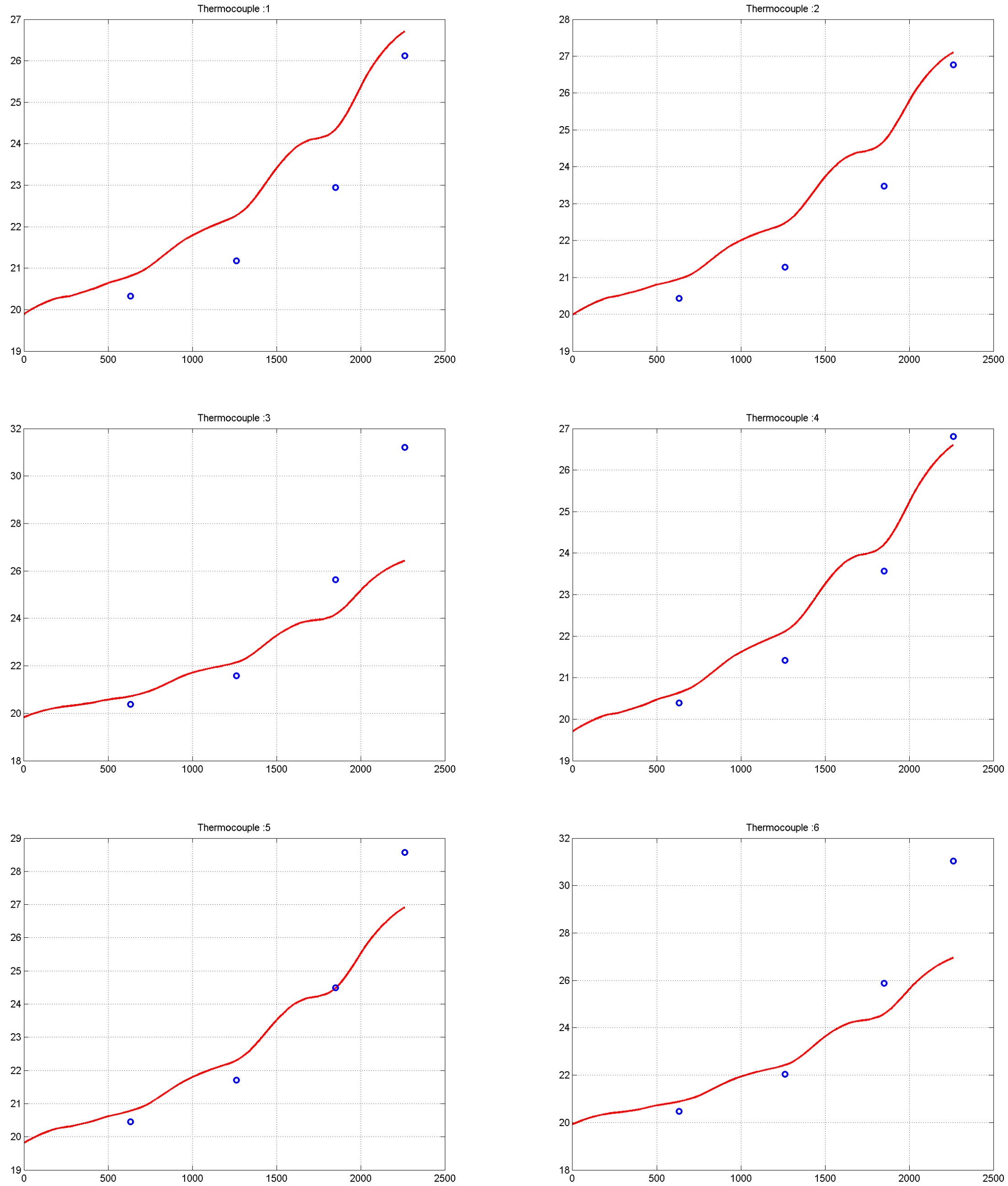

Figure A.16.: Comparison between experimental results (red line) and numerical results (blue dot); At 20 °C.

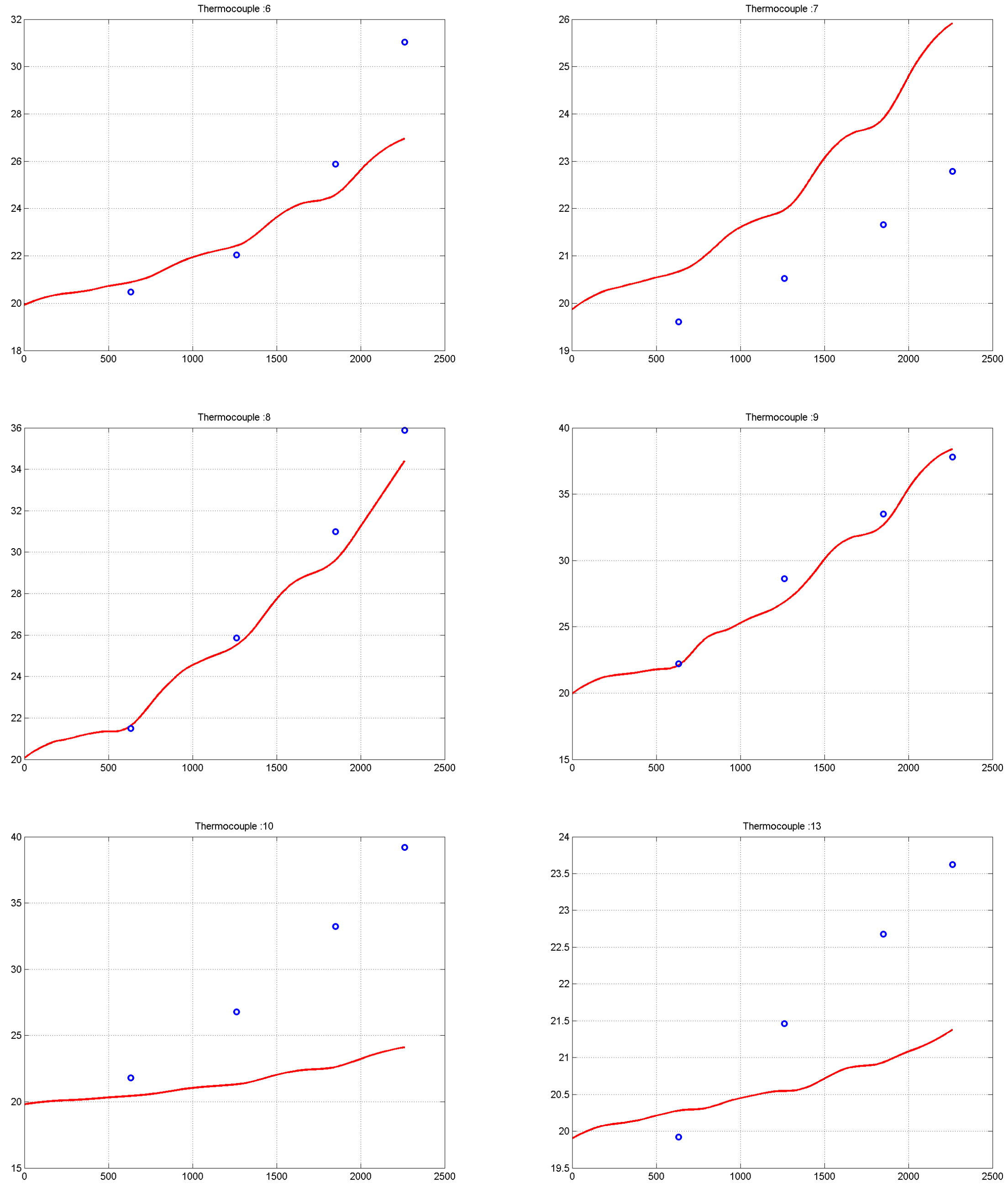

Figure A.17.: Comparison between experimental results (red line) and numerical results (blue dot); At 20 °C.

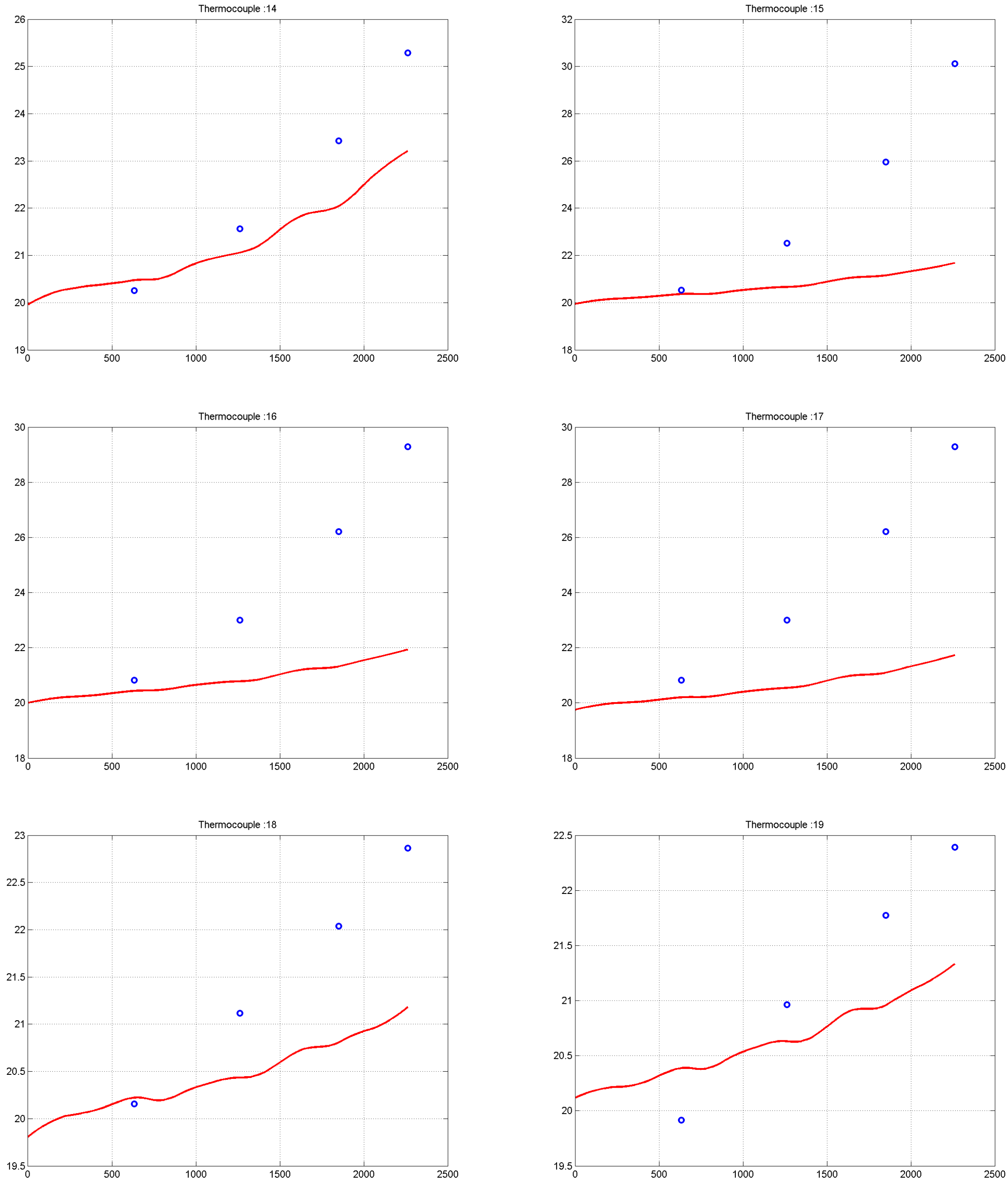

Figure A.18.: Comparison between experimental results (red line) and numerical results (blue dot); At 20 °C.

A.4. Both immersed objects are heated

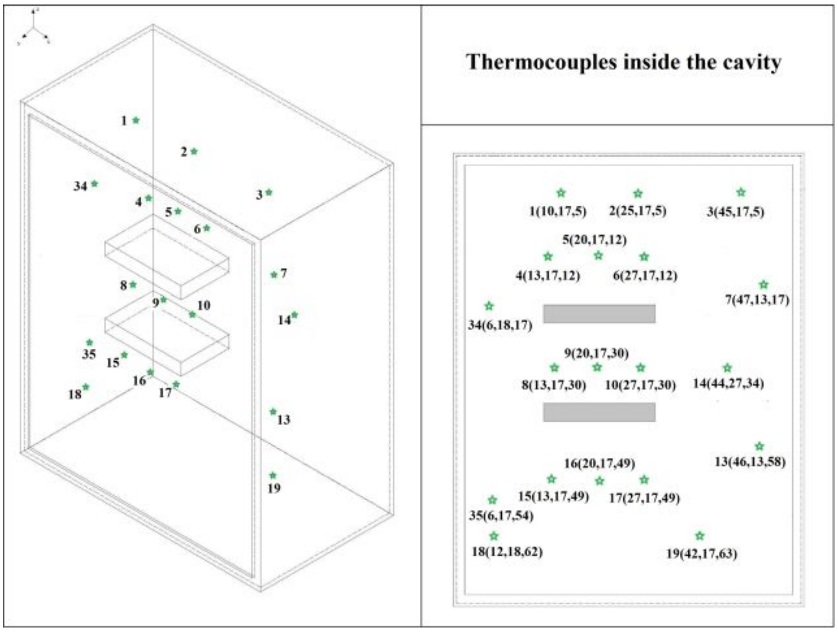

Figure A.19.: Thermocouple placement

Further measurements:

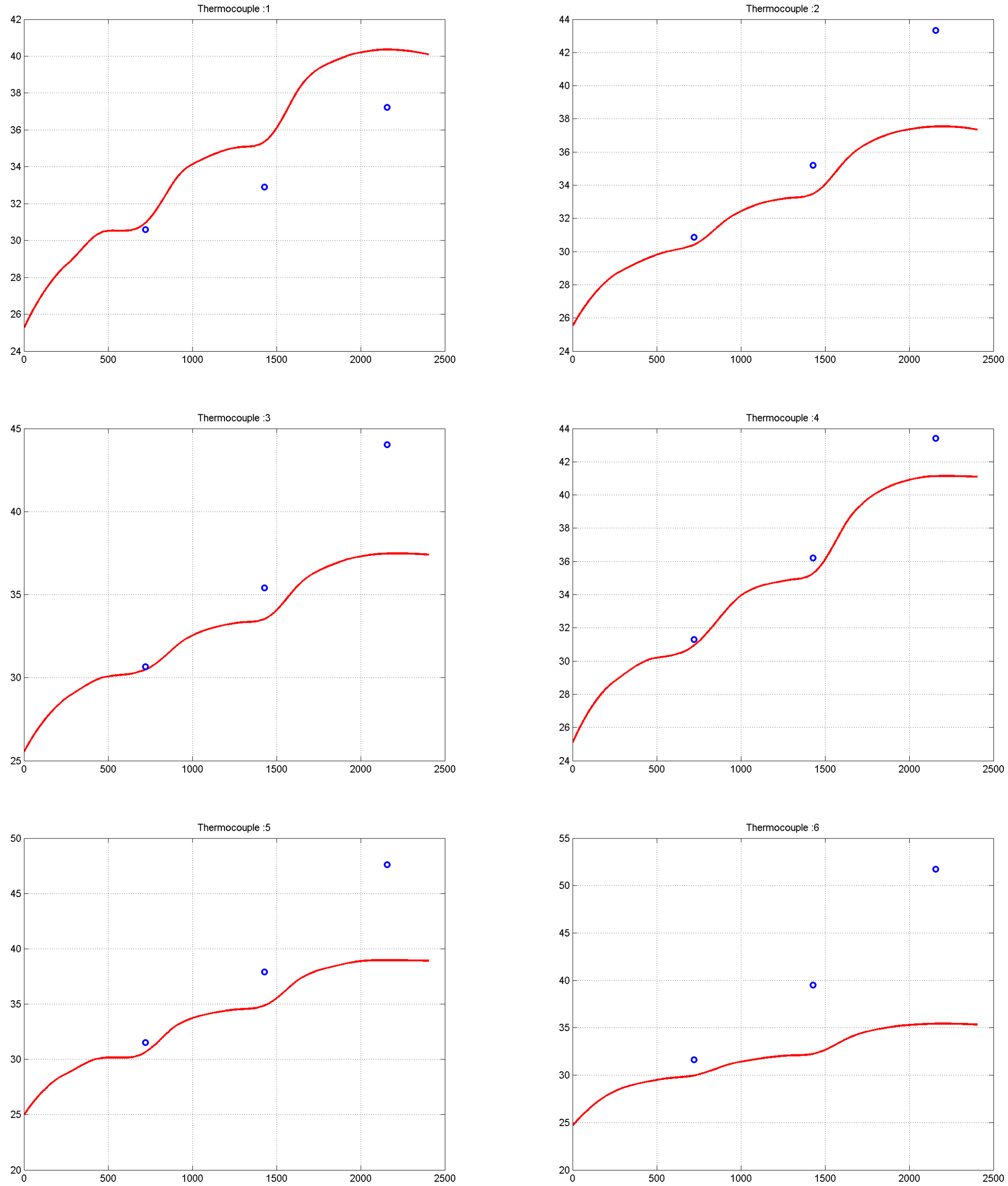

Figure A.20.: Comparison between experimental results (red line) and numerical results (blue dot); At 20 °C.

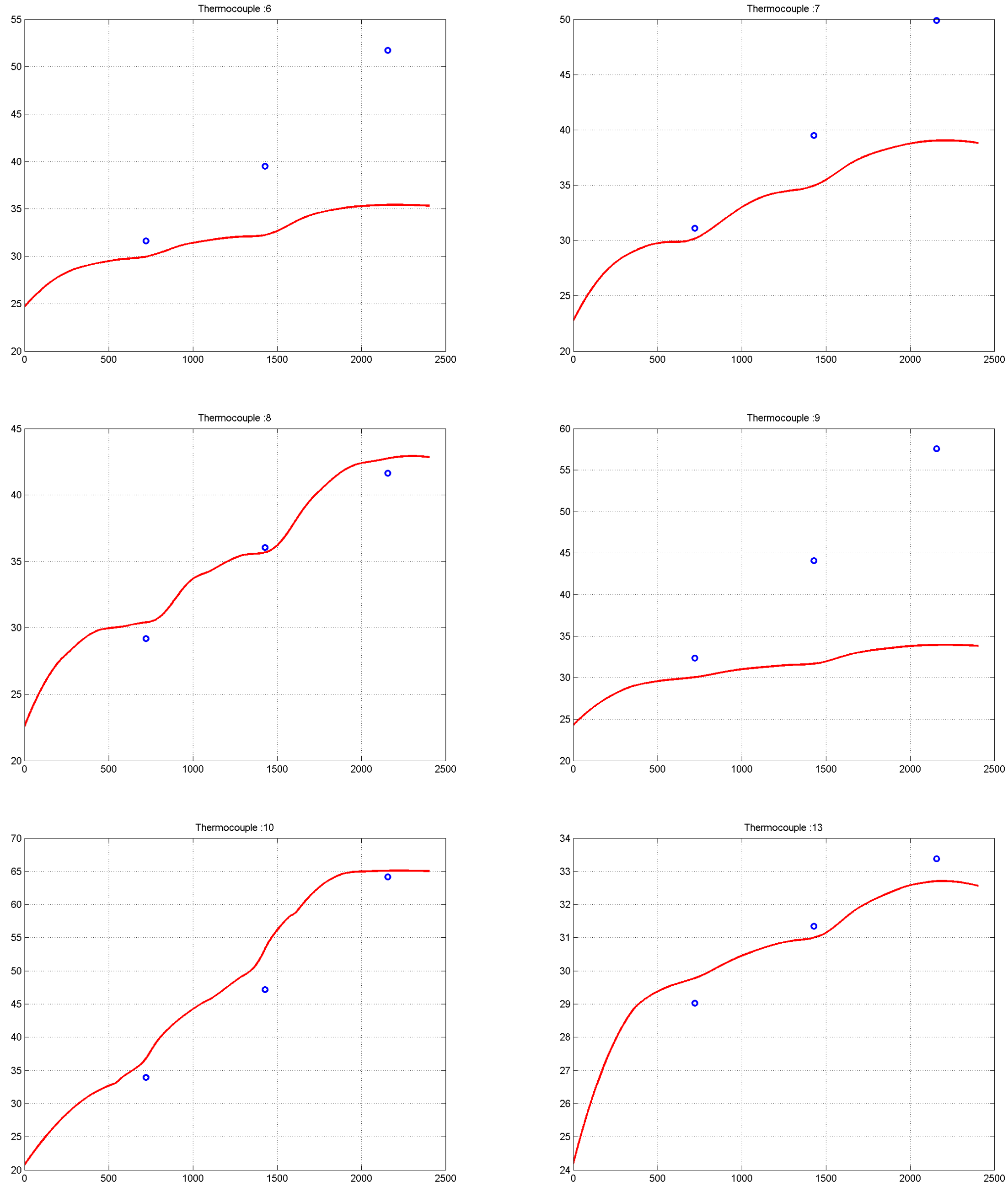

Figure A.21.: Comparison between experimental results (red line) and numerical results (blue dot); At 20 °C.

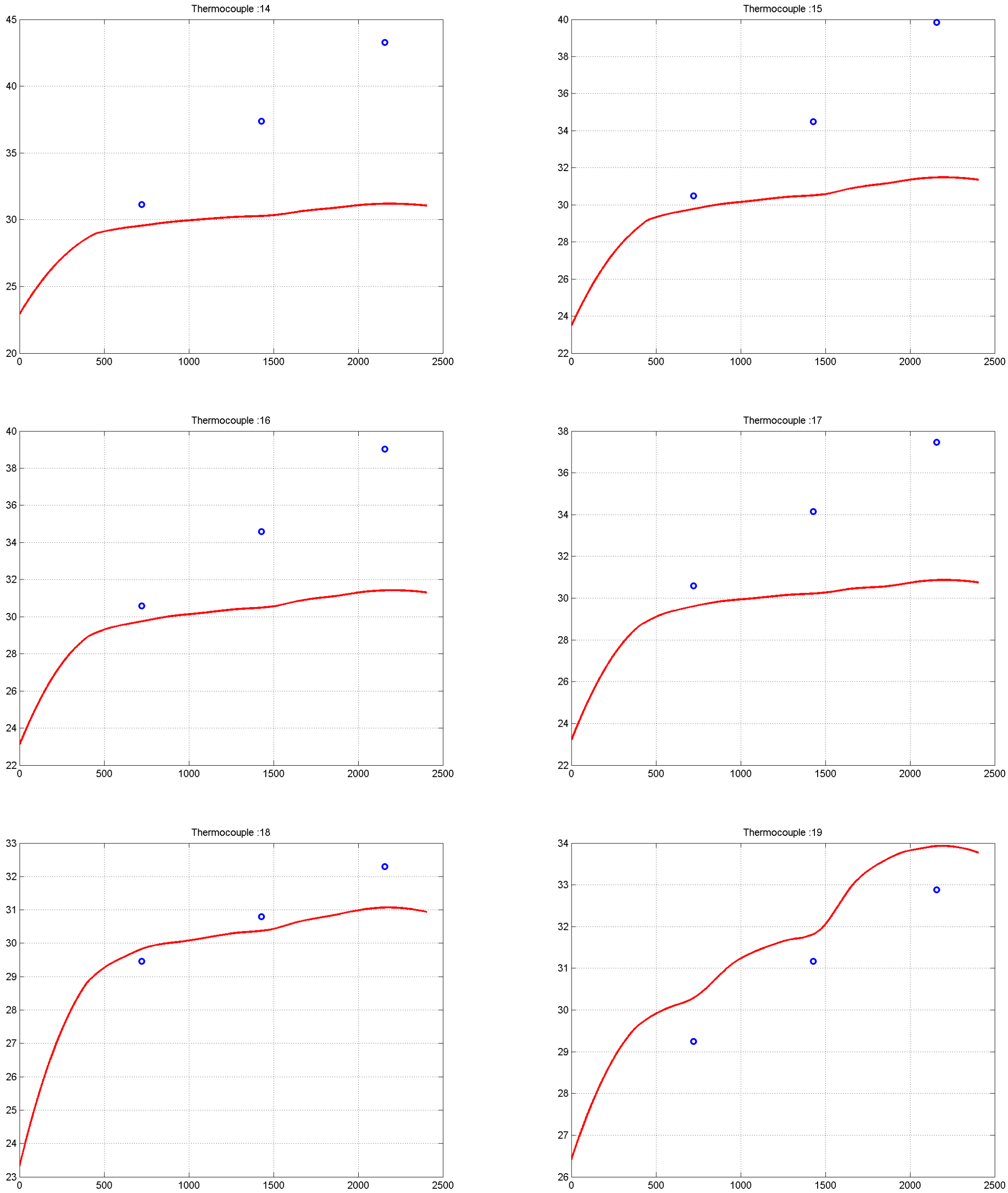

Figure A.22.: Comparison between experimental results (red line) and numerical results (blue dot); At 20 °C.

Bibliography

T. Acikalin, S.M. Wait, S.V. Garimella and A. Raman. Experimental investigation of the thermal performance of piezoelectric fans. *Heat Transfer Engineering*, 25(1):4–14, 2004.

D. Angirasa, J.G. Eggels and F.T.M. Nieuwstadt. Numerical simulation of transient natural convection from an isothermal cavity open on a side. *Numerical Heat Transfer, Part A: Applications*, 28(6):755–767, 1995.

D. Angirasa, M.J.B.M. Pourquie and F.T.M. Nieuwstadt. Numerical study of transient and steady laminar buoyancy–driven flows and heat transfer in a square open cavity. *Numerical Heat Transfer*, 22(2):223–239, 1992.

K. Azzouz, D. Leducq and D. Gobin. Performance enhancement of a household refrigerator by addition of latent heat storage. *International Journal of Refrigeration*, 31(5):892–901, 2008.

C. Balaji and S.P. Venkateshan. Combined conduction, convection and radiation in a slot. *International Journal of Heat and Fluid Flow*, 31(5):892–901, 2008.

E. Balaras. Modelling complex boundaries using an external force field on fixed Cartesian grids in large–eddy simulations. *Computers & Fluids*, 33(3):375–404, 2004.

M. Ballestra. *Etude numérique de la formation et de la dissipation des tourbillons créés par un jet conique monophasique.* Rapport de stage de DESS de mathématiques appliquées, Paris 6 et Institut Français du Pétrole, 2002.

G. Barakos, E. Mitsoulis and D. Assimacopoulos. Natural convection flow in a square cavity revised; Laminar and turbulent models with wall function. *International Journal for Numerical Methods in Fluids*, 18(7):695–719, 1994.

G. Barrios, R. Rechtman, J. Rojas and R. Tovar. The lattice Boltzmann equation for natural convection in a two–dimensional cavity with a partially heated wall. *Journal of Fluid Mechanics*, 522:91–100, 2005.

C. Benard, D. Gobin and A. Zanoli. Moving boundary problem: Heat conduction in the solid phase of a phase–change material during melting driven by natural convection in the liquid. *International Journal of Heat and Mass Transfer*, 29(11):1669–1681, 1986.

S. Benteboula. *Résolution des équations de Navier–Stokes à faible nombre de Mach : Application à l'étude de l'anneau tourbillonnaire à masse volumique variable.* PhD thesis, Université de Marne–la–Vallée, 2006.

R.P. Beyer. A computational model of the cochlea using the immersed boundary method. *Journal of Computational Physics*, 98(1):145–162, 1992.

H. Bhowmik and K.W. Tou. Experimental Study of Transient Natural Convection Heat Transfer from Simulated Electronic Chips. *Experimental Thermal and Fluid Science*, 29(4): 485–492, 2005.

S.M. Bilski, J.R. Lloyd and K.T. Yang. An experimental investigation of the laminar natural convection velocity in square and partitioned enclosures. *Heat Transfer*, –:1513–1518, 1986.

B.J. Boersma. A staggered compact finite difference formulation for the compressible Navier–Stokes equations. *Journal of Computational Physics*, 208(2):675–690, 2005.

B.J. Boersma. A 6th order staggered compact finite difference method for the incompressible Navier–Stokes and scalar transport equations. *Journal of Computational Physics*, 230(12): 4940–4954, 2011.

F. Bouchon, T. Dubois and N. James. A second-order cut-cell method for the numerical simulation of 2D flows past obstacles. *Computers & Fluids*, 65:80–91, 2012.

P. Burmann, A. Raman and S.V. Garimella. Dynamics and topology optimization of piezoelectric fans. *Components and Packaging Technologies, IEEE Transactions*, 25(4): 592–600, 2002.

H.F. Busse. Non–linear properties of thermal convection. *Reports on Progresses in Physics*, 41(12):1929–1967, 1978.

C. Butler, D. Newport and M. Geron. Natural convection experiments on a heated horizontal cylinder in a differentially heated square cavity. *Experimental Thermal and Fluid Science*, 44(1):199–208, 2013.

Q. Cai, C.L. Chen and J.F. Asfia. Operating characteristic investigations in pulsating heat pipe. *Journal of Heat Transfer*, 128(12):1329–1334, 2006.

D. Calhoun. A Cartesian grid method for solving the two-dimensional stream function-vorticity equations in irregular regions. *Journal of Computational Physics*, 176(2):231–275, 2002.

Y. Cao, A. Faghri and W.S. Chang. A numerical analysis of Stefan problems for generalized multi-dimensional phase-change structures using the enthalpy transforming model. *International Journal of Heat and Mass Transfer*, 32(7):1289–1298, 1989.

D.M. Causon, D.M Ingram and C.G. Mingham. A Cartesian cut cell method for shallow water flows with moving boundaries. *Advances in Water Resources*, 24(8):899–911, 2001.

Y.A. Cengel. *Heat Transfer: A Practical Approach.* McGraw-Hill series in mechanical engineering. McGraw-Hill, 2003.

W. Chakroun. Effect of boundary wall conditions on heat transfer for fully opened tilted cavity. *Journal of Heat Transfer*, 126(6):915–923, 2004.

W. Chakroun, M.M. Elsayed and S.F. Al-Fahed. Experimental measurements of heat transfer coefficient in a partially/fully opened tilted cavity. *Journal of Solar Energy Engineering*, 119(4):298–303, 1997.

Y.L. Chan and C.L. Tien. A numerical study of two-dimensional natural convection in square open cavities. *Numerical Heat Transfer*, 8(1):65–80, 1985.

Y.L. Chan and C.L. Tien. Laminar natural convection in shallow open cavities. *Journal of Heat Transfer*, 108(2):305–309, 1986.

P. Charoensawan, S. Khandekar, M. Groll and P. Terdtoon. Closed loop pulsating heat pipes. Part A: Parametric experimental investigations. *Applied Thermal Engineering*, 23(16):2009–2020, 2003.

D.J. Chen, K.H. Lin and C.A. Lin. Immersed boundary method based lattice Boltzmann method to simulate 2D and 3D complex geometry flows. *International Journal of Modern Physics*, 18(4):585–594, 2007.

K.S. Chen, J.A.C. Humphrey and C. Miller. Note on the pulsating nature of thermally-driven open cavity flow. *International Journal of Heat and Mass Transfer*, 26(7):1090–1093, 1983.

K.S. Chen, J.A.C. Humphrey and F.S. Sherman. Free and mixed convective flow of air in a heated cavity of variable rectangular cross section and orientation. *Philosophical Transactions of the Royal Society of London. Series A, Mathematical and Physical Sciences*, 316(1535):57–84, 1985.

C.S. Chew, K.S. Yeo and C. Shu. A generalized finite-difference (GFD) ALE scheme for incompressible flows around moving solid bodies on hybrid meshfree- Cartesian grids. *Journal of Computational Physics*, 218(2):510–548, 2006.

J. Choi, J. Jeon and Y. Kim. Cooling performance of a hybrid refrigeration system designed for telecommunication equipment rooms. *Applied Thermal Engineering*, 27(11): 2026–2032, 2007.

A.J. Chorin. Numerical solution of the Navier–Stokes equations. *Mathematics of computation*, 22(104):745–762, 1968.

P. Chu and C. Fan. A three point combined compact difference scheme. *Journal of Computational Physics*, 140(2):370–399, 1998.

M.-H. Chung. An adaptive Cartesian cut-cell/level-set method to simulate incompressible two-phase flows with embedded moving solid boundaries. *Computers & Fluids*, 71:469 – 486, 2013.

Y.J. Chung, H.C. Kim, B.D. Chung, M.K. Chung and S.Q. Zee. Two-phase natural circulation and the heat transfer in the passive residual heat removal system of an integral type reactor. *Annals of Nuclear Energy*, 33(3):262–270, 2006.

P. Cinato, C. Bianco, L. Licciardi, F. Pizzuti, M. Antonetti and M. Grossoni. An innovative approach to the environmental system design for TLC rooms in Telecom Italia. In *Telecommunications Energy Conference, 1998. INTELEC. Twentieth International*, pages 770–776. IEEE, 1998.

A.M. Clausing. Convective losses from cavity solar receivers- comparisons between analytical predictions and experimental results. *Journal of Solar Energy Engineering*, 105(1):29–33, 1982.

A.M. Clausing, J.M. Waldvogel and L.D. Lister. Natural convection from isothermal cubical cavities with a variety of side-facing apertures. *Journal of Heat Transfer*, 109(2): 407–412, 1987.

T. Colonius, S.K. Lele and P. Moin. Sound generation in a mixing layer. *Journal of Fluid Mechanics*, 330:375–409, 1997.

G. Comini, G. Cortella and M. Manzan. Natural Convection in Rectangular Open Cavities. *Transactions on Engineering Sciences*, 12:13–22, 1996.

G.S. Constantinescu and S.K. Lele. Large eddy simulation of a near sonic turbulent jet and its radiated noise. *AIAA Paper*, 2001:376, 1991.

A. Cristallo and R. Verzicco. Combined immersed boundary/large-eddy-simulations of incompressible three-dimensional complex flows. *Flow, Turbulence and Combustion*, 77(1–4):3–26, 2006.

I. Danaila. *Code JETLES. Simulations numériques directes (DNS) et des grandes échelles (LES) des écoulements incompressibles en coordonnées cylindriques.* Documentation du code JETLES, Paris 6, 1999–2008.

I. Danaila and J. Hélie. Numerical simulation of the postformation evolution of a laminar vortex ring. *Physics of Fluids*, 20:073602, 2008.

I. Danaila, R. Moglan, F. Hecht and S. Le Masson. A Newton method with adaptive finite elements for solving phase-change problems with natural convection. -, -, submitted.

I. Danaila, C. Vadean and S. Danaila. Specified discharge velocity models for the numerical simulation of laminar vortex rings. *Theoretical and Computational Fluid Dynamics*, 23 (5):317–332, 2009.

P. De Palma, M.D. de Tullio, G. Pascazio and M. Napolitano. An immersed boundary method for compressible viscous flows. *Computers & fluids*, 35(7):693–702, 2006.

M.D. de Tullio, P. De Palma, G. Iaccarino, G. Pascazio and M. Napolitano. An immersed boundary method for compressible flows using local grid refinement. *Journal of Computational Physics*, 225(2):2098–2117, 2007.

G. de Vahl Davis. Natural convection of air in a square cavity: A benchmark numerical solution. *International Journal for Numerical Methods in Fluids*, 3(3):249–264, 1983.

G. de Vahl Davis and I.P. Jones. Natural convection of air in a square cavity: A comparison exercise. *International Journal for Numerical Methods in Fluids*, 3(3):227–248, 1983.

D. Delaunay. *Etude du couplage convection naturelle-conduction avec changement de phase: application au stockage périodique de l'énergie.* PhD thesis, Thèse d'Etat: Université de Nantes, 1985.

J.J.E. Dennis and R.B. Schnabel. *Numerical methods for unconstrained optimization and nonlinear equations.*, volume 16. Siam, 1983.

G.R. Dimmick, V. Chatoorgoon, H.F. Khartabil and R.B. Duffey. Natural–convection studies for advanced CANDU reactor concepts. *Nuclear engineering and design*, 215(1):27–38, 2002.

H. Ding, C. Shu, K.S. Yeo and D. Xu. Development of least-square-based two-dimensional finite-difference schemes and their application to simulate natural convection in a cavity. *Computers & fluids*, 33(1):137–154, 2004a.

H. Ding, C. Shu, K.S. Yeo and D. Xu. Simulation of incompressible viscous flows past a circular cylinder by hybrid FD scheme and meshless least square based finite difference method. *Computer Methods in Applied Mechanics and Engineering*, 193(9):727–744, 2004b.

F. Domenichini. On the consistency of the direct forcing method in the fractional step solution of the Navier–Stokes equations. *Journal of Computational Physics*, 227(12):6372–6384, 2008.

C. Eason, T. Dalton, C. O'Mathúna, M. Davies and O. Slattery. Direct comparison between five different micro–channels part 1: Channel manufacture and measurement. *Heat Transfer Engineering*, 26:79–88, 2005.

M.M. Elsayed and W. Chakroun. Effect of aperture geometry on heat transfer in tilted partially open cavities. *Journal of Heat Transfer*, 121(4):819–827, 1999.

Norme ETSI. *Environmental conditions and environmental test for telecommunications equipment.* Rapport technique, 2000.

K.J. Evans, D.A. Knoll and M. Pernice. Development of a 2D algorithm to simulate convection and phase transition efficiently. *Journal of Computational Physics*, 219(1):404 – 417, 2006.

E.A. Fadlun, R. Verzicco, P. Orlandi and J. Mohd-Yusof. Combined Immersed-Boundary Finite–Difference Methods for Three–Dimensional Complex Flow Simulations. *Journal of Computational Physics*, 161(1):35–60, 2000.

A. Faghri and Y. Zhang. *Transport Phenomena in Multiphase Systems.* Academic Press, 2006.

L. Fauci and C.S. Peskin. A computational model of aquatic animal locomotion. *Journal of Computational Physics*, 77(1):85–108, 1988.

K.J. Fidkowski and D.L. Darmofal. A triangular cut–cell adaptive method for high-order discretizations of the compressible Navier–Stokes equations. *Journal of Computational Physics*, 225(2):1653–1672, 2007.

L.A. Florio and A. Harnoy. Combination Technique for Improving Natural Convection Cooling in Electronics. *International Journal of Thermal Sciences*, 46(1):76–92, 2007.

A.L. Fogelson. A mathematical model and numerical method for studying platelet adhesion and aggregation during blood clotting. *Journal of Computational Physics*, 56(1):111–134, 1984.

A.L. Fogelson and C.S. Peskin. A fast numerical method for solving the three-dimensional Stokes equations in the presence of suspended particles. *Journal of Computational Physics*, 79(1):50–69, 1988.

T. Freund, S.K. Lele and P. Moin. Compressibility effects in a turbulent annular mixing layer part 1. Turbulence and growth rate. *Journal of Fluid Mechanics*, 421(1):229–267, 2000.

T. Fusegi, J.M. Hyun and K. Kuwahara. Numerical simulations of natural convection in a differentially heated cubical enclosure with a partition. *International Journal of Heat and Fluid Flow*, 13(2):176–183, 1992.

T. Fusegi, J.M. Hyun, K. Kuwahara and B. Farouk. A numerical study of three-dimensional natural convection in a differentially heated cubical enclosure. *International Journal of Heat and Mass Transfer*, 34(6):1543–1557, 1991.

L. Gamet, Ducros, F. F., Nicoud and T. Poinsot. Compact finite difference schemes on non-uniform meshes. Application to direct numerical simulation of compressible flows. *International journal for numerical methods in fluids*, 29(2):159–191, 1999.

P.L. George and H. Borouchaki. *Delaunay triangulation and meshing.* Hermès, Paris, 1998.

S. Ghader, A. Ghasemi, M.R. Banazadeh and D. Mansoury. High–order compact scheme for Boussinesq equations: implementation and numerical boundary condition issue. *International Journal for Numerical Methods in Fluids*, 69(3):590–605, 2012.

R. Ghias, R. Mittal and H. Dong. A sharp interface immersed boundary method for compressible viscous flows. *Journal of Computational Physics*, 225(1):528–553, 2007.

C. Gillot, A. Bricard and C. Schaeffer. Single- and two-phase heat exchangers for power electronic components. *International Journal of Thermal Science*, 39(8):826–832, 2000.

A. Gilmanov, F. Sotiropoulos and E. Balaras. A general reconstruction algorithm for simulating flows with complex 3D immersed boundaries on Cartesian grids. *Journal of Computational Physics*, 191(2):660–669, 2003.

D. Goldstein, R. Handler and L. Sirovich. Modelling a no–slip flow with an external force field. *Journal of Computational Physics*, 105(2):354–366, 1993.

M. Groll, M. Schneider, V. Sartre, M.C. Zaghdoudi and M. Lallemandl. Thermal control of electronic equipment by heat pipes. *Revue Générale de Thermique*, 37(5):323–352, 1998.

F.J. Hamady, K.T. Yang, H.Q. Yang and J.R. Lloyd. A Study of Natural Convection in a Rotating Enclosure. *Journal of Heat Transfer*, 116(1):136–143, 1994.

N. Hannoun, V. Alexiades and T. Z. Mai. A reference solution for phase change with convection. *International Journal For Numerical Methods In Fluids*, 48(11):1283–1308, 2005.

F.H. Harlow and J.E. Welch. Numerical calculation of time–dependent viscous incompressible flow of fluid with a free surface. *Physics of Fluids*, 8(12):2182–2189, 1965.

A. Harten. High resolution schemes for hyperbolic conservation laws. *Journal of Computational Physics*, 49(3):357–393, 1983.

D. Hartmann, M. Meinke and W. Schröder. A strictly conservative Cartesian cut–cell method for compressible viscous flows on adaptive grids. *Computer Methods in Applied Mechanics and Engineering*, 200(9):1038–1052, 2011.

F. Hecht, O. Pironneau, J. Morice, S. Auliac, A. Le Hyaric and K. Ohtsuka. *FreeFem++.* Third Edition, Version 3.22. Laboratoire Jacques–Louis Lions, Université Pierre et Marie Curie, Paris, 2012.

C.F. Hess and R.H. Henze. Experimental investigations of natural convection losses from open cavities. *Journal of Heat Transfer*, 106(2):333–338, 1984.

J.F. Hinojosa, G. Alvarez and C.A. Estrada. Three–dimensional numerical simulation of the natural convection in an open tilted cubic cavity. *Revista Mexicana de Física*, 52(2): 111–119, 2006.

J.F. Hinojosa and J. Cervantes de Gortari. Numerical simulation of steady–state and transient natural convection in an isothermal open cubic cavity. *Heat and Mass Transfer*, 46(6):595–606, 2010.

M. Hortmann, M. Peric and G. Scheuerer. Finite volume multi grid prediction of laminar natural convection: bench-mark solutions. *International Journal for Numerical Methods in Fluids*, 11(2):189–207, 1990.

G. Huelsz and R. Rechtman. Heat transfer due to natural convection in an inclined square cavity using the lattice Boltzmann equation method. *International Journal of Thermal Sciences*, 65(0):111 – 119, 2013.

H.J. Hussein, S.P. Capp and W.K. George. Velocity measurements in a high Reynolds number momentum-conserving axisymmetric turbulent jet. *Journal of Fluid Mechanics*, 258 (1):31–75, 1994.

D.M. Ingram, D.M. Causon and C.G. Mingham. Developments in Cartesian cut cell methods. *Mathematics and Computers in Simulation*, 61(3):561–572, 2003.

Mohd-Yusof J. Combined immersed boundary/B–Spline method for simulations offlows in complex geometries CTR annual research briefs. *Annual Research Briefs. NASA Ames Research Center; Stanford University Center of Turbulence Research: Stanford*, 171(1):132–150, 2001.

R.J.A. Janssen and R.A.W.M. Henkes. Influence of Prandtl number on instability mechanism and transition in a differentially heated cavity. *Journal of Fluid Mechanics*, 290: 319–344, 1995.

R.J.A. Janssen, R.A.W.M. Henkes and C.J. Hoogendoorn. Transition to time-periodicity of a natural–convection flow in a 3D differentially heated cavity. *International journal of heat and mass transfer*, 36(11):2927–2940, 1993.

P. Jany and A. Bejan. Scaling theory of melting with natural convection in an enclosure. *International Journal of Heat and Mass Transfer*, 31(6):1221 – 1235, 1988.

H. Ji, F.S. Lien and E. Yee. A robust and efficient hybrid cut–cell/ghost–cell method with adaptive mesh refinement for moving boundaries on irregular domains. *Computer Methods in Applied Mechanics and Engineering*, 198(3):432–448, 2008.

H. Ji, F.S. Lien and E. Yee. Numerical simulation of detonation using an adaptive Cartesian cut–cell method combined with a cell–merging technique. *Computers & Fluids*, 39(6):1041–1057, 2010a.

H. Ji, F.S. Lien and E. Yee. Numerical simulation of detonation using an adaptive Cartesian cut-cell method combined with a cell–merging technique. *Computers & Fluids*, 39(6):1041–1057, 2010b.

W. Jia, Y. Nakamura and M. Yasuhara. Natural convection flow solver in primitive variable form. *Journal of Japan Society of Fluid Mechanics*, 9(1):34–52, 1990.

L.F. Jin, K.W. Tou and C.P. Tso. Effect of Rotations on Natural Convection Cooling from an Array of Discrete Heat Sources in a Rectangular Cavity. *International Journal of Heat Mass Transfer*, 48(19):3982–3994, 2005.

W. Terrell Jr. and Ty.A. Newell. Localized heat transfer in buoyancy driven convection in open cavities. *Journal of Heat Transfer*, 129(2):167–178, 2007.

J.O. Juárez, J.F. Hinojosa and J.P. Xamánand Manuel Pérez Tello. Numerical study of natural convection in an open cavity considering temperature–dependent fluid properties. *International Journal of Thermal Sciences*, 50(11):2184 – 2197, 2011.

S. Khandekar, N. Dollinger and M. Groll. Understanding operational regimes of pulsating heat pipes: An experimental study. *Applied Thermal Engineering*, 23(6):707–719, 2003.

S. Khandekar and M. Groll. An insight into thermo–hydraulic coupling in pulsating heat pipes. *International Journal of Thermal Sciences*, 43(1):13–20, 2004.

B.S. Kim, D.S. Lee, M.Y. Ha and H.S. Yoon. A numerical study of natural convection in a square enclosure with a circular cylinder at different vertical locations. *International Journal of Heat and Mass Transfer*, 51(7):1888–1906, 2008.

D. Kim and H. Choi. Immersed boundary method for flow around an arbitrarily moving body. *Journal of Computational Physics*, 212(2):662–680, 2006.

J. Kim, D. Kim and H. Choi. An Immersed–Boundary Finite–Volume Method for Simulations of Flow in Complex Geometries. *Journal of Computational Physics*, 171(1):132–150, 2001.

J. Kim and P. Moin. Application of a fractional step method to incompressible Navier–Stokes equations. *Journal of computational physics*, 59(2):308–323, 1985.

Y. Koito, H. Imura, M. Mochizuki, Y. Saito and S. Torii. Numerical analysis and experimental verification on thermal fluid phenomena in a vapor chamber. *Applied Thermal Engineering*, 26(14):1669–1676, 2006.

J.L. Lage, J.S. Lim and A. Bejan. Natural convection with radiation in a cavity with open top end. *Journal of Heat Transfer*, 114(2), 1992.

M.C. Lai and C.S. Peskin. An immersed boundary method with formal second–order accuracy and reduced numerical viscosity. *Journal of Computational Physics*, 160(2):705–719, 2000.

S. Laizet and E. Lamballais. High–order compact schemes for incompressible flows: A simple and efficient method with quasi–spectral accuracy. *Journal of Computational Physics*, 228(16):5989–6015, 2009.

P. Lamberg and K. Siren. Approximate analytical model for solidification in a finite PCM storage with internal fins. *Applied Mathematical Modelling*, 27(7):491–513, 2003.

D.V. Le, B.C. Khoo and K.M. Lim. An implicit–forcing immersed boundary method for simulating viscous flows in irregular domains. *Computer Methods in Applied Mechanics and Engineering*, 197(25):2119–2130, 2008.

S. Le Masson, D. Nörtershäuser, D. Mondieig and H. Louahlia-Gualous. Towards passive cooling solutions for mobile access network. *Institut Télécom and Springer–Verlag*, 67:125–132, 2012.

P. Le Quéré and M. Behnia. From onset of unsteadiness to chaos in a differentially heated square cavity. *Journal of Fluid Mechanics*, 359(1):81–107, 1998.

S. Lee, H. Kang and Y. Kim. Performance optimization of a hybrid cooler combining vapor compression and natural circulation cycles. *International journal of refrigeration*, 32 (5):800–808, 2009.

S.S. Lee, S.K. Lele and P. Moin. Interaction of isotropic turbulence with shock waves: effect of shock strength. *Journal of Fluid Mechanics*, 340(1):225–247, 1997.

U. Leibfried and J. Ortjohann. Convective heat loss from upward and downward facing cavity solar receivers: Measurements and calculations. *Journal of Solar Energy Engineering*, 117(2):75–84, 1995.

S.K. Lele. Compact finite difference schemes with spectral–like resolution. *Journal of Computational Physics*, 103(1):16–42, 1992.

W.H. Leong, K.G.T. Hollands and A.P. Brunger. Experimental Nusselt numbers for a cubical–cavity benchmark problem in natural convection. *International Journal of Heat and Mass Transfer*, 42(11):1979–1989, 1998.

G. Leplat, E. Laroche, P. Reulet and P. Millan. Simulations Numériques 2D d'un Ecoulement Laminaire Instable de Convection Naturelle en Milieu Confiné. Congrès Français de Thermique, 2009.

R.J. Leveque and Z. Li. The immersed interface method for elliptic equations with discontinuous coefficients and singular sources. *SIAM Journal on Numerical Analysis*, 31(4): 1019–1044, 1994.

Z. Li and M.C. Lai. The immersed interface method for the Navier–Stokes equations with singular forces. *Journal of Computational Physics*, 171(2):822–842, 2001.

C.C. Liao, Y.W. Chang, C.A. Lin and J.M. McDonough. Simulating flows with moving rigid boundary using immersed–boundary method. *Computers & Fluids*, 39(1): 152–167, 2010.

L. Lin. Experimental investigation of oscillation heat pipes. *Journal of Thermophysics and Heat Transfer*, 15(4):395–400, 2001.

S.C. Lin and C.A. Chou. Blockage effect of axial–flow fans applied on heat sink assembly. *Applied thermal engineering*, 24(16):2375–2389, 2004.

T. Liszka. An Interpolation method for an irregular net of nodes. *International Journal for Numerical Methods in Engineering*, 20(9):1599–1612, 1984.

T. Liszka and J. Orkisz. The finite difference method at arbitrary irregular grids and its application in applied mechanics. *Computers & Structures*, 11(1):83–95, 1980.

T.J. Liszka, C.A.M. Duarte and W.W. Tworzydlo. Hp–Meshless cloud method. *Computer Methods in Applied Mechanics and Engineering*, 139(1):263–288, 1996.

G. Longworth and N. Hartley. Mössbauer effect study of nitrogen–implanted iron foils. *Thin Solid Films*, 48(1):95–104, 1978.

H. Luo, R. Mittal, X. Zheng, S.A. Bielamowicz, R.J. Walsh and J.K. Hahn. An immersed-boundary method for flow–structure interaction in biological systems with application to phonation. *Journal of Computational Physics*, 227(22):9303–9332, 2008.

Z. Ma and Y. Zhang. Solid velocity correction schemes for a temperature transforming model for convection phase change. *International Journal For Numerical Methods Heat Fluid Flow*, 16(2):204–225, 2006.

K. Mahesh, S.K. Lele and P. Moin. The influence of entropy fluctuations on the interaction of turbulence with a shock wave. *Journal of Fluid Mechanics*, 334:353–379, 1997.

G.D. Mallinson and G. de Vahl Davis. Three–dimensional natural convection in a box: A numerical study. *Journal of Fluid Mechanics*, 83(1):1–31, 1977.

J.Y. Malo, C. Bassi, T. Cadiou, M. Blanc, A. Messie and A. Tosseloand P. Dumaz. Gas–cooled fast reactors–DHR systems, preliminary design and thermal–hydraulics studies. *Nuclear Engineering and Technology*, 38(2):129–138, 2006.

M.A.H. Mamun, W.H. Leong, K.G.T. Hollands and D.A. Johnson. Cubical–cavity natural–convection benchmark experiments: An extension. *International Journal of Heat and Mass Transfer*, 46(19):3655 – 3660, 2003.

S. Marella, S. Krishnan, H. Liu and H.S. Udaykumar. Sharp interface Cartesian grid method I: An easily implemented technique for 3D moving boundary computations. *Journal of Computational Physics*, 210(1):1–31, 2005.

W.L. Marshall and C.T.A. Chen. Amorphous silica solubilities V. Predictions of solubility behaviour in aqueous mixed electrolyte solutions to 300 C. *Geochimica et Cosmochimica Acta*, 46(2):289–291, 1982.

G.E. McCreery. Liquid flow and vapor formation phenomena in a flat heat pipe. *Heat Transfer Engineering*, 15(4):33–41, 1994.

R.J. McGlen, R. Jachuck and S. Lin. Integrated thermal management techniques for high power electronic devices. *Applied Thermal Engineering*, 24(8–9):1143–1156, 2004.

F. Penot M.D. Pavlović and. Experiments in the mixed convection regime in an isothermal open cubic cavity. *Experimental Thermal and Fluid Science*, 4(6):648–655, 1991.

R. Mittal, H. Dong, M. Bozkurttas, F.M. Najjar, A. Vargas and A. von Loebbecke. A versatile sharp interface immersed boundary method for incompressible flows with complex boundaries. *Journal of Computational Physics*, 227(10):4825–4852, 2008.

R. Mittal and G. Iaccarino. Immersed boundary method. *Annual Reviews of Fluid Mechanics*, 37:239–261, 2005a.

R. Mittal and G. Iaccarino. IMMERSED BOUNDARY METHODS. *Annual Review of Fluid Mechanics*, 37(1):239–261, 2005b.

A.A. Mohamad. Natural convection in open cavities and slots. *Numerical Heat Transfer*, 27(6):705–716, 1995.

A.A. Mohamad, M. El-Ganaoui and R. Bennacer. Lattice Boltzmann simulation of natural convection in an open ended cavity. *International Journal of Thermal Sciences*, 48 (10):1870–1875, 2009.

J. Mohd-Yosuf. Combined immersed boundary/B–spline methods for simulation off low in complex geometries. *Annual Research Briefs. NASA Ames Research Center; Stanford University Center of Turbulence Research: Stanford*, pages 317–327, 1997.

P. Moin. Advances in large eddy simulation methodology for complex flows. *International Journal of Heat and Fluid Flow*, 23(5):710–720, 2002.

P. Moin, K. Squires, W. Cabot and S. Lee. A dynamic subgrid–scale model for compressible turbulence and scalar transport. *Physics of Fluids A: Fluid Dynamics*, 3:2746, 1991.

P. Moore, H.J. Slot and B.J. Boersma. Simulations and measurements of flow generated noise. *Journal of Computational Physics*, 224(1):449–463, 2007.

K. Morgan. A numerical analysis of freezing and melting with convection. *Computer Methods in Applied Mechanics and Engineering*, 28(3):275 – 284, 1981.

S. Nagarajan, Sanjiva K. Lele and J.H. Ferziger. A robust high–order compact method for large eddy simulation. *Journal of Computational Physics*, 191(2):392–419, 2003.

N. Nithyadevi, P. Kandaswamy and J. Lee. Natural convection in a rectangular cavity with partially active side walls. *International Journal of Heat and Mass Transfer*, 50(23): 4688–4697, 2007.

H. Noda, M. Ikeda, Y. Kimura and K. Kawabata. Development of high–performance heat sink 'crimped fin'. *Furukawa Review*, 27:14–19, 2005.

J.P. O'Conner and R.M. Weber. Thermal management of electronic packages using solid-to-liquid phase change techniques. *International Journal of Microcircuits and Electronic Packaging*, 20(4):593–601, 1997.

M. Okada. Analysis of heat transfer during melting from a vertical wall. *International Journal of Heat and Mass Transfer*, 27(11):2057–2066, 1984.

H. Okanaga and T. Tanahashi. Numerical analysis of natural convection in a square cavity at high Rayleigh numbers using the GSMAC finite-element methods. *Transactions of the Japan Society of Mechanical Engineers*, 56:2922–2929, 1990.

P. Orlandi. *Fluid Flow Phenomena: A Numerical Toolkit.* Springer, 2000.

P. Orlandi and R. Verzicco. Vortex Rings Impinging on Walls: Axisymmetric and Three–Dimensional Simulations. *Journal of Fluid Mechanics*, 256:615–615, 1993.

N. Ouertatani, N.B. Cheikh, B.B. Beya and T. Lili. Numerical simulation of two-dimensional Rayleigh–Bénard convection in an enclosure. *Comptes Rendus Mécanique*, 336 (5):464 – 470, 2008.

D. Pal and Y.K. Joshi. Melting in a side heated tall enclosure by a uniformly dissipating heat source. *International Journal of Heat and Mass Transfer*, 44(2):375–387, 2000.

J. Pallaras, I. Cuesta, F.X. Grau and F. Giralt. Natural convection in a cubical cavity heated from below at low Rayleigh numbers. *International Journal of Heat and Mass Transfer*, 39(15):3233–3247, 1996.

J. Pallares, I. Cuesta and F.X. Grau. Laminar and turbulent Rayleigh–Bénard convection in a perfectly conducting cubical cavity. *International Journal of Heat and Fluid Flow*, 23 (3):346 – 358, 2002.

S. Paolucci. Direct simulation of two dimensional turbulent natural transition in an enclosed cavity. *Journal of Fluid Mechanics*, 215:229–262, 1990.

S. Paolucci and D.R. Chenoweth. Transition to chaos in a differentially heated cavity. *Journal of Fluid Mechanics*, 201:379–410, 1990.

Y.G. Park, H.S. Yoon and M.Y. Ha. Natural convection in square enclosure with hot and cold cylinders at different vertical locations. *International Journal of Heat and Mass Transfer*, 55(25–26):7911 – 7925, 2012.

R. Pember and J. Bell. An adaptive Cartesian grid method for unsteady compressible flow in irregular regions. *Journal of computational Physics*, 120(2):278–304, 1995.

X.F. Peng. Convective heat transfer and flow friction for water flow in microchannel structures. *International Journal of Heat and Mass Transfer*, 39(12):2599–2608, 1996.

F. Penot. Numerical calculation of two–dimensional natural convection in isothermal open cavities. *Numerical Heat Transfer, Part A Applications*, 5(4):421–437, 1982.

C.S. Peskin. Flow Patterns Around Heart Valves: A Digital Computer Method for Solving the Equations of Motion. *PhD thesis.*, 1972.

C.S. Peskin. Numerical analysis of blood flow in the heart. *Journal of Computational Physics*, 25(3):220–252, 1977.

C.S. Peskin. Lectures on mathematical aspects of physiology. *Lectures Applied Mathematics*, 19:1–107, 1981.

C.S. Peskin and D.M. McQueen. A three–dimensional computational method for blood flow in the heart:(i)immersed elastic fibers in a viscous incompressible fluid. *Journal of Computational Physics*, 81(2):372–405, 1989.

O. Polat and E. Bilgen. Conjugate heat transfer in inclined open shallow cavities. *International Journal of Heat and Mass Transfer*, 46(9):1563–1573, 2003.

S. Popinet. A tree-based adaptive solver for the incompressible Euler equations in complex geometries. *Journal of Computational Physics*, 190(2):572–600, 2003.

M. Prakash, S.B. Kedare and J.K. Nayak. Investigations on heat losses from a solar cavity receiver. *Solar Energy*, 83(2):157–170, 2009.

R. Prasher and R. Mahajan. Two–phase cooling utilizing microchannel heat exchangers and channeled heat sink., June 2005. US Patent 6,903,929.

W. Qu and I. Mudawar. Experimental and numerical study of pressure drop and heat transfer in a single-phase micro–channel heat sink. *International Journal of Heat and Mass Transfer*, 45(12):2549–2565, 2002.

P. Le Quéré. *Étude de la transition à l'instationnarité des écoulements de convectionnarurelle en cavité verticale différentiellement chauffée par méthodesspectrales Chebyshev.* PhD thesis, Thèse s'Etat: Université de Poitiers, 1987.

P. Le Quéré. Accurate solutions to the square thermally driven cavity at high Rayleigh number. *Computational Fluids*, 20(1):29–41, 1991.

P. Le Quéré, J.A.C. Humphrey and F.S. Sherman. Numerical calculation of thermally driven two–dimensional unsteady laminar flow in cavities of rectangular cross section. *Numerical Heat Transfer*, 4(3):249–283, 1981.

M. Rai and P. Moin. Direct Simulations of Turbulent Flow Using Finite–Difference Schemes. *Journal of Computational Physics*, 96(1):15–53, 1991.

F. Roman, E. Napoli, B. Milici and V. Armenio. An improved immersed boundary method for curvilinear grids. *Computers & Fluids*, 38(8):1510–1527, 2009.

E.M. Saiki and S. Biringen. Numerical simulation of a cylinder in uniform flow: Application of a virtual boundary method. *Journal of Computational Physics*, 123(2):450–465, 1996.

T.S. Saitoh and K. Hirose. High–accuracy benchmark solutions to natural convection in a square cavity. *Computational Mechanics*, 4(6):417–427, 1989.

A. Samba, H. Louahlia-Gualous, S. Le Masson and D. Nörtershäuser. Two–phase thermosyphon loop for cooling outdoor telecommunication equipments. *Applied Thermal Engineering*, 50(1):1351–1360, 2013.

R.R. Schmidt and H. Shaukatullah. Computer and telecommunications equipment room cooling; a review of literature. *IEEE Transactions, Components and Packaging Technologies*, 26(1):89–98, 2003.

L. Schneiders, D. Hartmann, M. Meinke and W. Schröder. An accurate moving boundary formulation in cut–cell methods. *Journal of Computational Physics*, 235(0):786 – 809, 2013.

G.A. Sedelnikov, F.H. Busse and D.V. Lyubimov. Convection in a rotating cubical cavity. *European Journal of Mechanics – B/Fluids*, 31(0):149 – 157, 2012.

I. Sezai and A.A. Mohamad. Three–dimensional simulation of natural convection in cavities with side opening. *International Journal of Numerical Methods for Heat & Fluid Flow*, 8(7):800–813, 1998.

A.K.A. Shati, S.G. Blakey and S.B.M. Beck. An empirical solution to turbulent natural convection and radiation heat transfer in square and rectangular enclosures. *Applied Thermal Engineering*, 51(1-2):364 – 370, 2013.

T.W.H. Sheu and R.K. Lin. Newton linearization of the incompressible Navier–Stokes equations. *International Journal for Numerical Methods in Fluids*, 44(3):297–312, 2004.

T.W.H. Sheu and R.K. Lin. On a high–order Newton linearization method for solving the incompressible Navier–Stokes equations. *International Journal for Numerical Methods in Engineering*, 62(11):1559–1578, 2005.

T. M. Shih, C. H. Tan and B. C. Hwang. Effect of grid staggering on numerical schemes. *International Journal for Numerical Methods in Fluids*, 9(2):193–212, 1989.

A.L.F.L.E. Silva, A. Silveira-Neto and J.J.R. Damasceno. Numerical simulation of two–dimensional flows over a circular cylinder using the immersed boundary method. *Journal of Computational Physics*, 189(2):351–370, 2003.

S.W. Su, M.C. Lai and C.A. Lin. An immersed boundary technique for simulating complex flows with rigid boundary. *Computers & Fluids*, 36(2):313–324, 2007.

C.R. Swaminathan and V.R. Voller. Towards a general numerical scheme for solidification systems. *International journal of heat and mass transfer*, 40(12):2859–2868, 1997.

K. Taira and T. Colonius. The immersed boundary method: A projection approach. *Journal of Computational Physics*, 225(2):2118–2137, 2007.

F.L. Tan and C.P. Tso. Cooling of mobile electronic devices using phase change materials. *Applied Thermal Engineering*, 24(2–3):159–169, 2004.

C. Taylor and P. Hood. A numerical solution of the Navier–Stokes equations using the finite element technique. *Computers & Fluids*, 1(1):73–100, 1973.

B.Y. Tong, T.N. Wong and K. Ooi. Closed-loop pulsating heat pipe. *Applied Thermal Engineering*, 21(18):1845–1862, 2003.

F.J. Tou and W.X.F. Zang. Three-Dimensional Numerical Simulation of Natural Convection in an Inclined Liquid–Filled Enclosure with an Array of Discrete Heaters. *International Journal of Heat Mass Transfer*, 46(1):127–138, 2003.

Y.H. Tseng and J.H. Ferziger. A ghost–cell immersed boundary method for flow in complex geometry. *Journal of Computational Physics*, 192(2):593 – 623, 2003.

C.P. Tso, L.F. Jin, S.K.W. Tou and X.F. Zhang. Flow Pattern Evolution in Natural Convection Cooling from an Array of Discrete Heat Sources in a Rectangular Cavity at Various Orientations. *International Journal of Heat Mass Transfer*, 47(19–20):4061–4073, 2004.

D.B. Tuckerman and R.F.W. Pease. High performance heat sink for VLSI. *IEEE Electron Device Letter*, 2(5):126–129, 1981.

H.S. Udaykumar, R. Mittal, P. Rampunggoon and A. Khanna. A Sharp Interface Cartesian Grid Method for Simulating Flows with Complex Moving Boundaries. *Journal of Computational Physics*, 174(1):345 – 380, 2001.

H.S. Udaykumar, R. Mittal and W. Shyy. Computation of solid-liquid phase fronts in the sharp interface limit on fixed grids. *Journal of Computational Physics*, 153(2):535–574, 1999.

K. Vafai and W. Wang. Analysis of flow and heat transfer characteristics of an asymmetrical flat plate heat pipe. *International Journal of Heat and Mass Transfer*, 35(9):2087–2099, 1992.

L. Valencia, J. Pallares, I. Cuesta and F.X. Grau. Turbulent Rayleigh–Bénard convection of water in cubical cavities: A numerical and experimental study. *International Journal of Heat and Mass Transfer*, 50:3203 – 3215, 2007.

J. Valenzuela, T. Jasins and Z. Sheik. Liquid cooling for high–power electronics, power electronics. *Power Electronics Technology*, 31(2):50–56, 2005.

L.L. Vasiliev. Applied Thermal Engineering. *International Journal of Thermal Science*, 25: 1–19, 2005.

R. Velraj, R.V. Seeniraj, B. Hafner, C. Faber and K. Schwarzer. Heat transfer enhancement in a latent heat storage system. *Solar Energy*, 65(3):171–180, 1999.

R.W.C.P. Verstappen and A.E.P. Veldman. Symmetry–preserving discretization of turbulent flow. *Journal of Computational Physics*, 187(1):343–368., 2003.

R. Verzicco. Large–Eddy–Simulation of Complex Flows Using the Immersed Boundary Method. In *Engineering Turbulence Modelling and Experiments 6*. Elsevier Science B.V., 2005.

R. Verzicco and P. Orlandi. A finite–difference scheme for three–dimensional incompressible Flows in cylindrical coordinates. *Journal of Computational Physics*, 123(2):402–414, 1996.

G. Vidalain, L. Gosselin and M. Lacroix. An enhanced thermal conduction model for the prediction of convection dominated solid–liquid phase change. *International Journal of Heat and Mass Transfer*, 52(7–8):1753 – 1760, 2009.

M.R. Visbal and D.V. Gaitonde. On the use of higher–order finite difference schemes on curvelinear and deforming mesh. *Journal of Computational Physics*, 181(1):155–185, 2002.

V. Voller and M. Cross. Accurate solutions of moving boundary problems using the enthalpy method. *International journal of heat and mass transfer*, 24(3):545–556, 1981.

V.R. Voller. A fixed grid numerical modelling methodology for convection–diffusion mushy region phase–change problems. *International Journal of Heat and Mass Transfer*, 30(8): 1709–1719, 1987.

C.B. Vreugdenhil and B. Koren. *Numerical methods for advection–diffusion problems.* Notes on numerical fluid mechanics. Friedrich Vieweg & Sohn Verlagsgesellschaft, 1993.

S. Wakashima and T.S. Saitoh. Benchmark solutions for natural convection in a cubic cavity using the high–order time–space method. *International Journal of Heat and Mass Transfer*, 47(4):853 – 864, 2004.

E. Walsh and R. Grimes. Low profile fan and heat sink thermal management solution for portable applications. *International Journal of Thermal Sciences*, 46(11):1182–1190, 2007.

H. Wang and M.S. Hamed. Flow mode–transition of natural convection in inclined rectangular enclosures subjected to bidirectional temperature gradients. *International Journal of Thermal Sciences*, 45(8):782 – 795, 2006.

S. Wang, A. Faghri and T.L. Bergman. A comprehensive numerical model for melting with natural convection. *International Journal of Heat and Mass Transfer*, 53(9–10):1986 – 2000, 2010a.

X.Y. Wang, P. Yu, K.S. Yeo and B.C. Khoo. SVD–GFD scheme to simulate complex moving body problems in 3D space. *Journal of Computational Physics*, 229(6):2314 – 2338, 2010b.

R. Warrington and R. Powe. The transfer of heat by natural convection between bodies and their enclosures. *International Journal of Heat and Mass Transfer*, 28(2):319–330, 1985.

W. Wu and C.Y. Ching. Laminar natural convection in an air-filled square cavity with partitions on the top wall. *International Journal of Heat and Mass Transfer*, 53(9–10):1759 – 1772, 2010.

S. Xin and P. Le Quéré. Direct numerical simulations of two–dimensional chaotic natural convection in a differentially heated cavity of aspect ratio 4. *Journal of Fluid Mechanics*, 304:87–118, 1995.

S. Xin, P. Le Quéré and O. Daube. Natural Convection in a differentially heated horizontal cylinder: Effects of Prandtl number on flow structure and instability. *Physics of Fluids*, 9 (4):1014–1033, 1997.

J.J. Xu, Z. Li, J. Lowengrub and H. Zhao. A level–set method for inter facial flows with surfactant. *Journal of Computational Physics*, 212(2):590, 2006.

J.L. Xu, Y.X. Li and T.N. Wong. High speed flow visualization of a closed loop pulsating heat pipe. *International Journal of Heat and Mass Transfer*, 48(16):3338–3351, 2005.

S. Xu and Z.J. Wang. An immersed interface method for simulating the interaction of a fluid with moving boundaries. *Journal of Computational Physics*, 216(2):454–493, 2006a.

S. Xu and Z.J. Wang. Systematic derivation of jump conditions for the immersed interface method in three dimensional flow simulation. *SIAM Journal of Scientific Computing*, 27(6): 1948–1980, 2006b.

H. Yang, S. Khandekar and M. Groll. Performance characteristics of pulsating heat pipes as integral thermal spreaders. *International Journal of Thermal Sciences*, 48(4):815–824, 2009.

J. Yang and E. Balaras. An embedded–boundary formulation for large–eddy simulation of turbulent flows interacting with moving boundaries. *Journal of Computational Physics*, 215 (1):12–40, 2006.

T. Ye, R. Mittal, H.S. Udaykumar and W. Shyy. An Accurate Cartesian Grid Method for Viscous Incompressible Flows with Complex Immersed Boundaries. *Journal of Computational Physics*, 156(2):209 – 240, 1999.

J.H. Yoo, J.I. Hong and W. Cao. Piezoelectric Ceramic Bimorph Coupled to Thin Metal Plate as Cooling Fan for Electronic Devices. *Sensors and Actuators A: Physical*, 79(1):8–12, 2000.

H.S. Yoon, D.H. Yu, M.Y. Ha and Y.G. Park. Three–dimensional natural convection in an enclosure with a sphere at different vertical locations. *International Journal of Heat and Mass Transfer*, 53(15–16):3143 – 3155, 2010.

B. Zalba, J.M. Marin, L.F. Cabeza and H. Mehlin. Free–cooling of building with phase change materials. *International Journal of Refrigeration*, 27(8):839–849, 2004.

M. Zhang, Z. Liu and G. Ma. The experimental investigation on thermal performance of a flat two–phase thermosyphon. *International Journal of Thermal Sciences*, 47(9):1195–1203, 2008.

N. Zhang and Z.C. Zheng. An improved direct–forcing immersed–boundary method for finite difference applications. *Journal of Computational Physics*, 221(1):250 – 268, 2007.

Y. Zhang and A. Faghri. Heat transfer in a pulsating heat pipe with open end. *International Journal of Heat and Mass Transfer*, 45(4):755–764, 2002.

H. Zhao, J.B. Freund and R.D. Moser. A fixed–mesh method for incompressible flow–structure systems with finite solid deformations. *Journal of Computational Physics*, 227(6): 3114–3140, 2008.

N. Zheng and R. Wirtz. A hybrid thermal energy storage device, part 1: design methodology. *Journal of Electronic Packaging*, 126(1):1–7, 2004.

Y. Zvirin, A. Shitzer and G. Grossman. The natural circulation solar heater–models with linear and nonlinear temperature distributions. *International Journal of Heat and Mass Transfer*, 20(9):997–999, 1997.